UNIVERSITY OF
LIVERPOOL
SCHOOL OF
ENGINEERING

Control of Biological Responses by Isolated Synthetic Material Variables

Thesis submitted in accordance with the requirements of the University of Liverpool

for the degree of

Doctor of Philosophy

by I-Ning Lee

February, 2019

Abstract

It is well established that cells sense and respond to stimuli at the sub-micron and nanometre scale, a factor that must be considered in future biomaterial design. The understanding of how biological entities interact with material features at this scale is limited due to the limitations of material fabrication techniques that can readily isolate enrichment of a surface with a chemical group, whilst reproducibly controlling nanotopography and stiffness.

Polymer pen lithography (PPL), a nanotechnology that has advanced the technique of single probe nanolithography in combination with traditional microcontact printing, has since been introduced due to its capability of fabricating high throughput surface patterns over large surface areas (multiple cm^2) in a short period of time.

In this work, PPL has been used as a powerful nanotechnique to fabricate reproducible surface nanofeatures with a size of 300 nm with various centre-to-centre distances using a range of chemicals as “inks” with presentation of pre-selected carboxyl and amino groups on appropriate surfaces as “papers”. These fabricated surfaces have been used to evaluate the isolated and combitorial effects of changes in surface chemistry and topography on mesenchymal stem cell and chondrocyte adhesion and phenotype *in vitro*. Carboxylic acid terminated nanoarrays with various centre-to-centre distance have been proven to induce mesenchymal stem cell towards chondrogenesis and hypertrophic chondrogenesis. In addition, the selected carboxylic acid terminated nanoarrays successfully promoted the maintenance of chondrogenic phenotype of articular chondrocytes over 3 experimental passages. Conversely, amino terminated nanoarrays with various centre-to-centre distance potentially supported mesenchymal stem cell differentiation towards adipogenesis.

In addition to understanding the role of surface chemistry on initial cell response, the *in situ* control of stiffness at a molecular level has been studied. A range of photoresponsive molecules were synthesised and incorporated within the hydrogel network. Preliminary cell-surface interactions were established with these hydrogels. The developed nanofabrication methodology and established parameters exhibited unprecedented control of cell morphology, differentiation and maintenance of phenotypes that has improved the fundamental understanding of mechanical signalling events.

Table of Contents

Table of Figures

List of Tables

List of Schemes

Acknowledgements

First of all, I would like to thank my supervisors Dr. Judith Curran, Dr. Nick Rhodes and Prof. John Hunt for their guidance, patience and support throughout my PhD. Especially Jude, her commitment and guidance every step of the way has been the most helpful inspiration in my life. Without her, none of this would have been possible. I would like to thank Dr. Rui Chen not only for his assistance and training on various aspects of this project. He has been my mentor especially with guidance in choice of future career.

To all my friends and colleagues whom I shared the labs with, I would like to thank you for cheering me up during the bad days, entertained me while I was losing my mind. Thank you for doing chores for me while I was split in multiple locations with random schedules.

I would like to especially thank my brother who has always helped me, in the middle of the night, with random chemistry questions I came up with. My father who devoted and sacrificed his life raising me up, you are the reason I am who and where I am today.

I suppose I should also thank Tommy, mainly because he asked for it, for bearing with my temper during bad days (most of the days were probably bad days…). He also played an important role while I was writing up this thesis – keeping me fed and hydrated while I was stuck with my laptop.

List of Abbreviations

Abbreviation	**Long names**
2D	Two-dimensional
3D	Three-dimensional
AFM	Atomic force microscopy
ALP	Alkaline phosphatase
AM	Acrylamide
ANOVA	Analysis of variance
APTES	(3-Aminopropyl)triethoxysilane
Asc	Ascorbic acid
AUT	11-Amino-1-undecanethiol hydrochloride
BMP	Bone morphogenetic proteins
BPTS	(3-Bromopropyl)trimethoxysilane
C/EBPβ	CCAAT/enhancer binding protein β
CBFA1	Core-binding factor subunit alpha-1
cDNA	Complementary deoxyribonucleic acid
DAPI	4',6-Diamidino-2-phenylindole
DCC	N,N’-Dicyclohexyl carbodiimide
DCM	Dichloromethane
Dex	Dexamethasone
DIC	N,N’-Diisopropyl carbodiimide
DMEM	Dulbecco's modified eagle's medium
DMF	N,N-Dimethylformamide
DPBS	Dulbecco's phosphate buffered saline
DPN	Dip-pen nanolithography
dsDNA	Double-stranded deoxyribonucleic acid
ECM	Extracellular matrix
EDC	N-(3-Dimethylaminopropyl)-N'-ethylcarbodiimide hydrochloride
ESEM	Environmental scanning electron microscope

EtOAc	Ethyl acetate
EtOH	Ethanol
FA	Focal adhesion
F-actin	Filamentous actin
FAK	Focal adhesion kinase
FBS	Fetal bovine serum
FDTS	Perfluorodecyltrichlorosilane
FGF	Fibroblast growth factor
FHL2	LIM-domain protein with 4.5 LIM domains
FITC	Fluorescein isothiocyanate
FN	Fibronectin
FPN	Fountain-pen nanolithography
GAG	Glycosaminoglycan
GAPDH	Glyceraldehyde 3-phosphate dehydrogenase
HDF	Human dermal fibroblasts
HOAt	1-Hydroxy-7-azabenzotriazole
HOBt	N-Hydroxybenzotriazole
HOSu	N-Hydroxysuccinimide
IBMX	Isobutyl-methylxanthine
IGF	Insulin-like growth factor
IM	Indomethacin
LAS	Leica application suite
LED	Light emitting diodes
LFD	Large field detector
MAPK	Mitogen-activated protein kinase
MHA	16-Mercaptohexadecanoic acid
MMP	Matrix metalloproteinase
m-PEG	(11-Mercaptoundecyl)hexa(ethylene glycol)
mRNA	Messenger ribonucleic acid
MSC	Mesenchymal stem cell
NaH	Sodium hydride

NaOH	Sodium hydroxide
NHAC	Normal human knee articular chondrocyte
PA	Polyacrylamide
PDMS	Polydimethylsiloxane
PEG	Polyethylene glycol
PFA	Paraformaldehyde
$pFAK_{Y397}$	Phosphorylated focal adhesion kinase at tyrosine 397
PKC	Protein kinase C
PLA	Polylactic acid
PLGA	Poly(lactic-co-glycolic acid)
PPARγ	Peroxisome proliferator-activated receptor γ
PPL	Polymer pen lithography
PSS	Photostationary state
PU	Polyurethane
qPCR	Quantitative polymerase chain reaction
RGD	Arginine−glycine−aspartate
RT-PCR	Reverse transcription polymerase chain reaction
SAMs	Self-assembled monolayers
SE	Secondary electron
SEM	Scanning electron microscope
SOX9	SRY-box 9
SPM	Scanning probe microscopy
TCP	Tissue culture polystyrene
TE	Tris-EDTA
TEA	Triethylamine
TEMED	*N,N,N',N'*-Tetramethylethylenediamine
TFA	Trifluoroacetic acid
TG2	Tissuetransglutaminase
TGF-β1	Transforming growth factor beta 1
THF	Tetrahydrofuran
XPS	X-ray photoelectron spectroscopy

β-Gly	β-Glycerophosphate
μCP	Microcontact printing

Chapter 1

Introduction and Literature Review

1.1 Tissue engineering

Tissue engineering, an interdisciplinary field, is concerned with the application of the principles of biology and engineering to the development of functional substitutes for damaged tissue.[1] It is a relatively new field which applies living cells, biocompatible materials (biomaterials), biochemical and physical factors to establish the simulation of *in vivo* systems as efficient treatment options where all other medical treatments have failed.[2] Tissue engineering was first proposed by Langer and Vacanti and stated as an interdisciplinary field which applies the principles of biology and engineering to the development of functional substitutes for damaged tissue.[1]

The ability to restore tissue function is a significant target in clinical research due to the ageing population as the development of new cost-effective therapies is required to meet the demands of the ageing population. The main targets of this type of therapy are those tissues which are exposed on the surface, prone to injury, disease or degeneration, such as skin, the nervous system or organs. The majority of tissue engineered therapeutic methods utilise living cells which are mostly obtained from donor tissue, stem cells or progenitor cells. A key requirement for the application of effective tissue engineering is a suitable cellular environment which mimics some critical properties in native tissues, thus allowing cells to function as they would be in the human body. A good artificial biocompatible material, such as scaffolds, would allow cells to be implanted and support three-dimensional tissue formation and have certain properties, such as mechanical rigidity or flexibility and allowing cell attachment and migration. Based on these requirements, it is generally accepted that porous environments perform well.[3-5]

A wide range of cell types have the potential to be used in tissue engineering applications, depending on the nature of the cell phenotype required and the tissue destined for repair. However, many traditional clinical applications require cell collection and *in vitro* expansion of terminally differentiated cells to produce a populated matrix resembling the native tissue.[6] The invasive nature of cell explantation and the potential for these cells to be in a diseased state makes it challenging for this treatment approach to be applied in tissue engineering.

1.1.1 The role of stem cells in tissue engineering

Stem cells are known for their ability to self-renew and their multilineage differentiation potential. In particular, mesenchymal stem cells (MSCs) have the capacity to readily differentiate into connective tissues.[7] MSCs are defined as adult stem cells that could be terminally differentiated into, but not limited to, bone, cartilage or adipose cells, *etc*.[8] Bone-marrow derived MSCs have the capability to undergo extensive replication *ex vivo* and can also be used in *in vivo* transplant applications.[9] Prior to transplant, the cells in culture must be combined with an appropriate supporting carrier or scaffold so that a vascular bed can be established, enabling the transplanted cells to differentiate and form the targeted tissue.[9]

As the field of tissue engineering has advanced, a number of novel scaffolds have been developed using various types of materials such as three-dimensional scaffolds[10-12] and hydrogels[13, 14] using conventional or novel polymers. These biocompatible materials are known as biomaterials and have been developed to act as an appropriate carrier for stem cells in tissue engineering applications.[15]

1.2 Biomaterials

Biomaterials are natural or synthetic materials that interact with biological systems and often support an improvement in, or replace natural functions *in vitro* or *in vivo*, when combined with the appropriate cell type. They are used to temporarily or permanently replace the lost or malfunctioning tissues in order to maintain or improve the quality of life of an individual. Biomaterials can be classified into non-degradable or degradable biomaterials.

Non-degradable biomaterials were initially developed for use as permanent implants, such as tooth fillings and metal implants for bone replacement.[16] However, these implants have major limitations including limited healing, destructive inflammation and the development of biomaterial-associated infection.[17] Bacterial infection can occur at any stage of the lifetime of the implant, sometimes caused by an infection elsewhere in the body.[18]

To address the issue of infection risk, a range of degradable biomaterials were introduced. It has been reported that the use of degradable biomaterials, instead of non-degradable biomaterials, has been effective in decreasing the risk of bacterial infection in pre-clinical *in vivo* studies.[19, 20] In addition, some clinically-tested degradable biomaterial implants have shown evidence of the reduction in pain, allergic reactions, implant migration and growth restrictions.[17, 21]

Degradable biomaterials of a bioactive nature present both physical and chemical properties that mimic living tissues. A range of degradable biomaterials can be classified into three types.

Naturally-derived matrix such as polysaccharide-derived alginate, a non-toxic and non-inflammatory natural polymer has controllable properties and the potential of linking with other biological molecules.[22] However, alginate-based matrices alone suffer from certain limitations including mechanical weakness and poor cell adhesion, requiring the incorporation of other polymers or biological molecules.[23]

Acellular matrices are obtained from the decellularisation of tissues by crosslinking using chemical treatments, typically glutaraldehyde or water soluble carbodiimides.[24] These pre-treatments aimed to sterilise the materials while enhancing the resistance of enzymatic or hydrolytic degradation and reducing their immunogenicity. However, these pre-treatment methods tend to alter the mechanical properties of the matrix increasing the risk of failure at an early stage by tearing or through calcification of the tissue.[25]

Synthetic polymer-based degradable materials such as polylactic acid (PLA) and poly(lactic-co-glycolic acid) (PLGA) have been introduced in therapeutic applications. This wide range of polymers or co-polymers have been developed with the capacity of controlling physical, chemical, biological, mechanical and degradation properties to suit various requirements for individual therapy.[26] The versatile potential of these polymeric materials that control the essential properties of materials has resulted in rapid replacement of metals and alloys in biomaterials applications.

Degradable polymers undergo either hydrolytic or enzymatic degradation.[26, 27] The capability of a hydrolytically-degradable polymeric matrix to degrade depends on the hydrolytically-sensitive bond present within it. The rate of degradation depends on the bulk hydrophilicity of the polymeric structure that impacts water uptake, its porosity and material surface area combined with the pH of the surrounding environment.[27] It has been reported that hydrophilic polymer chains, such as polyethylene glycol (PEG), can be incorporated within bulk polymer chains in order to increase hydrophilicity thus accelerating hydrolytic degradation and complete polymer erosion to within 24 h rather than years.[28]

Enzymatically-degradable polymeric matrices degrade at the point of contact with enzymes secreted by microorganisms.[29] Enzymatic degradation occurs either by oxidation or hydrolysis. For example, polyurethane (PU)-based polymeric structures degrade by oxidative enzymes such as horseradish peroxidase, catalase or xanthine oxidase.[30] The degradable polymer could also undergo enzymatic-catalysed hydrolysis by hydrolases, such as proteases, esterases, glycosidases, and phosphatases.[31] The degradation rate can be affected by chemical modification of the polymeric substrate such as crosslinking or alteration of the polymer chain.

This research focuses on the surface modifications of degradable and non-degradable biomaterials to enhance clinical performance and control of cell function.

1.2.1 Cell interactions on biomaterial surface

Cell responses to biomaterials can be characterised based upon timelines.[32] When biomaterials are placed in a biological environment, a water shell layer is created within the first few nanoseconds. The hydrophilicity and surface patterning control this interaction and determine the adhesion of proteins and other factors on the surface following surface hydration. The surfaces of biomaterial substrates are then covered in an absorbed layer of proteins as extracellular matrix (ECM).

From minutes to hours of introduction of the biomaterials into the environment, cells attach and interact with the surface-bound proteins. These adhered cells then migrate and/or differentiate, a phenomenon that is affected by the surface-absorbed ECM, cell membrane proteins and cytoskeleton proteins. Cell-surface interactions are also affected by the physicochemical properties of the surface such as surface chemistry, topography and porosity at the micron to nano-scale.

Engineered biomaterials, from naturally-derived or synthetic polymers, are rarely flat at the molecular level. The majority of surface modification methods intentionally or unintentionally introduce additional features such as topography or dynamic alteration.[33, 34] These topographic differences at the micron to nano-scale have been shown to significantly affect initial cell adhesion and ultimately the potential to differentiate.[35-37] These surface modifications are therefore of interest for understanding the effects of surface chemistry and topography in terms of cellular response.

1.2.2 Stem cell interactions on biomaterials

Stem cells have the ability to detect and respond to stimuli at the sub-micron scale.[38, 39] Therefore, in order to control protein and cellular interactions, synthetic biomaterials should be designed at a sub-micron scale. Previous research has identified a number of methods such as microcontact printing (µCP) to modify selected areas with chemical patterns and/or bulk coating of self-assembled monolayers (SAMs) for full coverage of surface materials with pre-selected chemical groups.[2] More recently, three-dimensional (3D) hydrogel scaffolds with simple chemical functionality have been observed to have the ability to induce stem cell differentiation, indicating that material-induced control of stem cell phenotype is viable on both model surfaces and 3D materials.[40] In terms of surface functionalised materials, previous research has identified a number of chemical modifications (*i.e.,* amino, carboxylic, hydroxyl and methyl) that can be used to enhance selective protein adsorption and trigger stem cell differentiation on a number of base substrates.[41]

Biomaterials can be used to assess the effect of modification of chemistry, topography or physical environment on cells. Recently, the effect of these variables on the differentiation and self-renewal of stem cells has been studied.[2] In the past decades, a few studies on stem cell differentiation in normal culture with supplementation of differentiation factors have been published.[42, 43] Relatively recently, researchers have published preliminary results demonstrating that nanotopography can induce differentiation without the need for supplementation of specific culture media.[44]

It has been observed that the interaction of human MSCs with a surface presenting alkyl groups results in an increase in protein adhesion, deposition and retention of MSC markers.[45] In contrast, surfaces presenting amino groups enhanced vitronectin adsorption, inducing osteogenic differentiation of the stem cell. In addition, substrates presenting carboxylic and hydroxyl groups have been observed to preferentially absorb fibronectin, resulting in chondrogenic differentiation. Yet the ability to isolate variables using these methods remains limited and the information about the relationship between ECM adsorption and MSC differentiation is inadequate.

1.2.3 Cellular mechanotransduction

Cells and tissues adapt to physical forces and chemical stimuli locally in the human body. Mechanotransduction is the process by which living cells integrate these signals to biochemical processes resulting in changes in gene expression.[46] Mechanotransduction coordinates cell adhesion, migration, morphology and regulation of cell fate and is potentially controlled by stimuli received from the external environment, both physically and mechanically, with formation of focal adhesions.

The majority of cells in the living body require attachment to an ECM, a polymer-like structure, to function properly. It has long-since been discovered that arginine−glycine−aspartate (RGD) from fibronectin is the primary transmembrane molecule that mediates cell-matrix adhesion.[47] Subsequently many integrin subtypes have been discovered consisting of various combinations of α and β integrin heterodimers. When an integrin is inactive, ECM proteins, such as fibronectin, or cytoplasmic proteins, such as talin, can induce integrin activation.[48] Integrin activation alone is insufficient for many crucial cellular functions such as cell morphology, proliferation and differentiation. Focal adhesions (FAs), protein complexes consisting of clustered groups of integrins and other cytoplasmic proteins, have been reported to signal mechanical force to cytoskeletons.[46]

Forces generated by the cellular cytoskeleton are sensed by adhesion sites and lead to change in morphology through intercellular processes.[49] Mechanical force plays a critical role in integrin-mediated mechanical signalling. It is now accepted that the primary role of integrins is to mediate mechanical signalling and to recruit cytoplasmic proteins to the FAs.[46]

Many mechanical cues have been reported to influence stem cell fate including chemistry, topography and elasticity.[2]

1.2.3.1 The role of surface chemistry in mechanotransduction

The versatility of synthetic chemistry provides a potential platform for an enhanced definition of the composition of the surface. In turn, this enables the control of pre-designated ligands to be controlled and presented on a surface.[2] This has allowed individual chemical groups as found in ECM to be studied in cell signalling. Surfaces can be funtionalised using μCP to produce specific regions enriched with a selected chemical group or SAMs to potentially achieve homogeneous layers enriched with chemical groups.[50-53]

Microcontact printing has been studied and shown to induce changes in cell shape, area of spreading and ECM density that has an influence on mechanical signalling during terminal differentiation.[54] Whereas SAMs can precisely tailor the density of desired ligands attached to the surface. This was initially achieved by the surface binding of RGD at low and high densities and different orientations to study the influence on cell fate.[55] More recently, presentation of "pure" chemistry has been developed to investigate the use of synthetic chemical functional groups presenting on the surface and their associated influences of cell fate.[56]

Using simple chemistry, surface enrichment with selected groups has been shown to encourage deposition of appropriate adsorption of protein from serum onto surfaces, subsequently dictating MSC differentiation or retention of phenotype and preservation of stem cell growth.[33, 57, 58] An achievement of purely synthetic surface chemistry avoids the complications of use of protein ECM and its batch-to-batch variation, thus potentially improving the reproducibility and cost effectiveness of material-induced control of cell fate.

1.2.3.2 The role of topography in mechanotransduction

Topographically-defined surfaces have also been used to study cellular mechanotransduction.[36, 59, 60] Early research identified that topographical signalling with cellular interactions has an effect on cell proliferation, morphology and gene expression.[36]

Nanotopography has been reported to induce changes in focal adhesion assembly, cytoskeletal organisation and mechanical properties.[35] It has been established that MSCs respond to nanotopography through an integrin-focal adhesion-cytoskeleton pathway. More specifically, it has been reported that nanotopography has the potential to modulate stem cell differentiation *via* focal adhesion kinase (FAK) through FAK phosphorylation.[59] Nanotopography can also enhance the specific cellular phenotypes in addition to surface chemistry.[33]

1.2.3.3 The role of elasticity in mechanotransduction

Different tissues within the body exhibit a range of elasticities and local ECM allows cells to regulate appropriate cellular functions. Solid tissues exhibit different elasticity (stiffness) in various microenvironments. Cells respond to the corresponding stiffness in the microenvironment by initial adherence to the substrate, at a molecular scale, therefore highlighting the role of stiffness in mechanotransduction.[38]

Cellular mechanotransducers generate signals based on the forces received and with stem cell fate being affected. To investigate the role of stiffness, studies have employed a range of biocompatible elastic surfaces to mimic corresponding microenvironments. Polydimethylsiloxane (PDMS) was first used with a range of ratios of monomer to crosslinker to generate environments of varying stiffness.[61, 62] Surface-functionalised PDMS was subsequently studied to screen cell response to modified surfaces of controlled stiffness.[63] However, PDMS-based elastic materials are limited in their range of stiffness as the minimum of stiffness developed are in the range of tens of kPa.[61] Any micro-environments in the range of muscle (~10 kPa) or brain (~1 kPa) is difficult to mimic using PDMS. A group of crosslinked non-degradable hydrogels have since been developed to study mechanical signalling events in this range.

1.2.4 Hydrogels

Hydrogels, both synthetic and naturally-derived, are widely used as scaffolds in tissue engineering. Hydrogels offer a potential platform to control systematic stiffness alteration and surface chemistry. Hydrogels are formed by crosslinked polymers that are water insoluble but have the ability to absorb a large volume of water within its network while retaining a 3D network.[64] Hydrogels crosslinked with synthetic polymers have been commonly used as model surfaces to study the influence of mechanical properties on cell behaviour.[65]

Polyvinyl-based hydrogels are especially widely used in the research of cell and tissue culture as they represent a favourable mimic of the *in vivo* environment. In particular, polyacrylamide-based hydrogels have been widely used as model soft materials in studies of cell−substrate interactions. Crosslinked polyacrylamide hydrogels are non-cytotoxic, have controllable physical properties (*e.g.,* stiffness and porosity) that can be systematically varied by altering their formulation ratios and/or concentration.[66, 67] These soft materials have been shown to mechanically induce stem cell differentiation lineages commensurate with substrate stiffnesses.[38]

1.3 Understanding stem cell fate

MSCs are reported to have the capability to differentiate into mesenchymal tissues such as bone, cartilage, muscle, ligament, tendon and adipose and contribute to their regeneration.[68] *In vitro* MSC differentiation has been thoroughly researched using various inhibitors and environmental, local, and hormonal factors.[69]

1.3.1 Osteogenic differentiation

It is well established that stem cells can be chemically induced along an osteogenic differentiation lineage with dexamethasone (Dex), ascorbic acid (Asc) and β-glycerophosphate (β-Gly) for a continuous period of at least 2 to 3 weeks.[70] Dex increases levels of alkaline phosphatase (ALP) and activates WNT/β-catenin signaling-dependent core-binding factor subunit alpha-1 (Cbfa1) expression through mediation of LIM-domain proteins with 4.5 LIM domains (FHL2).[71] Asc induces secretion of type I collagen which is abundantly synthesised by osteoblasts. It is proposed that osteoblast-like cells secrete a complex ECM containing collagenous protein especially type I collagen, noncollagenous proteins, and bone morphogenetic proteins (BMPs). The induction and maintenance of osteogenic differentiation responds through a type I collagen-α2β1 integrin interaction and mitogen-activated protein kinase (MAPK). MAPK activity phosphorylates and activates the osteoblast-specific transcription factor Cbfa1 and allows stimulation of osteoblast differentiation by an increase in transcription of osteoblast marker genes (*e.g.,* osteocalcin, osteopontin).[72]

It has been reported that mineralised biomaterials such as alginate matrix are beneficial to bone regeneration.[73] Alginate hydrogel scaffolds that incorporate ALP have been introduced as they have a high affinity for divalent cations, such as Ca^{2+} and liberate phosphate ions that generate a polymer/hydroxyapatite scaffold. The scaffold complex mimics the composition of bone therefore they exhibit the osteogenic differentiation capacity of MSCs.

1.3.2 Chondrogenic differentiation

MSCs are commonly differentiated along a chondrocytic lineage in the presence of growth factors such as transforming growth factor-β (TGF-β), bone morphogenic proteins (BMPs), insulin-like growth factor (IGF) and fibroblast growth factor (FGF).[74] The presence of TGF-β significantly enhances secretion of type II collagen (an important marker expressed in articular cartilage and contributing to the regulation of chondrocyte function) and aggrecan. BMP, on the other hand, has been established to induce both chondrogenic and osteogenic differentiation of MSCs which may lead to terminal MSC differentiation into hypertrophy.

It is understood that intracellular signalling from the ECM to cells is mediated through integrins, which serve as transmembrane links between the extracellular environment and FAs within the cell.[75] Interaction of integrins with the ECM at these FAs leads to the recruitment of several signalling molecules such as paxillin, vinculin, talin and FAK. Interactions between integrin-β1 and type II collagen in chondrocytes protects cells against apoptosis and mediates the response to external changes by maintaining the composition of the tissue and mechanical properties of articular cartilage.

In addition, a number of transcription factors such as SRY-box 9 (SOX9) have been reported to play an essential role during the sequential steps of chondrocyte differentiation.[76] SOX9 is reported to be continuously expressed during chondrogenic differentiation and in all differentiated chondrocytes, however, not in hypertrophic chondrocytes. Hypertrophic chondrocyte differentiation is reported to be induced by the soluble enzyme tissuetransglutaminase (TG2) which has been reported to be associated with integrin α1β1, α3β1, α4β1, α5β1 and α9β1.[77-79] Specifically, integrin α5β1, the major fibronectin receptor is reportedly upregulated upon chondrocyte hypertrophic differentiation, where chondrocytes are reported to express rich amount of type X collagen matrix and express Cbfa1 at the stage of both pre-hypertrophy and hypertrophy.[80]

1.3.2.1 Maintenance of terminally differentiated chondrocytes

The terminally differentiated phenotype of chondrocytes is characterised by the synthesis and deposition of cartilage-specific ECM molecules, such as type II collagen and aggrecan.[81]

Differentiated chondrocytes are difficult to maintain and rapidly lose their phenotype during *in vitro* monolayer culture. De-differentiation, the loss of phenotype, is a major restriction in applications such as cell therapy.[82] When isolated chondrocytes are cultured in monolayers at a low density, they lose their typical round shape and clustered chondrocyte morphology and instead transform into a flattened fibroblast-like morphology. The change in morphology is directly associated with a change in ECM expression of type II collagen and a shift towards the expression of type I collagen.

Integrin-mediated cell adhesion of type II collagen plays an important role in chondrocyte function as the interaction between integrin β1 and type II collagen maintains tissue composition and the mechanical properties of chondrocytes, protecting cells against apoptosis.[75] Interaction between integrin β1 and type I collagen, however, induces matrix metalloproteinase (MMP)-13 secretion and degradation of type II collagen.

Dedifferentiated chondrocytes have been reported to re-express their cartilage-specific ECM matrix components after treatments such as 3D culture in hydrogels[81, 82] or spatially-arranged peptides.[83] PEG hydrogel with functional groups has been used to pattern RGD peptides in various spatial arrangements. It has been suggested that chondrocytes retain a round morphology with larger RGD spacing and demonstrate a more fibroblast-like spread morphology with smaller RGD spacing. Chondrocytes have been subsequently shown to express a greater quantity of type II collagen on surfaces with larger RGD spacing.

1.3.3 Adipogenic differentiation

MSCs can be induced to differentiate towards adipocytes when cultured in the presence of adipogenic factors such as Dex, isobutyl-methylxanthine (IBMX), insulin and indomethacin (IM) for medical applications for energy storage.[7, 84] It has been reported that after adipogenic differentiation, transcription factors such as peroxisome proliferator-activated receptor γ (PPARγ) and C/EBPα are mediated by the expression of early adipose genes such as CCAAT/enhancer binding protein β (C/EBPβ) and C/EBPδ.[85] A switch in expression of integrin α5, the receptor for fibronectin, and α6, the receptor for laminin, appeared during adipogenesis where integrin α5 diminished during the differentiation of adipocytes from pre-adipocytes while that of α6 increased substantially.

The use of inhibitors and environmental, local and hormonal factors are, however, costly, therefore are less economical to use in tissue engineering applications. Biomaterials have been developed as a more cost-effective method of creating homogeneous cell populations.

1.4 The role of surface chemistry in control of cell adhesion

Material surfaces have been used to investigate biological responses as they can be modified using a wide range of methods such as SAMs or surface chemical addition reactions.

1.4.1 Self-assembled monolayers

SAMs with various functional groups have been widely studied in the past decades for their versatility in surface functionalisation.[86] Various mechanisms of SAM formation have been studied including alkylthiolate chemisorption on gold and alkylsilane crosslinking on hydroxylised surfaces. Naturally, SAM formation results in highly ordered supermolecular hierarchical organisation on the surfaces.[87]

The formation of alkylthiol on gold occurs at the interface of a solid substrate (Scheme 1.1).[88] The assembly occurs based on spontaneous adsorption of the organosulfur compounds from a solvent directly onto a substrate. An advantage of this mechanism is that gold, as a substrate, is a relatively inert metal and does not form a stable oxide layer under ambient conditions. Long-chain alkylthiols tend to form a densely packed and highly structured monolayer on gold.[88]

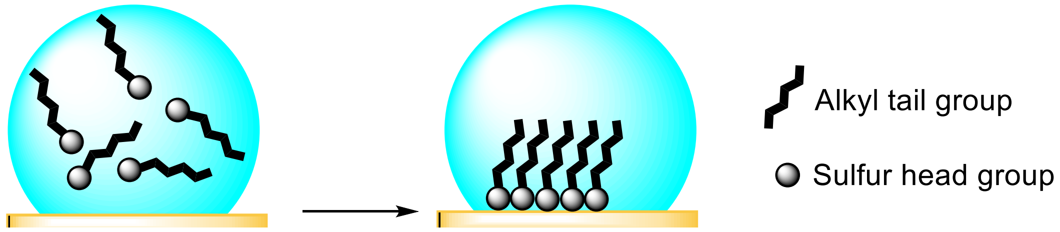

Scheme 1.1 Schematic illustration of alkylthiol adsorption on the surface of gold upon contact with sulfur head groups.

In addition to thiol-gold chemisorption, alkylsilane on hydroxylated surfaces are important systems that provide versatile potential in tailoring surface properties with various functional groups. Alkylsilanes, typically with trichloro or trialkoxy surface-active head groups, demonstrate a higher chemical and physical stability than thiol-gold monolayers due to their covalently crosslinking mechanism. It therefore provides a broader range of chemical modification of surface monolayers.[89] The crosslinking mechanism is however more complicated than thiol-gold chemisorption and organosilicon molecules, especially tricholorosilanes, are more reactive than organosulfur molecules. The self-assembly of these alkylsilanes shows increasing interest as the functionalisation of the surfaces provides the possibility of tailoring surface properties such as hydrophilicity, friction, adhesion and conductivity. Therefore, this technology has been used in a wide range of applications, especially thin-film technology, nanotechnology, cell and protein adsorption, amongst others.[58, 90, 91]

Some reports have suggested that growth of alkoxysilane SAM on surfaces undergo island-type growth while others suggested the monolayers are formed through an initial homogeneous but disordered growth (Scheme 1.2).[92]

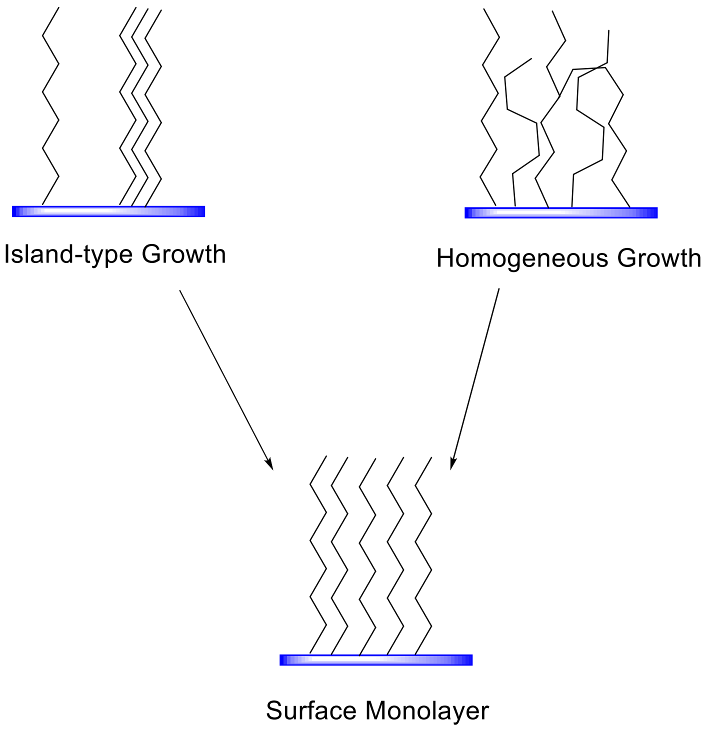

Scheme 1.2 An illustrative scheme of island-type and homogeneous type SAM growth.[92]

The mechanism of the formation of SAMs through alkylsilane is reported to undergo a series of reactions including hydrolysis, condensation and finally covalent bond formation (Scheme 1.3).[93]

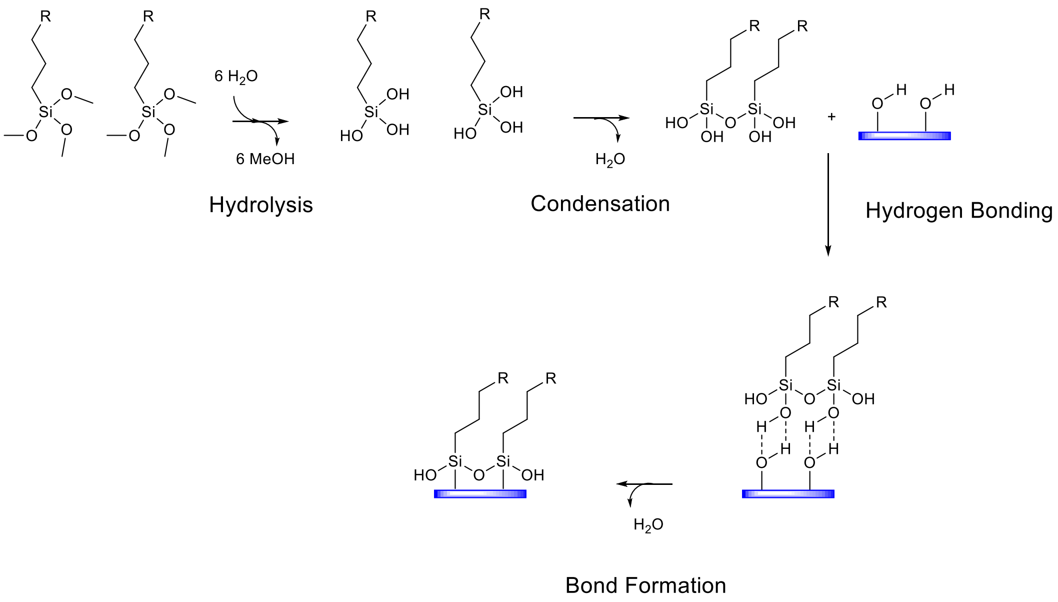

Scheme 1.3 Schematic illustration of alkylsilane reaction on hydrolysed surfaces. Trimethoxysilane is used as an example for the illustrative reaction scheme.[93]

Trimethoxysilane as an example, the methoxy head groups are first hydrolysed to form hydroxyl head groups, which are then ideally condensed with neighbouring molecules to form polymer networks. Hydrogen bonding is then formed between the hydroxyl groups on the alkylsiloxane polymer network and hydrolysed surface. The surface then undergoes a curing process to form a covalently bonded silane-functionalised surface.

Due to the complicated alkylsilane surface reaction, a few conditions have been reported as critical parameters to control during the self-assembly process.[89]

It has been reported that selection of an anhydrous solvent could affect the density of film deposition whereas, dependant on the type of alkoxysilane, vapour deposition could yield a smooth and reproducible monolayer film.[94] More importantly, it has been reported that use of anhydrous hydrophobic solvents would result in slow SAM formation but densely packed surface layers whereas with non-anhydrous hydrophilic solvent SAMs would deposit on surface at a much faster speed but form a surface with higher roughness.[92] This is due to the properties of hydrophobic solvent, such as toluene, has the ability to extract excess water from the surface and environment leaving only a thin layer of water on the surface for alkxoysilane to react with.

In addition, the reaction environment could have an impact on the reactivity of the molecules.[95] For example, carbon dioxide could react with amino-terminated alkoxysilanes to yield a bicarbonate salt that could reduce its reactivity when coupling on a hydrolysed surface, especially when amines on the amino-terminated silanes also play a role in self-catalysing the reaction (Panel A, Scheme 1.4). Amines on amino-terminated alkoxysilanes could also form imines under atmospheric conditions (Panel B, Scheme 1.4).

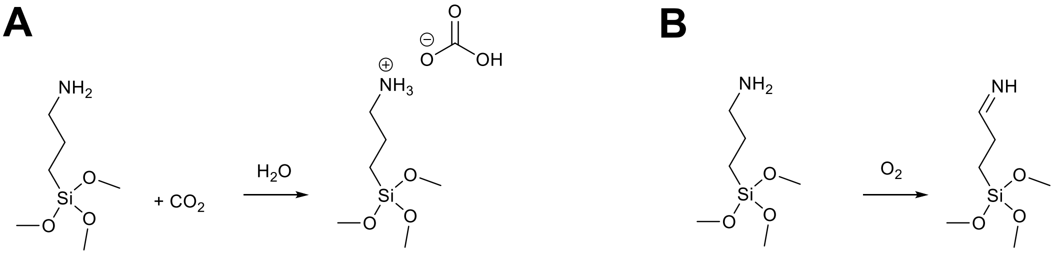

Scheme 1.4 Illustration of amino-terminated silane reactions with (A) CO_2 and (B) O_2 from the environment, forming by-products that affect the self-assembly process.

It has been previously reported that surface siloxane formation undergoes different curing processes and this could result in different thicknesses.[96] The thickness of the siloxane layer increases after curing in air due to disruption of the hydrogen bonding that eventually leads to polysiloxane formation. The thickness could be preserved if the samples were cured in a desiccator while a decreased thickness is observed for thermal curing due to evaporation of loosely-bound molecules.

The length of alkyl chains within the alkoxysilane molecules plays an important role in stabilising surface ordering and packing density of the monolayer by inter-chain van der Waals interactions.[50] Hence, it could be expected that alkoxysilane molecules with shorter alkyl chains would form a less ordered surface monolayers and thus higher roughness.[33]

1.4.2 Surface chemical addition reactions

The formation of SAMs on surfaces not only provide the possibility of tailoring the terminal end groups to alter surface functionality and selection of reactive end groups but also serves as surface linkers to provide a wide range of possible modifications that provides a vast variety of possibilities as a powerful tool for surface functionalisation.[89] A few classic routes have been studied.

1.4.2.1 Nucleophilic substitution

Nucleophilic substitution reactions typically involve a nucleophile to attack a positively-charged or partially positively-charged atom that is connected to a leaving group. Commonly seen nucleophiles include NH_3, -CN, water, -OH, $-N_3$, *etc*.

Bromine-terminated SAMs have been evoluated in surface modification applications into various functional end groups (Scheme 1.5).[97, 98]

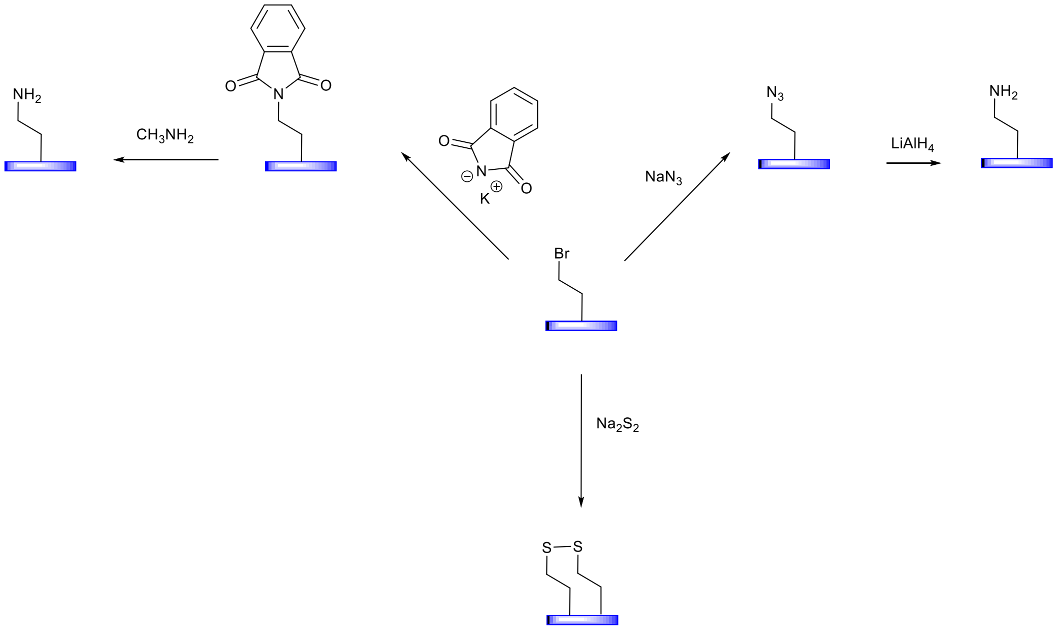

Scheme 1.5 Schematic illustration of nucleophilic substitution reactions on bromine-terminated SAMs.

This reaction mechanism on surface SAMs, although providing versatile potential for surface modifications, has been reported to be relatively slow due to its S_N2 mechanism that requires the nucleophile to penetrate below a densely packed surface monolayer to attack the carbon underneath the bromine, resulting in a kinetic barrier for nucleophilic substitution.[97]

In addition, maleimide-functionalised surfaces provide a vastly wide range of biological applications (Scheme 1.6).[51, 99, 100]

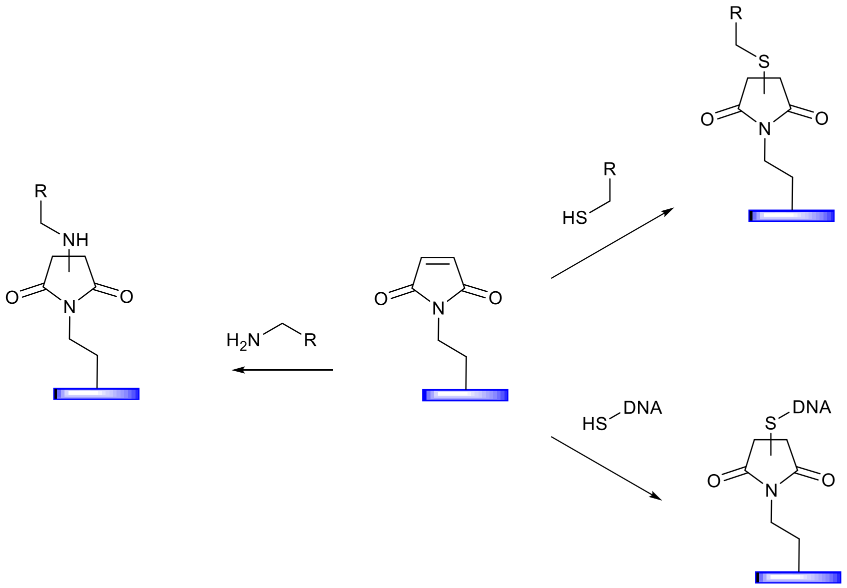

Scheme 1.6 Schematic illustration of nucleophilic substitution on maleimide-terminated SAMs.

Under physiological conditions, thiolated molecules undergo spontaneous nucleophilic attack to the electrophilic carbon in the maleimide ring and form thioether bonds. This mechanism has enabled attachment of thiolated DNA and proteins. With increased pH > 8.0, aliphatic amines could also attack the maleimide and form non-specific binding in molecular biology applications.[101]

Amino terminated SAMs have been widely developed for their chemical reactivity, due to the amine often performing a self-catalytic role, and potential in biological applications.[91, 102, 103] Among the most commonly seen reaction routes is the nucleophilic substitution reaction, typically with alkyl halides or maleimide under the controlled conditions described above. Another frequently used method is amide bond formation with carboxylic acids.[104] Amide bond formation plays a particularly major role in biological systems, for example, the main bond to building blocks of amino acids to form peptides or proteins. Amide bonds are typically synthesised by combining carboxylic acids and amines (Scheme 1.7).

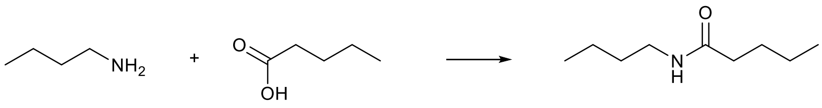

Scheme 1.7 Schematic illustration of amide bond formation.

This reaction, however, does not occur spontaneously under ambient conditions. Therefore activation of carboxylic acids is usually essential for this reaction route.[105] To activate a carboxylic acid, a group of coupling reagents is typically used. These coupling reagents operate as stand-alone reagents that generate a variety of active leaving groups such as esters, anhydrides, acid chlorides, *etc*.[105] The reaction typically involves activation of carboxylic acid followed by nucleophilic attack of the amine at the active carboxylic groups. The choice of coupling reagent is critical to fit in the requirements to react with a broad range of amines with varying reactivity portfolio. In general, amide bond formation could be conducted with two major types of coupling reagent systems.[105]

Cabodiimides as coupling reagents have been reported to activate carboxylic acid which then reacts with amines to yield amide compounds (Scheme 1.8). They are frequently used in amino-terminated alkoxysilane applications, such as (3-aminopropyl)triethoxysilane (APTES), due to its amino-terminated group enabling versatile possibilities such as solid-phase peptide coupling and covalent protein binding.[106, 107]

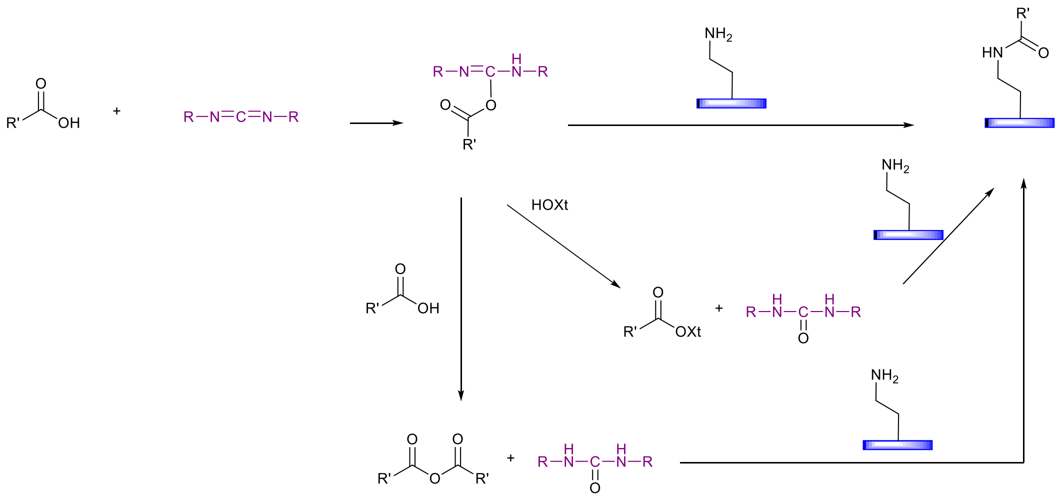

Scheme 1.8 Reaction scheme of amide bond formation through carbodiimide as a coupling reagent.

The reaction of carboxylic acid activated by carbodiimide could directly react with amines and form amide bonds. If more than 1 equivelant of carboxylic acid is used in the reaction, the activated carboxyl groups could react with excessive carboxylic acids and yield in symmetric acid anhydride. To stabilise the reaction and avoid the loss of configuration at the carboxylic acid residue, an N-hydroxy based compound as additive could be added in the activation process to yield in an active ester. This ester can then react with amines to form amide bonds. Examples of commonly used carbodiimide and additives are shown in Scheme 1.9.

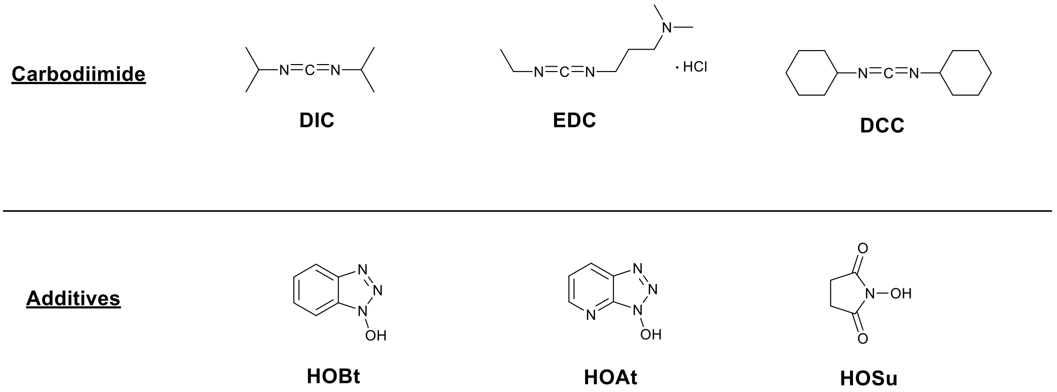

Scheme 1.9 Examples of commonly used carbodiimide and additives.

N,N’-Dicyclohexyl carbodiimide (DCC) and N,N’-diisopropyl carbodiimide (DIC) are most commonly used in peptide synthesis, especially solid-phase peptide synthesis, depending on the reaction environment, including the properties of by-products.[108] N-(3-Dimethylaminopropyl)-N'-ethylcarbodiimide hydrochloride (EDC) is commonly used where an aqueous reaction environment is required. The by-product is water soluble and easy to remove in aqueous solvent mixture.

1-Hydroxy-7-azabenzotriazole (HOAt) and N-hydroxybenzotriazole (HOBt) are commonly used as additives. The use of these additives acts as suppressor for racemization and protects the stereochemical integrity in α-amino acid couplings in peptide coupling. HOBt is reported less stable than HOAt with a greater risk of explosion. HOAt is reported to enhance coupling rate than HOBt. This is suggested due to the additional nitrogen placed within the aromatic rings.[108] The electron withdrawal of this nitrogen atom affects the stability of the leaving group resulting in a greater reactivity. The structural location of this nitrogen also provides extra hydrogen bonding with amine and carboxyl groups.

N-Hydroxysuccinimide (HOSu) is an additive commonly used in conjunction with EDC for aqueous coupling reactions. Although HOSu has slower reaction rate than HOBt and HOAt, it is also found used in conjunction with other carbodiimide coupling reagents for its stability.

1.4.2.2 “Click” chemistry

The term “click” chemistry was introduced as reactions that are modular, wide in scope, high yield, generate inoffensive by-products, and are stereospecific.[109] This family of reactions serve the nature of being insensitive to water and oxygen. In most cases these reaction can occur in water or an easily removable solvent. In general, this family of reactions includes cycloadditions of unsaturated species, nucleophilic substitution, Michael additions and addition to carbon-carbon multiple bonds.

Thiol-click reaction combines the high potential reactivity advantage of thiols and the advantage of "click" chemistry.[110] The reaction is triggered by radical or base catalyst. Thiolated molecules can react through multiple pathways such as thiol-ene click reaction (Scheme 1.10).

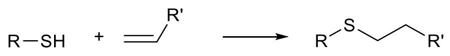

Scheme 1.10 General scheme of thiol-ene coupling.

Thiol-ene "click" reaction could be initiated by radical based reactions, such as photopolymerisation. The ideal thiol-ene radical reaction is particularly used in step-growth polymerisation.[110] Thiol-ene "click" reaction could also undergo catalyst-based Michael addition when the alkene moiety is attached to an electron withdrawing group. The Michael addition is characterised as the reaction of enolate-type nucleophile in presence of catalyst.[111] When thiol-ene "click" reaction undergoes base-catalysed condition, it is referred to as thiol-Michael "click".[112]

Thiol, as a soft nucleophile, has vast possibilities in various "click" chemistry scenarios, such as thiol-halogen "click" reactions.[110] Thiol-halogen "click" reaction has been reported as an efficient "click" chemistry route. It is especially mentioned that with a weak base or aliphatic amines in the reaction system could also be in favour of the reaction rate.

The broad range of reaction routes has provided versatile possibilities in surface modifications, especially under ambient and clean environment, for various biological applications. In particular, a selection of reaction routes detailed in this section provides possibilities of the choice of solvents therefore provides a wider versatilities for this application to be used in conjunction with certain biocompatible surfaces such as degradable polymers and hydrogels.

In addition to the bulk surface modifications for cell biology applications, other advanced techniques, such as atomic force microscopy (AFM), could evolve the surface functionalisation to nanoscale precision.

1.5 Nanolithography

It has been reported that cells sense and respond to stimulus at the sub-micron scale.[113, 114] To understand the effect of isolated biological response, a methodology is required to be developed to control the deposition of chemistries at this level.

Nanolithography is a fabrication category where nano-scale features of product are formed under 100 nm in at least one dimension.[115] The progress of nanotechnology depends on the ability to position and manipulate reliable features, structures on materials. Recent developments focus on scanning probe microscopy (SPM) derived methods, in particular atomic force microscopy (AFM) predominately due to its accuracy in locating probes onto a surface with imaging resolution at sub-10 nm scale.

AFM was invented in 1986 with the application of directly imaging surface morphology within atomic resolution.[116] This process is achieved by recording and transducing the forces being detected by a scanning probe as it is scanned across the surface. AFM is compatible with a wide range of sample conditions with the ability to operate in liquid, air or vacuum condition. Various AFM-based nanolithographic approaches have been developed within the last few decades. Briefly, three approaches can be categorised, thermomechanical writing[117], mechanical indentation[118, 119] and dip-pen lithography (DPN)[120].

1.5.1 Dip-pen nanolithography

DPN is a scanning-probe based direct-write tool introduced in 1999 for generating surface-patterned chemical functionality at a nano- to sub-micron feature scale.[120] DPN is a direct-write scanning probe-based lithography using an AFM tip as nano-sized pen to directly deposit “ink” onto any surface to generate nano-scale feature mapping (Figure 1.1).

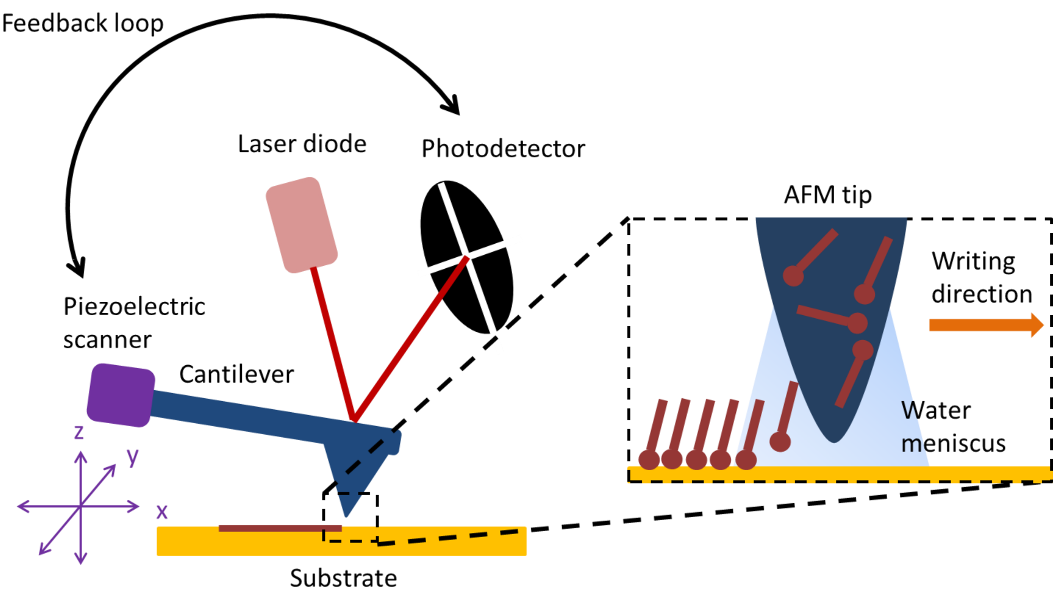

Figure 1.1 Diagrammatic representation of dip pen nanolithography pattern mechanism with a zoomed-in view of molecular deposition at the apex of cantilever tip.

In DPN applications, molecules are selected as “inks” and corresponding substrates are chosen as “paper” that are expected to react with each other in a facile and predicted manner to yield in reproducible patterns.[90] A typical pattern reaction of DPN is to deposit alkylthiol SAMs on to gold surfaces which could generate high resolution structures due to its immediate completion of reaction and stability at ambient conditions. In addition, 1-octadecane-thiol (ODT) and 16-mercaptohexadecanoic acid (MHA) patterns could be used as gold-etch resists so that both metal and semiconductor nanostructures could be generated using DPN to generate patterns in nano to submicron scale.[121] DPN has been developed to pattern a variety of “inks” on suitable substrates.

Alkoxysilane has been reported used as “ink” to pattern on silicon wafer as “paper”.[90, 122, 123] Alkoxysilane molecules were patterned on siloxane surface as functional groups to generate selective reactive surface for potential modification on substrates. In addition, fluorescent molecules such as Rhodamine 6G has been patterned on negatively charged glass surfaces.[124]

DPN is compatible with range of various inks, from small organic molecules[90, 122] to larger biological matters, such as protein and lipid.[125] DPN can be used to pattern surfaces ranging from metals to insulators and to pattern on top of monolayers presenting functional groups adsorbed on a variety of surfaces. However, the main obstacle of SPM-derived nanolithography is the throughput. The limitation address here has indicated that the fact of DPN as a single probe deposition method has less ability to easily and rapidly define micro- and nanoscaled morphology in a single experiment.[126] Early effort has been made to address a development of two dimensional cantilever arrays that has been reported ability to fabricate features in cm^2 areas.[127] In addition, the need of fragile and costly two-dimensional cantilever arrays to achieve larger area patterning with DPN system which leads to the method being unusable for *in vitro* cell culture investigation.

1.5.2 Polymer pen lithography

Due to the limitations of DPN addressed above, polymer pen lithography (PPL), a low cost, large area, cantilever-free lithographic approach was introduced in order to generate large-area molecular surface to determine and investigate the potential of PPL manufactured surfaces to control cell responses.[126] The development of PPL addressed this issue by replacing the costly two dimensional cantilever arrays with elastic pyramidal arrays fabricated with PDMS (Scheme 1.11).

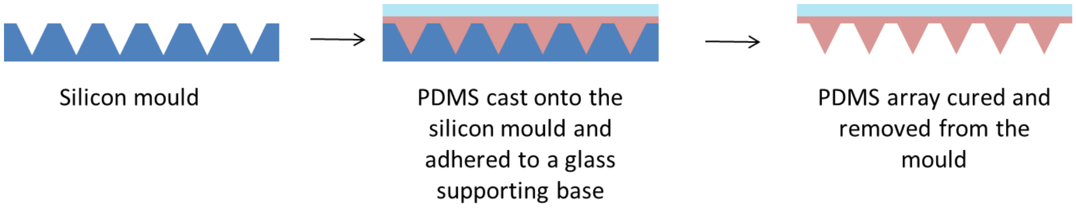

Scheme 1.11 Schematic diagram showing the fabrication of PPL arrays. Silicon moulds were cast with PDMS elastomer and sandwiched onto a supporting glass base. After curing, the PDMS array was peeled off the mould with the glass base.

PPL enables a digitized pattern to be printed at spot sizes ranging from 90 nm to hundreds of mm simply by changing the force and contact time over with which the ink is delivered.[126] In contrast with DPN and other SPM-based lithography methods, PPL use an array of elastic pyramidal PDMS tips instead of cantilevers to deliver “ink”. The “ink” is delivered at the points of contact of the array with the surface.

In addition to classic alkylthiol-based “inks”, wide-area chemical patterns utilising PPL techniques have been introduced in combination with surface click-chemistry using chemically coupled azide as an “ink” to pattern alkyne-functionalised surfaces at 60 – 80% relative humidity for allergic response studies.[128] HOSu coupled natural “inks” such as biotin and fluorescent molecules such as fluorescein isothiocyanate (FITC) have also been used in combination with AFM-based nanocontact printing techniques to fabricate high density nanoarrays for drug discovery applications. ECM proteins such as fibronectin[125, 126] and multicoloured bioinks[129] have been used as “ink” on model surfaces such as surface coated hydrogel or glass coverslips for cell adhesion and pattern observation applications.

Based upon the previous reports, simple chemistries that present carboxyl, amino or methyl groups have shown to influence stem cell fate.[41, 130] These research findings are based on precise deposition of the chemistry of interest, over, however, a relatively small area. PPL offers an exciting opportunity to produce large area chemical nanoarrays that can be used to control cell-material interactions and increase the efficiency of material induced cell responses.

1.6 Aims and Objectives

The strategic aim of this work is to fundamentally understand stem cell fate under defined synthetic surface and dynamic parameters at nano- to submicron scale. This work aim to investigate the potential of replacing biological agents with synthetic chemistries to control initial cell adhesion and understand cell-surface interaction for potential applications in regenerative medicine.

In order to select and control protein binding and subsequent cell adhesion and spreading resulting in controllable cell function, large-area nanofeatured synthetic substrates were designed, characterised and manufactured as model surfaces to study fundamental interactions of cells. To accomplish the target of homogeneous cell response across a large area, this project was designed to develop a homogeneous environment of nanofeatured chemistry presented across the entirety of a substrate for stem cell culture. Theoretically controlled changes in sub-micron material chemistry, stiffness and topography are features that can be controlled by PPL technologies, features that will be investigated for the production of cell culture substrates within this research project.

To investigate the potential and reproducibility of modification of cell behaviour on designed substrates (model substrates with well-defined chemical nanoarrays and associated sub-micron topographical features), this project aimed to derive fundamental data establishing that the modification using chemically defined nanoarrays, nanotopography in addition to stiffness of the base substrates can alter protein adhesion and therefore cell function, significantly increasing the potential for material-induced biological responses.

In order to produce large-area homogeneous nanotopographic features, PPL was introduced as a powerful tool that allows various chemistries as “inks” that can be transported onto surfaces and transferred into a controllable range of feature size, stiffness, topography and functionalised patterns. Further to address the cell response to chemical nanoarrays, the surfaces were passivated using the inverse of patterns in order to isolate patterns from base substrates. This should avoid non-specific ECM adsorption and cell adhesion on non-patterned areas. For extended study of MSC differentiation and the retention of chondrogenic phenotype, cells were cultured and differentiation markers were investigated over prolonged periods.

Surface Nanolithography for Stem Cell Fate

2.1 Introduction

Tissue engineering is a relatively new field which applies living cells, biocompatible materials, biochemical and physical factors to establish the simulation of *in vivo* systems as an efficient treatment where all other medical treatments failed. It is well documented that cells respond to wide range of variables such as surface chemistry, topography and stiffness.[2]

The use of chemistry to pattern surfaces was established during the early stage of biomaterial development and introduced mainly by microcontact printing (µCP) on selected regions with patterns and/or bulk coated with self-assembled monolayers (SAMs) for full coverage surface materials.[52, 131] More recently, advanced chemical modification, *i.e.,* a chemically functionalised group of interest immobilised on the surface of a synthetic material, have been shown to induce substantial stem cell responses.[41, 56] In terms of chemically modification of surfaces, a few methodologies have been introduced, such as wet silane modification[56, 58] and surface self-assembled monolayers (SAM)[132], where desired chemical groups have been introduced onto surfaces and the response of stem cells investigated. These approaches have demonstrated that introduction of selected chemical groups can be used to induce a level of cell function, however, it is imperfect as the introduction of chemistry usually incorporates other variables such as a change in surface morphology making it, therefore, difficult to distinguish isolated material variables resulting in a heterogeneous cellular response.

The initial mechanism of cell adhesion occurs *via* integrin binding to form focal adhesion in the tens of nano- to sub-micron scale. Therefore homogenous control of initial cell adhesion has not been achieved in previously published literature where all surface characterisation was achieved at the macro-scale, the mechanism of nano-scale integrin expression associated with cell response remaining unclear.[56, 58] To address this, materials with controlled sub-micron features should be studied.

2.1.1 Nanotechnology applications in cell biology

Nanofabrication is referred to as the design, construction and fabrication of materials typically with features smaller than 100 nm.[133] Two approaches, top-down and bottom-up, have been used in the production of nanoscale structures. The bottom-up methodology employs various interactions between molecules and colloidal particles to assemble three-dimensional structures, while the top-down method carves nanoscale structures by controlling the removal of materials from bulk solid or chemistry topography.

It has been established that changes in surface chemistry, energy and topography can be used as a powerful tool to provide a micro-environment to cells in order to control protein adsorption, cell–cell and cell–matrix adhesions.[113] Previous research has established the potential of chemistry to induce a level of control over cell function[58], demonstrating that cells respond to changes in surface chemistry such as carboxylic acid ($-CO_2H$), amine ($-NH_2$) and alkyl ($-CH_3$) groups which occur naturally in extracellular matrix (ECM).[41, 58]

Recent research efforts have studied the effect of cell responses with ECM adsorption in nanoenvironments demonstrating that cells respond to nano-scale arrangements.[41, 44] Studies into the effects of nanotopography on biological response have shown that cells sense and respond to stimuli at a nano- to sub-micron level. Yet the ability to isolate variables, at the sub-micron scale with methods such as µCP, stereolithography and 3D printing is limited. Therefore, methods that are able to control variables at the sub-micron scale are an exciting prospect in terms of advancing and understanding fundamental knowledge and improving material design criteria to enhance the efficiency of material induced biological responses and realise the potential of biomaterials and tissue engineering in modern day society.

Recently, dip pen nanolithography (DPN), a scanning probe methodology for the deposition of functionalised chemical nano-topography was introduced in biomaterials research for controlled cell response studies.[41] Alkylthiol molecules with various functional groups were deposited on gold via alkylthiol chemisorption in order to produce chemical nanoarrays that presented different functional groups whilst controlling nanotopography. Nanotopographical surfaces with end groups of amino, carboxyl, hydroxyl and methyl alkylthiol have been introduced in cell fate studies which have indicated that altering the spatial resolution of the functional groups significantly affected cell response, *e.g.,* cell adhesion, alignment and differentiation.

The limitations addressed here suggest that DPN as a single probe deposition method does not have the ability to easily and rapidly define micro- and nanoscaled morphology in a single experiment.[126] Therefore, polymer pen lithography (PPL), a low cost, large area, cantilever-free lithographic approach was introduced in order to generate large-area molecular surfaces modification to determine and investigate the effect of sub-micron chemical group deposition on cell response.

2.1.2 Multiplexed nanolithography

The issues of high throughput nanolithography for biological applications have been addressed with multi-probe arrays such as fountain-pen nanolithography (FPN) or DPN with 2D-probe arrays[127, 134] and cantilever-free techniques such as PPL[126] for patterns for areas in the range of cm^2. The shortcomings of these techniques, however, are that all probes must be precisely parallel with a surface to perform uniform pattern fabrication. Even with small misalignments, 2D-probe array based patterning can cause large differences in feature size from one edge to another.[135]

Early work on PPL patterning relied purely on visual inspection using a camera mounted on top of the probe arrays as a guide to achieve parallel alignment.[136] Recently, an algorithm that employs automated alignment of a 2D PPL probe array to ensure it is parallel with the patterning substrate has been introduced.[137] The published algorithm has been reported to reduce the misalignment to less than 0.004° typically within 2 hours of the operation.[135] A major benefit of this breakthrough is that it enables high-throughput fabrication of surface materials for cell culture experiments.

2.2 Aims and objectives

In order to select and control protein binding for subsequent cell adhesion and spreading to control cell function, large-area nano-featured synthetic substrates were designed, characterised and manufactured as model surfaces to provide fundamental knowledge on how cells react with selected surface chemistry at the sub-micron scale.

It was planned to address shortcomings of previous reported methods by utilising polymer pen lithography as a tool for fabrication of large-area homogeneous surface materials. To accomplish the target of homogeneous cell response across a large area, this project was designed to develop a homogeneous environment of nano-featured chemistry presented across the entirety of a substrate for stem cell culture. Theoretically controlled changes in sub-micron material chemistry and topography are features that can be controlled by PPL technologies, a feature that is being investigated for the production of cell culture substrates within this research project.

The chemical nanoarrays were designed to attach to gold as a model surface through thiol-gold chemisorption. The patterned surfaces were then passivated with (11-mercaptoundecyl)hexa(ethylene glycol) (m-PEG) in order to restrict cell-matrix interaction on non-patterned areas (Scheme 2.1). MSCs were cultured in contact with designed nanoarrays to study stem cell function *via* control of initial protein/cell adhesion events. Furthermore, a comprehensive screening of a potential mesenchymal stem cell (MSC) differentiation pathway was conducted in relation to controlled surface chemistry.

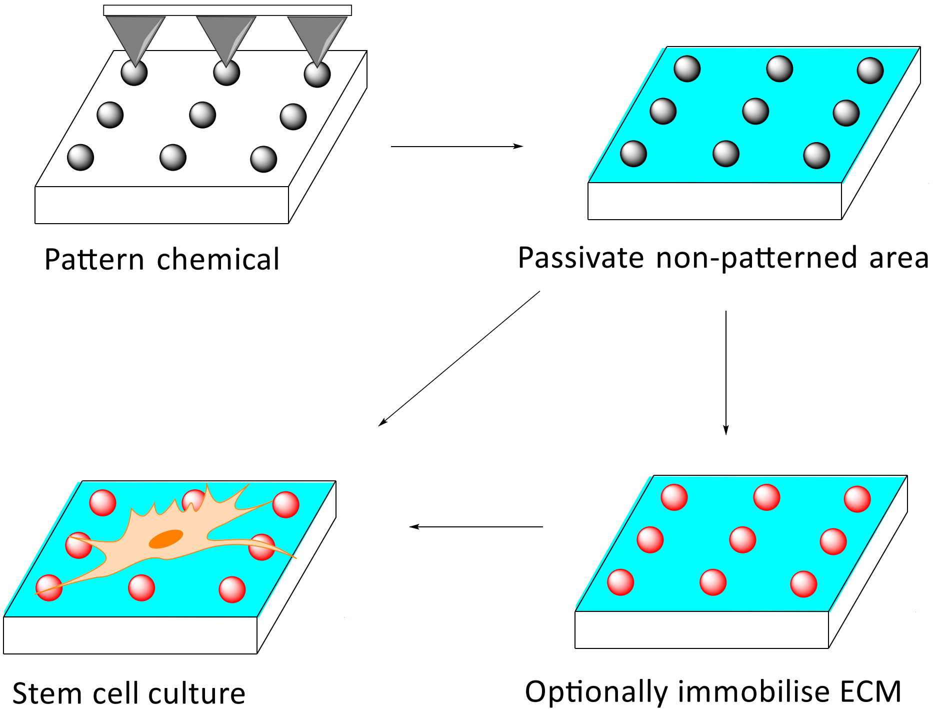

Scheme 2.1 A schematic diagram illustrating the procedure of PPL fabricated model surfaces and its passivation prior to *in vitro* cell culture.

2.3 Experimental methods

2.3.1 Materials and instrumentation

Fabrication of nano-patterns was conducted on FlexAFM with a C3000 controller (Nanosurf, Liestal, Switzerland) with a nominal translation range of 100 µm in the X and Y axes and 11 µm in the Z axis. The AFM was placed above a custom built (by Nanosurf) five-axis translation stage with maximum X, Y and Z movement of 72 mm, 46 mm and 5 mm, respectively, with a step resolution of 0.3 µm, 0.3 µm and 0.1 µm, respectively. The stage was able to tilt in both θ and ϕ axes across ±5 ° with a maximum resolution of 0.3 m°.

Incorporated into the sample stage are three metal foil strain gauges operating as load cell sensors (FUTEK, Irvine, CA, USA), each with a sensitivity of 2 µN. The automatic alignment program code was written in LabVIEW V13.0 (32-bit).[137] A user interface was designed allowing operators to insert inputs defining coarse and fine steps. The automatic alignment program outputted into a real-time amplitude monitor window and an Excel file containing the results including forces and positional data gathered during the alignment procedure through a USB dynamic linking library supplied by FUTEK.

A Megafuge 16R centrifuge was purchased from Thermo Scientific. A plasma cleaner (PDC-32G-2) and PlasmaFlo Gas Flow Mixer (PDC-FMG-2) were purchased from Harrick Plasma. All chemicals were purchased from Sigma-Aldrich unless otherwise stated. PDMS co-polymer solutions for pen arrays were purchased from Flurochem. SuperClean2 glass substrate slides for further metal coating were purchased from Arrayit® Corporation. Titanium and gold were coated using an Edwards Auto500 electron-beam evaporator equipped with a microscope slide sample stage.

Human mesenchymal stem cells (PT-2501) and growth medium (MSCGM™ Mesenchymal Stem Cell Growth Medium BulletKit™, PT-3001) were purchased from Lonza, UK. Dulbecco's phosphate buffered saline (D1408) was diluted 1 to 10 with dH_2O and autoclaved before use. Trypsin-EDTA solution (T4174) was diluted 1 to 10 with DPBS. Four % (w/v) paraformaldehyde (PFA, P/0840/53, Fisher Scientific) was prepared in DPBS containing Mg^{2+} and Ca^{2+}. Triton™ X-100 (T8787) was diluted 0.5% (v/v) in DPBS containing Mg^{2+} and Ca^{2+}. Rabbit anti-type II collagen antibody (ab34712, Abcam), mouse anti-type X collagen antibody (ab49945, Abcam), rabbit anti-fibronectin antibody (ab2413, Abcam), mouse anti-osteocalcin antibody (ab13418, Abcam), rat anti-CBFA1 antibody (MAB2006, R&D Systems), mouse anti-vinculin antibody (V9131, SigmaAldrich), goat anti-rabbit IgG secondary antibody (Alexa Fluor® 594 conjugate, R37117, Invitrogen), donkey anti-mouse IgG secondary antibody (Alexa Fluor® 594 conjugate, R37115, Invitrogen), goat anti-rat IgG secondary antibody (Alexa Fluor® 594 conjugate, ab150160, Abcam), and goat anti-mouse IgG secondary antibody (Alexa Fluor® 488 conjugate, A11001, Invitrogen) were used for immunofluorescence. Alexa Fluor® 488 phalloidin (A12379, Life Technologies) was used for actin filament staining. ProLong™ antifade diamond mounting media with DAPI (P36966, Thermo Fisher Scientific) was used to stain cell nuclei and sample mounting.

Fluorescent images were collected using either a Zeiss LSM 800 confocal microscopy, Zeiss Apotome.2 or Olympus BX51 upright microscope.

Images collected on an Olympus BX51 upright microscope used a 4x / 0.13 UPlan FLN or 10x / 0.30 UPlan FLN objective and captured using a Coolsnap ES2 camera (Photometrics) through Metavue v7.8.4.0 software (Molecular Devices). Specific band pass filter sets for DAPI, FITC and Texas red were used to prevent bleed through from one channel to the next. Images were then processed and analysed using Fiji ImageJ.

Images collected on the Zeiss LSM 800 confocal microscopy used either 20x / 0.8 ∞ / 0.17 Plan-APOCHROMAT or 40x / 1.4 oil DIC ∞ / 0.17 Plan-APOCHROMAT objectives and captured using an Axiocam 506 mono camera through Zen 2.3 system (blue edition) software. Immersol™ 518F immersion oil was used. Images were visualised using an HXP 120V lamp and captured for DAPI, Alexa Fluor® 488 and Alexa Fluor® 594. Images were then processed and analysed using Fiji ImageJ.

Images collected on the Zeiss Apotome.2 microscopy used either 10x / 0.25 ph1 A-Plan (421041-9910), 20x / 0.35 ph1 var1 LD A-Plan (421251-9920) or 40x / 1.3 oil DIC (UV) VIS-IR Plan-APOCHROMAT objectives and captured using an Axiocam MRm camera through Zen 2 pro system (blue edition) software. Immersol™ 518F immersion oil was used. Images were visualised using an HXP 120C lamp and captured for DAPI, Alexa Fluor® 488 and Alexa Fluor® 594. Images were then processed and analysed using Fiji ImageJ.

Optical images were collected on a Leica DM 2500M upright microscope using either a 5x / 0.12 NPlan EPI, 10x / 0.25 NPlan EPI, 20x / 0.40 NPlan EPI, 50x / 0.75 NPlan EPI, or 100x / 0.85 NPlan EPI objective and captured using a Leica DFC295 camera through Leica Application Suite (LAS) v4.2.0 (Build 607) software. Images were aquired using a reflected light source. Images were then processed and analysed using Fiji ImageJ.

Live cell images were collected using a Nikon ECLIPSE Ti microscope under bright field using a 4x PhL DL Plan-Fluor objective captured through NIS-Element AR

4.50.00 software. Samples were placed in 12-well plates in an Okolab humidified chamber supplemented with 5 % CO_2. Images were aquired at 20 min intervals for 24 h and converted into video.

2.3.2 Buffer and solution preparation

2.3.2.1 DPBS containing Ca^{2+} and Mg^{2+}

To prepare 10X DPBS containing Mg^{2+}, 80 g of NaCl, 2 g of KCl, 11.5 g of Na_2HPO_4, 2 g of KH_2PO_4, and 1 g of $MgCl_2{\cdot}6H_2O$ were dissolved in 800 mL of dH_2O, then adjusted to a total volume of 900 mL solution. 10X $CaCl_2$ was prepared by dissolving 1 g of $CaCl_2$ in 80 mL of dH_2O prior to adjusting total volume to 100 mL.

To prepare 1X DPBS containing Mg^{2+} and Ca^{2+}, 100 mL of 10X DPBS containing Mg^{2+} were diluted with 700 mL of dH_2O and separately 10 mL of 10X $CaCl_2$ were diluted in 90 mL of dH_2O and the two solutions mixed. The pH was adjusted to 7.4 and the buffer adjusted to a total volume of 1 L.

2.3.2.2 Paraformaldehyde fixation solution

One hundred mL of 10X DPBS containing Mg^{2+} were diluted in 700 mL of dH_2O. 40 g of paraformaldehyde (PFA) were dissolved in this solution at 60 °C. The fully dissolved solution was then allowed to cool to room temperature. Ten mL of 10X $CaCl_2$ were diluted in 90 mL of dH_2O and the two solutions mixed. The pH was adjusted to 7.4 and the final buffer to 1 L.

The solution was then stored at -20 °C and heated to 37 °C prior to cell fixation. The solution was passed through a 0.2 µm filter prior to use in contact with cells.

2.3.2.3 Blocking solution for immunofluorescence

Twenty µL of Triton x-100 and 0.2 g of bovine serum albumin (BSA) were dissolved in 15 mL of DPBS containing Mg^{2+} and Ca^{2+}. Two mL of normal horse serum (S-2000, Vector laboratories) were added to the mixture and the final volume of the solution adjusted to 20 mL.

2.3.3 Fabrication of nano-patterns on gold surface

2.3.3.1 Fabrication of PDMS probe arrays

The PDMS pen array for PPL was constructed by thorough rotations of a mixture of 250 g of (7-8% (w/w) vinylmethylsiloxane)-dimethylsiloxane copolymer with an additional 172 µL of 1,3,5,7-tetravinylcyclotetrasiloxane and 10 µL of a complex solution of platinum(0)-1,3-divinyl-1,1,3,3-tetramethylsiloxane. A 1.7 g quantity of PDMS precursor was then mixed with 0.5 g of premixed (25-35% (w/w) methylhydrosiloxane)-dimethylsiloxane co-polymer. The mixed PDMS solution was then degassed on a silicon mould (custom made by NIL Technology) in a vacuum desiccator attached to a vacuum line (200 mTorr) for 20 min or until all bubbles had dissipated. A glass coverslip was then carefully placed onto the mould and placed in an oven at 80 °C for 24 h to thermally cure the PDMS pen array. Once the curing was complete the array was removed from the oven and allowed to cool. The array was removed with a razor blade by wedging in the corner and prying it apart from the mould. A 0.5 mm strip was then carefully scraped off the 4 edges of the array and any loose PDMS was removed using stream of N_2 gas.

2.3.3.2 Gold substrate preparation

SuperClean2 glass substrates were used for the compatibility on electron-beam evaporator. The substrates were treated with argon plasma and coated with a 4 ± 0.5 nm layer of titanium followed by 10 ± 2 nm gold using an electron-beam evaporator. Coated gold slides were then used without further treatment.

2.3.3.3 “Inking” of MHA

Trimmed arrays were securely taped on the lid of a glass petri dish with double sided carbon tape. A small quantity of MHA solid was added and evenly spread in the bottom of the petri dish. The petri dish was placed in a vacuum desiccator at atmospheric pressure to reduce contamination and the desiccator placed in an oven at 80 °C for 50 min. The desiccator was then removed and allowed to cool to room temperature for 15 min. The coating procedure was then repeated twice (Scheme 2.2).

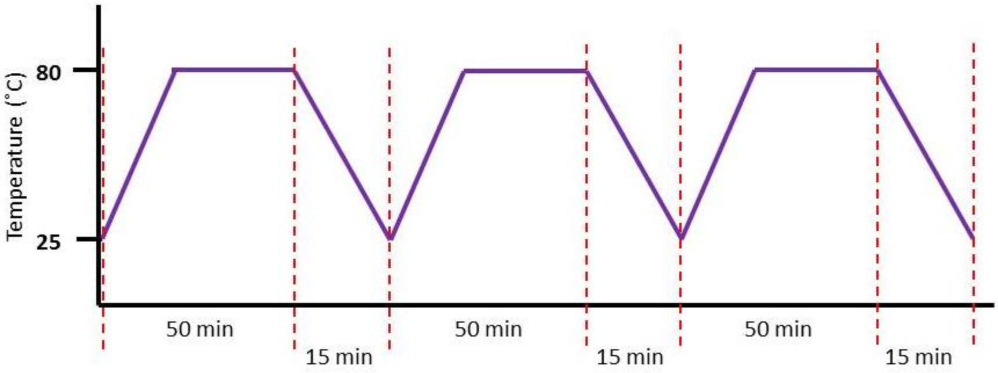

Scheme 2.2 Scheme showing the procedural cycle of vapour coating of MHA or AUT on PPL pen array.

2.3.3.4 "Inking" of AUT

In a process similar to that of MHA inking, a small quantity of AUT solid was added and evenly spread in the bottom of a petri dish. The petri dish was placed in a vacuum desiccator which was reduced in pressure to 300 mTorr to increase sample vapour pressure. The desiccator was then placed in an oven at 90 °C for 50 min and allowed to cool to room temperature for 15 min. The coating procedure was then repeated twice.

2.3.3.5 Pen array alignment algorithm

The developed automated alignment program employed an iterative approach-observe-withdraw-adjust process.[137]

2.3.3.5.1 Experimental assembly

A stage controller setup program (SetupNSF.exe) was operated to obtain absolute stage levels prior to alignment. The C3000 controller software was then turned on and the gold substrate secured on the sample stage with adhesive tape. The coated pen array was secured on an array holder with double-sided carbon tape. The substrate was manually advanced to the array in 20 µm steps using the stage controller until the substrate was approximately 1 mm away from the pen array. A stage sensor was released for 10 min prior to alignment. In the LabVIEW V13.0 user interface, the coarse step was typically set at 0.6 µm, the fine step at 0.2 µm and angle step at 0.15˚. The AFM scan head oscillation was initiated using a repetitive motion of advancing 10 µm over 100 ms, with a pause of 250 ms, a retraction of 10 µm over 100 ms with a pause of 250 ms at which point the sensor under the stage was released. During automated alignment, the stage was gradually moved towards the pen array until a force threshold of 588 µN was detected. The Z position was recorded, the stage tilted by 50 m° and the following measurement commenced. Once Z positions at all angles were established, the results were recorded in an Excel file and optimised θ and φ angles calculated. The sample stage was then tilted accordingly (Figure 2.1).

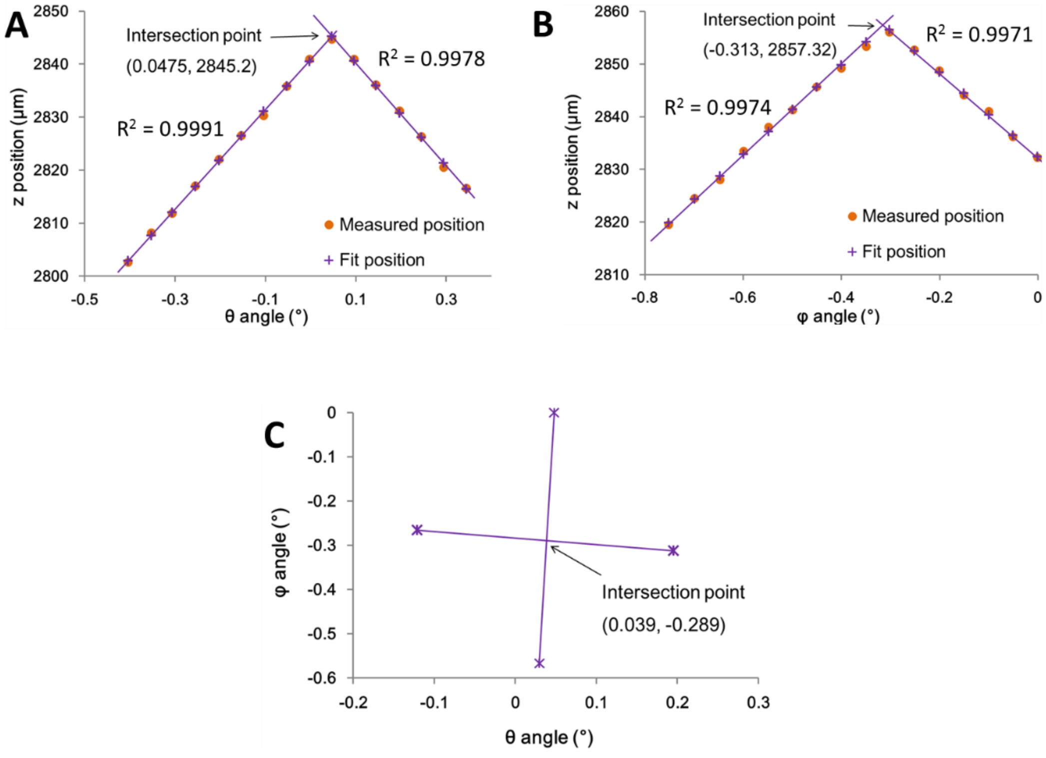

Figure 2.1 An example of a set of graphs illustrating successful alignment. Graphs of Z position against the tilt angles (A) θ and (B) φ after successful alignment, where ● indicates the actual values measured and + indicates the best fit using a least-squares method. (C) Graph of φ against θ fitted angles with the four points where the maximum Z-position was reached. The intersection point marked is the final optimum tilt angle across both axes. The example graphs were adopted from the published paper.[135]

2.3.3.6 Nanolithography

Upon completion of automated alignment, the atmospheric isolation chamber was mounted onto the AFM with the humidity generator set at 45% relative humidity (RH) and initial water flow at 500 mL. Water flow was then reduced to 300 mL upon approaching the desired humidity to ensure that it was maintained accurately and stably during lithography.

Upon completion of lithography, the sample stage was retracted by 500 µm. The atmospheric isolation chamber was removed and stage sensor then isolated from the stage before removal of the samples.

2.3.3.7 Pattern visualisation

To examine the fabricated nanoarrays over large areas, the gold surface was etched using a previously published protocol.[135, 138] Briefly, aqueous solutions of 40 mM thiourea, 27 mM iron(III) nitrate and 100 mM hydrochloric acid were separately prepared. Prior to etching of the surface, equal quantities of each of the three etchants were mixed then used freshly prepared. Samples were immersed in the solution for 3 min at an approximate rate of 3 nm min^{-1}. Samples were then rinsed three times with ultrapure water then dried under a stream of dry N_2 and visualised using an optical microscope. The etched samples were unsuitable for cell culture as the unpatterned gold area was etched and unable to be immobilised with m-PEG.

2.3.3.8 Surface passivation

Prior to culture of MSC, unpatterned areas were passivated with 1 mM (11-mercaptoundecyl)hexa(ethylene glycol) (m-PEG) solution in ethanol for 1 h. Samples were then rinsed with copious volumes of ethanol and dried under a stream of dry N_2.

2.3.3.9 ECM immobilisation

Prior to ECM immobilisation, selected nanoarrays were passivated with 1 mM m-PEG solution in ethanol for 1 h. Samples were then rinsed with copious volumes of ethanol and dried under a stream of dry N_2.

2.3.3.9.1 Fibronectin immobilisation on MHA nanoarrays

Selected MHA nanoarrays were immersed in 10 mM $Co(NO_3)_2$ aqueous solution for 5 min and rinsed with copious volumes of water. Fibronectin (F0895, SigmaAldrich) was diluted to a concentration of 50 μg mL^{-1} using DPBS and drop-coated onto the surface for 16 h at 4 ˚C. The fibronectin solution was then removed and the samples then rinsed with copious volumes of with DPBS prior to storage in DPBS at 4 ˚C before testing in cell culture experiments.

2.3.3.9.2 Fibronectin immobilisation on AUT nanoarrays

AUT arrays were immersed in a 2.5% glutaraldehyde solution at room temperature for 1 h. The solution was then removed and the surface washed copiously with water. Fibronectin was diluted to a concentration of 50 µg mL^{-1} using DPBS and drop-coated onto the surface for 16 h at 4 ˚C. The fibronectin solution was then removed and the samples then rinsed copiously with DPBS prior to storage in DPBS at 4 ˚C until testing in cell culture experiments.

2.3.4 hMSC culture

MSCs were cultured in growth media for both initial morphology and examination of differentiation. MSCs used for experiments were between passage 4 and 6 and seeded at a density of 10^4 cells cm^{-2}. All experiments were repeated 3 times unless otherwise stated.

2.3.5 Immunofluorescence

DPBS contained Mg^{2+} and Ca^{2+} was used in all cases unless otherwise stated.

At each time point, samples were rinsed with DPBS and fixed with pre-warmed 4% PFA for 20 min at room temperature then washed with copious volumes of DPBS.

2.3.5.1 Stain for vinculin, fibronectin and F-actin

Cells were permeabilised with 0.5% Triton-X100™ in DPBS for 15 min at room temperature and washed copiously with DPBS. Primary antibodies were diluted 1:100 with DPBS containing 1% BSA and stained for 16 h at 4 ˚C. Samples were washed copiously with DPBS containing 0.1% Tween™ 20 (PBST). Fluorescent conjugated secondary antibodies were then diluted according to manufacturer’s instructions and used to stain samples for 1 h at room temperature then washed with copious volumes of DPBS. F-actin was then stained with Alexa Fluor® 488 phalloidin at a dilution of 1:250 with DPBS for 30 min at 4 ˚C and washed copiously with DPBS. ProLong™ antifade diamond mounting media with DAPI was then dropped onto sample and a No. 1.5 glass coverslip mounted on top for microscopy.

2.3.5.2 Stain for differentiation markers

Samples were permeablised and non-specific binding blocked using blocking solution (previously described) for 45 min at room temperature. Primary antibodies were diluted 1:100 with DPBS containing 5% BSA and stained for 16 h at 4 ˚C. Samples were washed copiously with PBST. For fluorescent-conjugated secondary antibodies staining, relevant Alexa Fluor® 488 and Alexa Fluor® 594 conjugated antibodies were mixed to a dilution of 1:100 and 2 drops mL^{-1} according to the manufacturer’s instructions with DPBS containing 5% BSA, respectively. The mixture was then drop coated onto samples and stained for 1 h at room temperature then washed copiously with DPBS. ProLong™ antifade diamond mounting media with DAPI was then dropped onto each sample and a No. 1.5 glass coverslip mounted on top for microscopy.

2.4 Results and discussion

2.4.1 Material characterisation

Designed chemical nanoarrays were fabricated using a PPL technique. The fabricated nanoarrays were either imaged on AFM or unpatterned gold areas were etched and the patterns observed using optical microscopy to assess the homogeneity of the array features throughout a wide area (Figure 2.2).

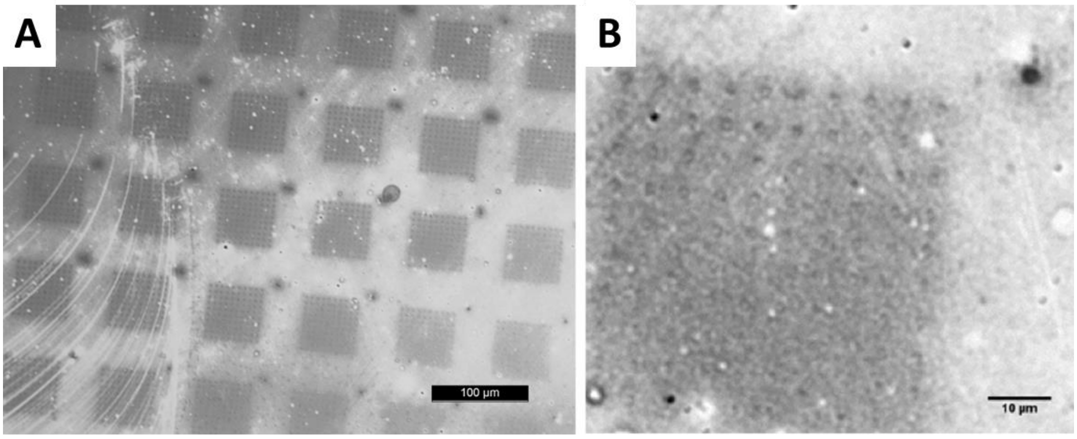

Figure 2.2 A representative image of (A) large-area fabricated PPL patterns and (B) a zoomed-in view of an individual pattern. A fabricated gold model surface was etched to create contrast between the patterned and unpatterned areas on the surface. The image was collected on a Leica DM 2500M upright microscope. Scale bars represent 100 µm and 10 µm, respectively.

Fabricated patterns were selectively etched and observed by optical microscopy as a quality control of wide area fabrication. The etched surfaces were then discarded as they could not be used as a chemical nanoarray for experiments because the unpatterned area would be exposed to the adhesive titanium layer which could not be passivated with m-PEG after etching.

2.4.2 Nanoarray design

A range of MHA and AUT arrays were selected to study initial hMSC morphology (Table 2.1 and Figure 2.3).

Table 2.1 A list of 6 selected candidate surfaces detailing the parameters within the patterns.

Candidate	Centre to Centre Distance (dα, µm)	Array of Feature	Area of Pattern (µm)	ECM coating	Feature size (dβ, nm)
MHA20	3.14	20 x 20	60 x 60	N/A	300 ± 5
MHA40	1.53	40 x 40	60 x 60	N/A	300 ± 5
MHA60	1.01	60 x 60	60 x 60	N/A	300 ± 5
AUT20	3.14	20 x 20	60 x 60	N/A	300 ± 5
AUT40	1.53	40 x 40	60 x 60	N/A	300 ± 5
AUT60	1.01	60 x 60	60 x 60	N/A	300 ± 5

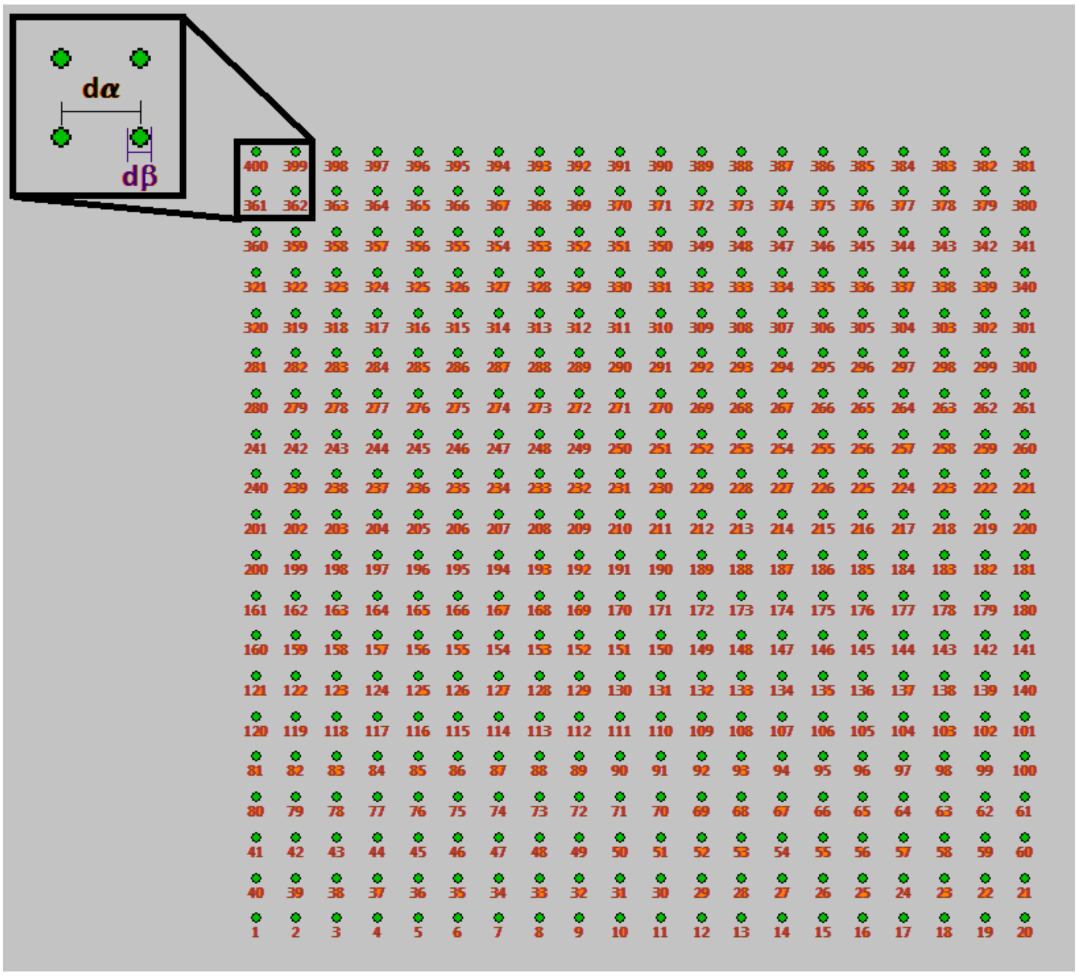

Figure 2.3 An illustrative image of a single pattern with 20 x 20 arrays of features with defined centre-to-centre distance (dα) and individual feature size (dβ).

A minimum adhesion site of 110 μm^2 required to provide initial MSC adhesion was previously optimised over an area of 3600 μm^2 (a square pattern of 60 x 60 μm) using a pen array with 180 × 180 μm pen spacing.[139] Therefore a minimum of 20 x 20 arrays of the feature were fabricated with an optimised and reproducible individual mean feature size of 300 nm. The centre-to-centre distance (dα) was systematically reduced to study the potential effects in MSC differentiation.[41]

Two presenting chemistries, MHA with carboxyl groups and AUT with amino groups, were selected to fabricate the surface nanoarrays. All candidate materials had identical areas with individual patterns of 60 μm x 60 μm and altered in a number of features patterned in each array. For example, MHA20 represented a nanoarray fabricated using MHA as the “ink” in arrays of patterns consisting of features that were 20 x 20 dots, *i.e.,* 400 features in total within each area of 60 µm x 60 µm patterns. MHA20 featured a centre-to-centre distance, dα, of 3.14 µm between each neighbouring dot with individual dots having a feature size of 300 ± 5 nm. Each 60 µm x 60 µm pattern of features were a distance of 40 µm from its neighbouring pattern due to the nature of the polymer pen array moulds manufactured with a 100 µm centre-to-centre distance between each pen pyramid.

2.4.3 Fluorescent imaging of nanoarrays

Fibronectin was coated on MHA20 and AUT20 patterns, candidates named as MHA20-FN and AUT20-FN, respectively (Table 2.2).

Table 2.2 List of 2 ECM bound nanoarray candidates and design parameters

Candidate	Centre to Centre Distance (dα, µm)	Array of Feature	Area of Pattern (µm)	ECM coating	Feature size (dβ, nm)
MHA20-FN	3.14	20 x 20	60 x 60	fibronectin	300 ± 5
AUT20-FN	3.14	20 x 20	60 x 60	fibronectin	300 ± 5

These surfaces were initially stained with fluorescent antibodies and used to visualise pattern-cell interaction under fluorescent microscopy. They were subsequently used as an ECM in order to distinguish initial cell response isolated nanoarray patterns from presenting chemistry stimuli (Figure 2.4).

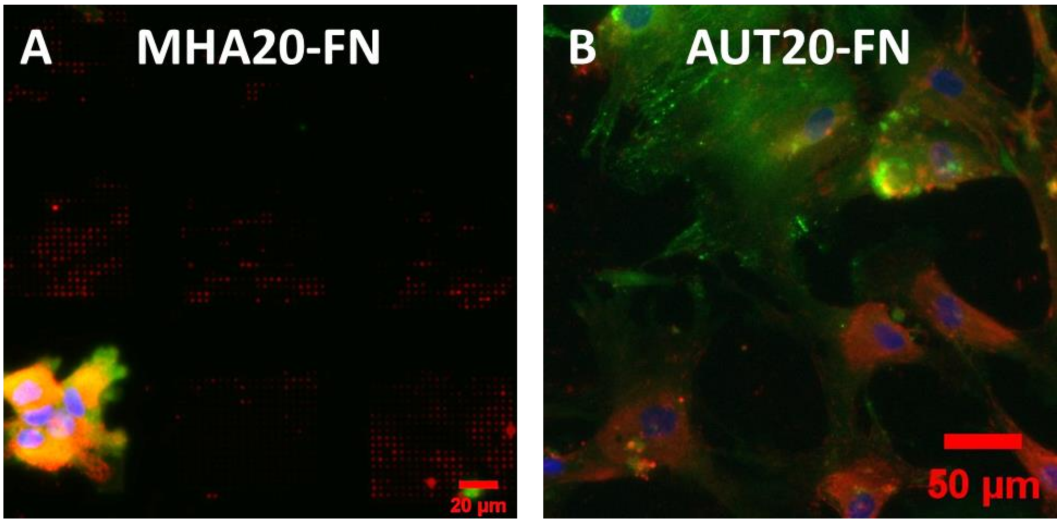

Figure 2.4 Representative fluorescent images of hMSC cultured in contact with (A) MHA20-FN and (B) AUT20-FN. Subsequent to hMSC culture, cells were fixed with 4% PFA and counterstained with F-actin (green), fibronectin (red) and nuclei (blue). Images were acquired using a Zeiss Apotome.2 microscope.

Fibronectin was bound to MHA-functionalised areas firstly through chelation of Co(II) by the terminal carboxylic acid groups on the MHA.[140] Fibronectin was then selectively bound to Co(II) *via* its collagen-binding domain.[141] As such, fibronectin would only bind to the patterned area masking active carboxyl groups, leaving the passivated area unaffected (Panel A, Figure 2.4).

On AUT-patterned surfaces, terminal amine groups were first reacted with one end of the carbonyl groups on glutaraldehyde. Fibronectin was then expected to bind on the other end of glutaraldehyde.[91] The result, however, showed no specific fibronectin adhesion to amine sites making pattern visualisation impossible (Panel B, Figure 2.4). This could have been caused by the reversibility of glutaraldehyde under uncontrolled pH environments as previously reported.[142]

An example of hMSC adhesion on a PPL fabricated large-area nanoarray is shown in Figure 2.5.

Figure 2.5 Representative large-area image of hMSC cultured in contact with MHA20-FN for 7 days. F-actin (green), vinculin (red) and nuclei (blue) were stained. Individual images were taken separately on an Olympus BX51 upright microscope using a 4x / 0.13 UPlan FLN then stitched using Fiji ImageJ.

It was established that the PPL technique could be used to successfully fabricate large-area homogeneous nanoarrays for initial hMSC adhesion. The representative image, as an example, shows that MSCs successfully adhered to the patterned surface, with 64.79% of patterns with adhered MSCs, calculated using Fiji ImageJ. Amongst which 26.61% of patterns had isolated MSCs adherent to a single array. MSC attachment was absent on the remaining, presumably patterned, areas. There are multiple possible reasons for this.

Firstly, during fabrication of the PPL pen array, a small number of invisible air bubbles could be trapped within some of the reverse pyramids of the probe on the silicon moulds resulting in an absence of pen arrays.

Secondly, after repeated usage of the PPL mould, the originally deposited perfluorodecyltrichlorosilane (FDTS) layer might be damaged during the cleaning process leaving bare silicon exposed. Upon detaching of the glass-supported probe arrays, some probes might be adhered to the silicon and break from the glass base causing some locations to have an absence of probes for the PPL patterning process.

Finally, even though cells were seeded in a homogeneous suspension in cell culture media, cells may not evenly attach onto all patterned arrays. In cases of initially adhered cells, cells that were adhered on nanoarrays were shown to have the ability to detach and relocate onto neighbouring arrays (Appendix 1). Adhered cells could also attract cells in suspension so that they adhered, sharing the same non-restricted locations.

Regardless of these limitations, these data demonstrated that PPL has potential in enabling high-throughput surface fabrication for cell applications over large areas (multiple cm^2).

2.4.4 Initial mesenchymal stem cell morphology

Initial cell morphology was examined with MSCs cultured in contact with fabricated model surfaces for 24 h (Figure 2.6).

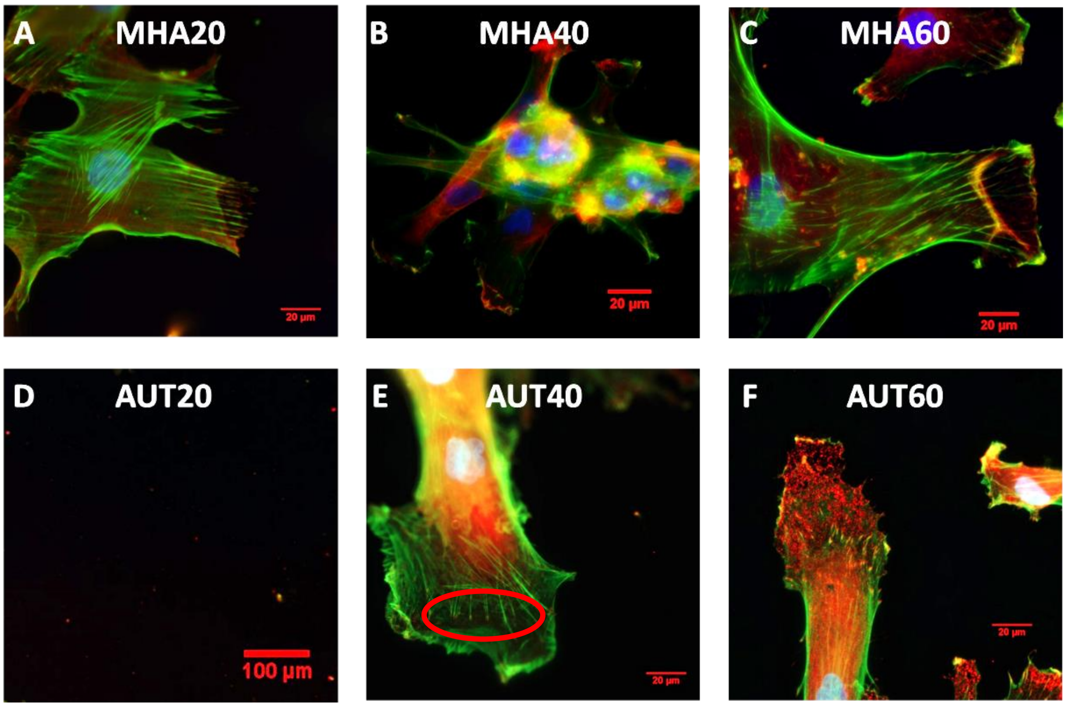

Figure 2.6 Representative fluorescent images of MSCs cultured in contact with (A) MHA20 (B) MHA40 (C) MHA60 (D) AUT20 (E) AUT40 (F) AUT60 nanoarrays for 24 h. Subsequent to hMSC culture, cells were fixed with 4% PFA and counterstained with F-actin (green), vinculin (red) and nuclei (blue). Images were acquired using a Zeiss Apotome.2 microscope. Scale bars represent 20 µm except (D) which represents 100 µm.

As PPL fabricated nanoarrays would be invisible under fluorescent or optical microscopy unless pre-coated with fibronectin and stained with fluorescently conjugated antibodies, the extent of patterned areas was estimated based on cell morphology, if appropriate. For example, cells would be expected to adhere to patterned nanoarrays and restricted by non-patterned areas that were passivated with m-PEG.[114] However, certain levels of cell bridging over neighbouring patterns could be expected, providing insufficient pen array spacing (*i.e.,* 100 x 100 µm spacing with 60 x 60 µm patterned area leaving only a 40 µm passivated region between neighbouring patterns) and variant MSC size from 15 to 50 µm in 2D culture (Appendix 2).[143]

MSCs cultured in contact with selected nanoarrays exhibited distinct initial morphological differences within 24 h. MSCs adhered onto MHA20 with a flattened cell shape and aligned cytoskeleton but unrestricted within the patterned areas (Panel A, Figure 2.6). In contrast, F-actin-stained MSCs on MHA40 exhibited reduced alignment on patterned areas (Panel B, Figure 2.6). However, the cells appeared aggregated in contrast to the flattened morphology on MHA20. On MHA60, MSCs demonstrated a more defined cytoskeleton at the edge of the cells (Panel C, Figure 2.6).

Conversely, on AUT20, which had identical feature orientation to MHA20 but presenting amino groups (-NH_2), no cell attachment was visible for up to 24 h of culture (Panel D, Figure 2.6). On AUT40 nanoarrays, MSCs exhibited adhesion on the patterns in contrast to AUT20 (Panel E, Figure 2.6). In comparison to their morphology on MHA40, cells on AUT40 exhibited relatively clear vinculin co-localised with actin filaments as highlighted in red in panel E, Figure 2.6. Moreover, MSCs on AUT60 nanoarrays exhibited the most distinct adhesion on the patterned nanofeatures as vinculin demonstrated clear features on the patterned regions (Panel F, Figure 2.6).

The effect of surface chemistry was isolated from nanoarray feature stimulus by pre-coating with fibronectin, a commonly used ECM protein, on the patterned areas. Initial cell morphology on MHA20 was compared with MHA20-FN (Figure 2.7).

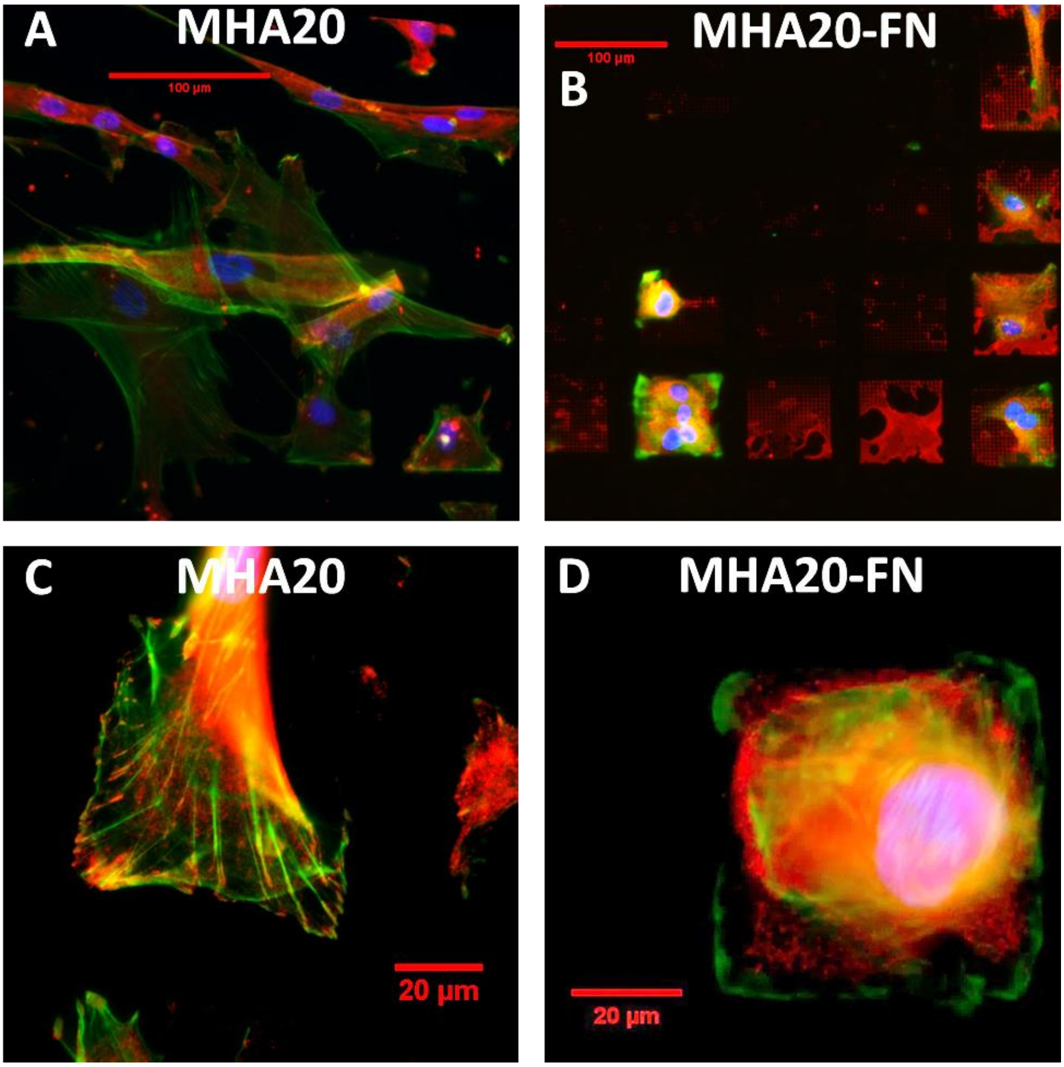

Figure 2.7 Representative fluorescent images of MSCs cultured in contact with patterned nanoarrays for 24 h. Cells were fixed and counterstained with (A) and (C) F-actin (green), vinculin (red) and nuclei (blue) on MHA20 and (B) vinculin (green), fibronectin (red) and nuclei (blue) (D) F-actin (green), fibronectin (red) and nuclei (blue) on MHA20-FN. Images were acquired using a Zeiss Apotome.2 microscope. Scale bars in (A) and (B) represent 100 µm, in (C) and (D) 20 µm.

As previously stated, MSCs adhered to the MHA20 nanoarrays interacted with the patterned areas but were not strongly restricted within the patterns (Panel A, Figure 2.7). In panel C, Figure 2.7, hMSC exhibited cytoskeleton that were clearly within the patterns. However, the cytoskeleton was absent on the upper right corner of the pattern, displaying a trace of vinculin. This might be due to MSC initial adherence but detachment over time or migration towards a neighbouring pattern. In contrast, MSCs on the fibronectin pre-coated array, MHA20-FN, adhered and were restricted within the border of the individual patterns (Panel B, Figure 2.7). Cells exhibited a relatively high level of cytoskeletal organisation at the edges of the patterns but were less distinct within the patterned arrays (Panel D, Figure 2.7).

Interactions of MSCs on isolated arrays of nanofeatures were also assessed on the fibronectin pre-coated patterns MHA20-FN, to evaluate the effect of feature size without chemistry (Figure 2.8).

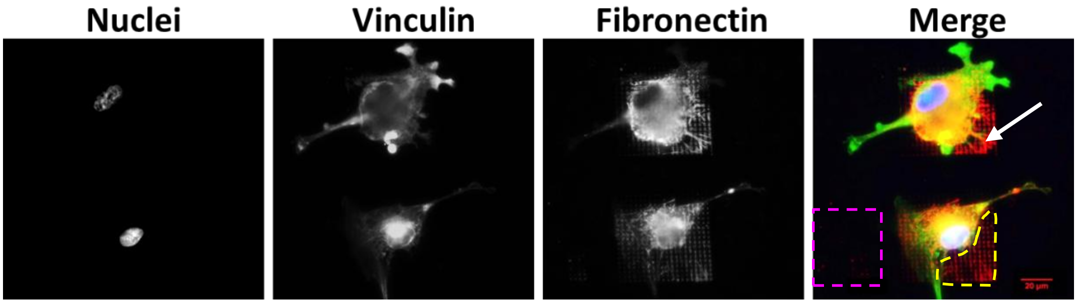

Figure 2.8 Representative images of MSCs cultured in contact with MHA20-FN for 24 h showing clear cell-matrix interaction on the patterned features. Fibronectin pre-coated patterns were stained with fluorescently conjugated antibody (red) subsequent to fixation after 24 h MSC culture. The sample was counterstained with vinculin (green) and nuclei (blue). Yellow and magenta highlighted areas were used for measurements of fibronectin feature sizes as an indication of feature size affected post-cell adhesion as opposed to no cell attachment, respectively. Scale bar represents 20 µm.

Focal adhesion between MSCs and individual patterns was assessed by active vinculin localisation associated with isolated fibronectin patterns. Vinculin is a membrane-cytoskeletal protein that associates with cytoplasmic interfaces of both cell-cell and cell-ECM adhesion.[144] Active vinculin adhesions were expected to appear as bright and distinct focal patches at the end of F-actin as a part of the focal adhesion mechanism.[145] On isolated nanopatterns, active vinculin foci appeared to be small and the cells lacked elongated vinculin plaques. However, on the upper pattern (Figure 2.8 indicated by the white arrow in the merged panel), MSCs exhibited fibronectin and vinculin co-localisation, with fibronectin extended onto extracellular fibronectin. Similar observations were previously reported where vinculin could occasionally integrate with fibronectin fibres although fibronectin is frequently extended to inter-cellular distribution whereas vinculin is strictly cellular.[146]

It should be noted that where MSCs had adhered to fibronectin patterns, they appeared visually to have a considerably larger size, at 1.47 ± 0.31 µm (calculation based on the area highlighted in yellow, Figure 2.8) compared with the neighbouring pattern on its left at 350.8 ± 86.2 nm (calculation based on the area highlighted in magenta, Figure 2.8) where presumably no cells were adhered at any point. The feature size differences were thought to be caused by the deposition of fibronectin from cells at the point of adhesion. The absence of cell attachment on the yellow highlighted area, as judged by the vinculin immunofluorescence signal, could be explained by cells that had detached from the region and migrated towards the other end.

However, it should also be noted that fluorescent images were acquired based on the excitation and emission of the fluorophore in contrast with the background. Therefore, slight over- or underexposure could significantly affect measured feature sizes especially with nano- to submicron features. This could be among the reasons that measured feature sizes (as highlighted in magenta) were larger than the size of the initial PPL fabricated nanoarrays.

Another possible reason could be that the fibronectin feature size was enlarged following indirect immunofluorescence methods. During indirect immunofluorescence methods, unconjugated primary antibodies were bound to a target antigen and multiple secondary antibodies were then expected to bind to each primary antibody resulting in amplification of fluorescent signals by enlarging the presence of antibodies (Appendix 3).

Initial cell morphology studies on the selected chemical nanoarrays indicated that MHA nanoarrays provided a better adhesion site to MSCs than did AUT nanoarrays with identical patterns as sufficient cell adhesion was observed on MHA20 and none on AUT20. In addition, fibronectin pre-coated nanoarrays supported MSC alignment and restriction within individual patterns.

2.4.5 Mesenchymal stem cell morphology after extended culture

Culture of MSCs on selected PPL-fabricated nanoarrays was extended to 7 days for observation of morphology (Figure 2.9). AUT20 nanoarrays were excluded for further study as no cells adhered on the surface for up to 24 h.

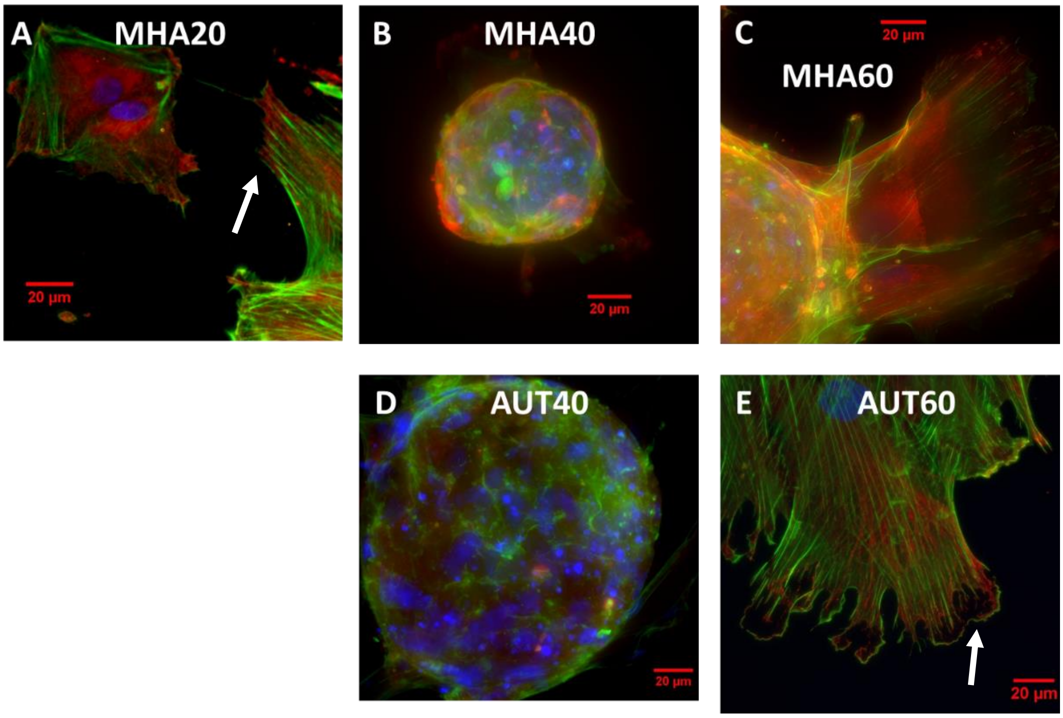

Figure 2.9 Representative fluorescent images of MSCs cultured in contact with PPL fabricated nanoarrays (A) MHA20, (B)MHA40, (C) MHA60, (D) AUT40, and (E) AUT60. Cells were fixed after culture for 7 days and counterstained with vinculin (red) F-actin (green) and nuclei (blue). White arrows in (A) MHA20 indicated aligned cytoskeleton and (E) AUT60 indicated ruffling membranes. Images were acquired using a Zeiss Apotome.2 microscope. Scale bars represent 20 µm.

After 7 days culture on PPL patterned nanoarrays, MSCs on MHA20 patterns exhibited a well-spread and flattened morphology with a well-defined and aligned cytoskeleton, as highlighted with a white arrow in Panel A, Figure 2.9. In contrast, cells on MHA40 exhibited a highly clustered morphology of approximately 30 µm in total height (Panel B, Figure 2.9, height recorded from original .czi stack image). Similar to MHA40, MSCs on MHA60 exhibited extensive clustering after 7 days of culture (Panel C, Figure 2.9). The height of the cluster was smaller than that on MHA40, measuring approximately 10 µm. In contrast, cells at the base of clusters on MHA60 exhibited an intense "skirt", presumably reaching out to neighbouring patterns. The observed "skirt" showed intense vinculin plaques and an aligned cytoskeleton. MSCs on AUT40 clustered to a height of less than 10 µm, similar to MHA40 (Panel D, Figure 2.9).

Clustering morphology has previously been observed in both chondrocytic culture and mesenchymal stem cell culture after chondrogenic differentiation.[11, 147] Therefore the initial morphology of cells on MHA40, MHA60 and AUT40 nanoarrays were thought to be possibly exhibiting the characteristics of chondrogenic differentiation.

On AUT60, however, MSCs demonstrated an extremely flattened morphology with distinct cytoskeletal and vinculin plaques (Panel E, Figure 2.9). The cytoskeleton was observed to be ruffled at the edge of cell membrane. Membrane ruffling corresponds to early stage structural change in response to newly polymerised actin filaments found on the cell surface and in the advancing front of a lamellipodium, a broad and fan-shaped protrusion with an F-actin–rich leading edge, in migratory cells.[148-150]

Stem cell migration was discovered to be regulated by a fibronectin crosstalk mechanism through the mediation of integrin α5β1.[151] Integrin α5β1 subunits have been reported to perform an essential role in osteogenic differentiation through the activation of focal adhesion kinase (FAK) and ERK1/2 signalling.[152, 153]

Cells on MHA20 and MHA20-FN were compared to validate the effect of isolated nanoarrays and presention of chemistry on stem cell morphology (Figure 2.10).

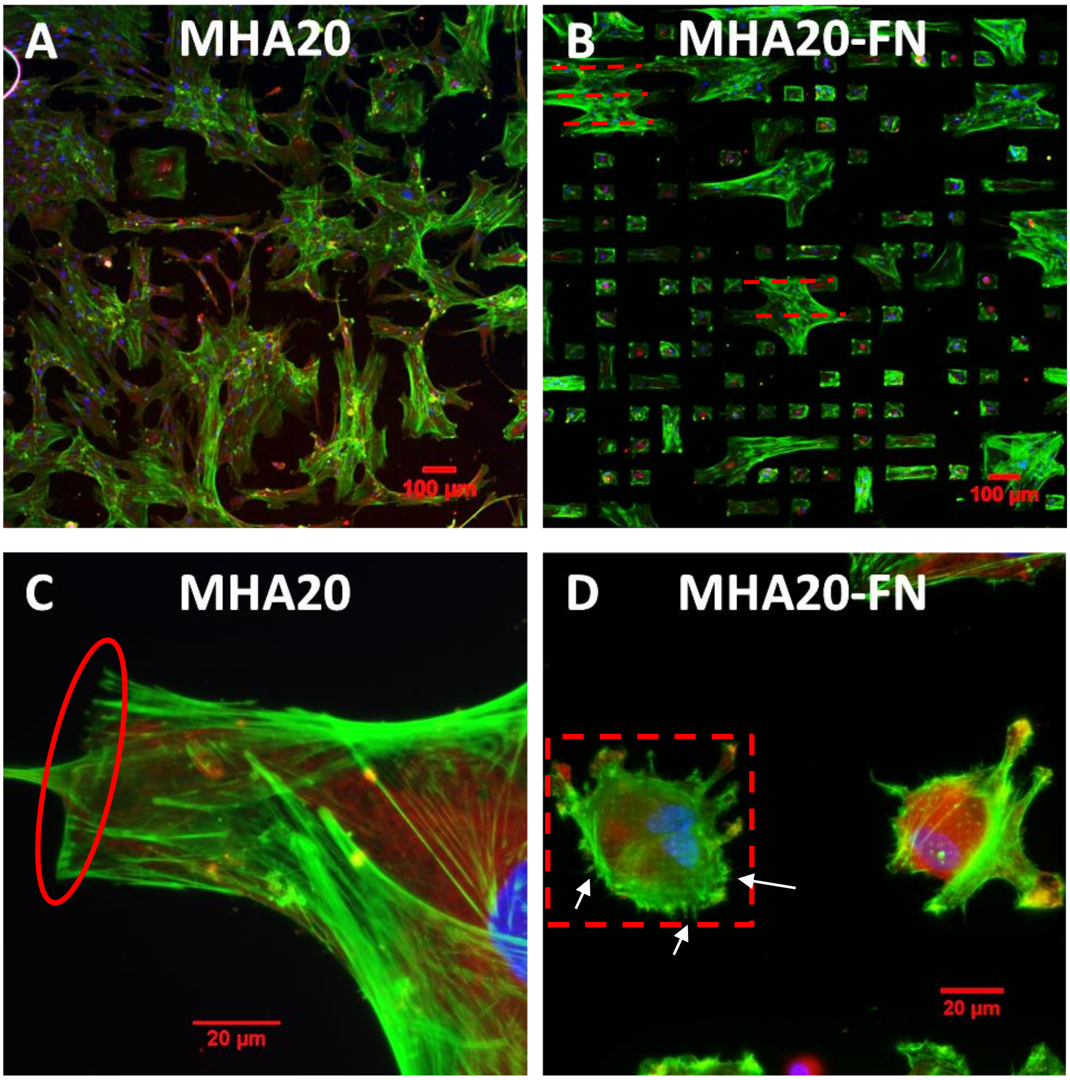

Figure 2.10 Representative fluorescent images of MSCs cultured in contact with PPL fabricated nanoarrays (A) and (C) MHA20, (B) and (D) MHA20-FN. Cells were fixed after culture for 7 days and counterstained with vinculin (red) F-actin (green) and nuclei (blue). Images were acquired using a Zeiss Apotome.2 microscope. Scale bars in (A) and (B) represent 100 µm, in (C) and (D) represent 20 µm.

MSCs demonstrated a distinct interaction with both MHA20 and MHA20-FN nanoarrays (Panel A and B, Figure 2.10). However, cells on MHA20 nanoarrays exhibited greater mobility on the surface of fabricated arrays in contrast with those on MHA20-FN, which appeared highly aligned, as shown in red dashes, if not completely restricted within the arrayed ECM patterns.

At the border of individual patterns where MSCs adhered, actin filaments demonstrated distinct polymerisation, especially visible at the end of a row in the array, as highlighted in red in panel C, Figure 2.10. Notably, MSCs on MHA20-FN ECM arrays exhibiting constrained mobility also demonstrated distinct focal adhesion to individual features within the patterns (Panel D, Figure 2.10). Shown with red dashed highlights, fluorescently stained F-actin in the cells reflected defined features in green. Note that fibronectin was not counterstained in the image. The image demonstrated that cells were adhered on individual features as nanoislands with actin outreach presumably to array features within the patterns, as highlighted with white arrows.

The extent of MSC clustering and cell spreading was assessed among the cluster-inducing nanoarrays: MHA40, MHA60 and AUT40, in contrast to well-spread morphology on AUT60 (Figure 2.11).

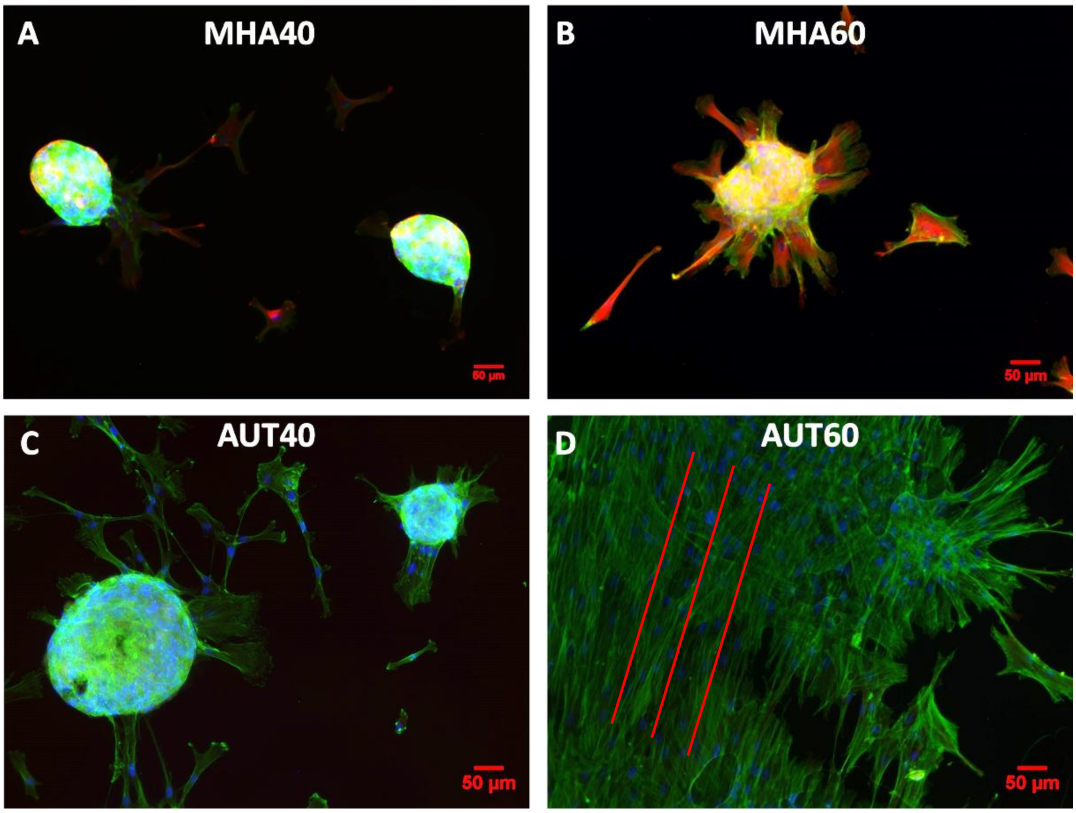

Figure 2.11 Representative fluorescent images of MSCs cultured in contact with PPL fabricated nanoarrays (A) MHA40, (B) MHA60, (C) AUT40 and (D) AUT60. Cells were fixed after culture for 7 days and counterstained with vinculin (red) F-actin (green) and nuclei (blue). Images were acquired using a Zeiss Apotome.2 microscope. Scale bars represent 50 µm.

The sizes of clustered cells on MHA40 nanoarrays were measured using Fiji ImageJ, at 15.5 x 10^3 and 12.9 x 10^3 µm^2 (Panel A, Figure 2.11). Underneath the clusters an extension from the base of the cells was observed, presumably reaching for neighbouring patterns. In contrast, MSCs on MHA60 clustered to a size of 17.7 x 10^3 µm^2 with extensive adhesion support outreaching to neighbouring patterns (Panel B, Figure 2.11). MSCs on MHA60 appeared visually, with a similarity to MHA40, to have a smaller population with the majority of cells clustered and few cells adhered on the surrounding regions.

On AUT40 nanoarrays, cell clustering appeared to be irregularly sized, measuring 47.6 x 10^3 µm^2 and 7.7 x 10^3 µm^2 (Panel C, Figure 2.11). Cell clustering was also observed with an extended base similar to that on MHA40. Stem cell on AUT60, however, exhibited distinctly different morphology on MHA40, MHA60 or AUT40. Cells were observed with a highly aligned morphology as indicated with red lines (Panel D, Figure 2.11).

It should, however, be noted that the majority of the area of interest had little cell attachment on MHA40, MHA60 or AUT40. This could be due to the cells that were seeded on MHA40, MHA60 and AUT40 experienced extensive clustering, resulting in appearing visually less populated and extensively-spread as on AUT60. Due to the nature of the clustering on MHA40, MHA60 and AUT40 nanoarrays, calculation of cell density using a cell nuclei count was not possible. It was hypothesized that MSCs retained their motility on chemically-defined nanoarrays. Thus, surfaces with chondrogenic-induction potential allowed cells to migrate and cluster over time whereas nanoarrays with potential for osteogenenic-induction induced cells to spread across the surface.

2.4.6 Mesenchymal stem cell differentiation

Results of the initial validation of hMSC morphology suggested that selected PPL-fabricated nanoarrays potentially induced chondrogenic or osteogenic terminal differentiation of MSCs, based upon changes in observed cell morphology. Specific differentiation pathways of the cells on these nanoarrays were therefore verified by detection of specific osteogenic markers such as osteocalcin and core-binding factor subunit alpha-1 (Cbfa1), and chondrogenic markers such as type II collagen.

Cbfa1 has been reported to be an important transcription factor for both chondrogenic and osteogenic differentiation.[154] Cells were stained with Cbfa1 after 14 and 28 days of culture (Figure 2.12, Figure 2.13, Figure 2.14 and Figure 2.15).

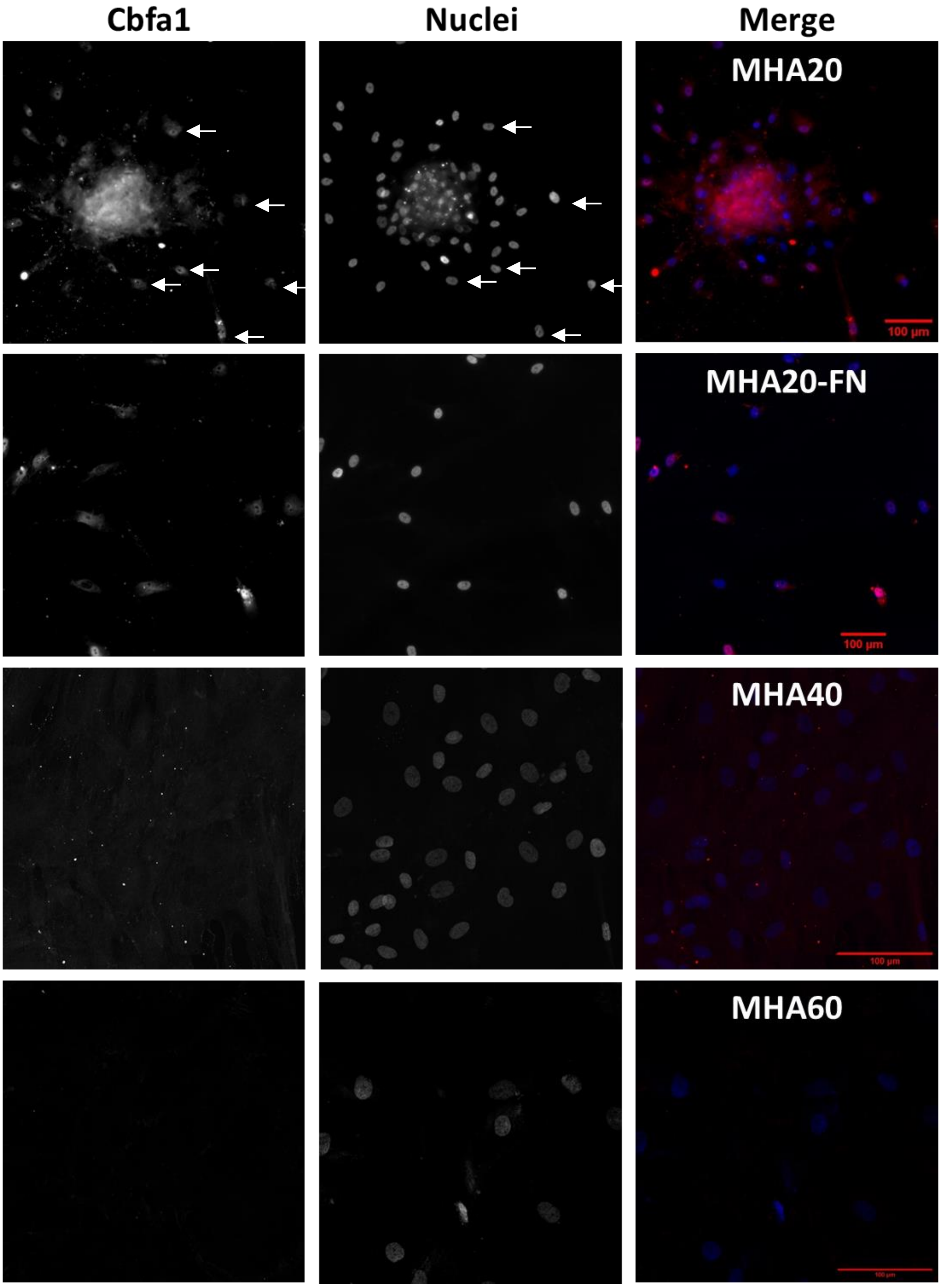

Figure 2.12 Representative fluorescent images of MSCs cultured on the PPL fabricated nanoarrays MHA20, MHA20-FN, MHA40 and MHA60. Cells were fixed after 14 days of culture and counterstained with Cbfa1 (red) and nuclei (blue). Images were acquired using a Zeiss Apotome.2 microscope or Zeiss LSM800 confocal microscope where MHA20, MHA20-FN showed positive in CBFA1. Scale bars represent 100 µm.

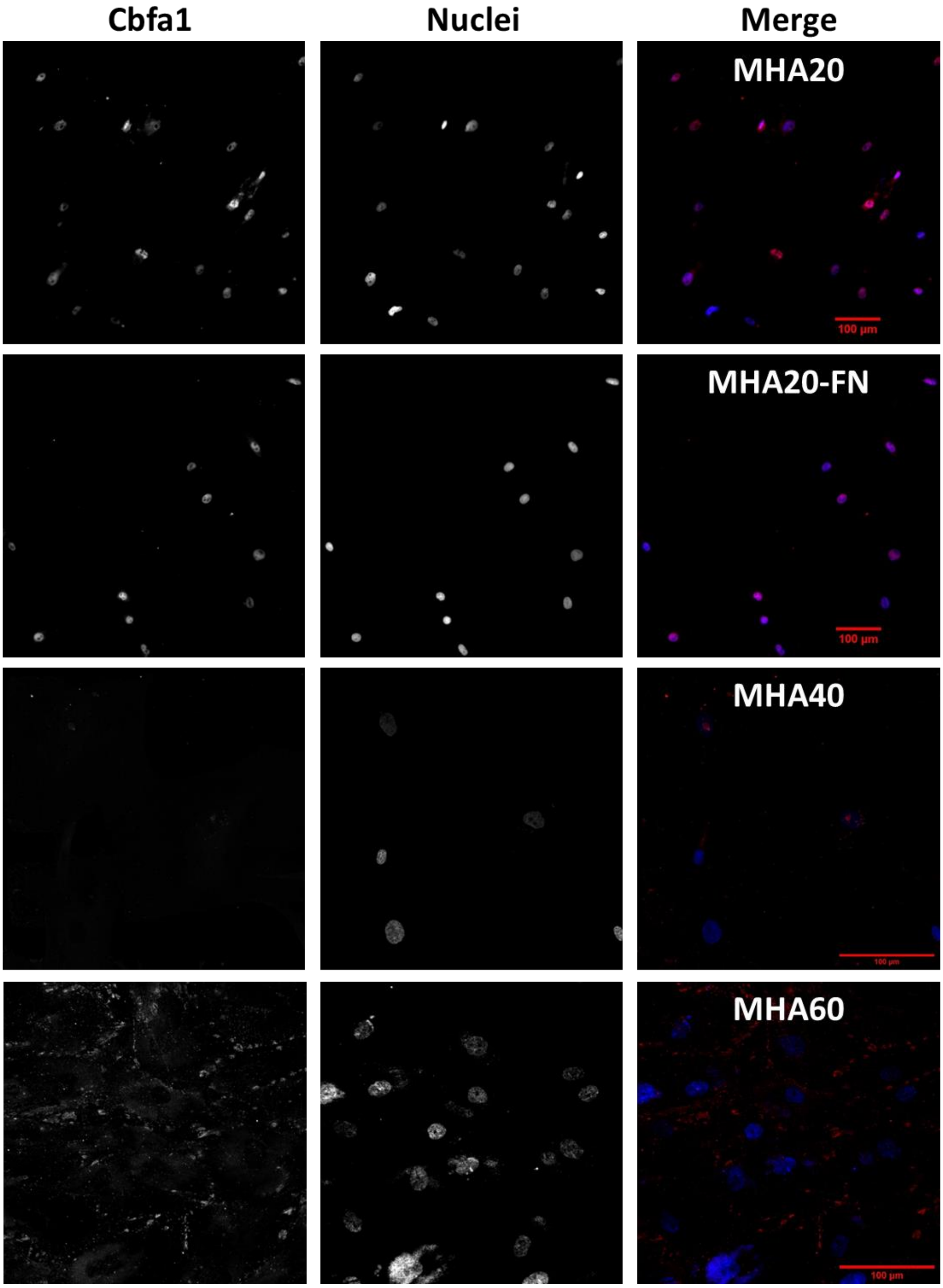

Figure 2.13 Representative fluorescent images of hMSC cultured on the PPL fabricated nanoarrays MHA20, MHA20-FN, MHA40 and MHA60. Cells were fixed after 28 days of culture and counterstained with Cbfa1 (red) and nuclei (blue). Images were acquired using a Zeiss Apotome.2 microscope or Zeiss LSM800 confocal microscope. MSCs on MHA20 and MHA20-FN were positive for Cbfa1. Scale bars represent 100 µm.

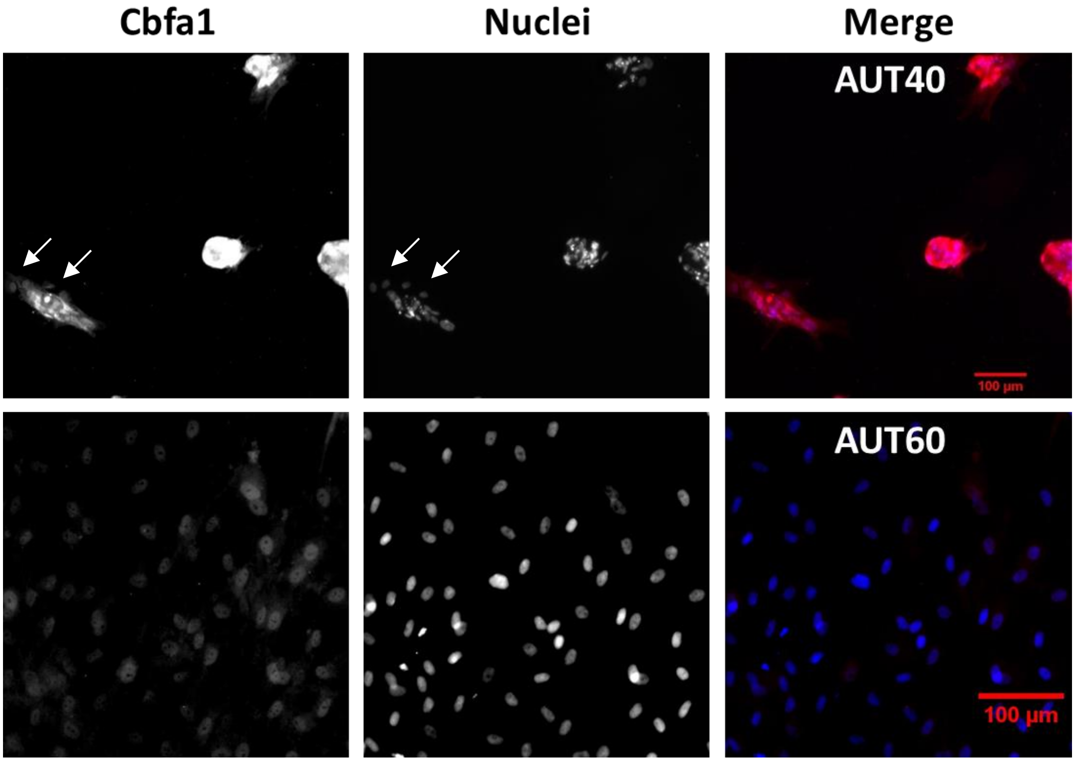

Figure 2.14 Representative fluorescent images of MSCs cultured on the PPL fabricated nanoarrays AUT40 and AUT60. Cells were fixed after 14 days of culture and counterstained with Cbfa1 (red) and nuclei (blue). Images were acquired using a Zeiss Apotome.2 microscope or Zeiss LSM800 confocal microscope. MSCs on both AUT40 and AUT60 were positive for Cbfa1. Scale bars represent 100 µm.

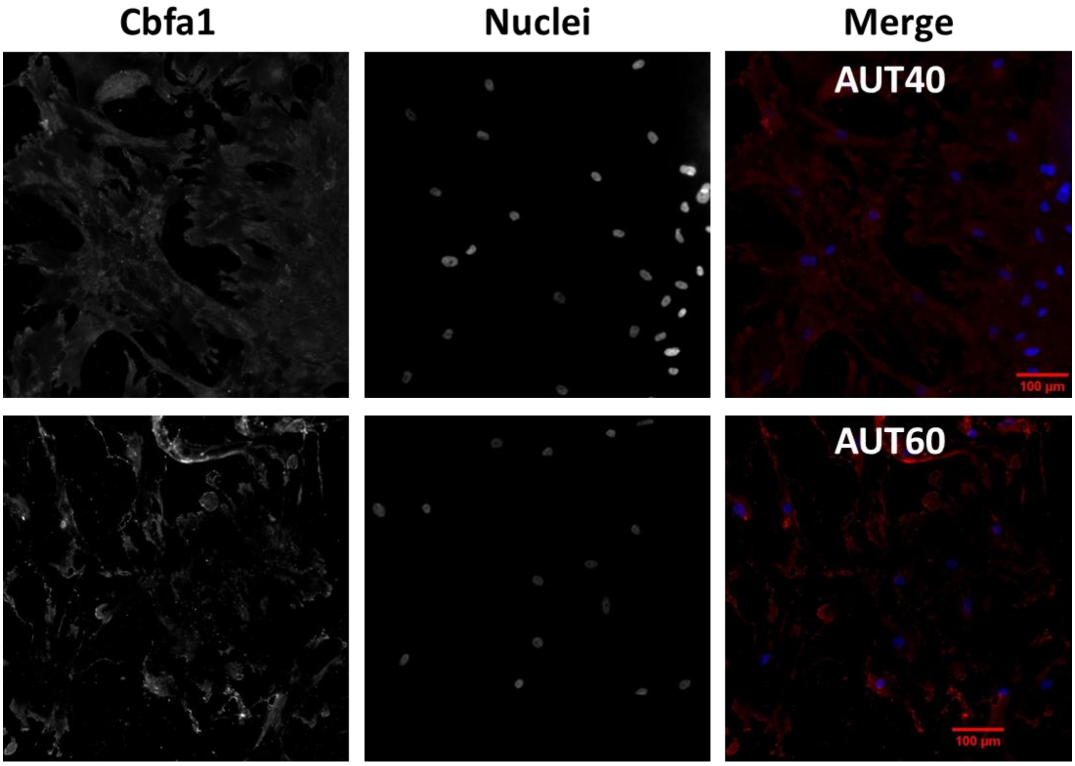

Figure 2.15 Representative fluorescent images of hMSC cultured on the PPL fabricated nanoarrays AUT40 and AUT60. Cells were fixed after 28 days of culture and counterstained with Cbfa1 (red) and nuclei (blue). Images were taken using a Zeiss Apotome.2 microscope or Zeiss LSM800 confocal microscope. MSCs on both AUT40 and AUT60 were negative for CBFA1. Scale bars represent 100 µm.

MSCs cultured on MHA20 for both 14 and 28 days exhibited positive staining for Cbfa1 (Figure 2.12 and Figure 2.13). In representative images of 14 days culture, a few examples can be seen, indicated by white arrows where Cbfa1 staining overlaps the DAPI stain. Cell clustering is also apparent, similar to the morphology appearing in earlier stages of culture on MHA40, MHA60 and AUT40, after 7 days (Panel B, C and D, Figure 2.9). MSCs on MHA20-FN ECM arrays also exhibited positive Cbfa1 staining, similar to the response to MHA20, after both 14 and 28 days of culture. In contrast, MSCs on MHA40, despite exhibiting extremely weak Cbfa1 expression, demonstrated no positive staining within the nucleus after both 14 and 28 days. Similarly, MSCs on MHA60 were negative for

Cbfa1 after both 14 and 28 days. Cells retained a similar clustered morphology on AUT40 after 14 days and stained positivefor Cbfa1 (Figure 2.14, top row). As MSCs were highly clustered, the Cbfa1 stain was not clearly distinguishable but on a smaller sized cluster it was clearly positive for Cbfa1 within the nucleus as indicated by white arrows in the representative images. However, after 28 days of culture, MSCs on AUT40 exhibited an absence of Cbfa1 (Figure 2.15). Cells on AUT60 were positive for Cbfa1 after 14 days of culture, in similarity to AUT40, but absence after 28 days. It has been previously reported that Cbfa1 deficiency results in inhibition of osteogenesis and potentially promotion of the adipogenesis pathway.[154]

MSCs on both AUT40 and AUT60 exhibited rich expression of Cbfa1 after 14 days of culture but the complete loss by 28 days suggests that AUT40 and AUT60, in the early stages, may potentially support the promotion of either chondrogenic or osteogenic differentiation pathways, but the effect was insufficient, causing depletion of Cbfa1 during the later stage and therefore suggests either an adipogenic or osteogenic differentiation potential.

Type II collagen has been reported to be a cartilage-specific ECM due to its synthesis and maintenance in chondrogenesis.[82] Cells were stained for type II collagen after 14 and 28 days of culture (Figure 2.16, Figure 2.17, Figure 2.18 and Figure 2.19).

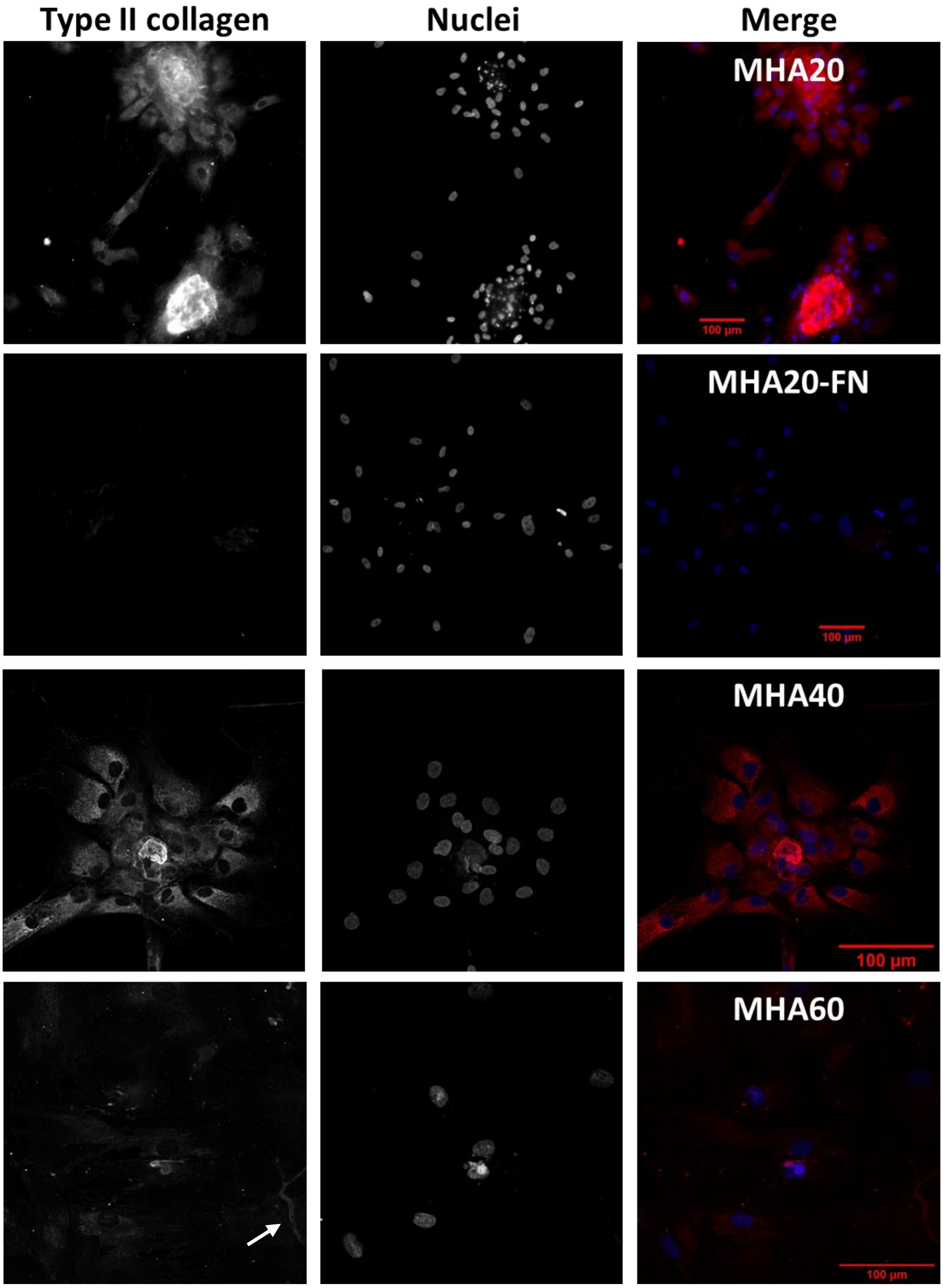

Figure 2.16 Representative fluorescent images of MSCs culturedon the PPL fabricated nanoarrays MHA20, MHA20-FN, MHA40 and MHA60. Cells were fixed after 14 days of culture and counterstained with type II collagen (red) and nuclei (blue). Images were acquired using a Zeiss Apotome.2 microscope or Zeiss LSM800 confocal microscope. MSCs on MHA20 and MHA40 were positive for type II collagen. Scale bars represent 100 µm.

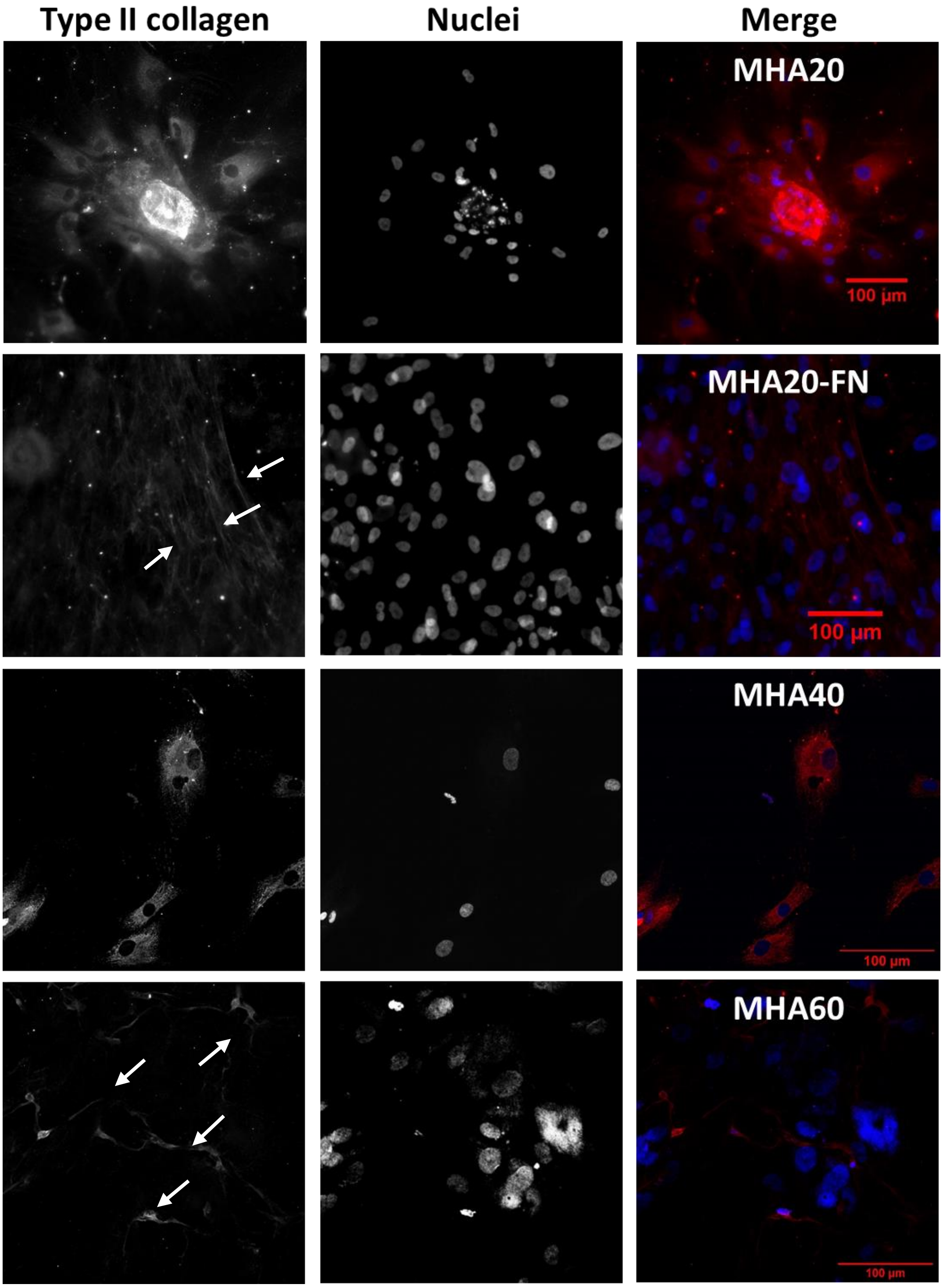

Figure 2.17 Representative fluorescent images of hMSC cultured on the PPL fabricated nanoarrays MHA20, MHA20-FN, MHA40 and MHA60. Cells were fixed after 28 days of culture and counterstained with type II collagen (red) and nuclei (blue). Images were acquired using a Zeiss Apotome.2 microscope or Zeiss LSM800 confocal microscope. MSCs on both MHA20 and MHA40 were positive for type II collagen. Scale bars represent 100 µm.

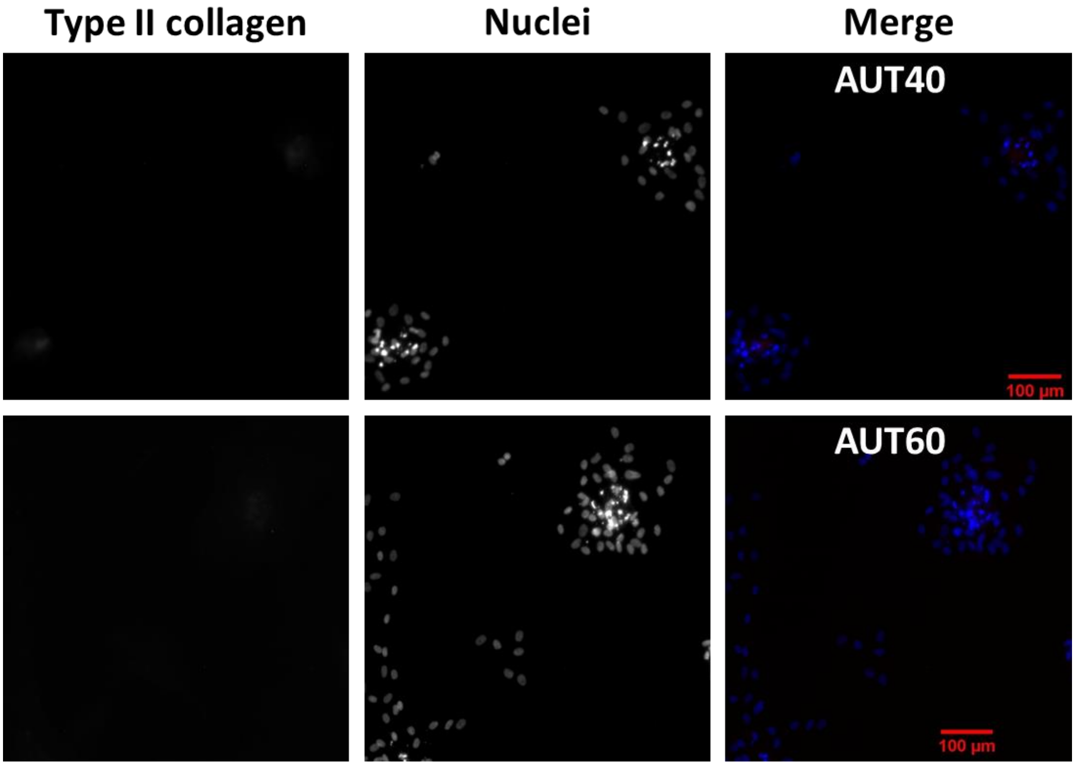

Figure 2.18 Representative fluorescent images of MSCs cultured on the PPL fabricated nanoarrays AUT40 and AUT60. Cells were fixed after 14 days of culture and counterstained with type II collagen (red) and nuclei (blue). Images were acquired using a Zeiss Apotome.2 microscope or Zeiss LSM800 confocal microscope. MSCs on both AUT40 and AUT60 were negative for type II collagen. Scale bars represent 100 µm.

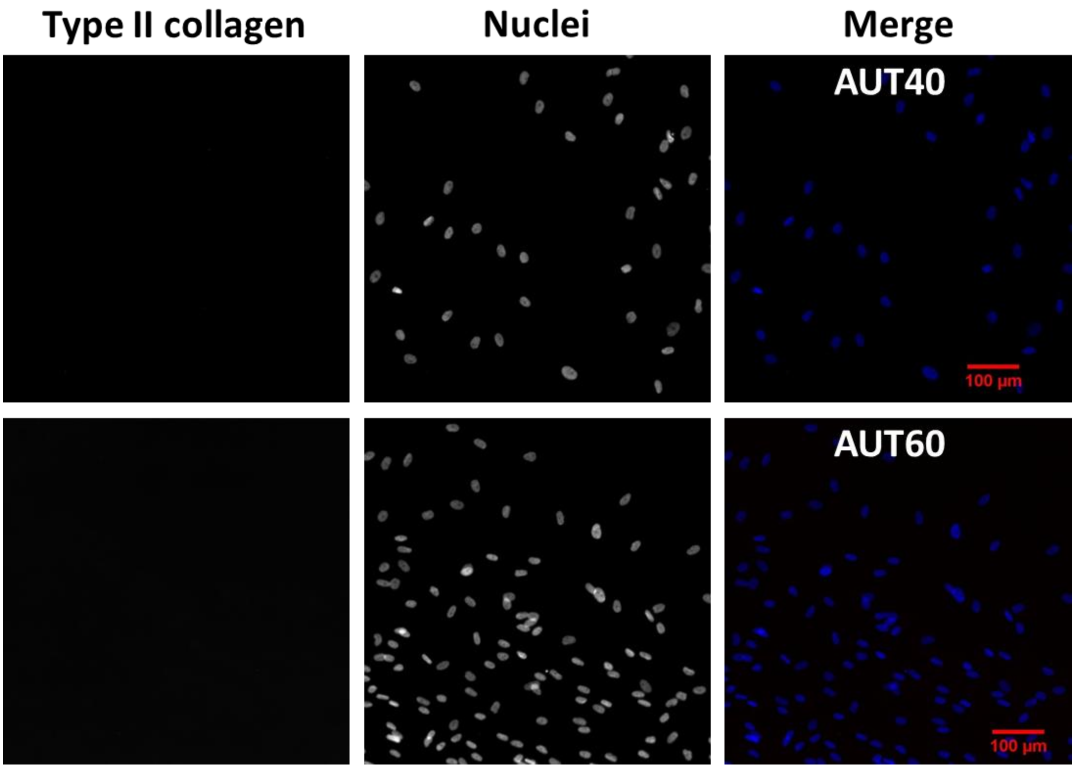

Figure 2.19 Representative fluorescent images of MSCs cultured on the PPL fabricated nanoarrays AUT40 and AUT60. Cells were fixed after 28 days of culture and counterstained with type II collagen (red) and nuclei (blue). Images were taken using a Zeiss Apotome.2 microscope or Zeiss LSM800 confocal microscope. MSCs on both AUT40 and AUT60 were negative for type II collagen. Scale bars represent 100 µm.

MSCs on MHA20 were positive for type II collagen expression after 14 days of culture (Figure 2.16) and remained positive up to 28 days of culture (Figure 2.17). In combination with previous observations of Cbfa1 marker, it was likely that MHA20 nanoarrays promoted MSCs towards chondrogenic or hypertrophic cartilage differentiation.

Cells on MHA20-FN ECM nanoarrays were observed to be negative in type II collagen expression after 14 days of culture and slightly positive for the appearance of matrix, as indicated with white arrows in Figure 2.17.

MSCs on MHA40 were positive for type II collagen expression after both 14 and 28 days. Weak expression of type II collagen was observed on MHA60 after 14 days of culture, with a trace of type II collagen matrix as indicated by the white arrow in Figure 2.16, remaining weakly expressed up to 28 days with increased appearance of matrix, as indicated with white arrows in Figure 2.17.

On both AUT40 and AUT60 nanoarrays, MSCs were negative for type II collagen expression throughout extended culture (Figure 2.18 and Figure 2.19). The absence of type II collagen expression on MSCs cultured on AUT40 and AUT60 nanoarrays could be characteristic of inhibited chondrogenesis tending towards adipogenesis due to the loss of Cbfa1 expression.[154]

Osteocalcin is commonly used as an osteogenic-specific differentiation marker to identify an osteogenic phenotype. Thus, MSCs cultured on nanoarrays for 14 and 28 days were stained with osteocalcin to further confirm the differentiation pathway (Figure 2.20, Figure 2.21, Figure 2.22, and Figure 2.23).

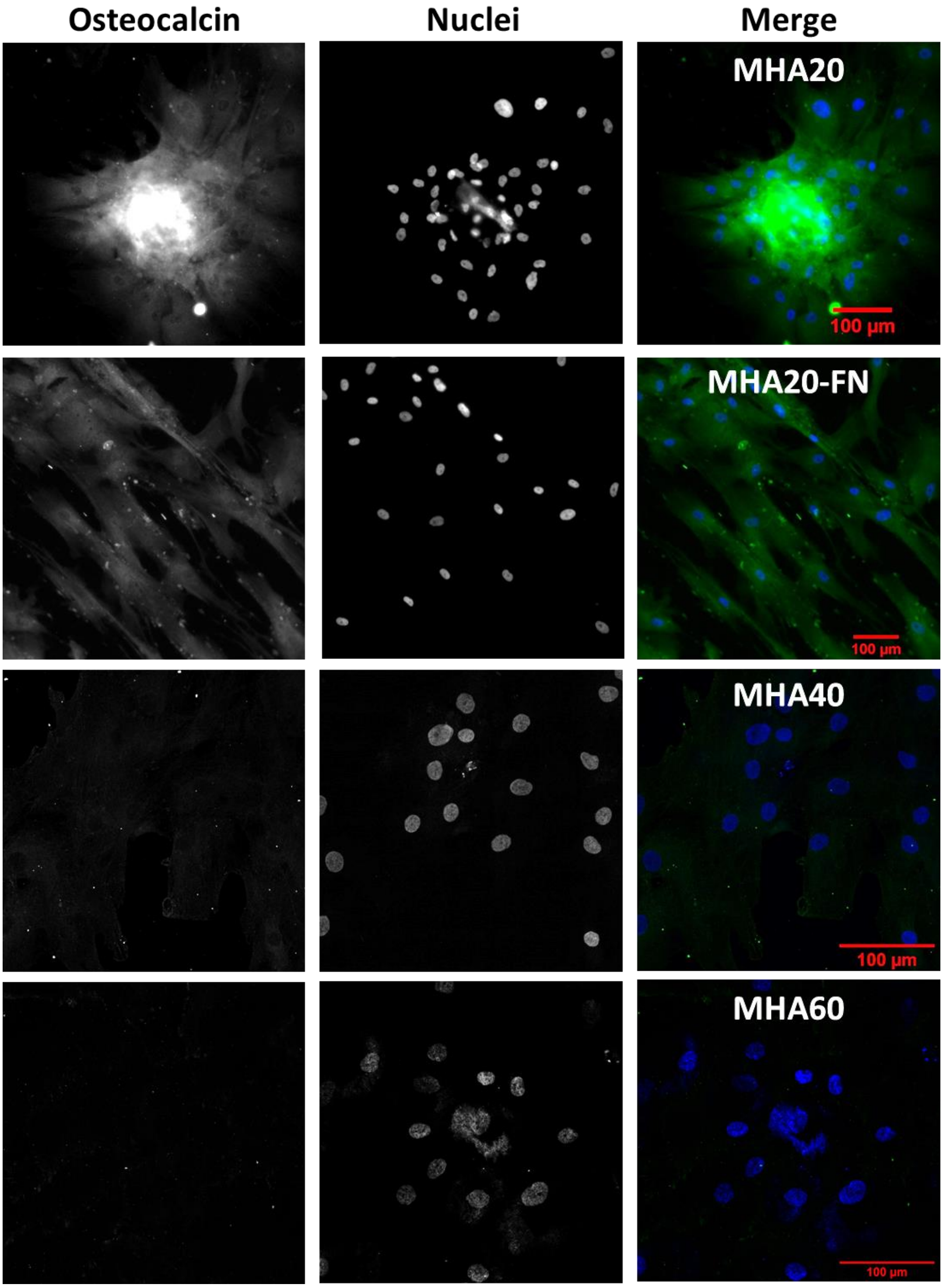

Figure 2.20 Representative fluorescent images of MSCs cultured on the PPL fabricated nanoarrays MHA20, MHA20-FN, MHA40 and MHA60. Cells were fixed after 14 days of culture and counterstained with osteocalcin (green) and nuclei (blue). Images were acquired using a Zeiss Apotome.2 microscope or Zeiss LSM800 confocal microscope. MSCs on MHA20 was positive for osteocalcin. Scale bars represent 100 µm.

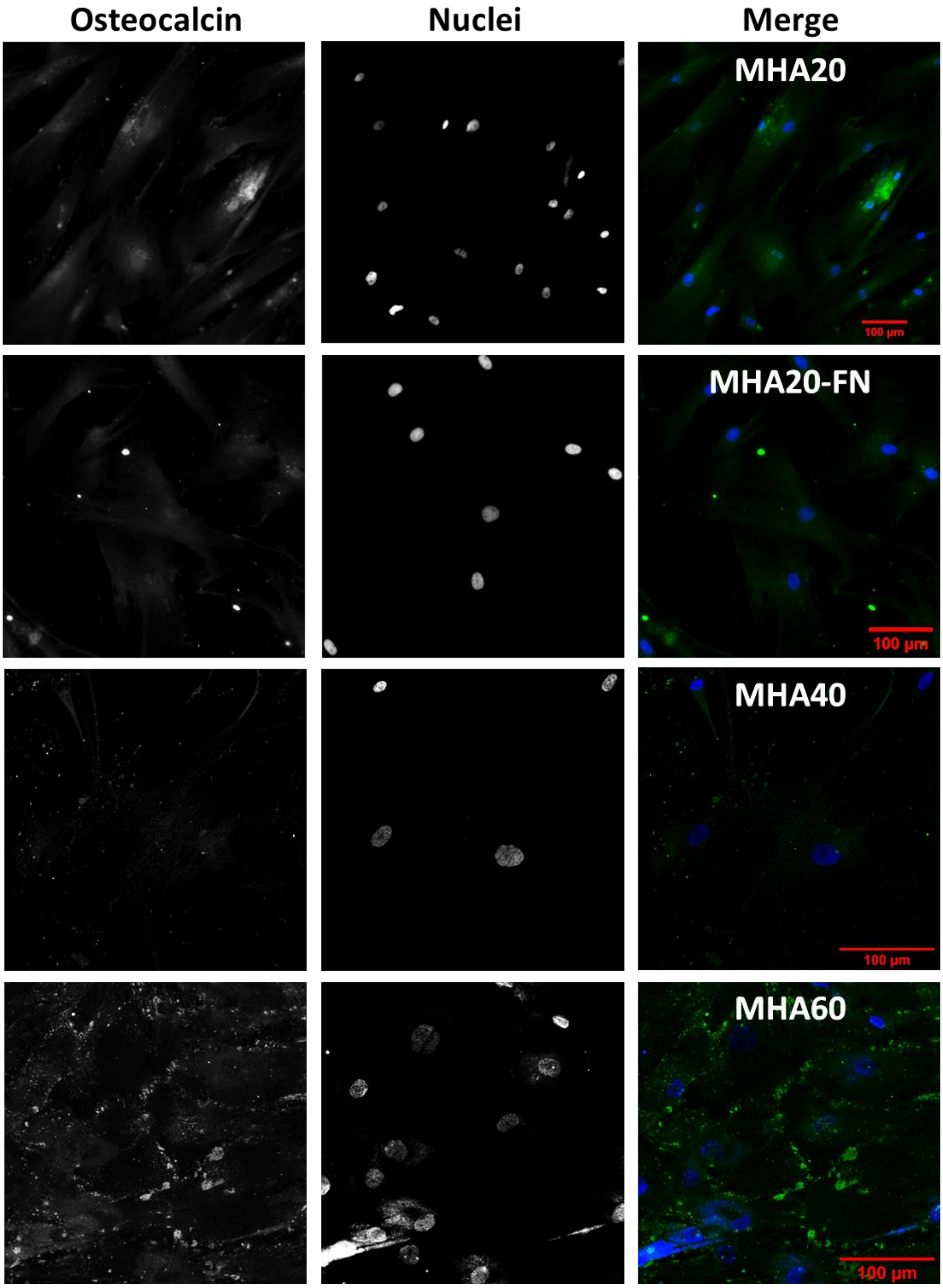

Figure 2.21 Representative fluorescent images of MSCs cultured on the PPL fabricated nanoarrays MHA20, MHA20-FN, MHA40 and MHA60. Cells were fixed after 28 days of culture and counterstained with osteocalcin (green) and nuclei (blue). Images were acquired using a Zeiss Apotome.2 microscope or Zeiss LSM800 confocal microscope. MSCs on MHA20, MHA20-FN and MHA60 were weakly positive for osteocalcin. Scale bars represent 100 µm.

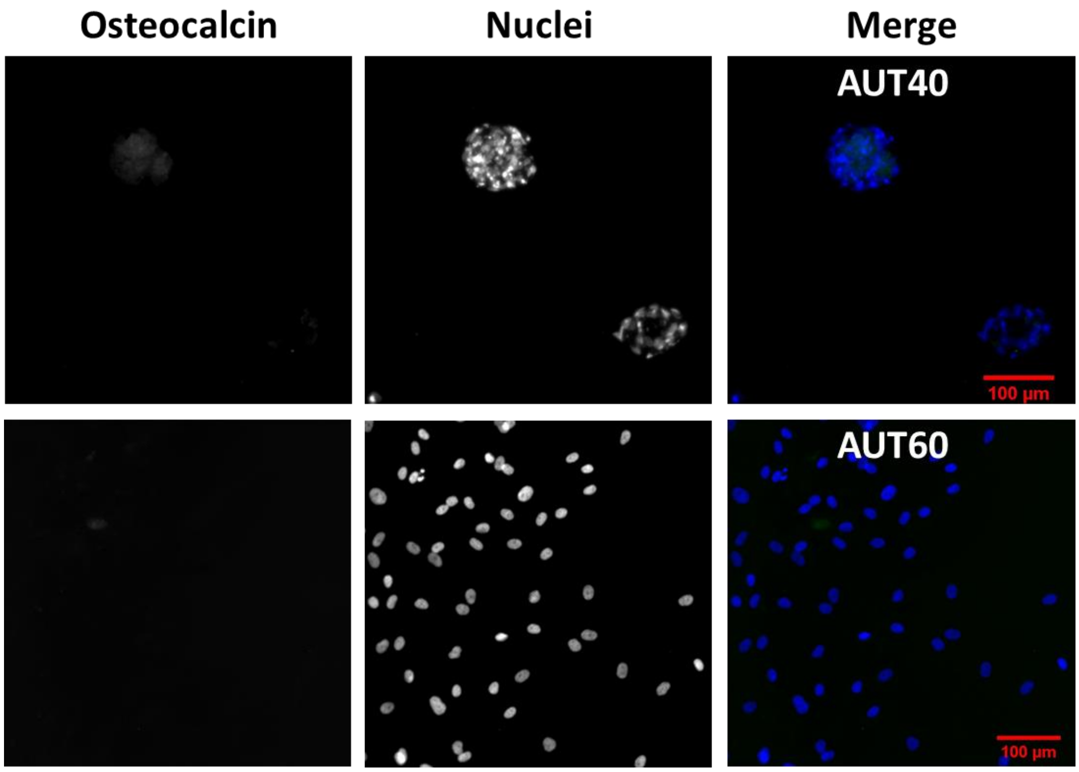

Figure 2.22 Representative fluorescent images of MSCs cultured on the PPL fabricated nanoarrays AUT40 and AUT60. Cells were fixed after 14 days of culture and counterstained with osteocalcin (green) and nuclei (blue). Images were acquired using a Zeiss Apotome.2 microscope or Zeiss LSM800 confocal microscope. Cells on both AUT40 and AUT60 were negative for osteocalcin. Scale bars represent 100 µm.

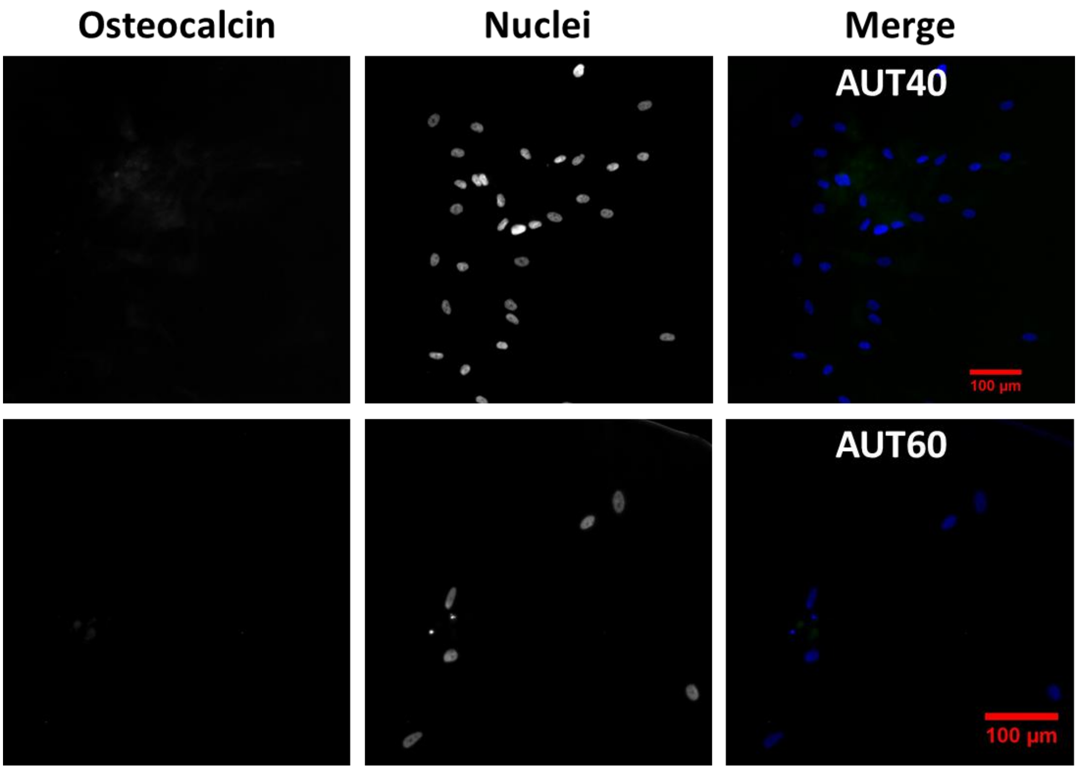

Figure 2.23 Representative fluorescent images of hMSC cultured on the PPL fabricated nanoarrays AUT40 and AUT60. Cells were fixed after 28 days of culture and counterstained with osteocalcin (green) and nuclei (blue). Images were acquired using a Zeiss Apotome.2 microscope or Zeiss LSM800 confocal microscope. MSCs on both AUT40 and AUT60 were negative for osteocalcin. Scale bars represent 100 µm.

Osteocalcin appeared to be weakly positively stained on MSCs cultured on both MHA20 nanoarrays and MHA20-FN ECM nanoarrays after 14 and 28 days (Figure 2.20 and Figure 2.21). MSCs on MHA40 nanoarrays were also weakly positive for osteocalcin after both 14 and 28 days. Conversely, MHA60 nanoarrays were negative for osteocalcin after 14 days of culture but became weakly positive after 28 days.

It has been previously reported that molecular osteogenic markers such as osteocalcin and osteonectin are expressed only after 7 to 14 days of differentiation.[155] MHA60 nanoarrays could potentially support osteogenesis at a later stage of *in vitro* MSC culture. The AUT nanoarrays, AUT40 and AUT60, however, expressed no osteogenic characteristics throughout the 28 day period of culture (Figure 2.22 and Figure 2.23).

As immunofluorescence staining on MSCs cultured on MHA20 nanoarrays were positive for both chondrogenic and osteogenic-specific differentiation markers, *i.e.*, type II collagen, Cbfa1 and osteocalcin, it was thus hypothesized that the stem cells were differentiating towards a hypertrophic cartilage pheotype.[81, 156] Staining of type X collagen, a hypertrophy-specific differentiation marker, was positive at both 14 and 28 days of culture (Figure 2.24, Figure 2.25, Figure 2.26, and Figure 2.27)

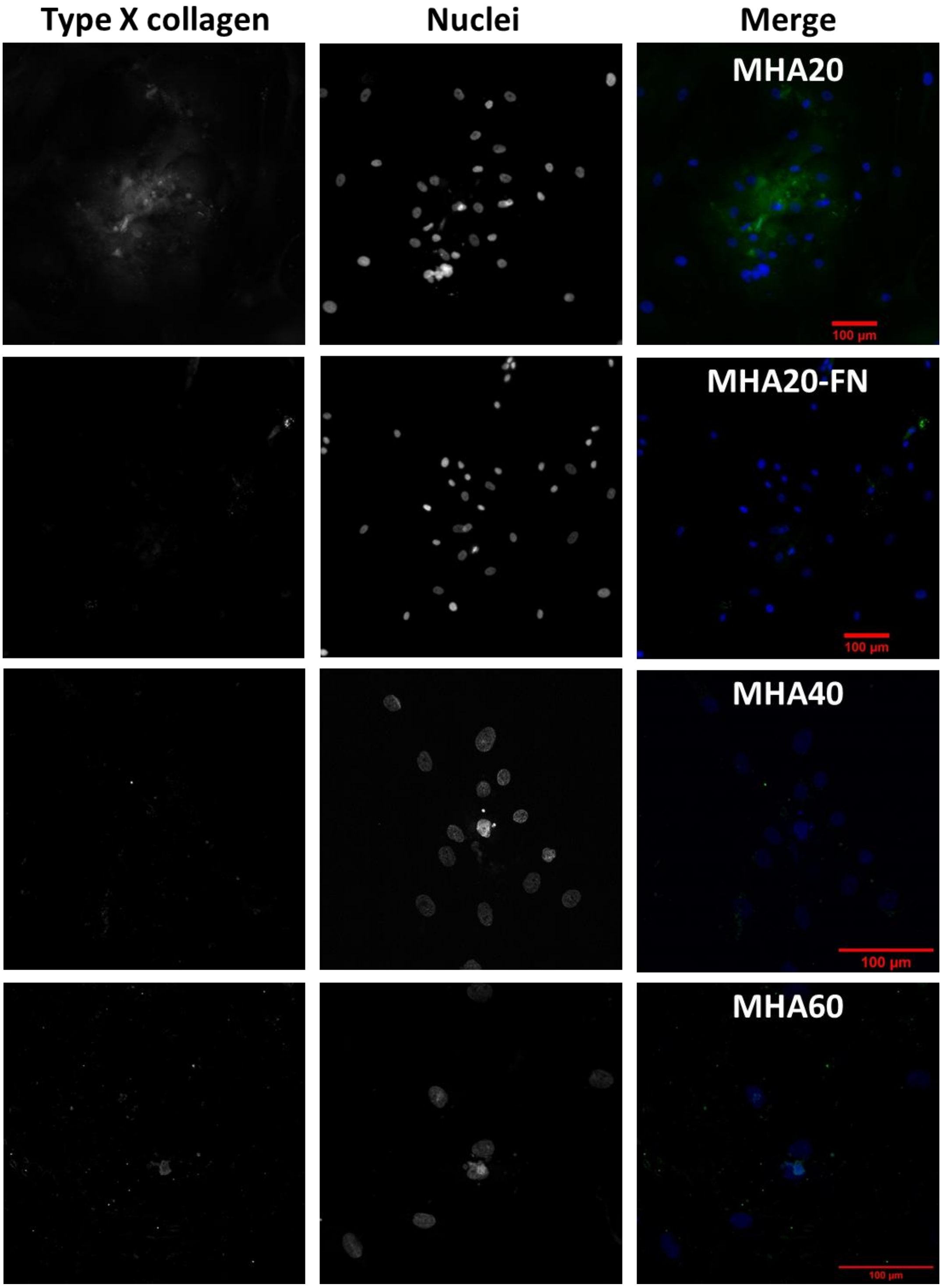

Figure 2.24 Representative fluorescent images of hMSC cultured on the PPL fabricated nanoarrays MHA20, MHA20-FN, MHA40 and MHA60. Cells were fixed after 14 days of culture and counterstained with type X collagen (green) and nuclei (blue). Images were acquired using a Zeiss Apotome.2 microscope or Zeiss LSM800 confocal microscope. MSCs on MHA20 appeared weakly positive for type X collagen. Scale bars represent 100 µm.

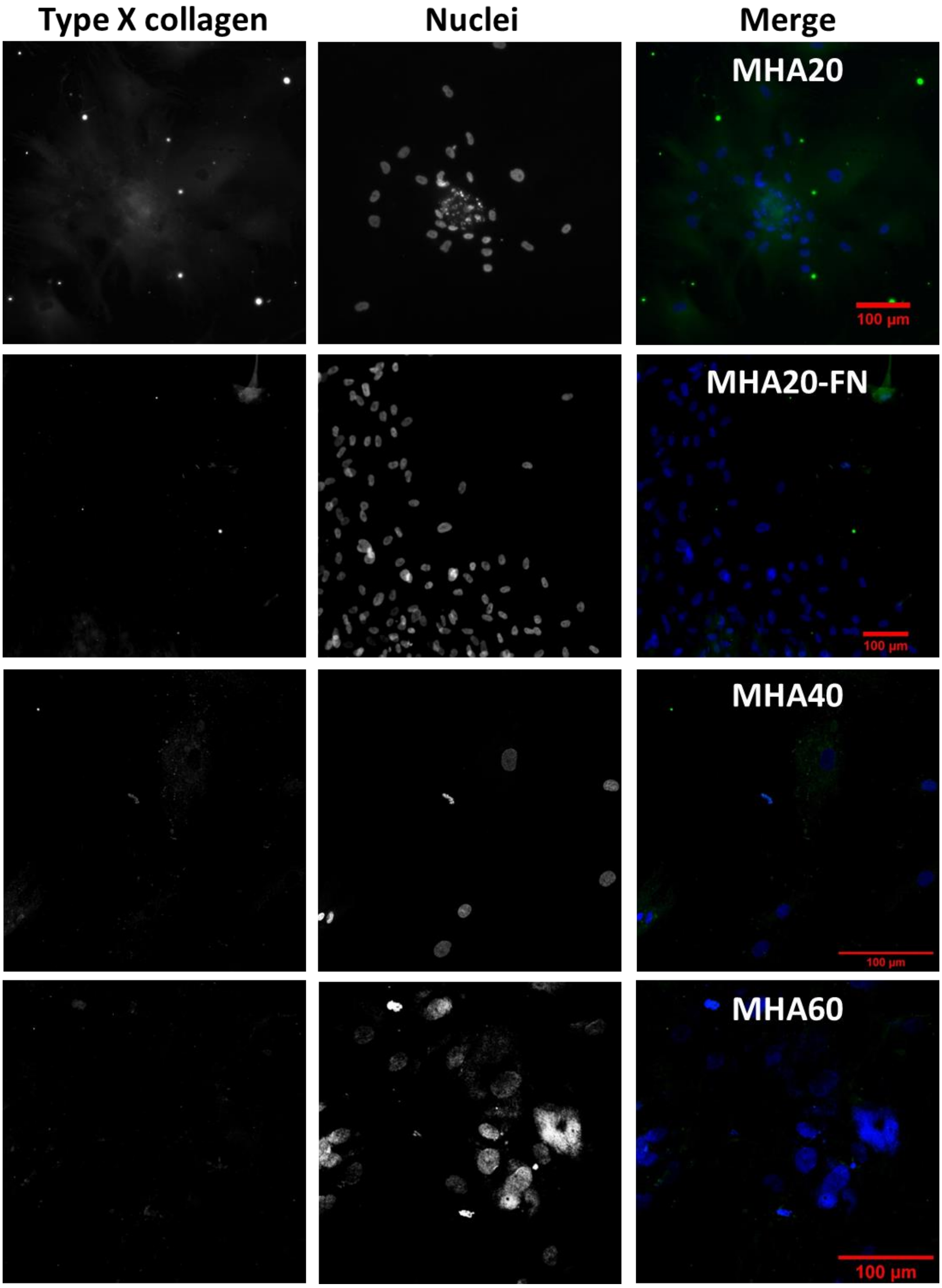

Figure 2.25 Representative fluorescent images of hMSC cultured on the PPL fabricated nanoarrays MHA20, MHA20-FN, MHA40 and MHA60. Cells were fixed after 28 days of culture and counterstained with type X collagen (green) and nuclei (blue). Images were acquired using a Zeiss Apotome.2 microscope or Zeiss LSM800 confocal microscope. MSCs on MHA20 appeared weakly positive for type X collagen. Scale bars represent 100 µm.

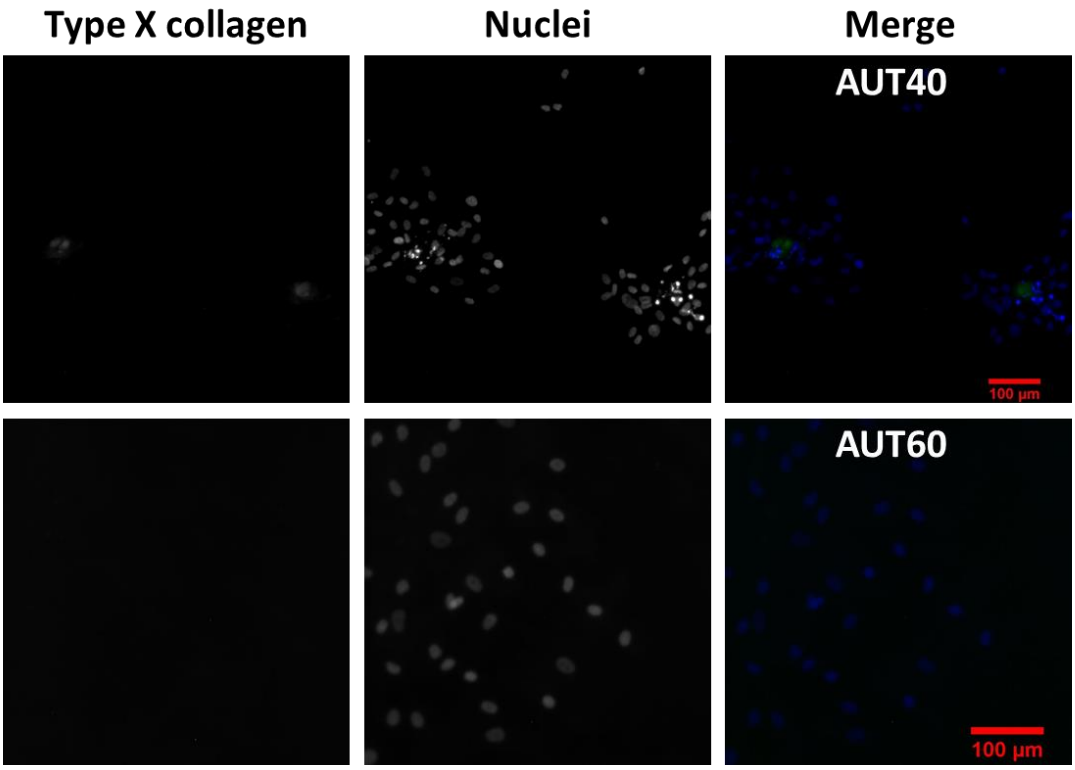

Figure 2.26 Representative fluorescent images of hMSC cultured on the PPL fabricated nanoarrays AUT40 and AUT60. Cells were fixed after 14 days of culture and counterstained with type X collagen (green) and nuclei (blue). Images were acquired using a Zeiss Apotome.2 microscope or Zeiss LSM800 confocal microscope. MSCs on both AUT40 and AUT60 were negative for type X collagen. Scale bars represent 100 µm.

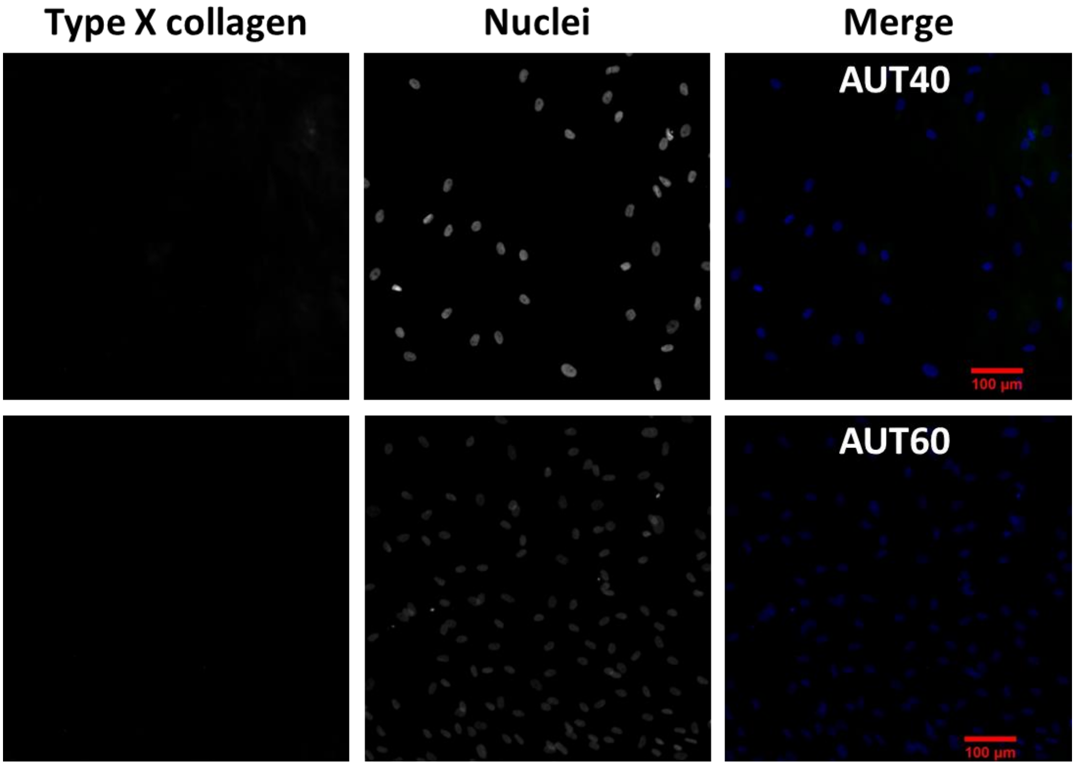

Figure 2.27 Representative fluorescent images of MSCs cultured on the PPL fabricated nanoarrays AUT40 and AUT60. Cells were fixed after 28 days of culture and counterstained with type X collagen (green) and nuclei (blue). Images were acquired using a Zeiss Apotome.2 microscope or Zeiss LSM800 confocal microscope. MSCs on both AUT40 and AUT60 were negative for type X collagen. Scale bars represent 100 µm.

Immunofluorescence results confirmed that the hypertrophy-specific differentiation marker, type X collagen, was positive only on MSCs cultured on MHA20 for 14 and 28 days (Figure 2.24 and Figure 2.25). On MHA20-FN, only a minority of cells stained with type X collagen at 28 days. In addition, type X collagen was negative on cells cultured on the remaining nanoarrays examined (Figure 2.24 to Figure 2.27).

Results obtained from immunofluorescence staining of the specific-differentiation markers, type II collagen, Cbfa1, osteocalcin, and type X collagen after both 14 and 28 days are summarised in Table 2.3.

Table 2.3 An overview of immunofluorescence results where "+": positive, "W+": weakly positive, and "-": negative for specific differentiation marker staining on cells cultured on candidate materials for both 14 and 28 days.

Culture time	Candidate	Collagen II	Cbfa1	Osteocalcin	Collagen X
14 day	MHA 20	+	+	+	W+
	MHA20-FN	-	+	W+	-
	MHA40	+	-	-	-
	MHA60	W+	-	-	-
	AUT40	-	+	-	-
	AUT60	-	+	-	-
28 day	MHA 20	+	+	W+	W+
	MHA20-FN	W+	+	W+	-
	MHA40	+	-	-	-
	MHA60	W+	-	W+	-
	AUT40	-	-	-	-
	AUT60	-	-	-	-

Results obtained from the immunofluorescence studies suggest that MHA20 supported hypertrophic chondrogenesis, as indicated by the positive staining of type X collagen combined with type II collagen, Cbfa1 and osteocalcin. On the MHA20-FN ECM arrays stem cells exhibited positive staining for osteogenic-specific markers Cbfa1 and osteocalcin after 14 days and 28 days. The results demonstrated that MHA20 with defined chemistry and spatial resolution induced hypertrophic differentiation within 14 days in contrast to the MHA20-FN ECM arrays which lacked the chemical stimulus that was likely required to differentiate the stem cells towards osteogenesis and possibly shift towards hypertrophy at a later stage. MSCs on MHA40 were positive for type II collagen throughout the 28-day culture suggesting that cells were induced towards chondrogenesis, although weakly positive for osteocalcin. On MHA60, MSCs appeared weakly positive for type II collagen with matrix formation throughout the culture period suggesting cells could be induced towards chondrogenesis.

Although the MSCs on both AUT40 and AUT60 were positive for Cbfa1 after 14 days, they appeared negative after 28 days with no positive stain for any other differentiation marker of interest, suggesting that the designed nanoarrays failed to induce stem cells towards either chondrogenesis or osteogenesis. Although the designed AUT nanoarrays might support the induction of adipogenesis, this conclusion could not be reached at the current stage of results.

2.5 Conclusions

In summary, the main aim of this project was to fabricate large-area chemical nanoarrays using PPL techniques introducing surface presenting chemical groups such as carboxyl and amino groups while passivating the unpatterned regions to isolate hMSC interaction purely on the chemical nanoarrays stimulus.

The selected candidate nanoarrays were fabricated utilising PPL techniques. Various thiolated molecules were chemically bonded through thiol-gold chemisorption to obtain nanofeatured SAMs. Six candidates were analysed in combination with 2 different surface presenting groups, carboxyl (-CO_2H, MHA) and amino groups (-NH_2, AUT), with three parameters of nanoarray region pattern. Amongst the 6 candidates, MHA20 was immobilised with fibronectin to generate an ECM-coated nanoarray, MHA20-FN, to observe the effects of spatial resolution in contrast with additional chemistry.

It was demonstrated that chemical nanoarrays with varying spatial resolution and quantitative differences in their features stimulate distinct initial morphologies. MHA20-FN, an ECM nanoarray, supported more restricted hMSC adhesion compared with the MHA20 chemical nanoarrays.

Qualitative immunofluorescence results suggest that fabricated MHA20 surfaces induced MSC along a hypertrophic lineage, MHA20-FN potentially induced MSC osteogenesis, whereas MHA40 and MHA60 potentially induced MSC chondrogenesis.

In comparison to previous works,[41, 139] The designed nanoarrays were proven to stimulate various MSC differentiation pathways with isolated material variables.Further work should be performed with quantitative confirmation of differentiation pathways by early stage integrin expression and differentiation markers using RT-qPCR to support the immunofluorescence evidence.

Chapter 3

Surface Nanolithography for Terminally Differentiated Cell Types

3.1 Introduction

Articular cartilage is known to have very little capability for self-regeneration.[157] Traditional therapies such as micro-fracture and insertion of implants have offered limited clinical satisfaction in repairing cartilage defects.[158] Amongst published treatments, autologous chondrocyte implantation (ACI) has become a popular therapy.[159] However, its efficiency in repairing cartilage defects is limited due to its variability in the formation of good quality hyaline cartilage.[160] This is due to the *in vitro* monolayer expansion of chondrocytes, a critical step in the process, causing loss of hyaline chondrogenic phenotype and thus remains a major challenge in the expansion of chondrocyte cultures *in vitro*.

3.1.1 Challenge in maintenance of chondrogenesis phenotype

The terminally differentiated phenotype of chondrocytes is characterised by the synthesis and maintenance of cartilage-specific ECM such as collagen types II, IX, XI and X and proteoglycans such as aggrecan in the hypertrophic zone.[82] Biosynthetic proteins; such as type II collagen, SOX9, protein kinase C (PKC) and focal adhesion kinase (FAK) are maintained during cartilage development, differentiation and repair.[75, 82] However, it is extremely difficult to maintain chondrogenic phenotype due to their rapid dedifferentiation upon serial *in vitro* mono-layer subculture. Dedifferentiation is a major challenge in clinical applications such as mass cell production for therapeutic purposes. Therefore, a number of synthetic and natural biomaterials have been studied in maintaining chondrogenic phenotype in both 2D and 3D cell cultures.

Despite the use of media supplemented with growth factors, chondrocytes rapidly dedifferentiated into fibroblast-like phenotype when cultured on 2D tissue culture polystyrene (TCP) at a relatively low density after which they synthesize large quantities of collagen types I, III and V.[81] Over the past decade researchers have developed various materials to address the differentiation and maintenance of chondrogenic markers in chondrocytic cell lines such as agarose gel, alginate, and collagen types I and II.[75, 161] In the cases where environments incorporate natural polymers, it has been suggested that geometric entrapment alone or in combination with chondrogenesis inducing proteins (*i.e.*, collagen and glycosaminoglycans (GAGs)) is essential for the maintenance of a chondrogenic phenotype.[24]

Type II collagen has been utilised as a substrate coating to enhance biosynthesis of collagen type II and GAGs in chondrocytes and activation of FAK through its auto-phosphorylation site, $\text{pFAK}_{\text{Y397}}$, when co-treated with transforming growth factor beta 1 (TGF-β1).[75] It has been reported that upregulation of $\text{pFAK}_{\text{Y397}}$ following the activation of FAK would trigger FAK_{Y925} phosphorylation. Phosphorylation of FAK_{Y925} would then regulate cell proliferation and differentiation.

Alternatively, unmodified type I collagen scaffolds with exposed free carboxyl groups and collagen modified with positive amino-presenting groups have been used previously for chondrogenic differentiation of human MSCs.[11] Unmodified scaffolds have been reported to successfully differentiate MSCs into chondrocytes within 21 days of culture, as detected by the upregulation of integrin α2β1, α5 and αv, promoting SOX9 nuclear localisation transcription activation, displaying a clear F-actin cytoskeleton. In contrast, aminated type I collagen scaffolds were demonstrated to block integrin-mediated ECM interaction, inhibiting chondrogenesis. Although the cells did exhibit a low level of interaction between fibronectin and integrin α5, they failed to express integrin α2 or αv with little to no support of focal adhesion. Therefore, it has been suggested that various surface modifications can impact the receptors of articular chondrocytes at the point of contact. To decipher the true potential of surface modifications for enhanced *in vitro* chondrogenic expansion, model surfaces allowing precise cell-surface interactions must be developed.

3.1.2 Effects of chondrogenesis on nanoscale spatial arrangements

Comprehensive studies have suggested that materials with nanoscale features have significant impact on cell behaviour such as adhesion, proliferation and differentiation.[36, 41, 44, 162] There has been, however, very little study of the dedifferentiation of terminally differentiated chondrocytes and their interaction with environmental nanocues.

A distinct nanoscale spatial arrangement has been reported to preserve or enhance chondrocyte phenotype.[83] It was reported that an arginine−glycine−aspartate (RGD) array of nano-features with a spacing greater than 70 nm would provide an environment that could sustain a chondrogenic phenotype.[83] In addition to the nanoenvironment, it has been observed that a controlled microenvironment combined with nanocues has a distinct effect on chondrocyte dedifferentiation.

It has been reported that in RGD nanoarrays a spacing greater than 95 nm would significantly inhibit F-actin assembly and support chondrogenesis, even though the environment would not benefit stem cell adhesion, whereas an identical material with a smaller nanospacing of 50 nm or less, enhanced chondrocyte dedifferentiation into fibroblasts.[163] However, there has not been a direct comparison in relation to the shape of the microenvironment associated with distinct nanocues between stem cell differentiation and the inhibition of dedifferentiation after terminal differentiation.

Polymer pen lithography (PPL) has been introduced with the potential of offering a novel platform to fabricate materials that can be used to study the effects of chemical surface and/or topography in cell applications.[135, 139] The model surfaces produced *via* PPL will enable the collection of fundamental data to ascertain the optimal combinations of surface chemistry and topography to cell function.

3.2 Aims and objectives

Based on the results in Chapter 2, it was established that chemical nano-arrays with various spatial orientations and presenting defined surface chemistries will activate MSC integrin and focal contact signalling transduction that could potentially induce different differentiation pathways. It was thus hypothesized such material-cell transduction events could support the maintenance of a differentiated chondrogenic phenotype *in vitro*.

The planned aims of this chapter were to maintain differentiated chondrocytes through series of subcultures and monitor the regulation/expression of differentiation markers for potential advanced *in vitro* chondrocyte culture.

It was then sought to decode the crucial impact of nano- and micro-environmental patterns on maintenance of chondrogenic phenotype and the relationship between MSC differentiation and chondrocyte de-differentiation on selected nano-arrays.

3.3 Experimental methods

3.3.1 Materials and instrumentation

Fabrication of nano-patterns were conducted on FlexAFM with a C3000 controller (Nanosurf, Liestal, Switzerland) as previously detailed in Chapter 2.

Fluorescent images were taken on either Zeiss LSM 780 or 800 confocal microscopy.

A Megafuge 16R centrifuge was purchased from Thermo Scientific. A plasma cleaner (PDC-32G-2) and PlasmaFlo Gas Flow Mixer (PDC-FMG-2) were purchased from Harrick Plasma. All chemicals were purchased from Sigma-Aldrich unless otherwise stated. PDMS co-polymer solutions for pen arrays were purchased from Fluorochem. (2,5-Dioxopyrrolidin-1-yl) octanoate was supplied by Manchester Organic. No. 5 13 x 13 mm glass coverslips for the base of the PPL arrays were purchased from Agar scientific. SuperClean2 glass substrate slides for further metal coating were purchased from Arrayit® Corporation. Gold was coated using an Edwards Auto500 electron-beam evaporator.

Normal human articular chondrocytes (NHAC-kn) and growth medium (CGM BulletKit, CC-3217 & CC-4409) were purchased from Lonza, UK. Dulbecco's modified eagle's medium (DMEM) for the maintenance experiment was purchased from Life Technologies (11995-065). Dulbecco's phosphate buffered saline (D1408) was diluted 1 to 10 with dH_2O then autoclaved before used. Trypsin-EDTA solution (T4174) was diluted 1 to 10 with DPBS. Paraformaldehyde (PFA, P/0840/53, Fisher Scientific) was prepared as a 4% (w/v) solution in DPBS. 0.5% (v/v) Triton™ X-100 (T8787) was diluted in PBS. Mouse anti-collagen type II antibody (ab150771, Abcam), rabbit anti-pFAK (phospho Y397) antibody (ab81298, Abcam), mouse anti-vinculin antibody (ab129002, Abcam), goat anti-mouse IgG secondary antibody (Alexa Fluor® 488 conjugate, A11001, Invitrogen) and chicken anti-rabbit IgG secondary antibody (Alexa Fluor® 594 conjugate, A-21442, Invitrogen), were used for immunostaining. Alexa Fluor® 594 phalloidin (A12381, Life Technologies) was used for staining actin filaments. Hoechst (83219, Anaspec Inc.) was used to stain for nuclei and ProLong™ antifade diamond mounting media (P36965, Thermo Fisher Scientific) was used to mount the slides.

3.3.2 Fabrication of nanoarrays

The chemical nanoarrays were fabricated as described previously in chapter 2.3.3.

3.3.3 Subculture of chondrocyte

Normal human knee articular chondrocytes (NHACs) were expanded to the 3rd passage in growth medium (Lonza, CDM BulletKit (CC-3226 & CC-4408)) to represent experimental P0. NHACs were seeded on materials at a density of 1.25 x 10^4 cells cm^{-2} in DMEM for 7 days for each passage. The experiment was conducted for 3 passages. All experiments were repeated 3 times unless otherwise stated.

3.3.4 Immunocytochemistry

At the completion of each passage, the culture medium was discarded and the NHACs were washed once with pre-warmed PBS containing Ca^{2+} and Mg^{2+} then fixed with pre-warmed 4% paraformaldehyde (PFA) for 20 min. Samples were permeabilised and blocked with PBS containing 0.1% Triton X-100, 1% BSA and 10% normal horse serum at room temperature for 45 min. Primary antibodies were diluted in PBS containing 5% BSA to dilutions of: anti-pFAK at 1:200, anti-vinculin at 1:100, anti-collagen type II at 1:200. The staining was performed at 4 °C for 16 h. Samples were washed copiously with PBS containing 0.1% Tween® 20 then stained with secondary antibodies at dilutions of 1:300 in PBS containing 5% BSA at room temperature for 1 h. Alexa Fluor® 594-conjugated phalloidin was stained at dilution of 1:250 in DPBS at 4 °C for 30 min. The nuclei were stained with Hoechst stain at a dilution of 1:1000 in DPBS at 4 °C for 30 min. Samples were then mounted with Prolong antifade diamond mounting media and imaged using an epifluorescent microscope or Zeiss LSM 780 confocal microscope.

3.3.5 RT-PCR

3.3.5.1 Sample preparation

At the conclusion of each experiment, samples were rinsed with DPBS then lysed with 200 µL of RNA lysis buffer (Promega, Z3051). All samples from 3 passages were collected and frozen at -80 °C before synthesis of messenger ribonucleic acid (mRNA).

3.3.5.2 Synthesis of mRNA

Total RNA was isolated using an SV 96 total RNA isolation system (Promega, Z3500) according to the manufacturer's instructions. Briefly, each sample lysate was transferred into the wells of the SV 96 binding plate that had been placed in a vacuum manifold base. Each well was rinsed with 500 µL of RNA wash solution. A vacuum was applied to the assembly to allow solution to pass through the plate. Twenty five µL of DNase incubation solution consisting of 20 µL yellow core buffer, 2.5 µL $MnCl_2$ and 2.5 µL DNase I was added to each well and the samples were incubated at room temperature for 10 min. Two hundred µL of DNase stop solution was added to each well and the assembly was again vacuumed to allow solution to pass through the plate. The vacuum was released and 500 µL of RNA wash solution added then the vacuum was applied again for 10 min to allow the binding matrix to dry.

A 96 well elution plate was sandwiched in the assembly and 100 µL of nucleus-free water was added to each well of the binding plate and incubated for 1 min. A vacuum was applied to allow the mRNA aqueous solution to pass through the elution plate such that mRNA samples were collected then stored on ice. Nucleic acid concentrations were measured on a plate reader by measuring the absorbance at 260 nm. Purity was determined from the ratio of the absorbance values at 260 and 280 nm ($A_{260/280}$) and the ratio at 260 and 230 nm ($A_{260/230}$). Complementary deoxyribonucleic acid (cDNA) was then synthesized immediately.

3.3.5.3 Synthesis of cDNA

To each PCR tube, 2 µL of random decamers (Invitrogen, AM5722G) were added prior to the addition of 47.8 µL of purified mRNA. The PCR tubes were then placed in a thermocycler (Biometra T-Gradient) and heated to 70 °C for 1 min. The samples were then removed and a 20.2 µL mixture of reverse transcription master mix comprising 14 µL of 5x MMLV-RT buffer, 3.5 µL of 10 mM dNTP mix, 0.7 µL of RNasin plus RNase inhibitor and 2 µL of 2000 U/ µL MMLV-RT was added in reaction tubes, the tubes were then returned to the thermocycler. The samples were heated through a cycle of 16 °C for 5 min, 37 °C for 15 min, 42 °C for 15 min, 45 °C for 15 min, 92 °C for 2 min. The samples were then cooled to 4 °C and 10 µL of RNase cocktail consisting of 9.8 µL of nucleus-free water and 0.2 µL of RNase-It ribonuclease cocktail were added to each tube. The samples were then heated to 37 °C for 30 min prior to cooling to 4 °C. Synthesized cDNA solution was stored at -20 °C until qPCR analysis.

3.3.5.4 qPCR analysis

Synthesized cDNA samples were diluted 1:10 with nuclease-free water. To each well of a 384-well qPCR reaction plate, 5 µL of diluted cDNA sample, 2 µL of target primer, 3 µL of nuclease-free water and 15 µL of SYBR green master mix (Roche, 04707516001) were added. Each time point and candidate of interest were measured with 3 repeats, with each cDNA sample being analysed in triplicate. The reaction plate was sealed and qPCR was conducted using a Roche LightCycler 480 for 40 cycles at 60 °C followed by analysis of the melt curve. Each sample was analysed in triplicate. Primers used for qPCR were type II collagen, aggrecan, SOX-9, type I collagen, and glyceraldehyde 3-phosphate dehydrogenase (GAPDH), which were purchased from QuantiTect Primer Assays.

Relative expression was normalised to GAPDH and experimental P0 using ΔΔCt method where the individual Ct value of each gene of interest was first normalised to GAPDH to obtain ΔCt and ΔCt was then normalised to the ΔCt value of the experimental P0 to obtain ΔΔCt. Results were then presented as $2^{-\Delta\Delta Ct}$ in all figures. Analysis of variance (ANOVA) was used for statistical analysis.

3.4 Results and discussion

3.4.1 Chondrocyte morphology on nanopatterned chemical arrays

Human chondrocytes in DMEM were cultured on a range of MHA and AUT arrays were (Table 3.1). Cell morphology was observed after 7 days of culture by immunostaining of F-actin and vinculin (Figure 3.1).

Table 3.1 List of 6 selected candidate materials with parameters within patterns. Each feature size was 300 ± 5 nm for all candidates.

Abbreviation	Centre to Centre Distance (µm)	Array of Feature	Area of Pattern (µm)
MHA 20	3.14	20 x 20 arrays	60 x 60
MHA 40	1.53	40 x 40	60 x 60
MHA 60	1.01	60 x 60	60 x 60
AUT 20	3.14	20 x 20	60 x 60
AUT 40	1.53	40 x 40	60 x 60
AUT 60	1.01	60 x 60	60 x 60

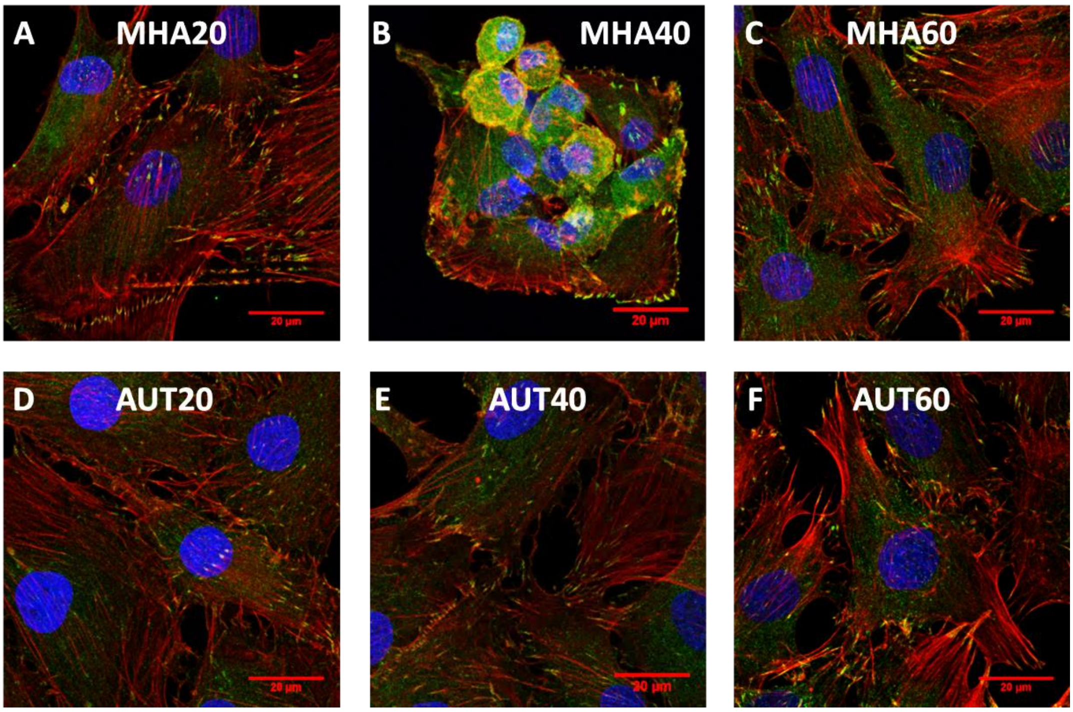

Figure 3.1 Chondrocytes cultured in contact with (A) MHA20, (B) MHA40, (C) MHA60, (D) AUT20, (E) AUT40 and (F) AUT60 for 7 days at experimental passage 1 and counterstained with vinculin (green), F-actin (red) and nuclei (blue). Scale bars represent 20 µm.

Direct interaction of chondrocytes with each nanofeatured pattern on MHA20 was observed through the formation of vinculin plaques (Panel A, Figure 3.1). The chondrocytes were, however, not restricted within individual patterned regions in spite of the chemical passivation of m-PEG on the non-patterned area. This suggests that the total surface area of a single pattern on MHA20 was insufficient to support chondrocyte adhesion.

In contrast to the elongated and well-defined F-actin morphology on MHA20, the cytoskeletal morphology of chondrocytes indicated a specific round shape and were aggregated within single MHA40 patterns where F-actin could be observed dense with rings at the periphery of the cells, that were punctate and cortical within the cell membrane (Panel B, Figure 3.1).

Chondrocyte adhesion was not restricted MHA60 within the patterns presented. Within these patterned areas, there was evidence of elongated cytoskeletons, not observed outside of the patterns (Panel C, Figure 3.1).

In contrast with results in Chapter 2 where MSC morphology on AUT20 with no viable cell adhesion observed, AUT20 supported homogeneous chondrocyte adhesion with defined intense vinculin expression (Panel D, Figure 2.6 and Panel D, Figure 3.1). On both AUT40 and AUT60, chondrocytes exhibited a widely spread morphology with elongated stress fibres, but no apparent interaction with the patterns was observed (Panels E and F, Figure 3.1). Notably, some chondrocytes on AUT60 exhibited an arched cytoskeleton around their nuclei in contrast with the widely flattened morphology on AUT20 and AUT40 (Figure 3.2).

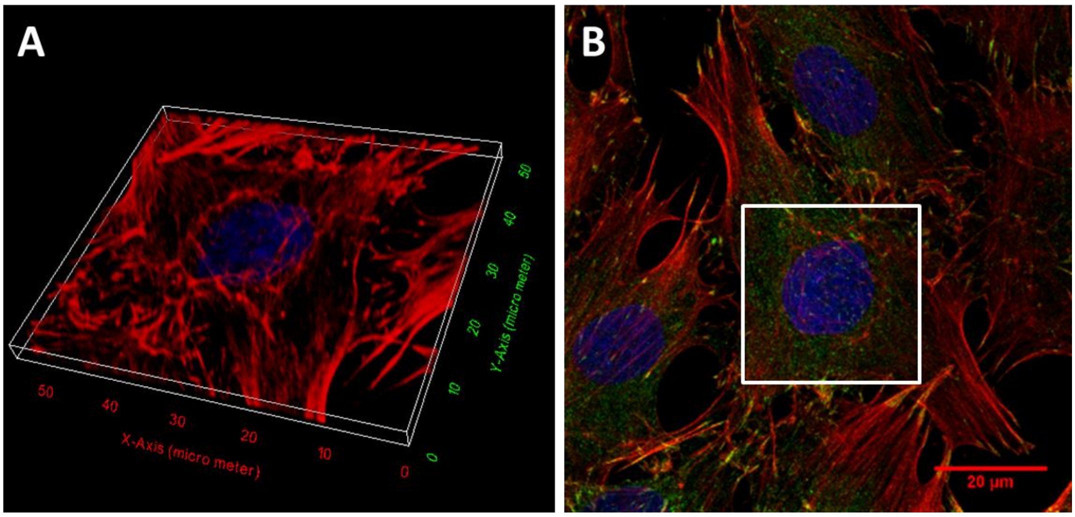

Figure 3.2 (A) 3D fluorescent images of 1st passage chondrocytes on AUT60 showing the arched cytoskeletal structure (red) around the nucleus (blue) and (B) its original image showing the region of the cells processed in the white square.

To validate the capability of the materials to maintain an *in vitro* chondrogenic phenotype, the selected candidates materials were cultured with human chondrocytes for 7 days for each passage through 3 passages (Figure 3.3 and Figure 3.4). The phenotype of the chondrocytes was assessed at the end of each passage *via* the staining of type II collagen, vinculin, F-actin and pFAK$_{Y397.}$

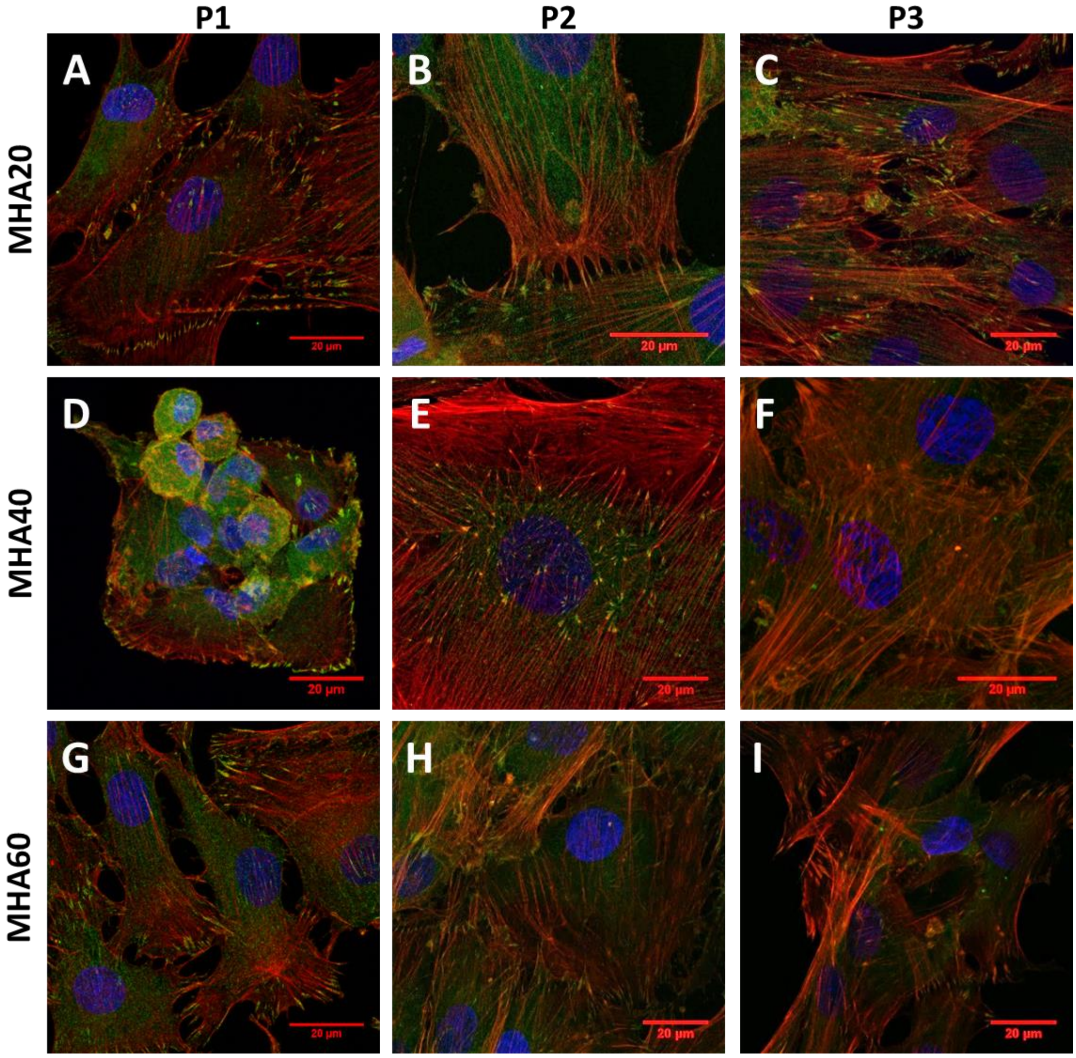

Figure 3.3 Chondrocytes subcultured on (A) to (C) MHA20, (D) to (F) MHA40, and (G) to (I) MHA60 through 1st (A), (D) and (G), 2nd (B), (E) and (H), and 3rd passage (C), (F) and (I), counterstained with vinculin (green), F-actin (red) and nuclei (blue). Scale bars represent 20 µm.

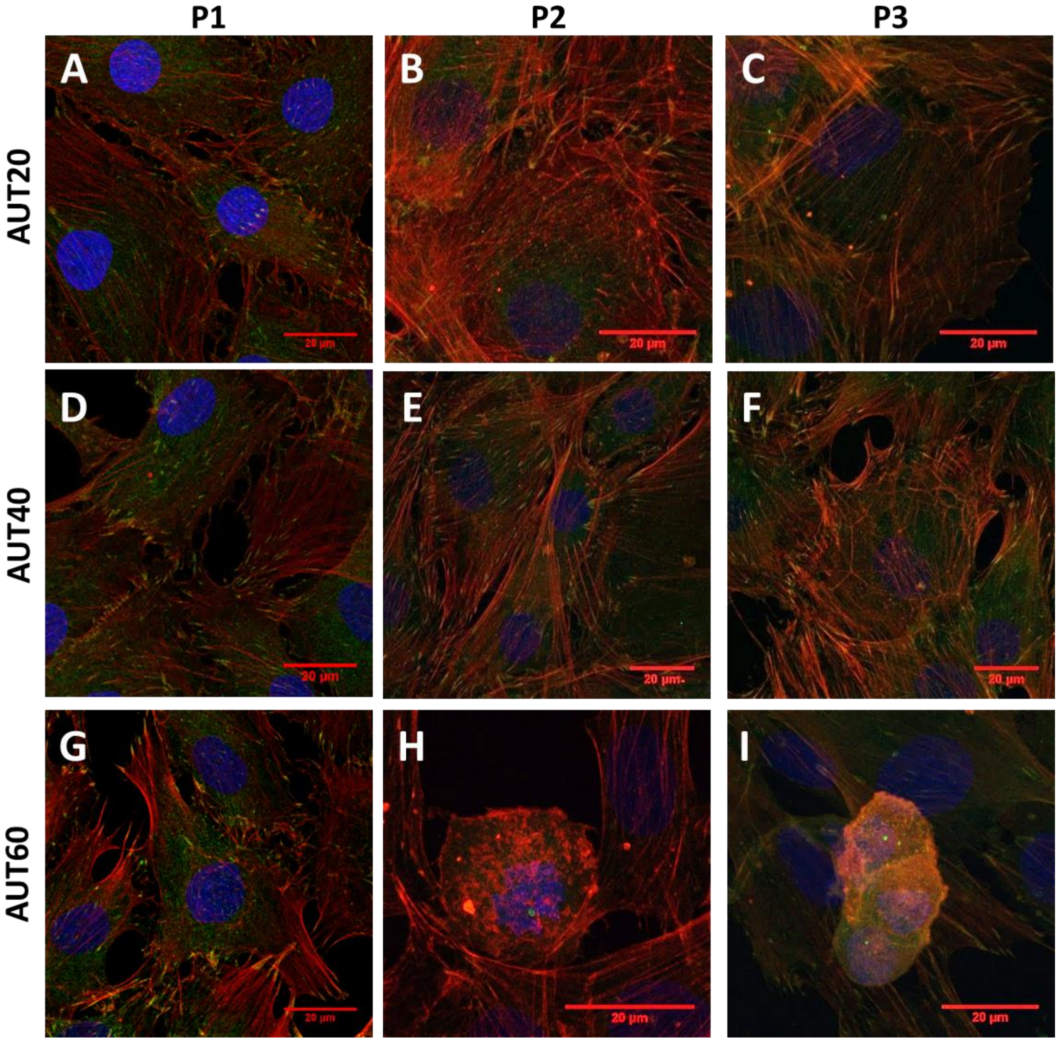

Figure 3.4 Chondrocytes subcultured on (A) to (C) AUT20, (D) to (F) AUT40, and (G) to (I) AUT60 through 1st (A), (D) and (G), 2nd (B), (E) and (H), and 3rd passage (C), (F) and (I), counterstained with vinculin (green), F-actin (red) and nuclei (blue). Scale bars represent 20 µm.

Amongst the 6 selected nanoarrays, chondrocytes were observed to have direct but unrestricted interaction with the MHA20 patterns through 2 passages (Panels A and B, Figure 3.3). Notably at 2nd passage on MHA20, the chondrocyte exhibited a scattered cytoskeleton, presumably within the patterned area similarly to the morphology observed on 1st passage of chondrocyte on MHA60 (Panel G, Figure 3.3). Nonetheless, aligned chondrocytes exhibiting fibroblast-like morphology were observed with clear stress fibres and vinculin at 3rd passage indicating loss of chondrogenic phenotype (Panel C, Figure 3.3).

MHA40 exhibited the best preservation of chondrogenic morphology amongst the MHA candidates. Chondrocytes were brought through a series of subcultures with cytoskeletal morphology observed to be spread out with short, disorganised and punctate F-actin at 2nd passage on MHA40 (Panel B, Figure 3.3) similar to 1st passage cells (Panel A, Figure 3.3) that were, however, no longer restricted within the individual patterns.

The 3rd passage chondrocytes exhibited partially short, punctate and curved cytoskeletons, similar to 1st passage cells, among elongated stress fibres (Panel C, Figure 3.3). On MHA60, the chondrocytes spread widely and were randomly distributed at 2nd passage (Panel H, Figure 3.3). The chondrocytes exhibited a relatively smaller cell shape at the 3rd passage on MHA60 compared with 2nd passage cells (Panel I, Figure 3.3).

Although AUT20 provided sufficient chondrocyte adhesion in contrast with that observed with MSCs, the chondrocytes were extremely flattened with no sign of morphological recovery throughout 3 passages of culture (Panels A to C, Figure 3.4). Similarly, AUT40 supported cell adhesion but the initial chondrocyte cytoskeletal morphology was flattened and randomly distributed with no apparent sign of morphological recovery throughout 3 passages of culture (Panels D to F, Figure 3.4)

Amongst the AUT candidates, AUT60 exhibited the best preservation of chondrogenic morphology. From a central arched morphology in 1st passage cells on AUT60, the chondrocytes demonstrated a typical round shape with dense F-actin amongst flattened cells through 2nd (Panels G and H, Figure 3.4, and Figure 3.5) and 3rd passage (Panel I, Figure 3.4 and Figure 3.6). The presented morphology indicated potential support for chondrogenesis throughout 3 passages.

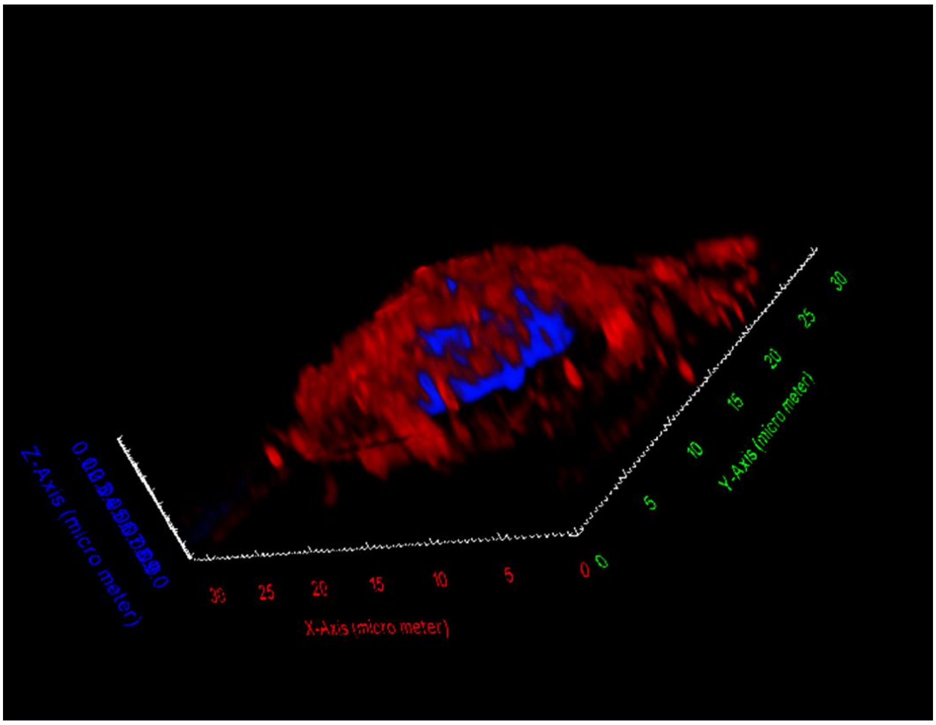

Figure 3.5 3D view of 2nd passage chondrocytes on AUT60 where it demonstrated a typical round shape with dense F-actin amongst neighbouring flattened cells. F-actin was labelled in red and nuclei in blue. X and Y axes are scaled 0 – 30 µm and Z axis 0 – 9 µm.

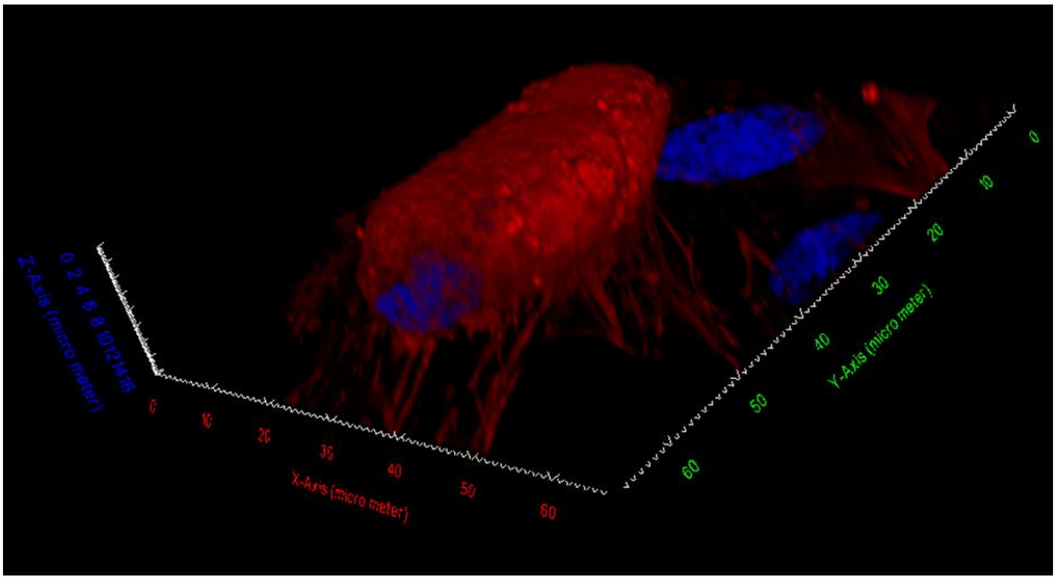

Figure 3.6 3D view of 3rd passage chondrocytes on AUT60. F-actin was labelled in red and nuclei in blue. X and Y axes are scaled 0 – 60 µm and Z axis 0 – 16 µm.

The selected 6 candidates successfully supported chondrocytic adhesion through 3 experimental passages. Amongst the MHA nanoarrays, the chondrocytes had distinct interactions with individual features on MHA20 but oversaw the passivation effect of m-PEG, which was presumably due to insufficient active adhesion areas provided on each pattern compared with MHA40 where multiple cells attached in multiple stacks on a single pattern.

Nonetheless, MHA40 did not maintain a preferred chondrocytic morphology over multiple passages. Similar to MHA40, MHA60 provided beneficial cell adhesion, although the patterns showed no restriction on the unpatterned area. First passage chondrocytes had potential interaction with the nanoarrays, but the cytoskeletal morphology was lost in the 2nd and 3rd passages.

On the AUT nanoarrays, AUT20, AUT40 and AUT60, chondrocytes exhibited no apparent interaction with the patterned features and no restriction from the m-PEG passivation was observed at any point during culture. Amongst the 3 AUT candidates, cytoskeletal morphology on AUT20 and AUT40 through 3 passages indicated detrimental chondrogenic dedifferentiation as the cells were observed to have a preference for spherical morphology.[164] Although there was no chondrogenic morphology readily apparent on the AUT60 nanoarrays in the 1st experimental passage, the chondrocytes demonstrated a positive trends towards spherical morphology through 3 experimental passages (Figure 3.5 and Figure 3.6).

3.4.2 Chondrogenic marker expression

In addition to the morphology experiments, selected PPL nanoarrays were subcultured using identical conditions, 7 days per passage for 3 passages in DMEM. The cells were subsequently counterstained for type II collagen and $\mathrm{pFAK}_{\mathrm{y397}}$ as indicators of chondrogenic phenotype (Figure 3.7, Figure 3.8, **Table 3.2**, Appendix 4 and Appendix 5).

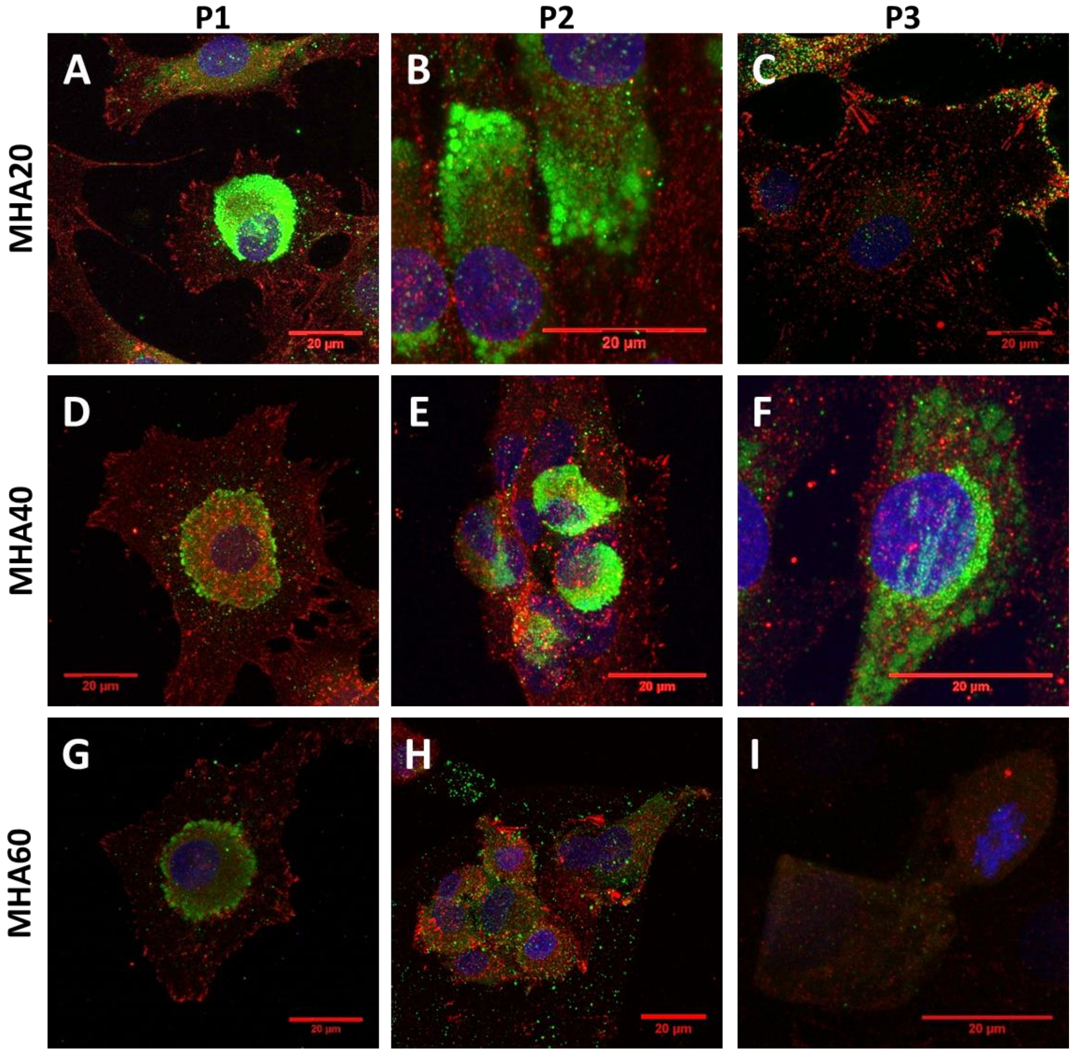

Figure 3.7 Chondrocytes subcultured on (A) to (C) MHA20, (D) to (F) MHA40, and (G) to (I) MHA60 through 1st (A), (D) and (G), 2nd (B), (E) and (H), and 3rd passage (C), (F) and (I), counterstained for type II collagen (green), pFAK$_{y397}$ (red) and nuclei (blue). Scale bars represent 20 µm.

Despite the chondrocytes initially exhibiting distinct direct interaction on both MHA20 and MHA60, type II collagen exhibited an apparent shift towards the cell membrane in the 2nd passage and 3rd passage cells in particular on both nanoarrays exhibited no type II collagen expression (Panel I, Figure 3.7). However, chondrocytes on MHA20 constantly exhibited apparent activated pFAK$_{y397}$ whereas on cells on MHA60, little to no activated pFAK$_{y397}$ was observed. Chondrocytes cultured on MHA40 nanoarrays were rich in type II collagen, mainly distributed close to the nucleoplasm through 3 passages with type II collagen slightly spread towards the cytoplasm at the 3rd passage while $pFAK_{y397}$ remained activated through 3 passages.

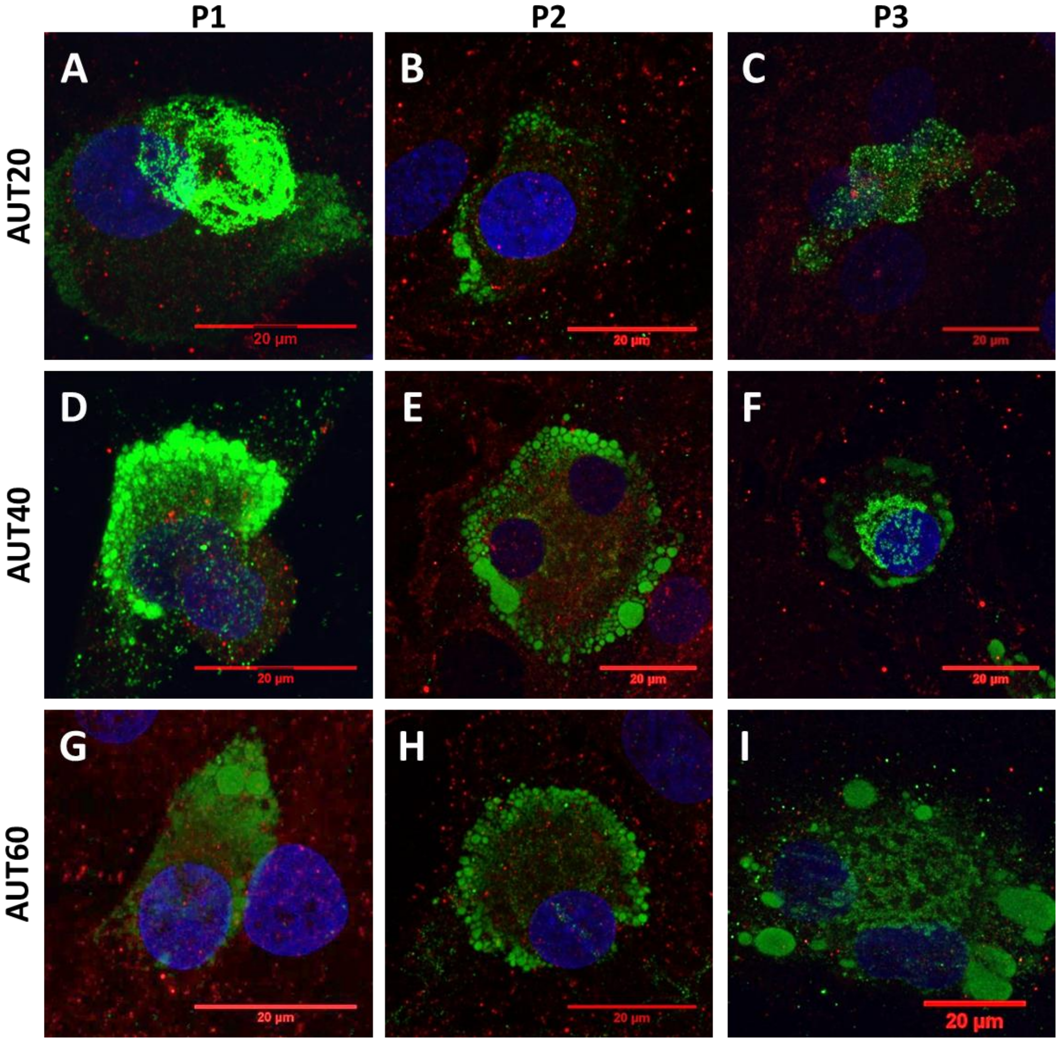

Figure 3.8 Chondrocytes subcultured on (A) to (C) AUT20, (D) to (F) AUT40, and (G) to (I) AUT60 through 1st (A), (D) and (G), 2nd (B), (E) and (H), and 3rd passage (C), (F) and (I), counterstained for type II collagen (green), $pFAK_{y397}$ (red) and nuclei (blue). Scale bars represent 20 µm.

AUT20 nanoarrays supported chondrocyte adhesion with type II collagen expression on 1st passage chondrocytes shifted towards the cytoplasm followed by a significant decrease in collagen expression at subsequent passages with little activated $pFAK_{y397}$ expressed throughout the 3 experimental passages.

Similarly, type II collagen expression on 1st passage cells on AUT40 nanoarrays was shifted towards the cell membrane with little activated $pFAK_{y397}$. At subsequent passages the chondrocytes exhibited a "skirted" appearance with type II collagen shifted towards the cell membranes indicating loss of collagen type II with decreased expression of activated $pFAK_{y397}$ at the 2nd and 3rd passages. Conversely, type II collagen expression in chondrocytes on AUT60 shifted slightly towards the cytoplasm but remained distributed around the nuclei.

Table 3.2 An overview of immunofluorescence results where "+": positive and "-": negative for type II collagen marker staining on cells cultured on candidate materials for 3 experimental passages (P1 to P3).

Candidate	P1	P2	P3
MHA 20	+	+	-
MHA40	+	+	+
MHA60	+	+	-
AUT20	+	+	-
AUT40	+	+	+
AUT60	+	+	+

Chondrogenesis is typically maintained by support of a round morphology with expression of chondrogenic markers, especially, type II collagen, enriched close to the nucleoplasm as confirmation of chondrocyte re-differentiation.[82, 165] Although chondrocytes showed indirect interaction with MHA40 and AUT60 nanoarrays, the cells successfully maintained rounded morphology indicating successful re-differentiation. This was confirmed by collagen type II expression where both candidates exhibited intense expression through 3 passages (Table 3.2).

In contrast, chondrocytes had distinct adhesion on individual feature of MHA20 and MHA60 but the morphology was flattened from the 1st passage without recovery, which resulted in rapid loss of type II collagen expression on both candidates.

On AUT20 and AUT40 nanoarrays, although the chondrocytes adhered on the surface, patterned nanofeatures were overseen and cells were equally distributed on the surface despite m-PEG passivation. These surfaces, however, better preserved type II collagen in comparison to chondrocytes on MHA20 and MHA60 although type II collagen was slightly distributed towards the cell membrane in subsequent passages. However, a decrease in $pFAK_{y397}$ activation was observed on AUT20 and AUT40 throughout the experimental passages.

3.4.2 RT-qPCR

To confirm expression of the chondrogenesis markers, gene expression was quantified using RT-qPCR, targeting collagen types I and II, aggrecan and SOX9. Relative expression was normalised to GAPDH and experimental P0 using the ΔΔCt method where individual Ct value of each gene of interest was first normalised to GAPDH to obtain ΔCt ,ΔCt was then normalised to ΔCt value of experimental P0 to obtain ΔΔCt. Results were then presented as $2^{-\Delta\Delta Ct}$ in all figures (Figure 3.9).

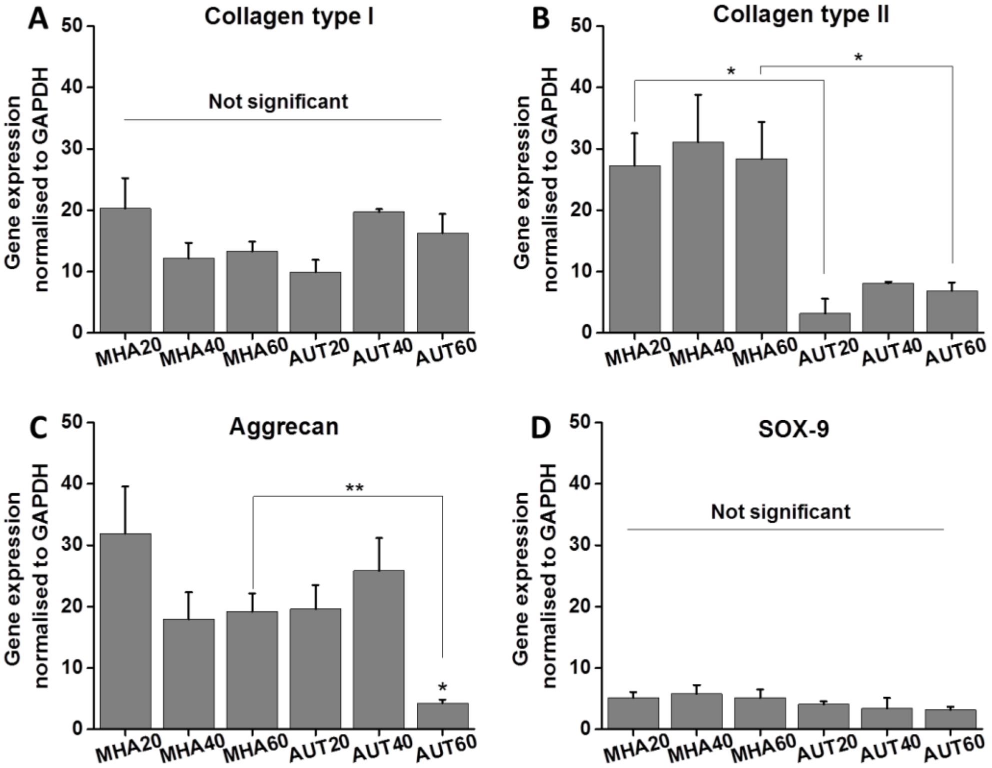

Figure 3.9 Dedifferentiation of chondrocytes on nanoarrays. qPCR detection of 1st passage chondrocytes isolated from nanoarrays after 7 days of culture. (A) Type I collagen (B) type II collagen (C) aggrecan and (D) SOX9 qPCR data were normalised using ΔΔCt method. Individual Ct values was first normalised to Ct value of GAPDH to obtain ΔCt, which was then normalised to the ΔCt value of experimental P0 to obtain ΔΔCt. Results were plotted as $2^{-\Delta\Delta Ct}$ with the *p* value determined using a one way ANOVA, where "*" represents $p < 0.05$, significant difference; "" represents $p < 0.01$, significant difference. Error bars represent standard error of the mean. n=5**

Normalised expression of collagen type I was not significantly different amongst all candidates at 1st passage (Panel A, Figure 3.9, and Appendix 6). While this was consistent with the immunocytochemistry results, amongst the candidate materials type II collagen expressions in chondrocytes cultured on AUT20 was lowest with expression on AUT40 and AUT60 at a higher level, although chondrocytes on the MHA nanoarrays MHA20, MHA40 and MHA60, exhibited a significantly higher level of expression (Panel B, Figure 3.9 and Appendix 7). More importantly, MHA20 had a significant higher expression than on AUT20. Similarly, cells on MHA60 expressed a significantly higher level of type II collagen than on AUT60. This initial result suggests that for an identical nanoarray with different presenting chemistry, carboxyl groups (-CO_2H, MHA) preserved type II collagen on chondrocytes in comparison with amino groups (-NH_2, AUT).

Although aggrecan expression in 1st passage cells on AUT60 was significantly downregulated, the remaining nanoarrays had a similar level of expression (Panel C, Figure 3.9 and Appendix 8). Notably, expression on MHA60 was significantly higher than on AUT60. No significant difference in SOX9 expression was observed amongst all nanoarrays (Panel D, Figure 3.9 and Appendix 9).

Selected candidates were subsequently cultured through 3 passages, then type I collagen, type II collagen, aggrecan, and SOX9 differentiation markers were examined (Figure 3.10 and Figure 3.11).

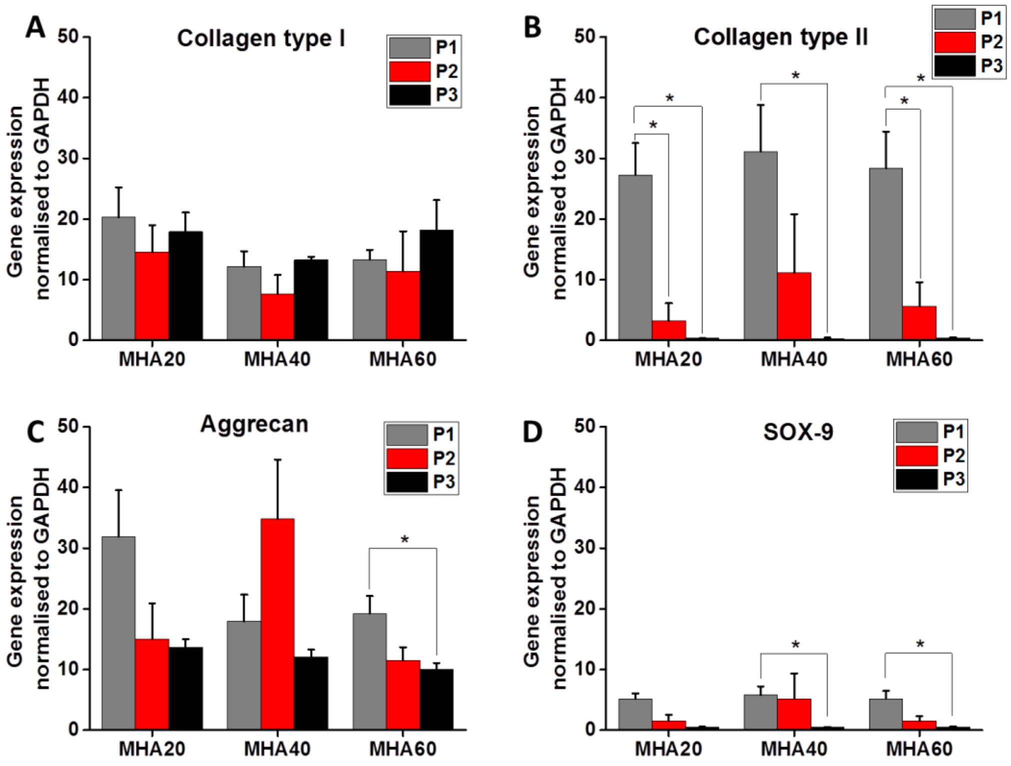

Figure 3.10 Dedifferentiation of chondrocytes on MHA nanoarrays. qPCR detection of chondrocytes isolated from nanoarrays after 7 days of culture at each passages for three passages. (A) Type I collagen (B) type II collagen (C) aggrecan and (D) SOX9 qPCR data, normalised using the ΔΔCt method. Individual Ct values were first normalised to Ct value of GAPDH to obtain ΔCt, which was then normalised to ΔCt value of experimental P0 to obtain ΔΔCt. Results were plotted as $2^{-\Delta\Delta Ct}$. *p* values was determined using one way ANOVA, where "*" represents $p < 0.05$, significant difference. Error bars represent standard error of the mean. n=5.

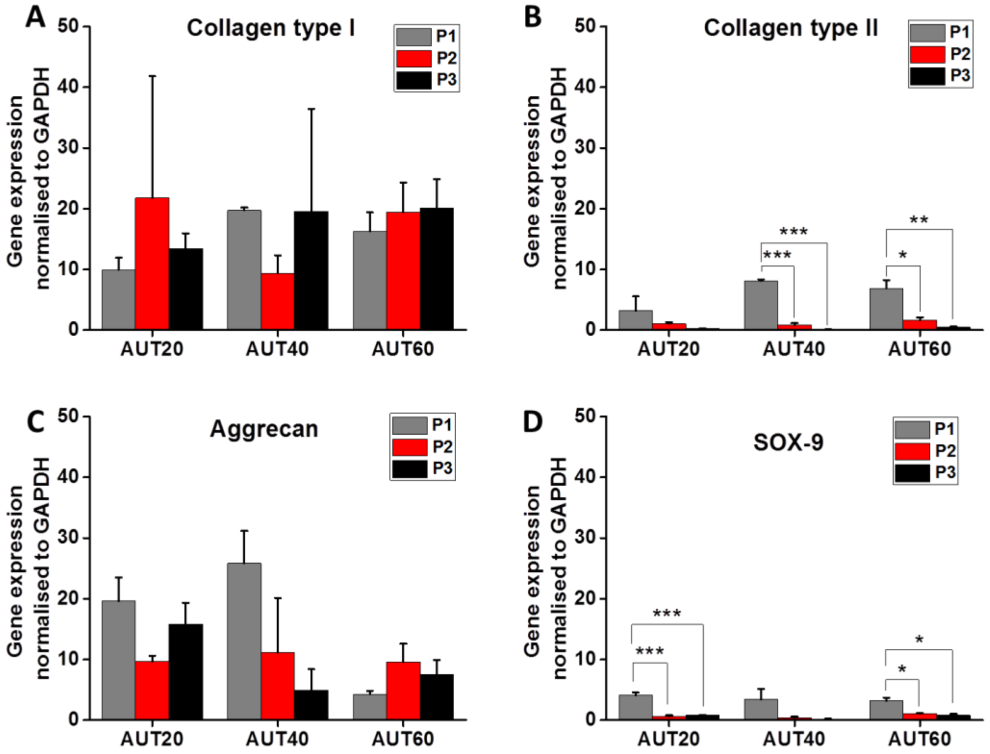

Figure 3.11 Dedifferentiation of chondrocytes on AUT nanoarrays. qPCR detection of chondrocytes isolated from nanoarrays after 7 days of culture at each passages for three passages. (A) Type I collagen (B) type II collagen (C) aggrecan and (D) SOX9 qPCR data were normalised using ΔΔCt method. Individual Ct value was first normalised to Ct value of GAPDH to obtain ΔCt, which was then normalised to the ΔCt value of experimental P0 to obtain ΔΔCt. Results were plotted as $2^{-\Delta\Delta Ct}$. *p* values was determined using one way ANOVA, where "*" represents $p < 0.05$, significant difference; "" represents $p < 0.01$, significant difference; "***" represents $p < 0.005$, significant difference. Error bars represent standard error of the mean. n=5.**

Amongst the three MHA nanoarrays, collagen type I expression remained constant through 3 passages (Panel A, Figure 3.10). On both MHA20 and MHA60, type II collagen was dramatically downregulated through each passage whereas on MHA40 type II collagen was better preserved with no significant difference in expression between the 1st and 2nd passages (Panel B, Figure 3.10). Aggrecan expression remained similar on MHA20 and MHA40 throughout 3 experimental passages. Notably, aggrecan expression was gradually downregulated on MHA60 through 3 passages (Panel C, Figure 3.10). Aggrecan gene expression in chondrocytes on MHA nanoarrays was consistent with that of type II collagen, mirroring the immunocytochemistry results, where chondrocytes on MHA60 had rapid loss then absence of type II collagen stain by the end of the 3rd passage.

SOX9 gene expression on all three nanoarrays was consistently relatively lower than those of type II collagen and aggrecan (Panel D, Figure 3.10). On MHA20, SOX9 was maintained at the same level of expression through 3 passages whereas it was slightly downregulated on MHA40 and MHA60 as passaging progressed.

Amongst the three MHA nanoarrays, MHA20 and MHA60 exhibited rapid downregulation in type II collagen, a result that was consistent with the immunocytochemistry results. Notably, MHA60 exhibited more rapid downregulation in the expression of type II collagen, aggrecan, and SOX9 indicating rapid chondrocyte dedifferentiation that is consistent with the immunocytochemistry results where type II collagen was absent and pFAK_{y397} was inactivated.

Regarding chondrogenic dedifferentiation, MHA40 best preserved the expression of a chondrogenic phenotype with the least overall loss of type II collagen and SOX9 at the mRNA level, and a steady level of aggrecan. Notably, there was no significant change over 2 passages. This can be observed by correlating with the immunocytochemistry results, where chondrocytes on MHA40 had a punctate and dense cytoskeleton with preservation of type II collagen expression close to the nucleoplasm through 3 passages.

In similarity with the MHA nanoarrays, type I collagen expression remained constant on the three AUT nanoarrays throughout 3 experimental passages (Panel A, Figure 3.11). Chondrocytes initially expressed the lowest level of type II collagen on AUT20 nanoarrays which was consistently downregulated through 3 passages (Panel B, Figure 3.11). Notably, on AUT40, type II collagen expression was drastically downregulated at each passage (p <0.005) supporting the immunocytochemistry results with a rapid shift of type II collagen towards the cell membrane at each passages. On the AUT60 nanoarrays, the chondrocytes exhibited a gradual loss in type II collagen but aggrecan expression was well preserved through 3 passages (Panel C, Figure 3.11). Chondrocytes on both AUT20 and AUT60 also experienced significant loss in SOX9 during the 2nd passage (Panel D, Figure 3.11). Chondrocytes on AUT20 experienced the most drastic loss in SOX9 ($p < 0.005$) during each passage.

The results demonstrated successful re-expression of initial type II collagen in chondrocytes cultured on all candidates, amongst which a significantly higher level of type II collagen was synthesised on the MHA nanoarrays. In subsequent passages, MHA40 successfully preserved collagen type II in comparison to MHA20 and MHA60.

In contrast, chondrocytes on the AUT nanoarrays had a significantly lower level of type II collagen mRNA expression throughout the experimental passages, with type II collagen subsequently shift towards the cytoplasm. Amongst the three AUT nanoarrays, AUT60 best preserved type II collagen with the least shift towards the cytoplasm.

Although overall type II collagen mRNA expression on all candidates suffered various degrees of sequential down regulation, it was established that protein expression of type II collagen on some candidates, especially MHA60 and AUT60, was maintained through 3 passages as exhibited in the evidence for immunocytochemistry. Previous cases have suggested that the mRNA levels can not directly be used as surrogates for corresponding protein expression.[166, 167]

It has been suggested that mRNA agreement with protein expression levels better predicts phenotypic outcome.[168] Ultimately protein abundance determines cell phenotype. Protein levels and activity do not necessarily directly correlate with mRNA transcription, as protein abundance also involves many other essential processes in gene expression such as mRNA decay, translation and protein degradation, many of which are well defined.[167, 169]

As previously observed, AUT caused less overall formation of focal adhesions than MHA nanoarrays, where MSCs successfully adhered on MHA20 but not on AUT20, suggesting that, although the functioning of chondrocytes was less dependent on cell adhesion, the effect of chemical nanoarrays may be neglected in mechanosignalling on AUT20. The chondrocytes had an initial direct interaction on MHA20 nanoarrays followed by rapid de-differentiation in the subsequent 2 passages. The effect was hypothesized to be due to the large feature centre-to-centre spacing, at 3.14 µm, forcing the chondrocytes into spread cytosketetal structures. On MHA60, the chondrocytes oversaw the patterned area, resulting in dramatic type II collagen degradation.

3.5 Conclusions

To summarise, the aim of this set of experiments was to preserve chondrocyte phenotype through serial passage with designed chemical nanoarrays based on the MSC differentiation pathways investigated in Chapter 2. This was hypothetically achieved by a combination of nanofeatures within nanoarrays and a presention of chemical groups on the surface that induced differentiation through various pathways on MSCs.

The selected nanoarray candidates were synthesised utilising PPL techniques. Various thiolated molecules were chemically bonded through thiol-gold chemisorption to result in nanofeatured SAMs. Six candidates were employed in combination with 2 different surface presenting groups, carboxyl (-CO_2H, MHA) and amino (-NH_2, AUT), with three parameters of nanoarray regions of patterning. Human chondrocytes were cultured through 3 experimental passages with protein expression visualised by immunocytochemistry and gene expression detected using RT-qPCR.

The information from the RT-qPCR results was limited, purely by mRNA expression after isolation. In addition, regulation of transcription alone is, despite its significance, insufficient to describe the abundance of proteins and therefore cell phenotype. Evidence obtained from immunocytochemistry has, however, successfully provided the distribution and intracellular location of the relevant differentiation markers.

In comparison to an earlier published RGD nanospcaing materials,[83] in addition to previous research analysing 3D structures and various ECM molecules for re-differentiation of chondrocytes,[11, 161] this study has provided an understanding of the fundamental mechanosignalling events in combination with the presenting chemistry, nanoscaled features and micro-spacing and their effects in the dedifferentiation and re-differentiation of chondrogenesis. Further investigations may be undertaken utilising the parameters observed to incorporate within the manufactured scaffold for cartilage regeneration applications.

Chapter 4

Advancing Surface Nanolithography

4.1 Introduction

Nanolithographic techniques have been widely used to create integrated circuits, biosensors and display units.[133] In particular, scanning probe microscopy (SPM)-derived atomic force microscopy (AFM) based nanolithographic approaches have been implemented to manipulate cell signalling events because of its capability in the nanometre scale resolution and registry.[115] Dip-pen lithography (DPN) and its advanced development technology polymer pen lithography (PPL), have been utilised in nanoscale biomaterial fabrication primarily using alkylthiol molecules with various functional groups deposited on gold via alkylthiol chemisorption.[125, 126, 138, 170] Recent research has established that mesenchymal stem cells (MSCs) respond to changes in surface chemistry of the presenting groups, such as carboxyl, amino and alkyl-terminated gold surfaces.[41, 57] These well-defined nanoscale lithographed surfaces are, however, limited to gold surfaces as a supporting base, dependent on thiol-gold chemisorption.

These techniques have so far been limited to model surfaces, *e.g.,* gold and silicon wafers. To realise the potential of these surface techniques, applications must be developed to pattern a wider range of materials.

4.1.1 Advanced single probe nanolithography

To address such limitations, a variety of molecules have since been attached onto SiO_2 and other non-metallic surfaces using DPN.[90, 123, 124, 171, 172] Numerous approaches have been used with alkoxysilane, trichlorosilane or silazane molecules as the “ink”, inspired from the commonly utilised surface modification of silane on SiO_2 surfaces.[90, 122, 123] In addition, natural molecules such as biotin and fluorescent molecules such as rhodamine 6G have been nanopatterned using DPN for applications in biosensor development or optoelectronic devices.[124, 171] Single probe DPN has also been used in solid-state nanopatterning applications instead of organic molecules.[172]

4.1.2 Challenges in novel "inks" used in nanolithography

It has been established that multiple parameters affect nanopattern feature sizes in DPN or DPN-derived methods such as PPL.[126, 138, 173] Amongst the addressed variables, controlled humidity plays an important role in the rate of "ink" transport.[174] "Ink" transport depends greatly on the water meniscus formed between the probes and surface at the point of approach (Scheme 4.1). It has been claimed that "ink" solubility determines the deposition rate as it is clear that water condenses on surfaces in all humidities. The mechanism of adsorbate adsorption and self-organisation of "ink" molecules on various surfaces must be taken into consideration.[174]

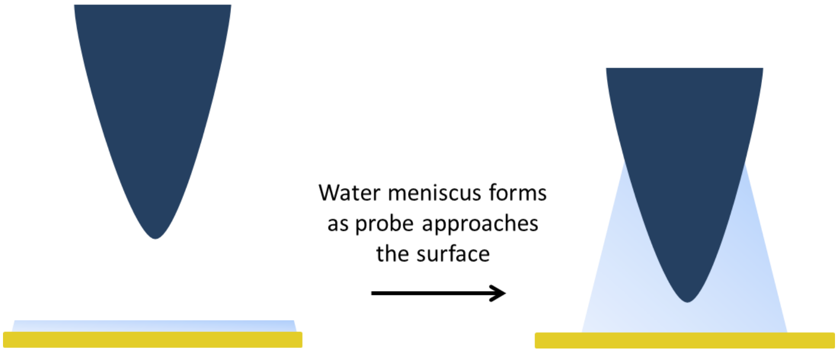

Scheme 4.1 Schematic diagram showing the formation of a water meniscus from residual water on a sample and probe surfaces.

Amongst the approaches described above, it has been hypothesized that alkoxysilane and trichlorosilane could polymerise in the water meniscus between the probe and pattern surface.[90] Published results have demonstrated promising nanopatterns fabricated under ambient conditions at 20 – 23 ˚C and 35 – 50% relative humidity.[122, 171]

4.1.3 Advanced multiplexed nanolithography

Large-area patterns have been developed using alkoxysilane molecules as “ink” utilising fountain-pen nanolithography (FPN).[134] Derived from DPN, FPN utilises modified AFM cantilevers with liquid reservoirs connected to microchannels as “ink” carriers instead of the “ink” being loaded on the tip of the AFM probes. The “ink” can then be delivered to point of contact with the surface. Although FPN applications have demonstrated consistent fabrication of alkoxysilane patterns, this technique suffers from the limitations of the pattern features at the micrometre range of scale.[175, 176]

In addition, wide-area chemical patterns utilising PPL techniques have been introduced in combination with surface click-chemistry using chemically coupled azide as the “ink” to pattern on alkyne functionalised surfaces at 60 – 80% relative humidity in allergic responses studies.[128] N-hydroxysuccinimide (HOSu) coupled natural “inks” such as biotin and fluorescent molecules such as fluorescein isothiocyanate (FITC) have also been used in combination with AFM-based nanocontact printing techniques to fabricate high density nanoarrays for drug discovery applications.[177]

4.2 Aims and Objectives

In previous chapters, thiol-gold chemisorption substrates as model surfaces with various controlled surface presenting functional groups (carboxyl and amino groups), controlled quantity of presenting groups, and feature to feature spacing were shown to have an impact on manipulating the fate of both human MSCs and articular chondrocytes. In the previous chapters, thiol-gold chemisorption surfaces with controlled parameters, such as the surface-presenting carboxyl/amino groups, their quantity and feature-to-feature spacing have demonstrated to have an impact on the fate of both human MSCs and articular chondrocytes. However, using gold as a nanopatterned surface base has limitations for applications in the realm of regenerative medicine. In consideration of biocompatible advanced materials, biodegradable polymers were ultimately used to support designed nanopatterns. This chapter aimed to transfer the designed nanoarrays onto biodegradable polymers. It was hypothesised that the transferred surface materials would reproduce the findings in Chapter 2 and 3 on MSC and articular chondrocyte phenotypes.

To assess the potential for advancing the PPL technique with degradable polymers, a number of surface reaction approaches were utilised, initially on stiff siloxane surfaces as a support base to achieve the desired reaction conditions. This approach also allowed optimisation of the crucial parameters for the PPL mechanism, for example, the relationship between feature size, relative humidity and rate of chemical transport. It was hoped that the reaction developed using this method could then be transferred onto selected biodegradable polymer thin films. Ultimately, it was sought to provide alternative PPL mechanisms to those previously published on stiff materials that could be applied on soft materials, especially biodegradable polymer films for future applications in regenerative medicine.

4.3 Experimental Methods

4.3.1 Materials and instrumentation

All chemicals were purchased from Sigma-Aldrich unless otherwise stated. (3-bromopropyl)trimethoxysilane was purchased from Fluorochem Ltd, UK. Silicon wafers were purchased with roughness of less than 2 nm for use with PPL technique (IDB Technologies, UK). Water contact angle was measured using a CDCA-100F contact angle analyser (Camtel Ltd., UK) programmed to record advancing angle of 6.5 mm into samples prepared on 13 mm glass coverslips. O_2 plasma on siloxane surfaces was conducted using an HPT-100 (Henniker Plasma, UK). FT-IR spectra were recorded using a Bruker Alpha FTIR spectrometer equipped with a diamond-ATR crystal. X-ray photoelectron spectroscopy (XPS) was measured using a Kratos Axis Ultra Hybrid with an Al Kα monochromated X-ray source. Fabrication of nano-patterns was conducted on a FlexAFM with a C3000 controller (Nanosurf, Liestal, Switzerland) as previously described in

Chapter 2. Surface topography and friction maps were imaged using a FlexAFM (Nanosurf, Liestal, Switzerland) or Park NX-10 (Park System, Santa Clara, USA) systems. A borosilicate glass vacuum desiccator was used for vapour deposition of APTES (Smith Scientific, UK).

4.3.2 Fabrication of Nano Patterns on Siloxane

All experiments were repeated 3 times unless otherwise stated.

4.3.2.1 Fabrication of (3-bromopropyl)trimethoxysilane or (3-mercaptopropyl)trimethoxysilane on siloxane surfaces

Silicon wafers or glass coverslips were treated with O_2 plasma at 18 W for 120 s prior to surface silanisation, which was performed in a glove bag filled with dry N_2 to minimise trace water in the surrounding atmosphere.[94] (3-bromopropyl)trimethoxysilane (BPTS) or of (3-mercaptopropyl)trimethoxysilane (McPTS) were diluted to 1% (v/v) in anhydrous N,N-dimethylformamide (DMF) and 200 μL cm^{-2} of which was drop coated on the silicon wafers or glass coverslips for 1 h. The surface was then washed copiously with anhydrous DMF and dried under a stream of dry nitrogen. The siloxane surfaces were then transferred to a glass petri dish and cured at 80 °C for 15 min (Scheme 4.2).

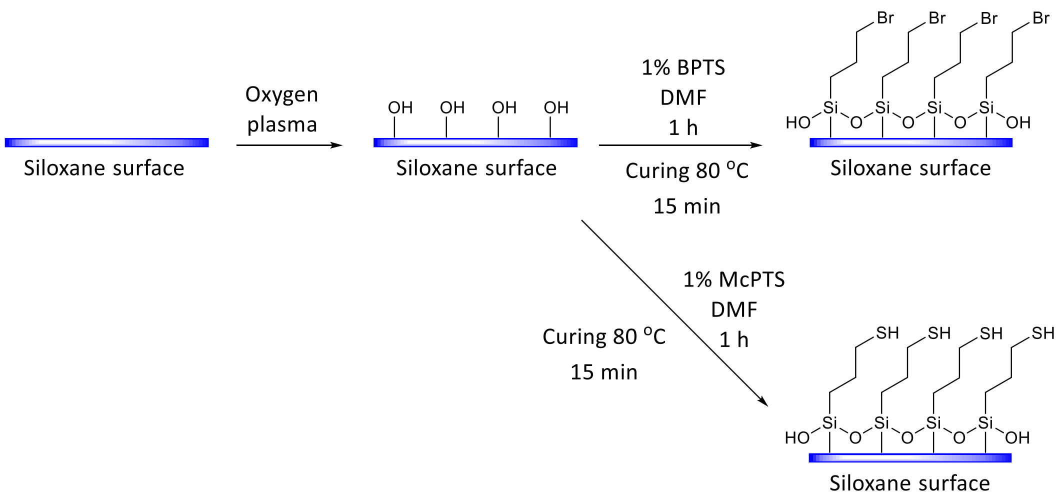

Scheme 4.2 Reaction scheme for bromo or mercapto functionalisation of the siloxane surface. Surfaces were first oxidised by oxygen plasma, then BPTS or McPTS was deposited followed by thermal annealing.

4.3.2.2 Fabrication of (3-aminopropyl)triethoxysilane on siloxane surfaces

Silicon wafer or glass coverslips were treated with O_2 plasma at 18 W for 120 s prior to surface silanisation. Vapour silanisation of (3-aminopropyl)triethoxysilane (APTES) was performed in a vacuum desiccator. Plasma-treated silicon wafers or glass coverslips were transferred to a vacuum desiccator and briefly vacuumed to remove air in the chamber and filled with dry N_2. To a small dish in the chamber, 1 mL of APTES was added and the chamber was quickly vacuumed to 300 mTorr, the outlet of chamber was closed, vacuum line was removed and sample was left in closed chamber for 12 h. Upon removal, the dish of APTES was removed and the chamber was refilled with dry N_2, the siloxane surfaces were allowed to cure for 2 days (Scheme 4.3).[106]

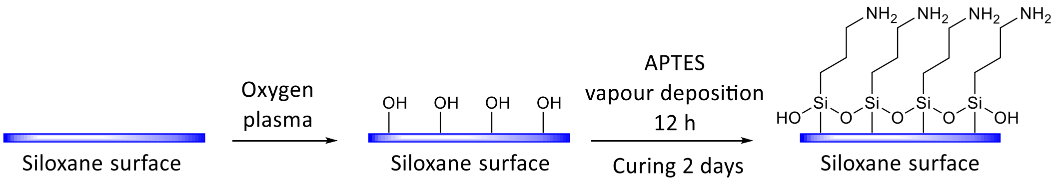

Scheme 4.3 Reaction scheme for amino functionalisation of the siloxane surface. Surfaces were first oxidised by oxygen plasma, APTES was then vapour deposited onto the surface followed by thermal annealing.

4.3.2.3 Surface coating of MHA on BPTS-functionalised surfaces for optimisation of reaction completion

On a BPTS coated glass coverslip, 1 mM of MHA in ethanol was drop coated at a surface density of 200 μL cm^{-2}, the reaction was carried out for up to 16 h. Upon completion of reaction the surface was rinsed copiously with ethanol and dried under a stream of dry N_2.

4.3.2.4 “Inking” of MHA

To pattern thiol on bromine-functionalised surfaces; MHA was deposited on PPL pen arrays as previously described in Chapter 2.

4.3.2.5 “Inking” of BPTS or McPTS

Prior to patterning BPTS or McPTS on silicon wafers, 20 µL of 1% (v/v) BPTS or McPTS diluted with acetone was drop coated on to the PPL pen arrays. Solvent was allowed to evaporate and the array was used immediately for patterns.

4.3.2.6 “Inking” of (2,5-dioxopyrrolidin-1-yl) octanoate

Twenty µL of 1% (v/v) (2,5-dioxopyrrolidin-1-yl) octanoate were dissolved in acetone and drop coated on to the PPL pen arrays. Solvent was allowed to evaporate and the array was used immediately for patterning on the APTES-modified surfaces.

4.3.3 Fabrication of functionalised self-assembled monolayers on polymer thin film

All experiments were repeated 3 times unless otherwise stated.

4.3.3.1 Polymer thin film preparation

E1001(1k), a tyrosine-derived polycarbonate (Scheme 4.4), was dissolved in THF to a concentration of 2 % (w/v) then sonicated for 1 h. The solution was filtered using a 0.45 µm PTFE filter prior to use. A glass coverslip was pre-cleaned by sonicating in iso-propanol for 15 min and dried under a stream of N_2. 50 µL of E1001(1k) solution was then spin-coated onto the pre-cleaned glass coverslip (ϕ = 12 mm) at 2000 rpm for 20 s. The coated glass coverslip was then transferred to a vacuum chamber and vacuum applied at -30 in Hg for 16 h.

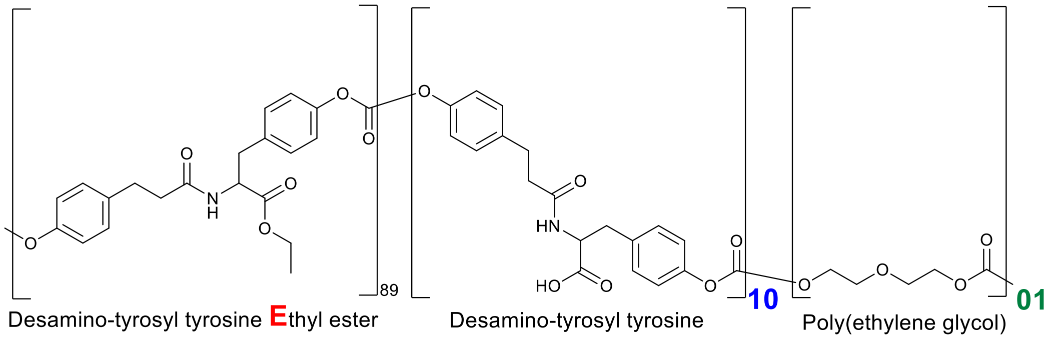

E1001(1k)

Scheme 4.4 Chemical structure of E1001(1k), a tyrosine-derived polycarbonate, where "E" represents the major polymer component, desamino-tyrosyl tyrosine ethyl ester, "10" represents 10% of the polymer chain co-polymerised with desamino-tyrosyl tyrosine, "01" represents 1% of the polymer chain co-polymerised with poly(ethylene glycol) and "(1k)" represents the molecular weight of poly(ethylene glycol).

4.3.3.2 E1001(1k) polymer surface silanisation

E1001(1k) polymer thin films were treated with O_2 plasma at 50 W for 150 s. Upon removal, the polymer thin films were transferred to a vacuum desiccator and briefly vacuumed to remove air in the chamber and filled with dry N_2. To a small dish in the chamber, 1 mL of APTES was added and the chamber was quickly vacuumed to 300 mTorr, the outlet of chamber was closed, vacuum line was removed and sample was left in closed chamber for 16 h.

4.3.3.3 Coupling of maleimido acid with APTES silanised surface

Fifty mg of 4-maleimidobutyric acid, 34.5 mg of N-hydroxysuccinimide and 57.9 mg of N-(3-dimethylaminopropyl)-N'-ethylcarbodiimide hydrochloride (EDC) was dissolved in 3 mL of H_2O. The polymer thin film was immersed in the aqueous solution for 2 h. The surface was then rinsed with H_2O and dried under a stream of dry N_2.

4.3.3.4 Maleimido-thiol click for bulk coated samples

A 0.86 mg quantity of MHA was dissolved in 3 mL of isopropanol. The polymer substrate was immersed in solution for 1 h and rinsed copiously with isopropanol and dried under a stream of dry N_2.

4.3.4 AlamarBlue assay for cytotoxicity

Modified polymer thin films were sterilised with 70% ethanol followed by UV irradiation for 20 min. Primary human dermal fibroblasts (HDF) were seeded at a density of 10^4 cells cm^{-2} for 1, 3 and 7 days. At each time point, the culture medium (Life Technologies, DMEM 11995-065 supplemented with 10% FBS) was discarded and replaced with 200 µL of pre-warmed 10% alamarBlue solution (Bio-rad, BUF012B) in culture media for 100 min. One hundred µL of the 10% alamarBlue solution was added into 4 wells of a 96-well plate and incubated for 100 min as blank. 100 µL of alamar blue solution incubated with cells was transferred into each wells of the 96-well plate containing blank controls. Fluorescence was measured using TECAN plate reader at 560 nm excitation and 590 nm emission with 85% gain. Results were obtained after subtraction of the blank values then plotted as fluorescence intensity.

4.3.5 Quant-iT picogreen dsDNA assay (Invitrogen, P7589)

Modified polymer thin films were sterilised using 70% ethanol followed by UV irradiation for 20 min. HDFs were seeded at a density of 10^4 cells cm^{-2} for 1, 3 and 7 days. At each time point the culture medium was discarded, washed once with PBS and cells were lysed with 500 µL cell lysis buffer prior to freezing at -80°C until all samples were collected.

4.3.5.1 Calibration curve for Quant-iT picogreen assay

In a 96-well plate, 100 µL of 1x Tris-EDTA (TE) buffer was added into each well. In a sequence of 7 wells of the first row, 100 µL of DNA solution at a concentration of 2 µg mL^{-1} was added and mixed. Subsequently 100 µL of DNA solution in each well was mixed and transferred into the next well. 100 µL of the mixture in the 7th well of the row was removed. Picogreen solution was then diluted 1:200 with TE buffer and 100 µL of the solution was added into each well.

4.3.5.2 Blank control

To each of 4 wells, 100 µL of 1x TE buffer was added and 100 µL of picogreen solution diluted at 1:200 with TE buffer was added.

4.3.5.3 Sample preparation

To each sample wells, 90 µL of 1x TE buffer was added and 10 µL of the lysed sample was added. One hundred µL of picogreen solution diluted 1:200 with TE buffer were added to each well.

Fluorescence was measured using a TECAN plate reader with 480 nm excitation and 520 nm emission. The results were first subtracted with blank control and the calibration curve was plotted and fluorescence of samples was converted into number of dsDNA based on the equation of calibration curve. The result was then multiplied by 10 and 0.5 to calibrate from the dilution (1:10 with TE) and total volume of buffer cells were lysed in (500 µL) and plotted as total DNA (µg mL^{-1}).

4.4 Results and discussion

4.4.1 Nanolithography of BPTS on siloxane surfaces

BPTS was patterned on O_2 plasma-treated silicon wafers as the surface functionalisation for MHA attachment through thiol-bromo click chemistry (Scheme 4.5). The relative humidity was reduced to 25% in order to minimise the degree of polymerisation of BPTS ink during printing.

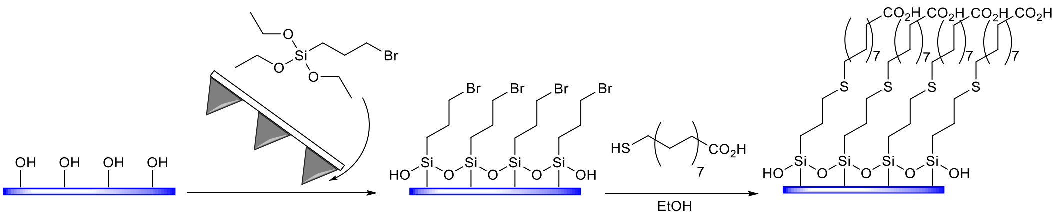

Scheme 4.5 A schematic diagram showing PPL patterning of BPTS followed by thiol-bromo click surface reaction.

The reaction conditions were examined using BPTS bulk coating on glass surfaces followed by MHA immersion on surface. The surfaces were examined by water contact angle measurements (Figure 4.1) and ATR-FTIR (Figure 4.2).

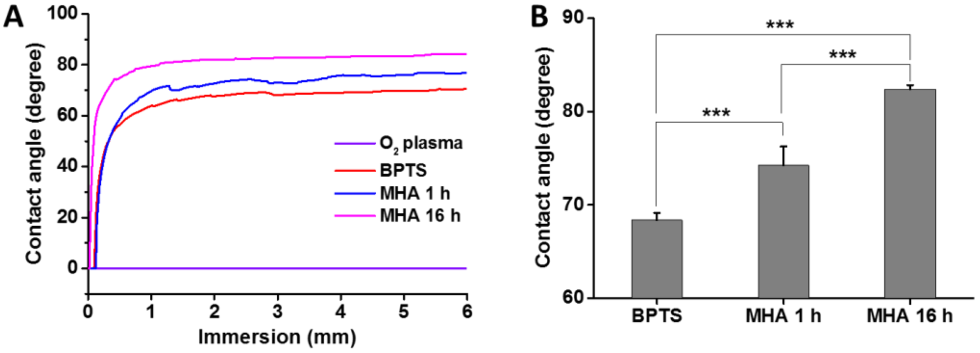

Figure 4.1 (A) A representative plot of water contact angle against immersion depth and (B) a water contact angle plot of glass surfaces slianised with BPTS and MHA coated on a BPTS surface via thiol-bromo click. *p* value was analysed using one way ANOVA where "*" represents p < 0.005, significant difference. Error bars represent standard deviation.**

BPTS was first silanised on glass coverslips. The contact angle was measured at 68.36 ± 0.80 ˚. MHA was then coated on bromine functionalised surfaces through thiol-bromo click for up to 16 h. At 1 h, reaction was optimised by water contact angle and a fluctuating curve was obtained with a mean of 74.24 ± 2.02 ˚ (Panel A, Figure 4.1). The fluctuation in contact angle measurements may be an indication of an incomplete reaction. BPTS surfaces were then coated with MHA for 16 h and reaction completion observed by water contact angle which obtained a mean of 82.40 ± 0.45 °. A longer reaction time was required to achieve completion than previously reported (16 h vs 1 h)[178], due to the lack of triethylamine (TEA) as a catalyst, which was absent because of the challenge of employing it in future applications of PPL pattern fabrication as a component of "ink" with MHA on BPTS surface as TEA is highly volatile, with a vapour pressure of 56.1 Torr at room temperature,[179] causing evaporation when inking with a PPL pen array.

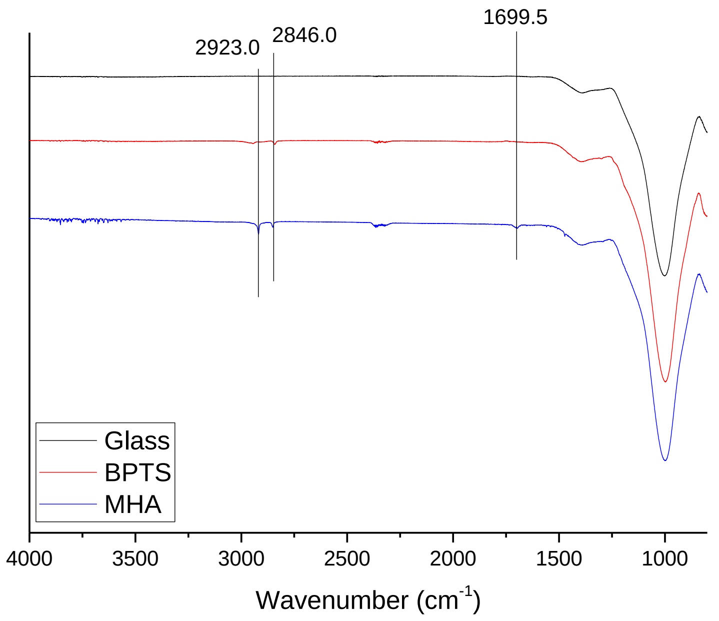

Figure 4.2 An ATR-FTIR spectrum of serial surface functionalisation on borosilicate glass. Glass was silanised with BPTS and MHA was subsequently immobilised on surface for 16 h.

A characterisation peak at 1008 cm^{-1} was found representing Si-O-Si of the glass substrate. A characterisation peak at 1400 cm^{-1} was found for BO_3 stretching of the borosilicate glass used as substrate. A characterisation peak 2846 cm^{-1} was found on BPTS and both 2846 and 2923 cm^{-1} were found on MHA representing C-H stretching. On MHA spectrum, between region of 3500 and 4000 cm^{-1} showed high in noise so no apparent peak was found for O-H stretching but a characterisation peak at 1699.5 cm^{-1} was found representing C=O stretching of acid.

Taking into account the solvent effect with PDMS pen arrays,[62] 1% (v/v) BPTS diluted with acetone was patterned using PPL on O_2 plasma-treated silicon wafers in a 5 x 5 array of features across a 20 µm x 20 µm region. The patterns were imaged using AFM to obtain height and friction maps (Figure 4.3), with a screen capture of the surface recorded at this region (Figure 4.4).

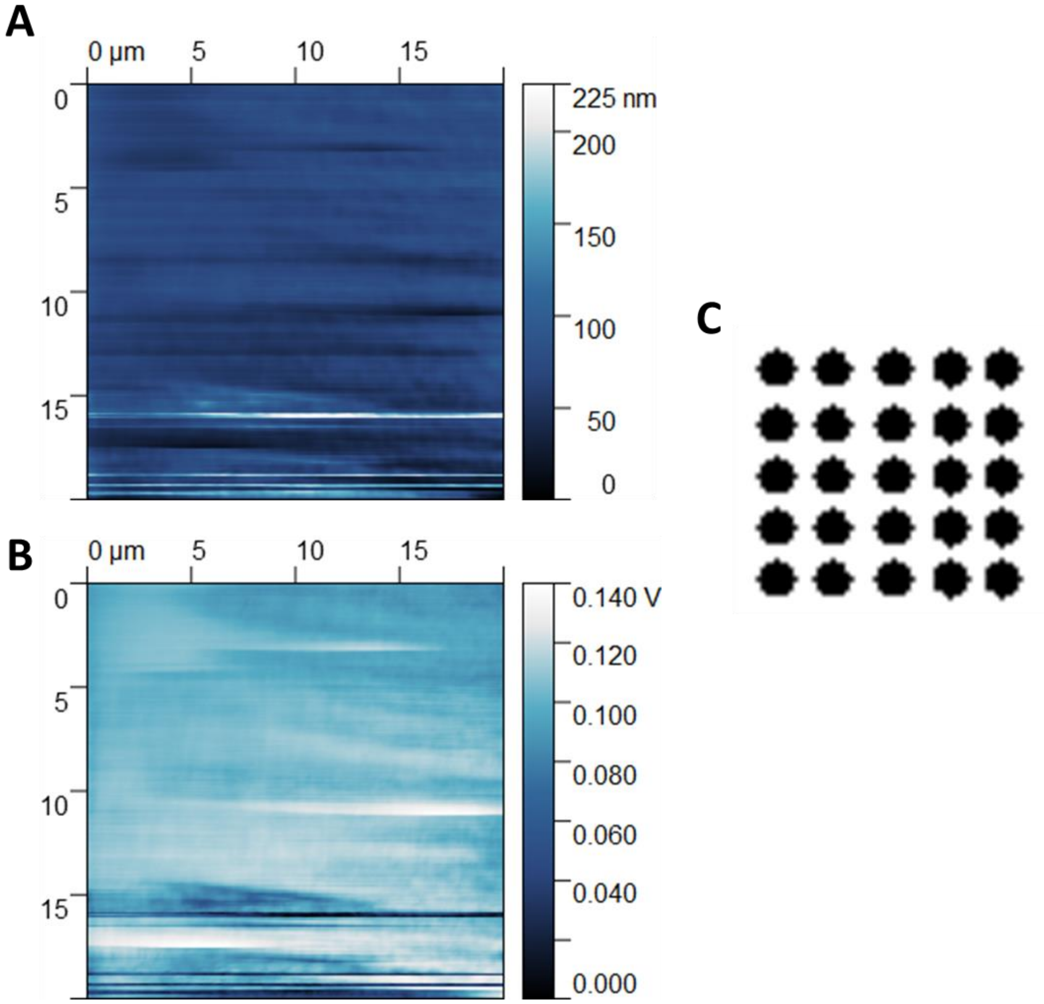

Figure 4.3 AFM images of PPL-patterned BPTS on O_2 plasma-treated silicon wafers. Representative (A) height map (B) qualitative friction map and (C) expected patterns. Images were scanned at 0.78 s per line across an area of 20 µm x 20 µm.

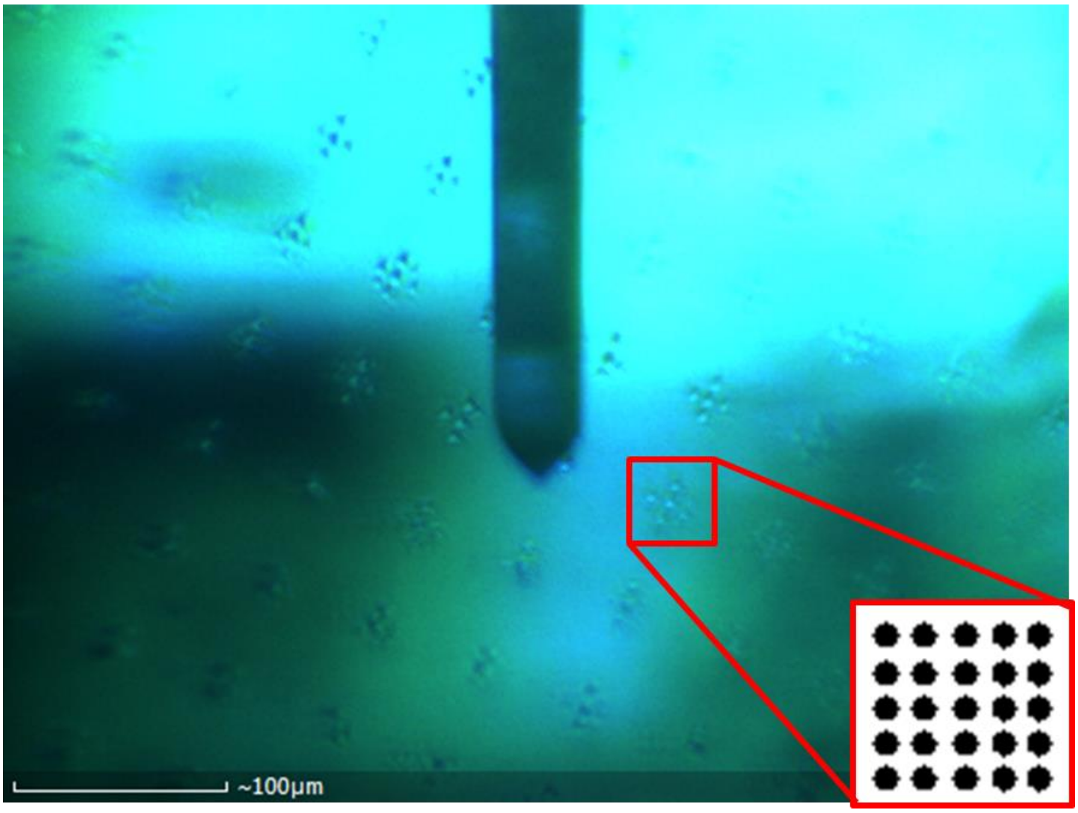

Figure 4.4 A representative screen capture of BPTS patterned silicon surface showing BPTS was visibly polymerised after PPL pattern fabrication. Expected pattern is highlighted in the red box.

Although BPTS was inked prior to PPL pattern fabrication and the designed features were fabricated within 1.5 min, BPTS had presumably polymerised upon or prior to PPL patterning due to its extreme moisture sensitivity. Patterned surfaces were imaged with AFM on the visible patterns where the cantilever was approached up to or close to visible BPTS polymer droplets (Figure 4.4). The AFM cantilever probes were contaminated with BPTS droplets as it scanned across the surface indicated by lateral noises detected in Panels A and B, Figure 4.3. The image height map suffered interference from an extreme height object consistent with friction variation, indicating loose BPTS droplets. BPTS-patterned surfaces exhibited repeated wide-area patterns across the surface, however, optical images displayed inconsistent arrays of features with the expected pattern due to rapid polymerisation of the BPTS under ambient conditions

(Figure 4.4). BPTS could be polymerised upon pattern fabrication of a feature to form large droplets and connected with neighbouring features.

Due to BPTS moisture sensitivity PPL surface features were alternatively fabricated by using MHA as "ink" on BPTS silanised surfaces (Scheme 4.6).

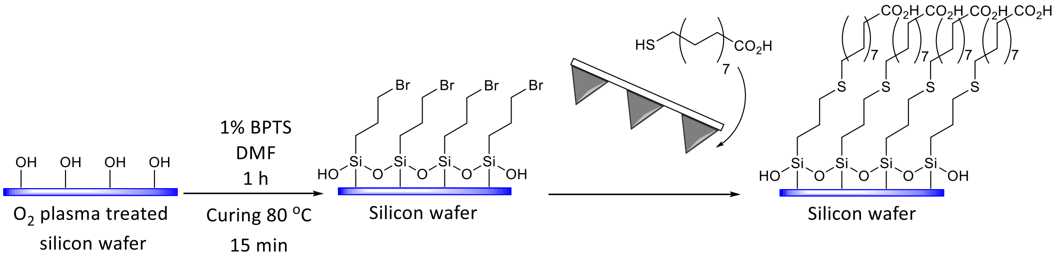

Scheme 4.6 Schematic diagram showing a siloxane surface that was first treated with O_2 plasma, BPTS was then silanised on surface and MHA was used as "ink" for PPL pattern fabrication.

Fabrication of identical patterns was attempted on BPTS surfaces with MHA as "ink" in a 5 x 5 array of features across a region measuring 20 µm x 20 µm with 45% relative humidity. The surface was incubated under atmospheric conditions for 16 h and the patterns then imaged by AFM, plotting height and friction maps where no apparent features were observed (Figure 4.5).

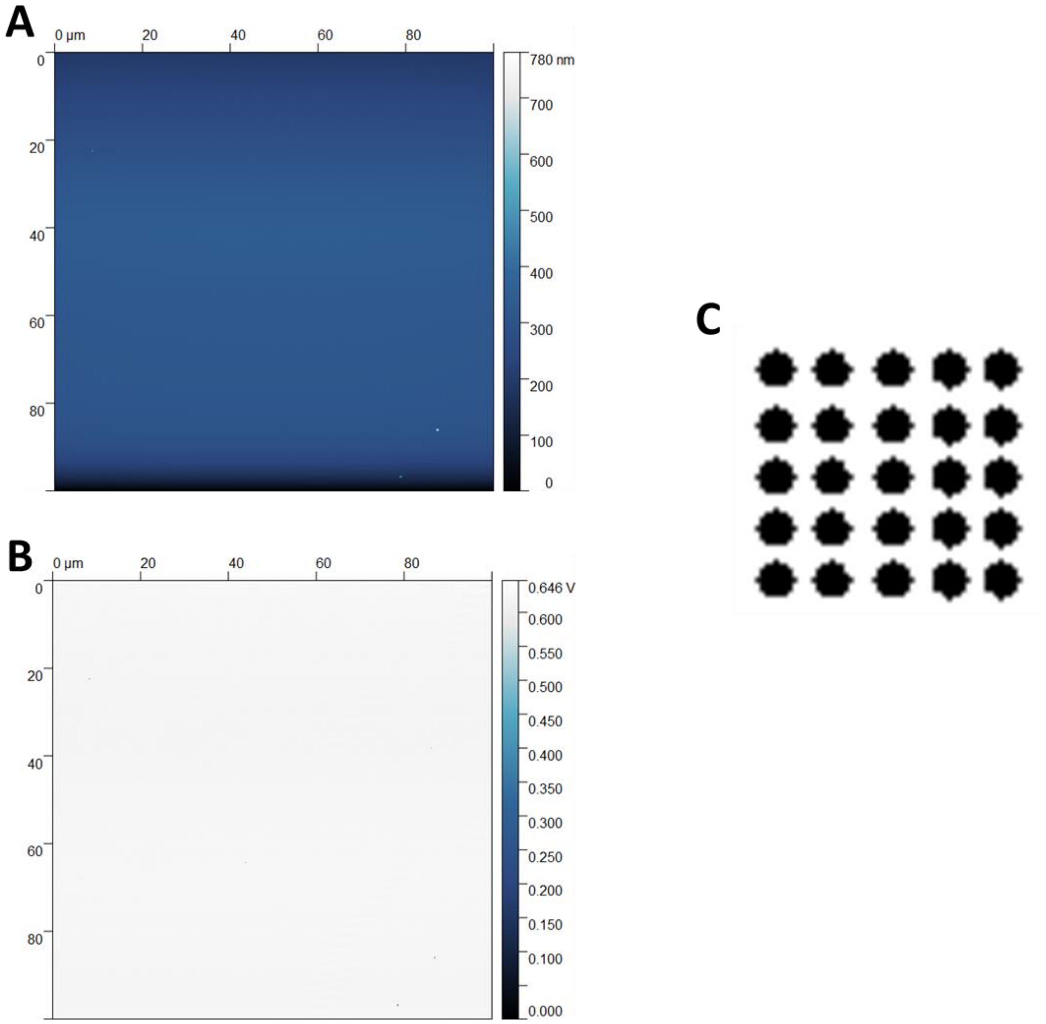

Figure 4.5 AFM images of PPL-patterned BPTS on O_2 plasma-treated silicon wafer. Representative (A) height map (B) qualitative friction map and (C) expected patterns. Images were scanned at 0.78 s per line across a region of 100 µm x 100 µm.

Two possibilities were considered for the failed reaction as shown in Scheme 4.7. BPTS, with primary alkyl bromide, could undergo a hydrolysis reaction with moisture in the atmosphere through rapid S_N2 nucleophilic substitution during alignment of the pen array and surface, taking up to 2 h, or post-fabrication incubation (Panel A, Scheme 4.7). Complete hydrolysation upon alignment would result in substitution of alkyl bromide with alcohol and the release of hydrogen bromide.

Another possibility might be due to the surface reactions. Poor reactivity could occur with alkyl bromide as a self-assembled monolayer (SAM), with nucleophiles being required to penetrate below the surface to attack the carbon underneath the bromide from the back which resulting in a substantial kinetic barrier of the nucleophilic substitution (Panel B, Scheme 4.7).[89]

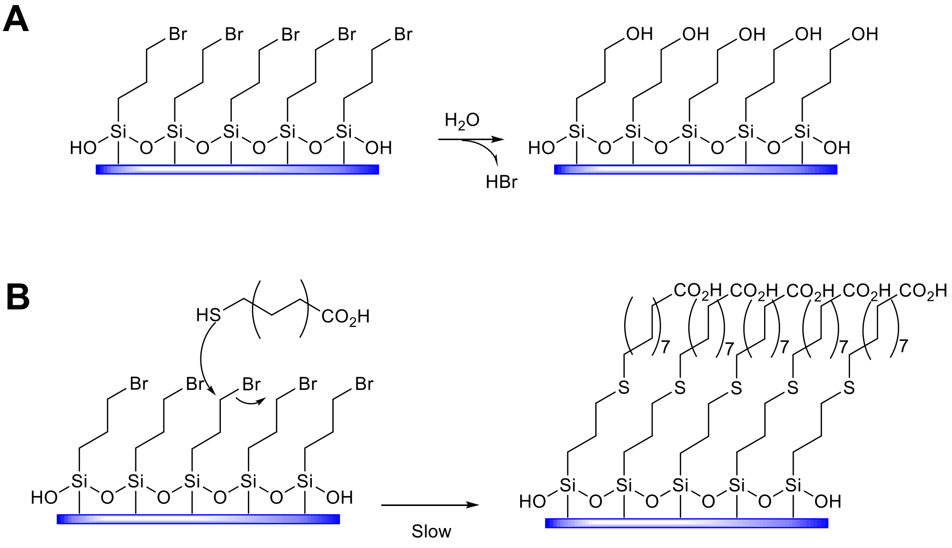

Scheme 4.7 Schematic diagram of possible theories for the failed PPL surface reactions including (A) hydrolysis of primary alkyl bromide and (B) kinetic barrier of thiol-bromo click chemistry undergoing S_N2 nucleophilic substitution.

4.4.2 Nanolithography of McPTS on the siloxane surface

Considering the possibility of the kinetic barrier and lower sensitivity to moisture compared with BPTS, McPTS was patterned on O_2 plasma-treated silicon wafers using a 1% (v/v) dilution using acetone at a 20% relative humidity followed by the suggested path shown in Scheme 4.8.

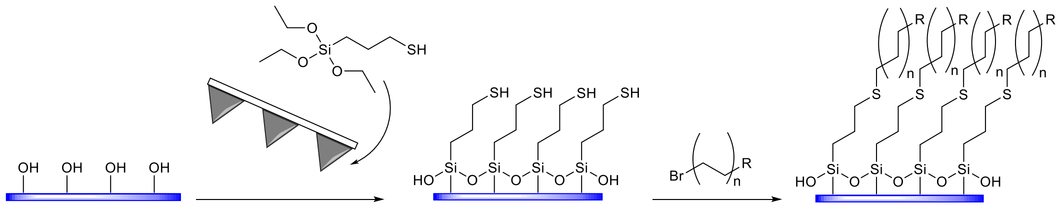

Scheme 4.8 Schematic diagram showing a siloxane surface that was first treated with O_2 plasma, with McPTS then used as "ink" for PPL pattern fabrication. Primary alkyl bromide was then reacted on the surface.

McPTS was fabricated using PPL onto the surface, as this would theoretically eliminate any substantial kinetic barrier of the thiol-bromo click surface reaction. McPTS was patterned on O_2 plasma treated silicon wafer in an array of features across a region of 40 µm x 40 µm, surface patterns being imaged using optical microscopy (Figure 4.6).

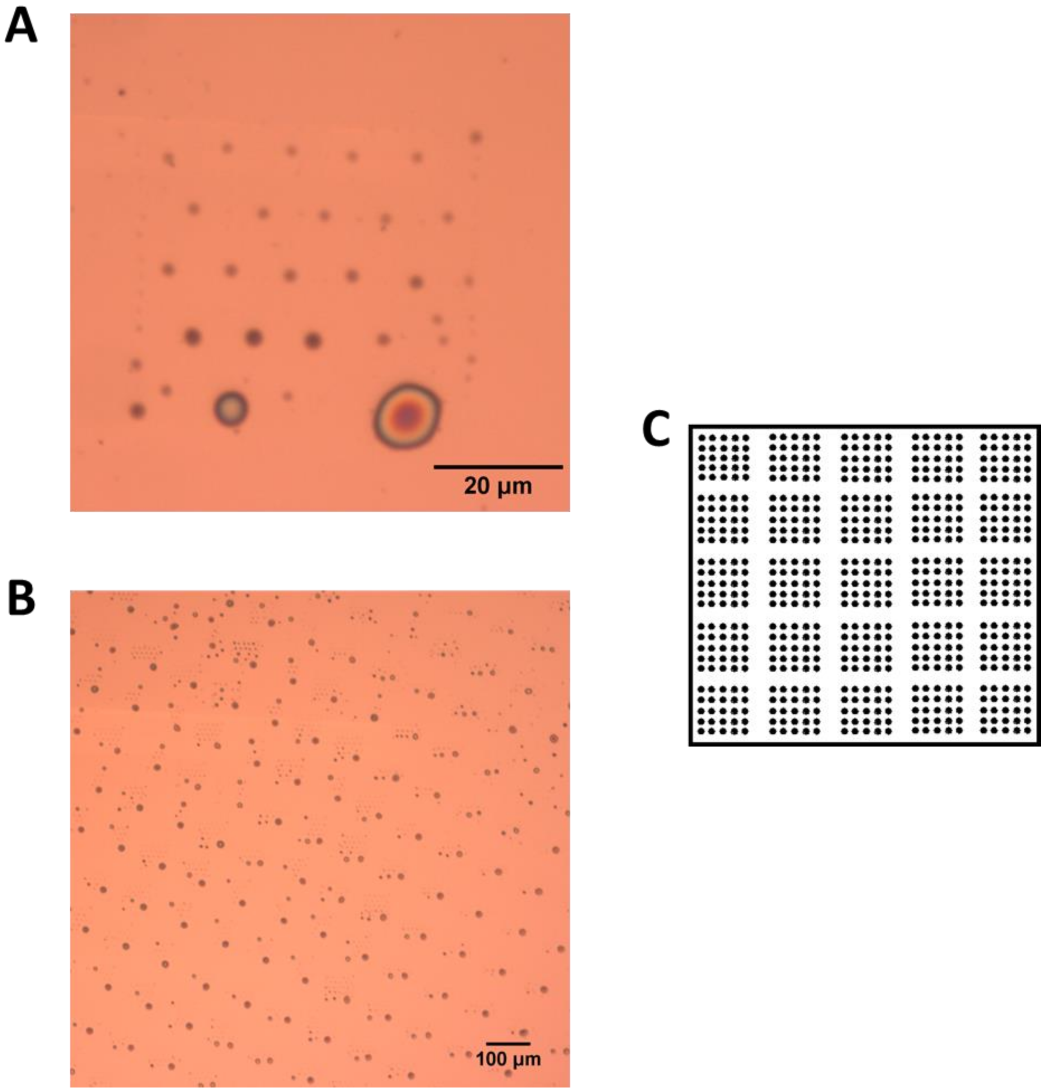

Figure 4.6 Optical images of PPL-patterned McPTS on O_2 plasma treated silicon wafers. Representative (A) individual patterns, (B) large area image and (C) expected patterns are shown.

Visible patterns suggest that McPTS polymerised on the surface and multiple layers were formed upon fabrication. The expected ‘frame’ of patterns presented as single features visible using optical microscopy, however, designed 5 x 5 arrays of features of deposited McPTS within the ‘frame’ were aggregated whilst patterns were being fabricated across the surface.

McPTS exhibited a lower surface reactivity than BPTS as BPTS had a greater degree of polymerisation on the surface than McPTS under identical relative humidity conditions (Scheme 4.9).

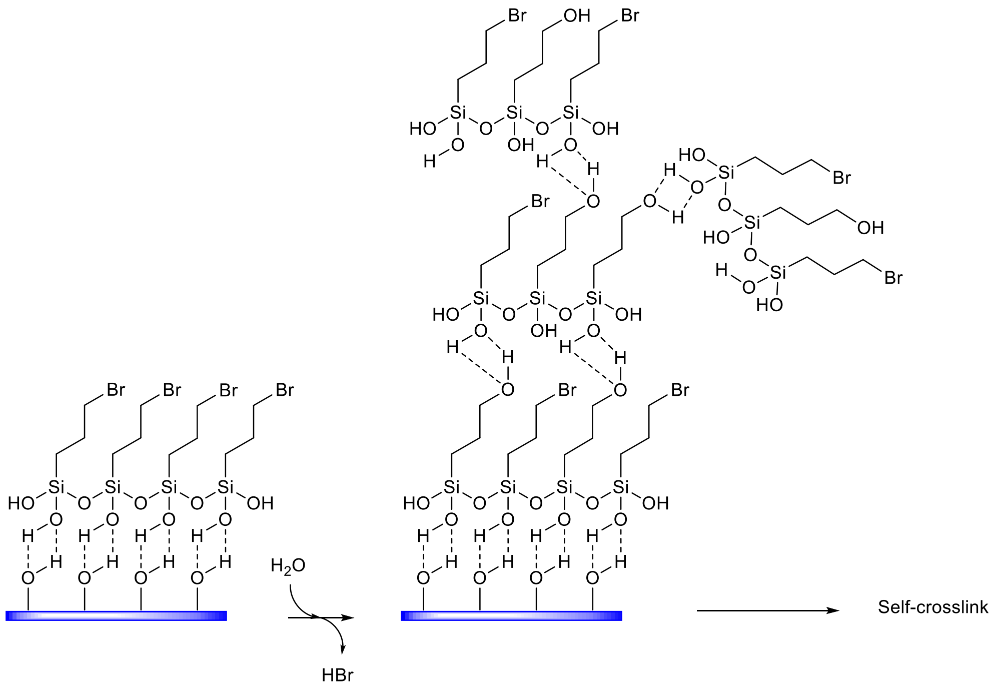

Scheme 4.9 Diagram showing hydrolysation of alkyl bromide occuring upon deposition of BPTS, resulting in polymerisation through self-crosslinking.

During PPL pattern fabrication, humidity was a critical parameter to enable “ink” transport as the chemical “inks” were delivered from the PDMS pyramids to pattern a surface through the water meniscus.[173] As humidity was introduced, potential hydrolysation of alkyl bromide would occur upon deposition of BPTS. The resulting hydroxyl groups formed upon hydrolysation could encourage hydrogen bonding between the BPTS and terminal hydroxyl groups to yield self-crosslinked polymer droplets on the surface. Sulfhydryl is a weaker leaving group than bromide and therefore slower hydrolysation would be expected.

Use of alkyl bromide was not attempted for patterning as an “ink” due to challenging homogeneous McPTS coating on surfaces. A 1% (v/v) of McPTS was coated on glass coverslip and ATR-FTIR results suggested no active sulfhydryl groups could be detected (Figure 4.7).

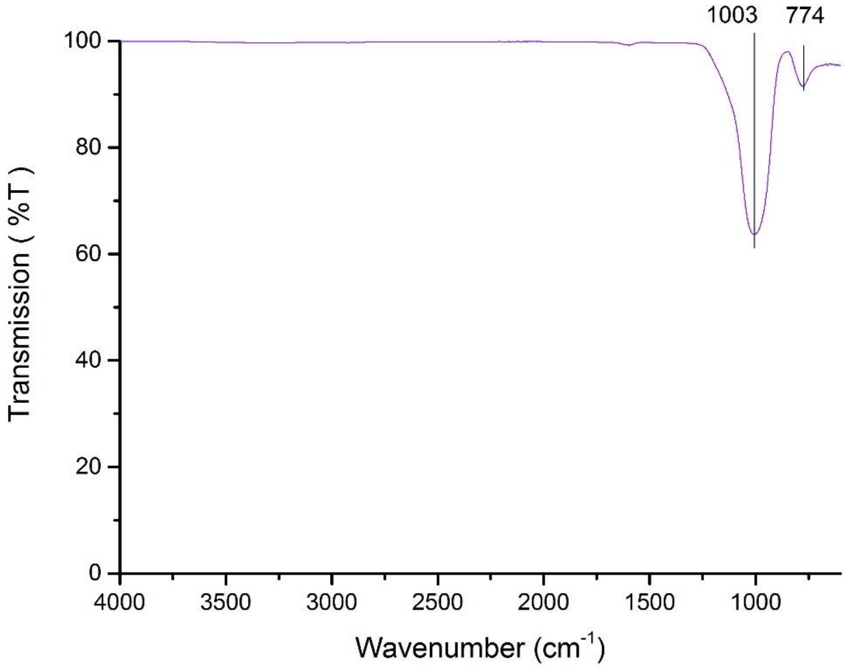

Figure 4.7 An ATR-FTIR spectrum of McPTS surface coating showing the characteristic peaks at 774 and 1003 cm^{-1} which represents symmetric Si-O-Si stretching and asymmetric Si-O-Si stretching, respectively.

An ATR-FTIR spectrum displays distinct characteristic peaks at 774 and 1003 cm^{-1} which represents symmetric and asymmetric Si-O-Si stretching, respectively.[180] However, no apparent peaks in the region of 2550 cm^{-1} were observed for S–H stretching indicating that no active sulfhydryl groups were present. McPTS could aggregate in a chemical state where sulfhydryl groups could click and form disulfide bonds, thus making it less surface reactive (Scheme 4.10).

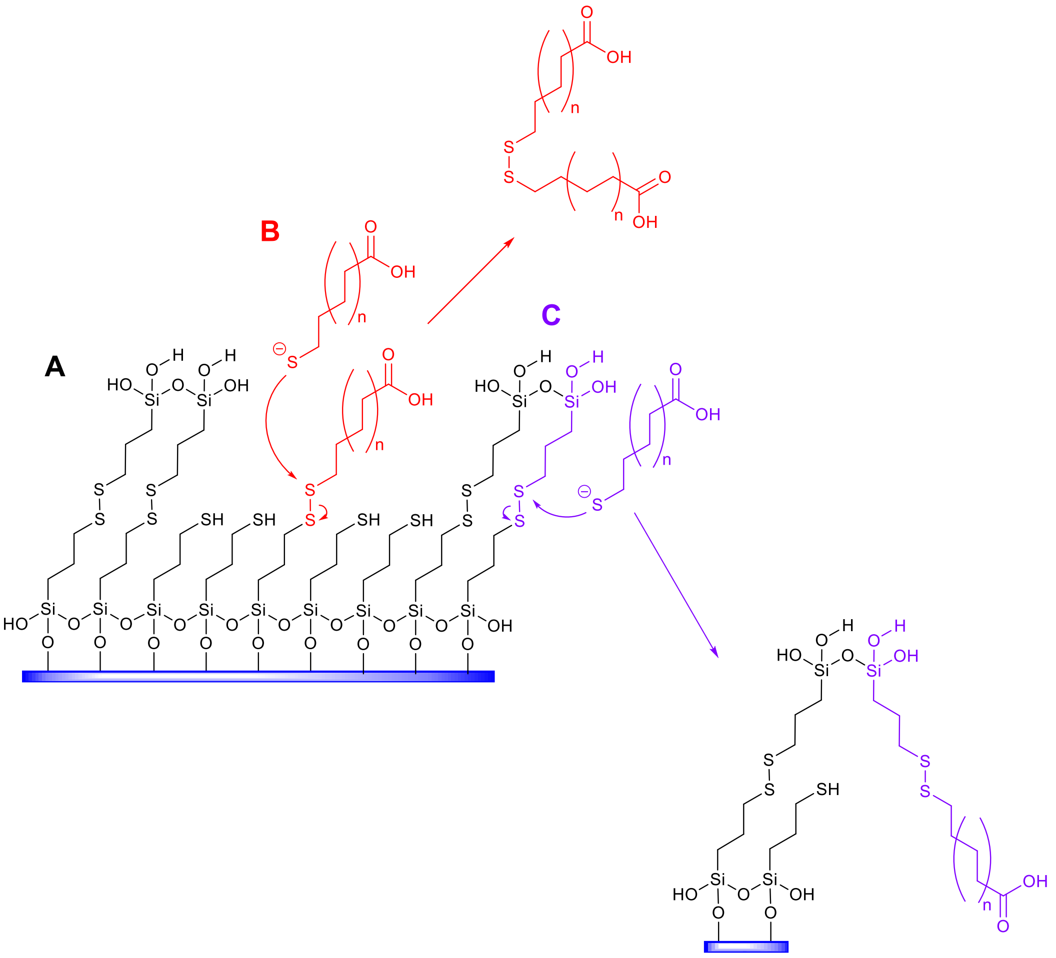

Scheme 4.10 Schematic diagram indicating potential versatile thiol-disulfide interchange where (A) McPTS aggregates via disulfide bond formation (B) excess thiolated chemicals attack disulfide bonds and cleave off expected pattern and (C) thiolated chemical attack aggregates McPTS to form disulfide bonds into heterogeneous surface functional groups.

In a chemical state or upon deposition on surfaces, active sulfhydryl groups on McPTS could partially form disulfide bonds. Interchange of disulfide bonds could result in aggregation of McPTS upon or prior to surface deposition thus limiting the quantity of active sulfhydryl terminal groups and increasing surface roughness (Scheme 4.10, A). The absence of active sulfhydryl groups limited the potential of thiol-bromo click of alkyl bromide as “ink” for PPL applications. Additionally, McPTS is a versatile silane compound. Using thiolated chemicals, such as MHA, would be expected to have limited reactivity and suitability *via* thiol-disulfide interchange.

Assuming McPTS was deposited as a homogeneous layer on a siloxane surface and thiolated chemicals, such as MHA, were used as "ink" for PPL pattern fabrication, the MHA would be expected to react with the presenting sulfhydryl groups and form disulfide bonds. However, excess MHA could attack these bonds and cleave off patterned chemicals to form disulfide carboxylic acids as by-products (Scheme 4.10, B). In addition, where aggregated McPTS molecules were present, thiolated chemical "ink" could attack the disulfide McPTS form where spatially accessible and potentially click on either end of the McPTS resulting in a chemical "ink" that was versatile but uncontrollable (Scheme 4.10, C).

Although thiol-disulfide interchange could form strong disulfide covalent bonds, with bonding energy *ca* 60 kcal mol^{-1}, it could be reversed under mild conditions, such as at room temperature and within physiological pH.[181] Thiol-disulfide interchange reactions are versatile, moderately fast and less controllable for surface functionality and potential roughness, thus applications for McPTS-functionalised surfaces in PPL nano-pattern fabrication is considered improbable.

4.4.3 Nanolithography of N-hydroxysuccinimide functionalised chemicals on amino-functionalised siloxane surfaces

HOSu-activated carboxylic acids are widely used in amide bond formation, especially solid phase coupling, as HOSu-activated carboxylic acids, are relatively stable as intermediates but remain spontaneously reactive during amide bond formation from amines under appropriate conditions.[182, 183] Here, isolated HOSu-activated carboxylic acids were used as "ink" for PPL nanopattern fabrication on amino-functionalised siloxane surface. APTES was first vapour deposited on silicon wafers and selected HOSu-activated carboxylic acids were used as "ink" for PPL nanopattern fabrication (Scheme 4.11).

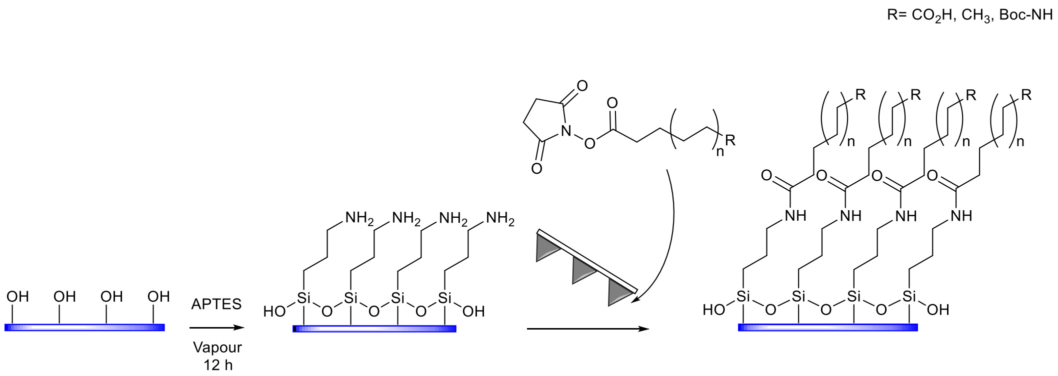

Scheme 4.11 Schematic diagram illustrating the design of PPL nanopattern fabrication where APTES is first vapour deposited on silicon wafers, the selected HOSu-activated carboxylic acids with various teminal groups such as alkyl, ester or Boc protected amines used as "ink".

To comply with the hypothesis based on previous DPN fabrication research that nanofeatured surfaces promote various MSC phenotypes,[41] **HOSu-activated carboxylic acids** with alkyl, carboxyl or amino terminal groups could be used for PPL nanopattern fabrication as "ink". However, due to **HOSu-activated**-end reactivity with amines, the amino terminated chemical "ink" would be protected with tert-butyl dicarbonate to prevent self-attack once reacted with HOSu and which could then be deprotected after completion of the PPL reaction. After PPL fabrication, the remaining active amino surfaces would be passivated with **HOSu-activated** PEG to isolate material variables.

APTES surface roughness was examined using an AFM at 3 randomly selected regions of 50 µm x 50 µm and roughness as root mean square height was calculated, measuring a mean of 1.08 ± 0.25 nm (Figure 4.8).

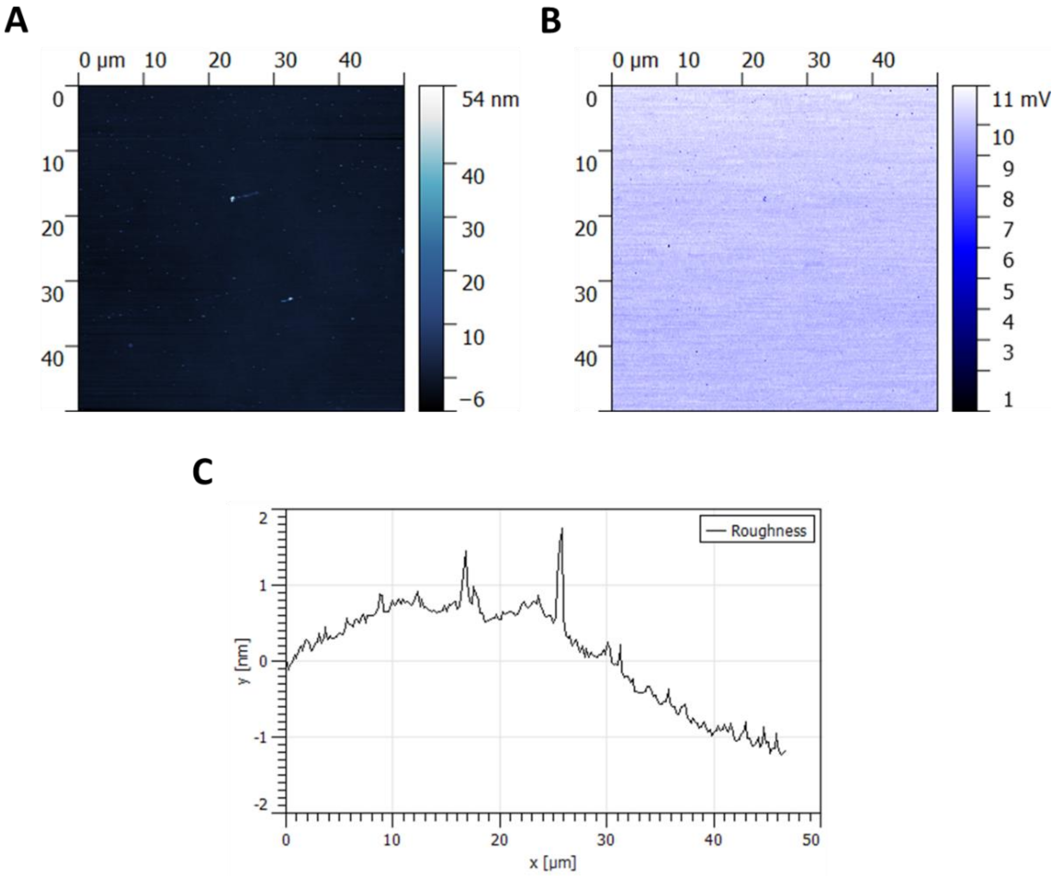

Figure 4.8 Representative images of (A) height map, (B) qualitative friction map and (C) an example of roughness across a line of 50 µm.

As potential "ink", (2,5-dioxopyrrolidin-1-yl) octanoate was coated on the APTES surface with the reaction monitored using water contact angle (Figure 4.9) and ATR-FTIR (Figure 4.10).

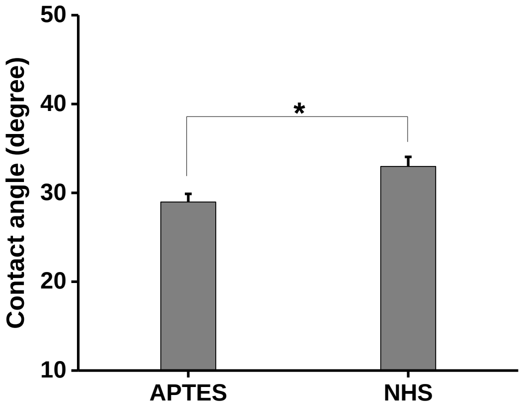

Figure 4.9 A representative water contact angle plot of glass surface slianised with APTES and (2,5-dioxopyrrolidin-1-yl) octanoate **was subsequently coupled on the surface via amide bond formation.** ***p*** **value was analysed using one way ANOVA method where "*" represents $p < 0.05$, significant difference. Error bars represent standard deviation.**

APTES was first silanised on glass coverslips and contact angle was measured at 28.97 ± 0.92 °.[184] The result was similar to previously reported APTES functionalisation on similar surface.[185] (2,5-Dioxopyrrolidin-1-yl) octanoate was then coated on amino functionalised surface through amide bond formation. Result was observed by water contact angle and a fluctuated curve was obtained at 32.97 ± 1.07 ˚.

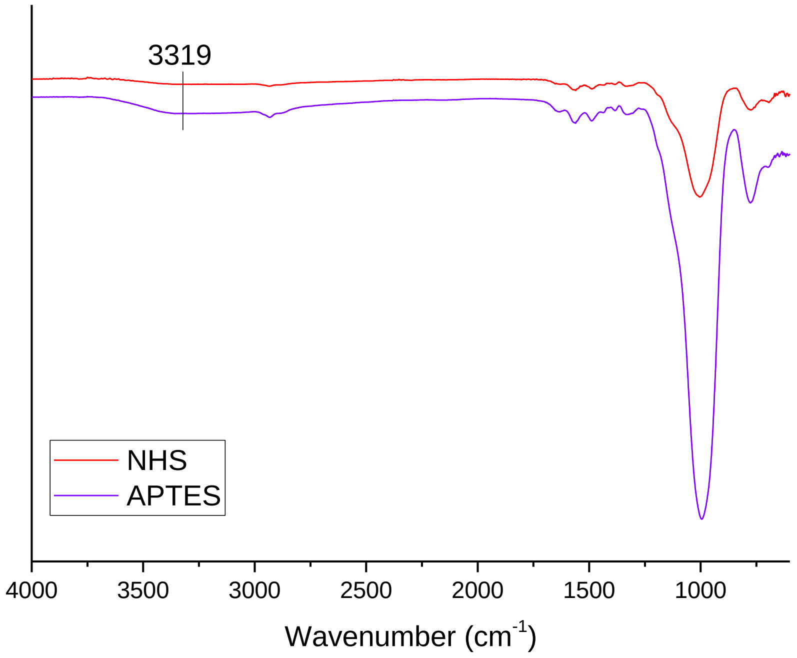

Figure 4.10 ATR-FTIR spectrum of APTES-functionalised surface and (2,5-dioxopyrrolidin-1-yl) octanoate coupled with APTES through HOSu-activated site showing the absence of a characteristic peak at 3319 cm^{-1} after coupling.

FT-IR characteristic peaks were observed at 776 and 1005 cm^{-1} due to symmetric and asymmetric Si-O-Si stretching, respectively. Peaks were observed at 1386, 1430, 1494, 1567, 1644 and 2927 cm^{-1} on the spectra of both APTES and (2,5-dioxopyrrolidin-1-yl) octanoate coupled surfaces. A characteristic peak at 3319 cm^{-1} was observed on the APTES surface but absent on the (2,5-dioxopyrrolidin-1-yl) octanoate coupled surface. Although the N-H stretch on primary amines should appear to have two bands in region 3300-3000 cm^{-1}, modified surfaces should form a monolayer on the siloxane surface and therefore it is expected that a smaller quantity would be detected. The results indicate that any amine on APTES is likely to have been consumed and coupled with (2,5-dioxopyrrolidin-1-yl) octanoate and amide bonds formed.

An attempt was made to use (2,5-dioxopyrrolidin-1-yl) octanoate as an “ink” for PPL nanopattern fabrication. The “ink” was freshly prepared prior to patterning to reduce hydrolysation of HOSu-activated functional groups. Patterns were first attempted at 45% relative humidity and the results imaged using AFM after 2 h incubation post-PPL fabrication (Figure 4.11).

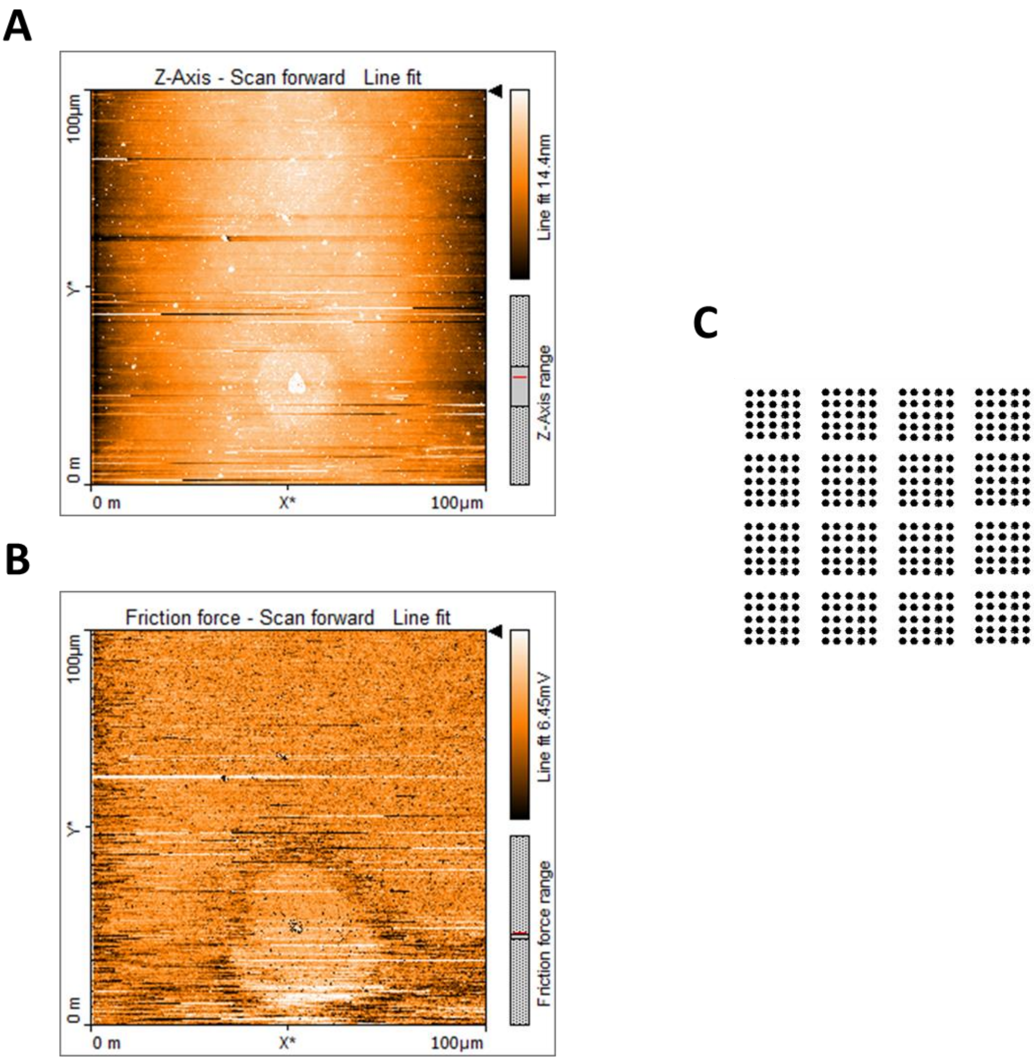

Figure 4.11 AFM images of PPL patterned (2,5-dioxopyrrolidin-1-yl) octanoate on amino-functionalised silicon wafers at 45% relative humidity. Representative (A) height map, (B) qualitative friction map and (C) expected patterns. Images were scanned at 0.78 s per line across a 100 µm x 100 µm region.

At 45% relative humidity, a feature was observed on the AFM images for both height and qualitative friction maps that indicates that (2,5-dioxopyrrolidin-1-yl) octanoate had reacted with the surface presenting amines, forming amide bonds. However, only a single feature was imaged at approximately each 100 µm apart spacing, it was possible that the single feature was the approach spot formed during stage and PPL pen array approach prior to pattern fabrication. This step typically requires no more than 10 s to optimise force in contact, it was therefore hypothesised that as a chemical “ink” for PPL applications, (2,5-dioxopyrrolidin-1-yl) octanoate exhibited a faster rate of transport than typically-used thiol ‘inks’ and that all the chemicals that had been deposited on the PDMS pen arrays were completely transferred onto the surface during the approach, over less than 10 s.

The experiment was then conducted at a reduced relative humidity, 25%, and the results imaged using AFM after 2 h incubation post-PPL fabrication (Figure 4.12).

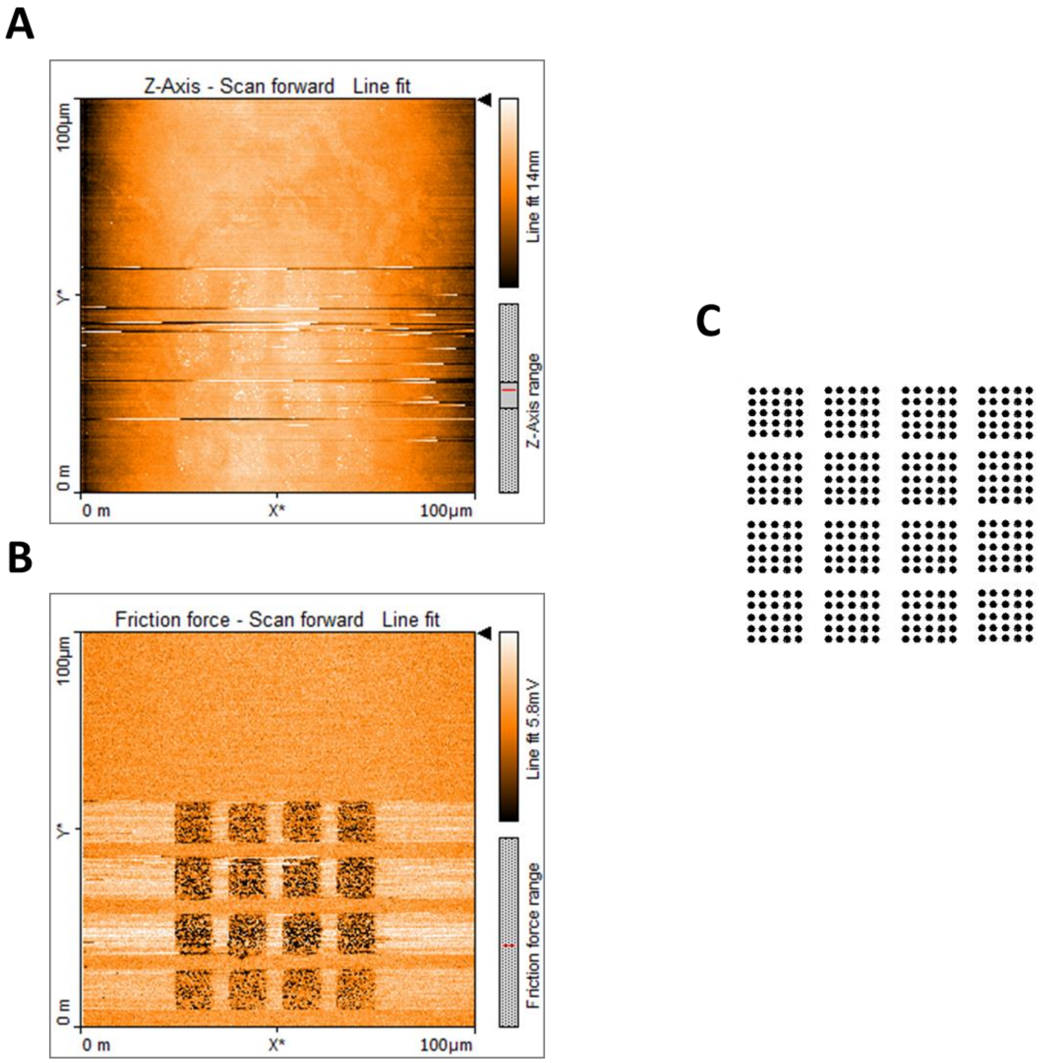

Figure 4.12 AFM images of PPL patterned (2,5-dioxopyrrolidin-1-yl) octanoate on amino-functionalised silicon wafer at 25% relative humidity. Representative (A) height map, (B) qualitative friction map and (C) expected patterns. Images were scanned at 0.78 s per line across an area of 100 µm x 100 µm.

As expected, at a reduced relative humidity, the rate of "ink" transport was reduced and pattern outlines were observed. However, defined features within the individual squares were unable to be imaged which suggests that, although the overall reaction hypothesis was supported, the rate of ink transport of the proposed chemical, **(2,5-dioxopyrrolidin-1-yl) octanoate**, was uncontrollable and unsuitable for PPL applications.

4.4.4 Maleimido-functionalised surface modification on siloxane surface and E1001(1k) polymer thin films for nanolithography of thiolated chemicals

Michael addition reactions have been broadly characterised as a method of efficient organic synthesis performed under environmentally friendly conditions.[186] Amongst these, the thiol-Michael click reactions have been extensively implemented in a range of applications, such as surface modification, polymer conjugation polymerisation and crosslinking of polymers.[100] Here, the thiol-maleimide click reaction was chosen as a PPL pattern fabrication mechanism because of the advantages that C=C of maleimide provides the greatest reactivity within typical Michael acceptors. In addition, in highly polar solvent systems, the thiol-maleimide click reaction proceeds without a catalyst as the thiolate anion forms due to the polarity of the solvent.[187]

The thiol-Michael click reaction scheme was used to modify the surface of biodegradable polymer thin films. E1001(1k), a tyrosin-derived polycarbonate, was generously provided by Professor Joachim Kohn and the experiment carried out under his supervision at the New Jersey Center for Biomaterial at Rutgers University, USA. An identical reaction was used to modify silicon wafers as the control surface.

Solvent effects on the topography of polymer thin films was assessed by dissolving E1001(1k) solid in dichloromethane (DCM) or tetrahydrofuran (THF) and imaged on an AFM (Figure 4.13 and Figure 4.14).

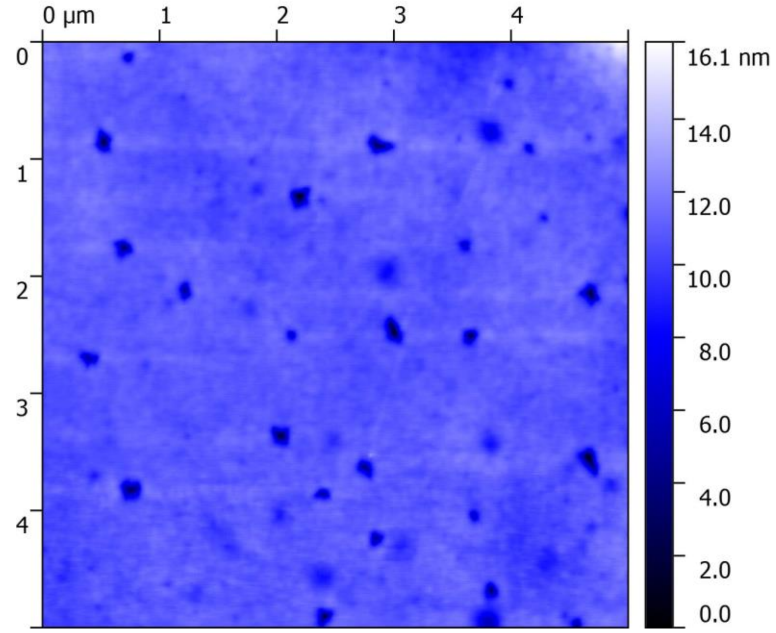

Figure 4.13 AFM image of surface topography on spun coated E1001(1k) solution in DCM.

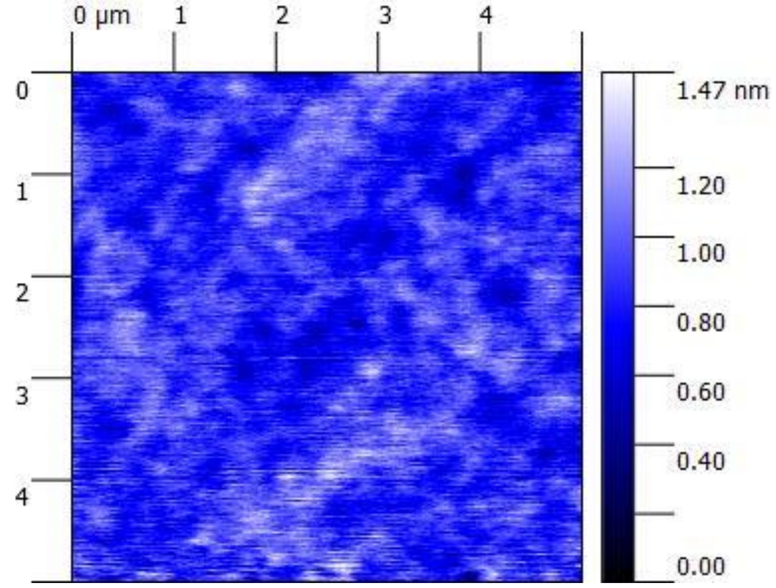

Figure 4.14 AFM image of surface topography of spun coat E1001(1k) solution in THF.

Two % (v/v) E1001(1k) solution in DCM was spin coated onto the surface, allowed solvent to evaporate for 16 h at -30 mmHg at room temperature. The surface height map shows numerous holes located in random locations, having irregular shapes and depths. It was suggested that surface flaws were caused by rapid DCM solvent evaporation. The solvent was likely evaporated before being transferred to the vacuum chamber, allowing such flaws to appear. Conversely, surface thin films spun coat with E1001(1k) in THF at an identical concentration, *i.e.,* 2% (v/v), exhibited observed no pores on the surface. Surface roughness was observed to be no greater than 1.5 nm and only the polymer chain structure was observed.

APTES was then vapour deposited onto surfaces for surface activation of amine presenting groups. The active amino surface was then coupled with 4-maleimidobutyric acid to create a maleimido-activated surface. The surfaces were then immobilised with MHA for confirmation of surface reactivity.

The reactions of the maleimido-activated surface were monitored using water contact angle, with 3 time points (1, 2 and 16 h) being measured (Figure 4.15).

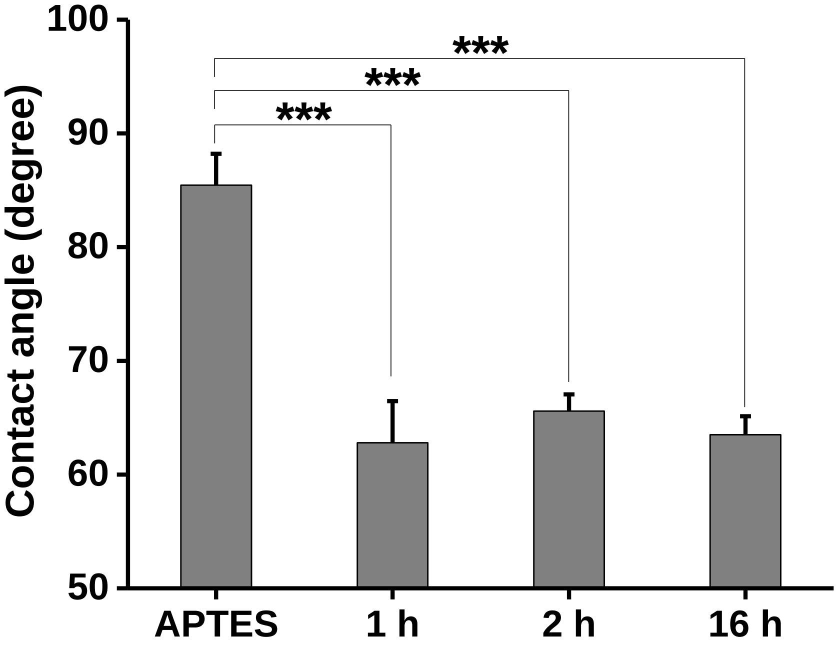

Figure 4.15 Plot of water contact angle at a series of time points, 1, 2 and 16 h, of the reaction of 4-maleimidobutyric acid on APTES-functionalised surfaces. "APTES" represents surface water contact angle prior to maleimide functionalisation. "1 h", "2 h" and "16 h" represent surface functionalisation of 4-maleimidobutyric acid after 1, 2 and 16 h, respectively. The *p* value was calculated using one way ANOVA, where "*" represents *p* < 0.005, significant difference. Error bars represent standard error of the mean.**

APTES functionalised surfaces were used as time point 0 h, measuring a mean water contact angle of 85.44 ± 2.77 ˚. Substrates were then immersed in one-pot aqueous reaction mixtures for 1, 2 and 16 h. At each time point, substrates were removed, rinsed copiously with H_2O then water contact angle measured, displaying a mean of 62.79 ± 3.66, 65.58 ± 1.47 and 63.50 ± 1.63 ˚, respectively. The results indicate that amide bond formation was likely completed within 1 h, with the chosen solvent system having little impact on the surface, *e.g.,* hydrolysis degradation, for up to 16 h. No significant difference was observed for surfaces obtained at 1, 2 or 16 h. The 2 h reaction was chosen, to allow the subsequent reactions to maximise amide bond formation and minimise the degradation effect.

Similarly, the progress of the thiol-Michael click reaction of MHA on the surface was monitored using water contact angle, at 4 time points: 0.5, 1, 2 and 16 h (Figure 4.16).

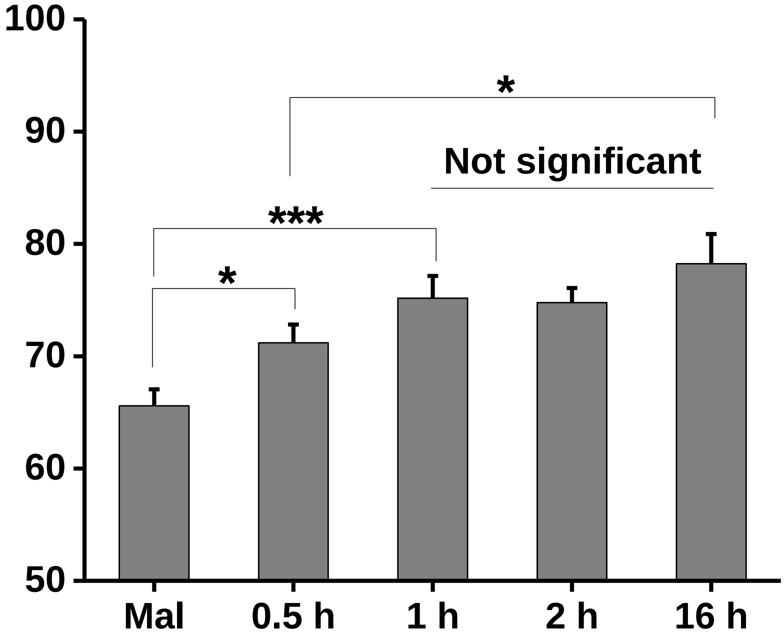

Figure 4.16 Plot of water contact angle at a series of time points: 0.5, 1, 2 and 16 h, of MHA reactions on maleimide-functionalised surfaces. "Mal" represents surface water contact angle prior to MHA *via* thiol-Michael click reaction. "0.5 h", "1 h", "2 h" and "16 h" represent surface functionalisation of MHA after 0.5, 1, 2 and 16 h, respectively. The *p* value was calculated using one way ANOVA, where "*" represents $p < 0.05$, a significant difference; "*" represents $p < 0.005$, a significant difference. Error bars represent standard error of the mean.**

The maleimide-functionalised surface was used as time point 0 h, for which a mean water contact angle of 65.58 ± 1.47 ° was measured. Substrates were then immersed in MHA in isopropanol for 0.5, 1, 2 and 16 h. At each time point, substrates were removed and rinsed copiously with isopropanol, with mean water contact angles measuring 71.20 ± 1.63, 75.17 ± 1.98, 74.77 ± 1.30 and 78.24 ± 2.64 °, respectively.

Water contact angles of the candidate materials gradually increased over the reaction time, with no significant difference observed after 1 h of reaction. The results indicated that the thiol-Michael click reaction was likely completed within 1 h and the chosen solvent system, *i.e.,* isopropanol, had no apparent impact on the surface for up to 16 h. The results obtained after 1, 2 and 16 h showed no significant difference, so a 1 h reaction was then chosen for subsequent reactions for material surface characterisation and cytotoxicity tests.

Chemically modified surfaces were examined with ATR-FTIR to observe adsorption peak transit (Figure 4.17).

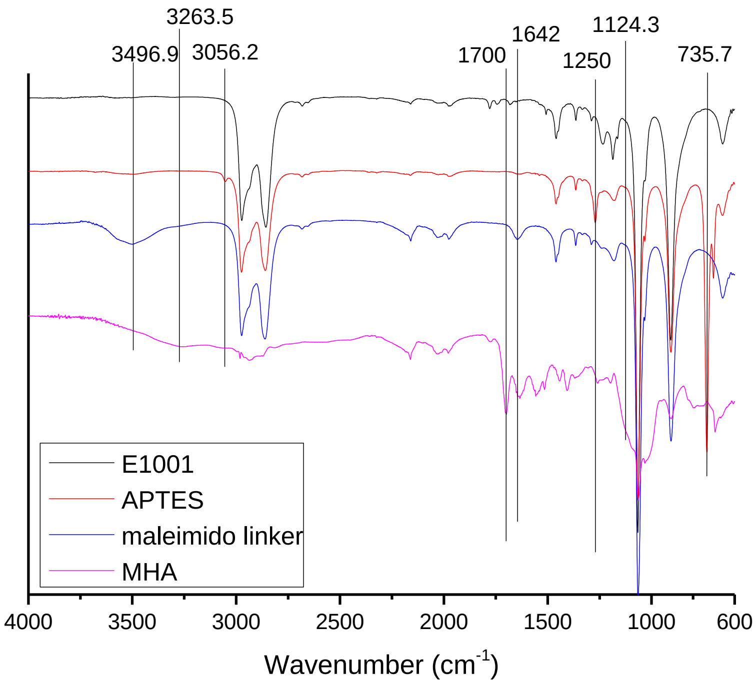

Figure 4.17 ATR-FTIR spectrum of serial surface functionalised on E1001(1k) where "E1001" represents raw E1001(1k) thin film on a glass coverslip; "APTES" represents APTES vapour-coated E1001(1k) surface; "maleimido linker" represents surface reacted with 4-maleimidobutyric acid through amide bond formation and "MHA" represents MHA reacted on maleimido-activated surface through a thiol-Michael click reaction.

The APTES surface was observed to have characteristic peaks at 735.7 and 1250 cm^{-1} which represents N-H wag and primary amine C-N stretching, respectively. In addition, the APTES surface exhibited a peak at 3056.2 cm^{-1} and a rather weak band at 3496.9 cm^{-1} indicating N-H stretching.[95] On the Maleimido surface, a peak at 1642 cm^{-1} was detected, attributed to C=O stretching.[188] On the MHA surface, a characteristic peak at 1700 cm^{-1} and a broad peak at 3263.5 cm^{-1} were observed indicating C=O and O-H stretching of carboxylic acid, respectively. The spectra measured suggested that layer-by-layer bottom-up surface modification was successful. In addition, X-ray photoelectron spectroscopy (XPS) of each layer of the bottom-up surface modification was examined (Figure 4.18, Figure 4.19 and Figure 4.20).

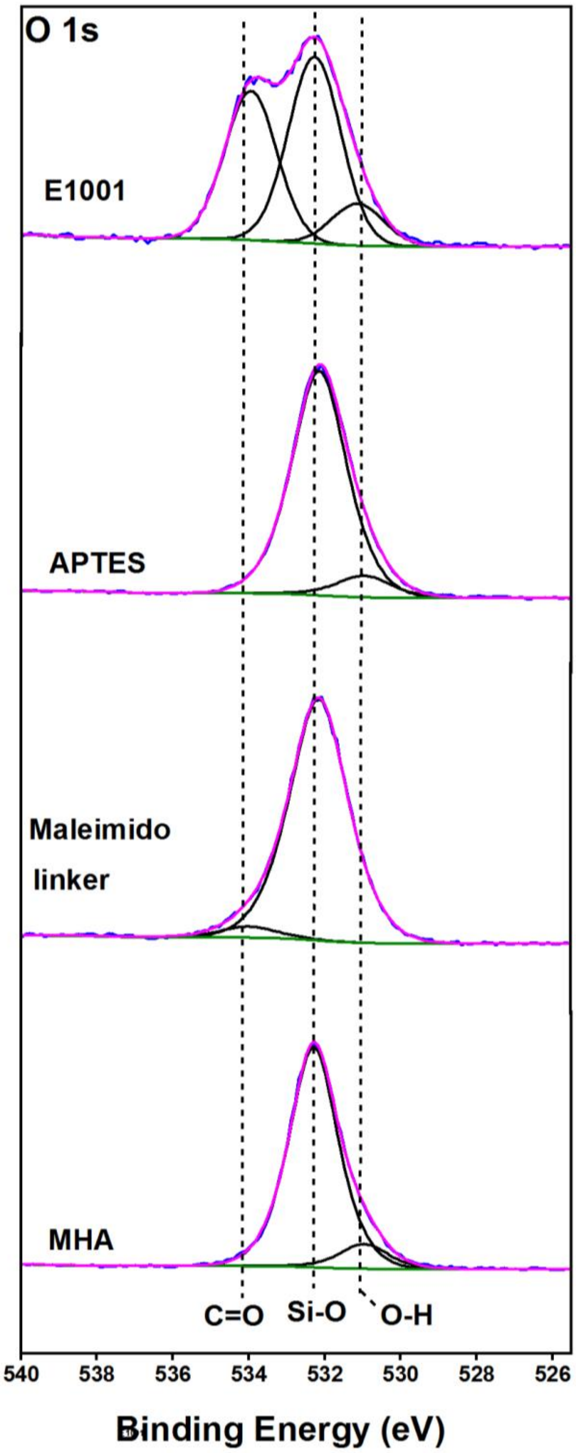

Figure 4.18 Fitted O 1s XPS spectra of each layer of bottom-up surface modification, *i.e.,* E1001 raw surface thin film, APTES silanised surface, maleimido crosslinked surface and finally MHA clicked surface.

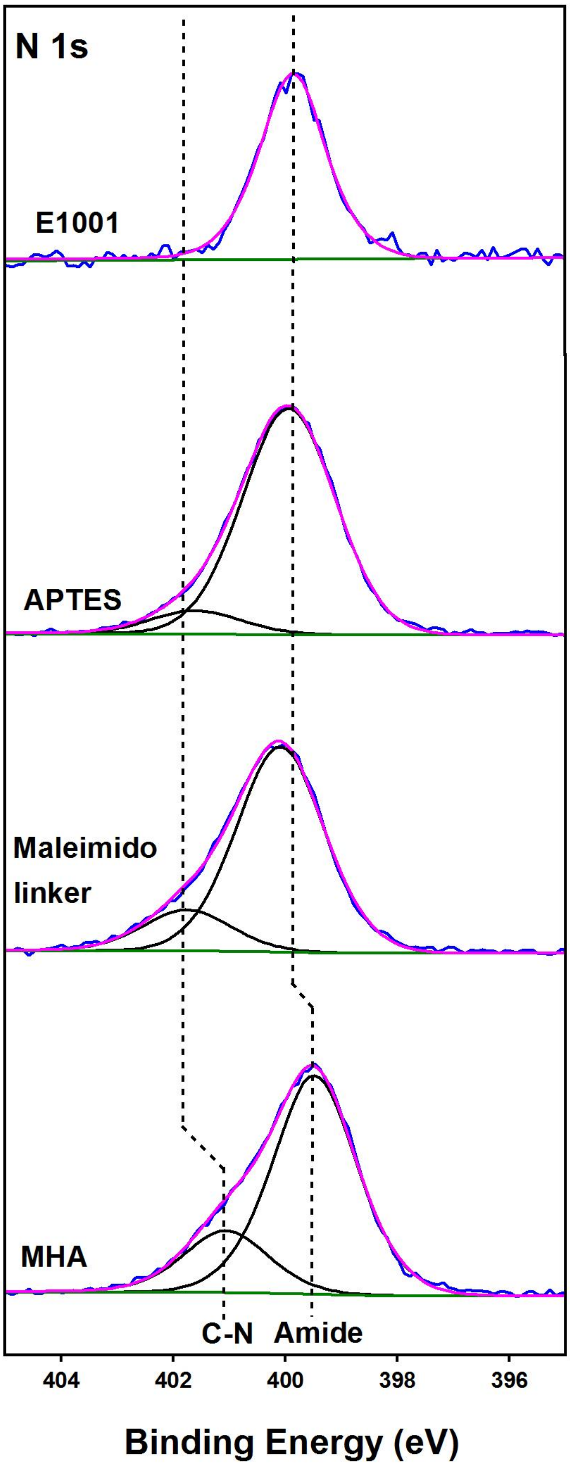

Figure 4.19 Fitted N 1s XPS spectra of each layer of bottom-up surface modification, *i.e.,* E1001 raw surface thin film, APTES silanised surface, maleimido crosslinked surface and finally MHA clicked surface.

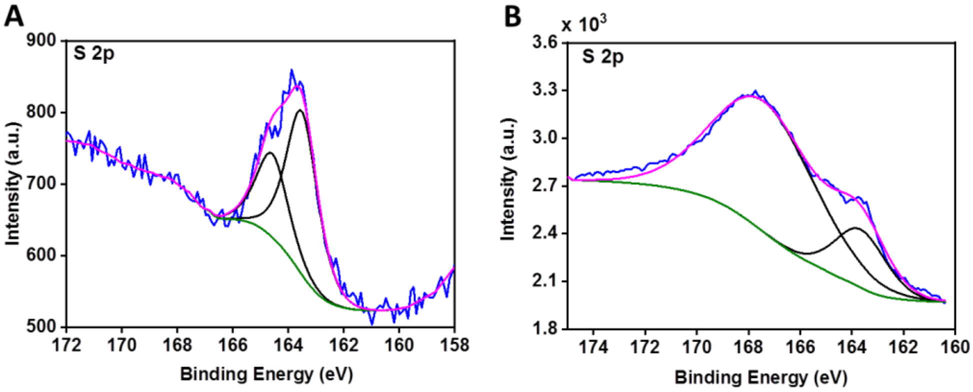

Figure 4.20 Fitted S 2p XPS spectra of final layer of modified material, *i.e.,* MHA, on (A) E1001(1k) substrate base and (B) siloxane substrate base as control.

In the O 1s envelope of all samples, a fitted peak at 532.3 eV was detected for Si-O, suggesting that on E1001(1k) surface x-ray beams penetrated through to glass substrate.[189] On chemically modified surfaces, either the anchor Si-O groups of APTES or a combination with the glass substrate was detected. In addition, a peak at 530.0 eV was detected in the O 1s envelope of E1001(1k), APTES and MHA layers indicating O-H groups. The presence of these peaks in the spectrum of E1001(1k) could be contributed to the fact that samples were tested after oxygen plasma treatment that generated hydroxyl groups on the surface thus detection of O-H groups on XPS. Conversely, the presence of such peak on the APTES surface might be an indication of APTES anchor molecules not undergoing complete reaction and had crosslinked due to surface moisture. Another possibility is that plasma activated hydroxyl groups did not completely crosslink with APTES. A peak at 534.0 eV was present in the spectra of surfaces presenting maleimido linker, indicating the presence of maleimide C=O groups.

In the N 1s envelope of all samples, a peak in region of 399.0 eV indicated the presence of amide linkages. In addition, a peak in region of 401.0 eV was found in the spectra of APTES,[190] malemide and MHA surfaces indicating presence of amine which might indicate that the reaction of maleimide crosslinking was incomplete.

In addition, only S 2p envelopes of MHA coated E1001(1k) and siloxane surfaces exhibited presence of peaks.

The surfaces of E1001(1k) modified with MHA were then examined to assess qualitative hydrolysis degradation capability using SEM (Figure 4.21).

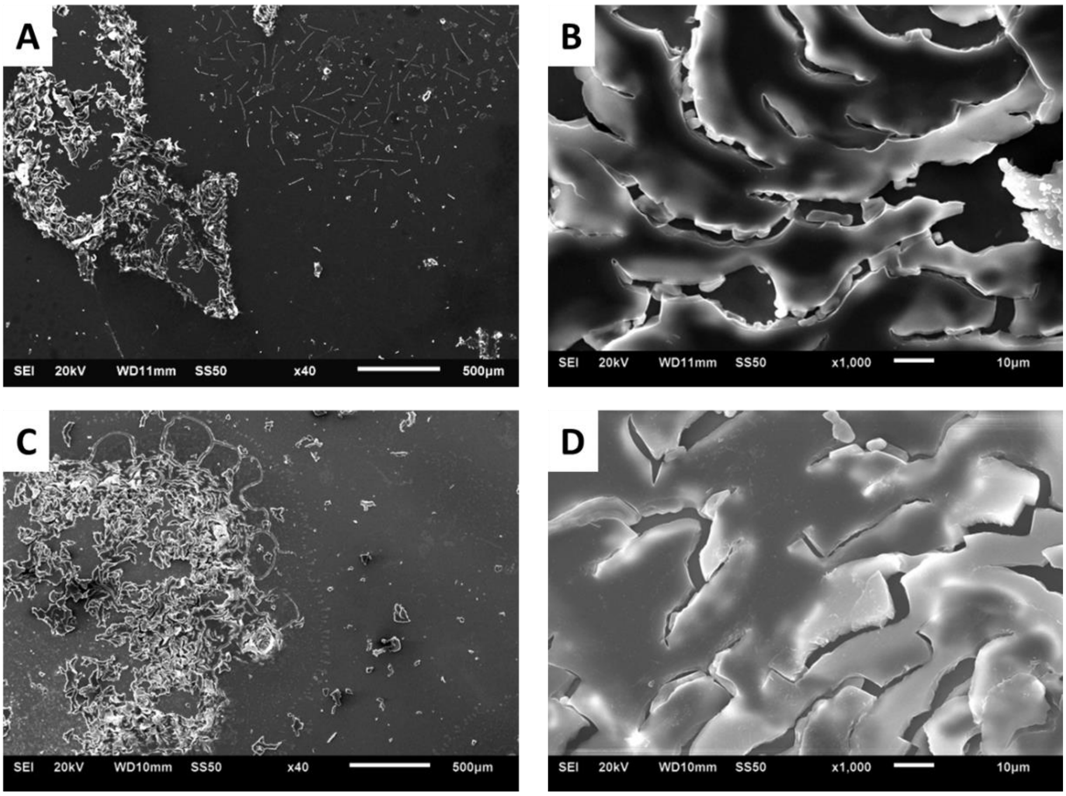

Figure 4.21 Representative SEM images of E1001(1k) modified with MHA to assess qualitative hydrolysis degradation after (A) and (B) 2 weeks, (C) and (D) 7 weeks.

The short term degradation study had indicated that the modified polymer thin films retained their ability to degrade in a hydrolysed state. The synthesised material surfaces were then assessed for cytotoxicity using a Quant-iT™ picogreen® dsDNA assay (Figure 4.22) and alamarBlue cell health indicator (Figure 4.23).

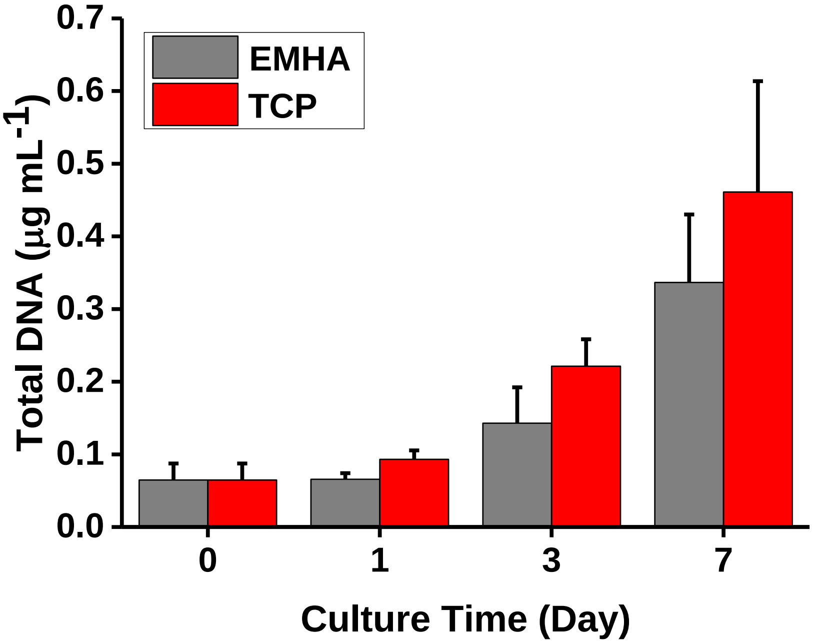

Figure 4.22 Quant-iT™ picogreen® dsDNA assay of human dermal fibroblasts cultured on MHA-coated E1001(1k) surface (EMHA) and tissue culture polystyrene (TCP) for 0, 1, 3 and 7 days. Error bars represent standard deviation. n=5

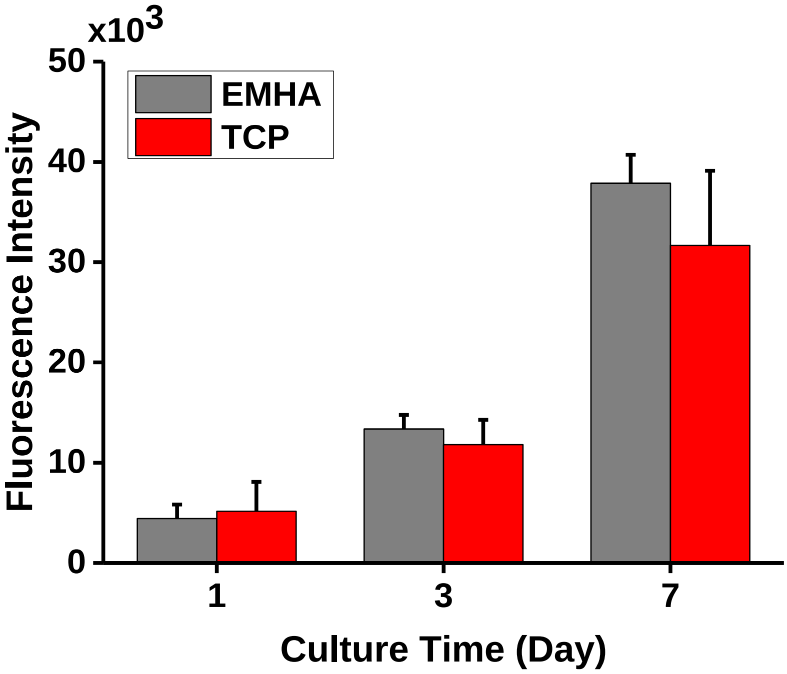

Figure 4.23 AlamarBlue assay of human dermal fibroblasts cultured on MHA-coated E1001(1k) surface (EMHA) and tissue culture polystyrene (TCP) for 1, 3 and 7 days. Error bars represent standard deviation. n=5

HDFs were cultured on the material surfaces for 1, 3 and 7 days. A time point 0 was collected for the Quant-iT™ picogreen® dsDNA assay. Quant-iT™ picogreen® dsDNA assay results demonstrated that the cell proliferation rate on the materials were not significantly different from the control TCP samples. In addition, cell metabolism was tested using an alamarBlue cell health indicator and results indicated that there was no significant difference in cell metabolism between the candidate material and TCP, as control samples.

Thus short term cytotoxicity studies suggest MHA-modification of E1001(1k) did not affect cell proliferation or metabolism for up to 7 days.

4.5 Conclusions

In summary, the aim of this chapter was to successfully introduce a novel fabrication methodology for biodegradable surfaces with nanofeatures that have been shown to induce various mesenchymal stem cells differentiation pathways using PPL techniques. A number of reaction schemes have been developed, including bromo-thiol click, amide bond formation and thiol-Michael click. Among these methods, it was found that nanofeatures of alkylsilane molecules were difficult to control during PPL fabrication due to their moisture sensitive nature that was against the principle of the PPL ink transport mechanism.

In contrast, the thiol-Michael click approach provided the best potential for PPL for creating defined nanofeatured surfaces of materials, since thiolated “ink” has been well optimised to use in PPL techniques. The mechanism of the thiol-Michael click reaction allowed easy access for thiol groups to attack the C=C on surfaces presenting maleimide. In addition, the reaction scheme was optimised on biodegradable polymer thin films, proving to be non-cytotoxic whilst retaining the capability of hydrolytic degradation.

The biodegradable polymer thin film E1001(1k) has been preliminarily examined with the thiol-Michael click mechanism and is has been successfully confirmed that the materials retained their capability to undergo hydrolysis degradation following layers of bottom-up synthesis. It has also been established that synthesised materials are potentially non-cytotoxic.

This characterised surface modification mechanism can be utilised for PPL patterning of well-defined nanofeatured arrays for the future targeted induction of mesenchymal stem cell differentiation pathways and, ultimately, in applications for regenerative medicine. The characterised surface modification pathway could overcome previously reported challenges use of silane molecules as “ink” in nanolithography techniques.[122, 128, 134]

Chapter 5

Photoresponsive Hydrogels for Potential use as Nanolithography "Ink"

5.1 Introduction

For many decades, *in vitro* cell biology was performed primarily on stiff substrates, such as glass and polycarbonate, generally coated with extracellular matrix proteins to enable cell adhesion and migration. However, it is now well accepted that by using "soft" materials that can be fabricated with a range stiffnesses, it is possible to investigate and manipulate cell behaviour in an environment that more closely simulates the mechanical properties of human tissues.[191]

The development of such materials with a range of defined flexibility is of particular interest in efforts to understand cellular mechanotransduction[192] and the development of tools for tissue repair and regeneration[193-195]. For example, it has been shown that culturing embryonic, adipose and mesenchymal stem cells on materials across a range of stiffnesses can alter their proliferation and differentiation responses.[196, 197] In this respect, hydrogels based on polyacrylamide (PA) have been widely used due to their lack of cytotoxicity and the fact that their mechanical properties, *e.g.,* stiffness or porosity, can be systematically varied by altering their formulation.[192, 198-200]

One limitation in these original experiments is that the physical properties of these hydrogels are essentially fixed. In order to conduct studies into the dynamic nature of cell behaviour, there is now demand for systems whose properties can be altered *in situ* by external stimuli. For this purpose, a number of PA hydrogels that incorporate photocleavable 2-nitrobenzyl-derived crosslinkers have been reported.[201, 202] Irradiation with near-UV light (typically ~ 365 nm) results in cleavage of these linkers and a softening of the gel, with subsequent alteration in cell behaviour. However, the change in the physical properties of these types of gel is unidirectional thus limited in their experimental scope.

5.1.1 Azobenzene-based photoresponsive hydrogels

Azobenzene is a photo-responsive molecule that undergoes *cis-trans* isomerisation upon exposure to UV light which results in transfer from the planar trans-azobenzene to *cis*-azobenzene. The trans to cis isomerization is normally induced with by 350 nm light, leading to a π-π* transition which results in a tilt of the angle between the two phenyl rings by 55 ˚. The isomerisation also accompanies an increase of dipole moment from 0.5 D to approximately 3.1 D and a decrease of distance from 9 Å to approximately 5.5 Å.[203-205] The reverse, *cis* to *trans* isomerisation, can be achieved by irradiation with 450 nm visible light or thermally, resulting in n-π* transition (Scheme 5.1). The isomerisation of *trans* to *cis* is normally fast but photoisomerisation of *cis* to *trans* can only achieve up to 95% of the *trans* isomer. In contrast to photoisomerisation, gradual thermal-isomerisation can quantitatively yield up to 100 % of the *trans* isomer.[206-208]

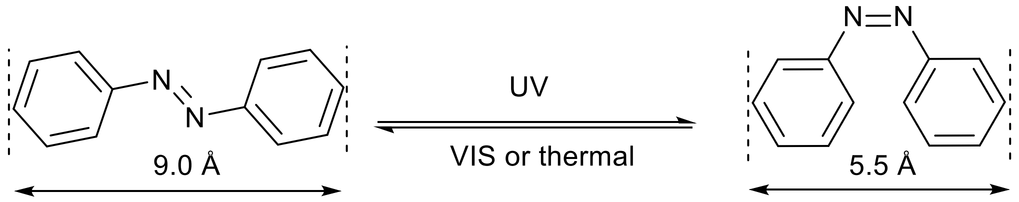

Scheme 5.1 Schematic illustration of isomerisation of the azobenzene molecule upon light irradiation.

Azobenzene-based hydrogels have been utilised in various applications.[209-211] For example, azobenzene-based monomer have been incorporated into hydrogel networks for drug release following UV irradiation (Scheme 5.2).[209]

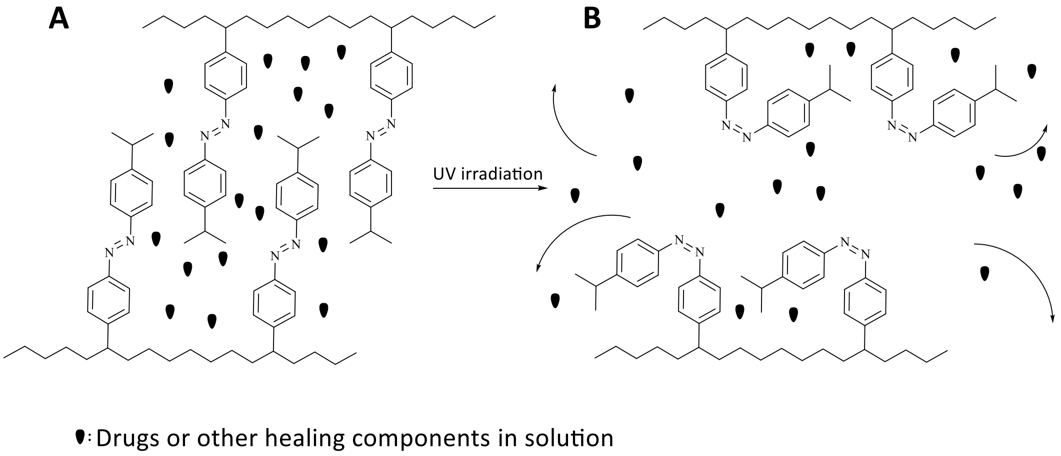

Scheme 5.2 A schematic diagram illustrating drug delivery utilising the photo-responsiveness of azobenzene molecules. (A) Drugs are stored in pores in the *trans*-azobenzene functional hydrogel network. (B) Irradiation leads to *cis*-azobenzene isomerisation. *Trans* to *cis* azobenzene isomerisation allows the release of entrapped healing components *in situ*.

The advantage of photoresponsive molecules is that they allow *in situ* structural alteration of the hydrogel network. There is currently an example of azobenzene-containing hydrogels incorporating poly(ethylene glycol)-peptide polymer matrix for cell culture applications.[212] The dynamic change (*i.e.,* stiffness) of the hydrogel was characterised following photoirradiation. However, it exhibited a relatively small dynamic range upon switching (< 1 kPa), and maintaining the softer (*cis* isomer) state for a short time (~ 10 h), which limits its usefulness in the context of cell biology.

5.2 Aims and objectives

There are several stimuli that could affect cell response to the micro-environment. In previous chapters, it was established that mesenchymal stem cells (MSCs) respond to chemical stimuli at the sub-micron scale. In this chapter, a series of polyacrylamide-based photoresponsive hydrogels were synthesised and characterised as model surface for the investigation of the effects of stiffness on *in situ* MSC response to the sub-micron scale. Proposed azobenzene-based crosslinkers were incorporated within the hydrogel network. Various formulations were first fabricated as bulk surfaces to allow characterisation. MSCs were cultured in contact with the hydrogel surface for preliminary examinations of morphology and cytotoxicity. It was aimed that the most appropriate hydrogel formulation would then be fabricated as nanoarrays to investigate the effects of MSCs to purely mechano-signalling events. Using previously described PPL techniques, arrays of characterised hydrogel could be fabricated to investigate the effects of stiffness on MSC response *in situ* at sub-micron scale. Ultimately, the aim was to combine the findings from previous chapters, to fabricate an array of materials using PPL techniques that combined controlled stiffness, chemistry and topography at sub-micron scale to generate new understanding of fundamental knowledge.

5.3 Experimental methods

5.3.1 Materials and instrumentation

All chemicals were purchased from either SigmaAldrich or Thermo Fisher Scientific (Waltham, MA, USA) and used without further purification unless otherwise stated. Antibodies were purchased from Abcam (Cambridge, UK) or Thermo Fisher Scientific (Waltham, MA, USA) and Alexa Fluor® 488-phalloidin from Cell Signalling Technology (Danvers, MA, USA). For cell culture experiments and tests of mechanical properties, the hydrogels were cast in glass-bottomed dishes (uncoated, γ-irradiated, MatTek Corp, MA, USA). Irradiation experiments were performed with light emitting diodes (LEDs) emitting at a λ_{max} of 365 nm (part no: M365L2) or 490 nm (M490L4), both powered by a DC4100 LED driver. All were supplied by ThorLabs (Newton, NJ, USA). Photon flux was measured by ferrioxalate actinometry using a 3 mL cuvette positioned 1.3 cm from the LED, the 365 and 490 nm LEDs measuring 32.5 and 11.9 mW cm^{-2}, respectively. Epifluorescence microscopy was performed using an Axioplan 2 microscope (Zeiss, Jena, Germany), with appropriately stained cells on cover slips mounted using Fluorescence mounting medium (Agilent, Santa Clara, CA, USA).

Environmental scanning electron microscopy (ESEM) images of the surface of hydrogels were captured in a hydrated state using a Quanta 650 FEG ESEM (FEI, USA) in variable pressure mode at 1.3 mBar using water vapour as make up gas. The instrument was operated at an accelerating voltage of 10 kV. Secondary electron (SE) images were collected using a large field detector (LFD).

5.3.2 Synthesis of crosslinkers

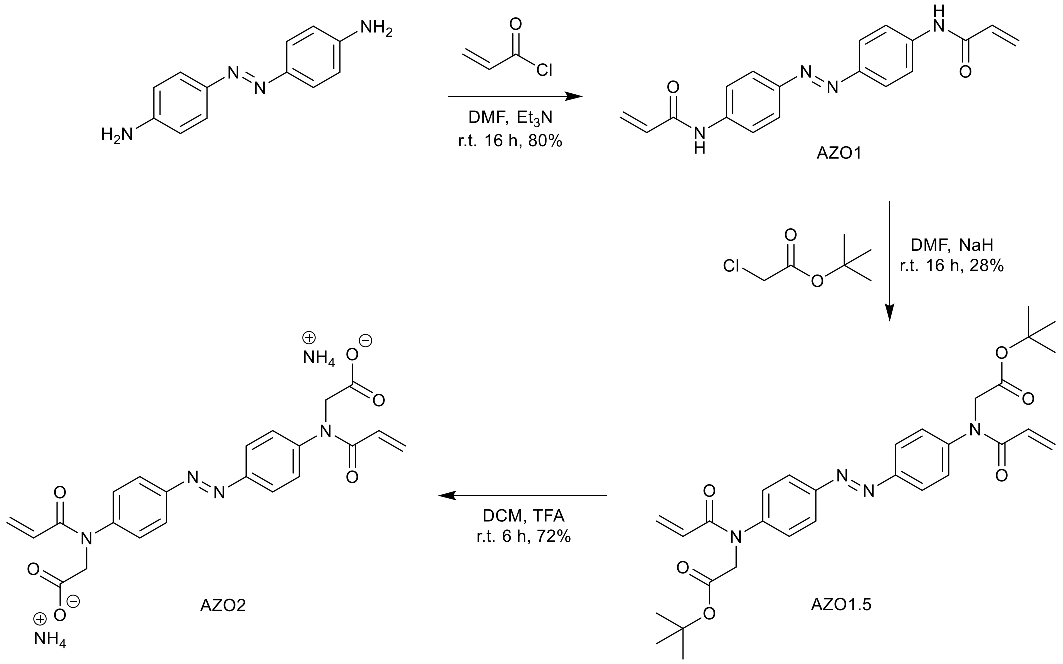

5.3.2.1 4,4’-di(acrylamido)azobenzene (AZO1)

4,4’-azoaniline (265 mg, 1.25mmol) was dissolved in dimethylformamide (DMF, 20 mL) and triethylamine (540 µL, 3.875 mmol) was added, followed by acryloyl chloride (305 µL, 3.75 mmol) in a dropwise manner. The reaction was stirred for 16 h at room temperature, after which the reaction was observed to be complete by thin-layer chromatography. The solution was poured into 600 mL water and the mixture adjusted to pH 4 by dropwise addition of concentrated aq. HCl. The precipitated orange solids were collected by filtration, washed once each with saturated $NaHCO_3$ and water, then lyophilized to yield the desired product as an orange powder (83.2%, 387.6 mg). R_f 0.38 (EtOAc); λmax/nm (THF) 377 (ε/dm^3 mol^{-1} cm^{-1} 33200); ν_{max}/cm^{-1} (Solid) 3310, 3067, 1670, 1248, 843; δH

(400 MHz; DMSO-d6) 5.81 (2H, C(1)H, d, J=10.1 Hz), 6.31 (2H, C(1)H, d, J=16.9 Hz) 6.49 (2H, C(2)H, dd, J=10.1, 16.9 Hz), 7.88 (8H, C(4,5)H, m) and 10.6 (2H, NH, s); δC (101 MHz, DMSO-d6) δ 119.41 (C(4)H), 123.56 (C(5)H), 127.74 (C(1)H2), 131.59 (C(2)H), 141.96 (C(6)), 147.82 (C(7)) and 163.48 (C(3)); m/z (ES+) 343 (100%, [M+Na]+); HRMS calculated for $C_{18}H_{16}N_4O_2$: 321.1535, found: 321.1352 ([M+H]+), δ 2.3 ppm.

5.3.2.2 Synthesis of di-tert-butyl 2,2'-((diazene-1,2-diylbis(4,1-phenylene)) bis(acryloylazanediyl))(E)-diacetate (AZO1.5)

AZO1 (300 mg, 0.91 mmol), was dissolved in 20 mL of anhydrous DMF and sodium hydride (NaH, 53.5 mg, 2.18 mmol) was added, followed by *tert*-butyl chloroacetate (312 µL, 2.18 mmol). The reaction was stirred for 16 h at room temperature, after which the reaction was observed to be complete by thin-layer chromatography. The reaction mixture was extracted by liquid-liquid extraction, the organic phase was collected and purified by column chromatography to yield the desired dense orange solid (28 %, 139.70 mg). ν_{max}/cm^{-1} (oil) 1660, 1741, 2929, 2978; δ_H (400 MHz, $CDCl_3$) 1.49 (s, 9 H) 4.42 (s, 2 H) 5.64 (dt, *J*=10.23, 1.90 Hz, 1 H) 6.19 (dd, *J*=16.74, 10.29 Hz, 1 H) 6.46 (dd, *J*=16.80, 1.77 Hz, 1 H) 7.47 (d, *J*=8.59 Hz, 2 H) 7.97 (d, *J*=8.59 Hz, 2 H); δ_C (101 MHz, $CDCl_3$) 28.06, 52.11, 82.14, 124.01, 127.87, 128.59, 128.87, 144.83, 151.37, 165.61, 167.86; m/z (ES+) 571 (100%, $[M+Na]^+$); HRMS calculated for $C_{30}H_{36}N_4O_6Na$ 571.2527 found: 571.2501, δ=-4.56 ppm.

5.3.2.3 Synthesis of (E)-2,2'-((diazene-1,2-diylbis(4,1-phenylene)) bis(acryloylazanediyl))diacetate (AZO2)

AZO1.5 (119 mg, 0.217 mmol) was dissolved in TFA (2 mL), DCM (2 mL) and water (0.04 mL) and stirred for 6 h at room temperature. The solvent was removed to give a red oil. This was purified by dissolving the compound in 0.1% $ammonia_{(aq)}$ and washing with hexane. The aqueous layer was freeze dried to yield an orange solid (68 mg, 72 %). δ_H (400 MHz, D_2O) 4.26 - 4.31 (m, 4 H) 5.60 -

5.70 (m, 2 H) 6.17 - 6.27 (m, 4 H) 7.44 (d, *J*=8.46 Hz, 4 H) 7.82 (d, *J*=8.46 Hz, 4 H); IR (cm^{-1}) 1644, 3035; MS (ES) m/z 435.2 $[M-2NH_4+H]^-$, 437.3 $[M-2NH_4+3H]^+$; HRMS (ES) m/z calculated for $C_{22}H_{19}N_4O_6$ 435.1310 found: 435.1312, δ=0.44 ppm.

5.3.3 Formation of Hydrogel

The prepolymer mixtures for initial screening were formulated according to the compositions specified in a previously published paper.[213] In general, AZO was dissolved in dimethylsulfoxide (DMSO), DMF or EtOH. Separately, aqueous solutions of acrylamide (AM, 40 % w/v) and *N,N'*-methylenebisacrylamide (BIS, 0.1 M) were mixed with Dulbecco's phosphate buffered saline (DPBS). The solutions of AZO and AM/BIS were then mixed with ammonium persulfate (APS, 10 % w/v in water, 10 µL) and *N,N,N′,N′*-tetramethylethylenediamine (TEMED, 1 µL). These mixtures were allowed to polymerise in Eppendorf tubes for 30 min prior to analysis. Polymer formulations that were subsequently tested for cell culture, mechanical and photochemical characterization, were cast on glass-bottomed dishes and coated with fibronectin. The glass surfaces of the dishes were surface treated with aq. NaOH (700 µL, 1 M) for 5 min, followed by washing three times with deionised water and then drying with a stream of N_2.

3-Aminopropyltriethoxysilane (700 µL) was then pipetted onto the glass, left to stand for 5 min and washed three times with water and dried as above. Glutaraldehyde (0.5 % v/v in water, 700 µL) was added, incubated for 30 min and the glass was then washed and dried as above. Separately, glass coverslips were prepared by drop coating with a rat fibronectin (FN) solution (120 µL, 0.05 mg mL^{-1} in DPBS), which was allowed to stand for 1 hour before drying under a stream of N_2. Thirty µL of the desired prepolymer mixture was the dropped onto the silanised glass surface of a glass-bottomed dish. The FN-coated coverslip was placed on top of the droplet, taking care to ensure even spreading of the prepolymer droplet and avoidance of any trapped bubbles. The polymerisation was allowed to proceed for 30 min, after which the coverslip was carefully removed and the FN-coated hydrogels stored in the dark under PBS at 25 °C and used freshly on the day of preparation.

5.3.4 Characterisation

All experiments were repeated 3 times unless otherwise stated.

5.3.4.1 UV-Vis absorption spectroscopy and photoirradiation

UV-Vis spectra of the AZO1 crosslinker were acquired in solution at a concentration of 21 µM in tetrahydrofuran (THF) in a glass cuvette of 1 cm pathlength. To irradiate the solutions, the same solution was placed in a cuvette holder (ThorLabs CVH100) coupled directly to the appropriate LED. During irradiation, the samples were removed intermittently and UV-Vis spectra recorded, before returning the sample for additional irradiation. The proportions of the isomers in the photostationary state (PSS) was calculated using a similar method similar to that previously reported.[214] Under 365 nm irradiation (*trans* to *cis*), the following formula was used:

$$f_{365} = \frac{A_E - A_{PSS365}}{A_E - A_Z}$$

where f_{365} is the fraction of the AZO population that is in the *cis* state at the PSS under 365 nm irradiation; A_E is the absorbance at the λ_{max} (in this case 380 nm) of the AZO solution before irradiation, which is assumed to be 100 % *trans* isomer; A_{PSS365} is the absorbance at 380 nm at the PSS under 365 nm irradiation (for this calculation, the absorbance after 100 s. irradiation was used); A_Z is the theoretical absorbance at 380 nm of the AZO solution at 100% *cis* isomer, which for this calculation was taken to be zero (*i.e.*, absorbance after subtraction of the solvent baseline). For the spectral measurements at 490 nm (*cis* to *trans*), the AZO solution was irradiated continuously for 30 min with 365 nm light, then irradiated at 490 nm for various time intervals with periodic UV-vis data collection. The f_{490} was calculated using:

$$f_{490} = 1 - \frac{A_E - A_{PSS490}}{A_E - A_Z}$$

where f_{490} is the fraction of the AZO population that is in the *cis* state at the PSS under 490 nm irradiation; A_E is the absorbance at the λ_{max} (in this case 380 nm) of the AZO solution before irradiation at 365 nm, which is assumed to be 100 % trans isomer; A_{PSS490} is the absorbance at 380 nm at the PSS under 490 nm irradiation (for this calculation, the value after 100 s irradiation at 490 nm was used); A_Z is the theoretical absorbance at 380 nm of the AZO solution for 100 % *cis* isomer, which for this calculation was taken to be zero (*i.e.,* absorbance after subtraction of the solvent baseline). For the irradiation of the hydrogels, the petri dish containing the hydrogel was placed on a Peltier cooler set to 25 °C, and PBS was added sufficient to keep the gel hydrated (approximately 200 µL). The LED was placed 1 cm above the gel. At the appropriate time intervals, the petri dishes were removed, any excess DPBS drained, the dish with the gel in place was placed in a UV-vis spectrometer and its spectra recorded. The dish and gel were then returned to the Peltier cooler, DPBS added and irradiation restarted until the next time interval, when the process was repeated.

5.3.4.2 Atomic force microscopy (AFM) of hydrogels

Stiffness of the hydrogels was quantified by AFM using a JPK CellHesion AFM with tipless cantilevers (Bruker NP-O10) attached to 10 µm diameter stiff polystyrene beads (Kisker Biotech PPS-10.0) using Loctite 3103 UV curing glue. The gels were immersed in DPBS during measurements, which were conducted on randomly selected 30 µm x 30 µm regions of each hydrogel. Measurements were performed in replicate at each point of an array of 4 x 4 in each region. Force curve data was fitted using the Hertz-model.[215]

5.3.4.3 Environmental scanning electron microscopy (ESEM) of hydrogels

Hydrogels were prepared and stored in DPBS at room temperature. Prior to imaging, hydrogels were photoirradiated as per experimental design and stored in DPBS. Each dish with attached gel was then fixed to a sample stud. Images of the hydrogel surfaces were then captured in a hydrated state using a Quanta 650 FEG ESEM (FEI, USA) in variable pressure mode at 1.3 mBar using water vapour as the make-up gas.

5.4 Results and discussion

All results have been published in a peer-reviewed journal.[213] A copy of the published paper is provided in the appendix.

5.4.1 Preparation of AZO1 crosslinker and formulation of AZO-PA hydrogels

5.4.1.1 Preparation of AZO1 crosslinker

To prepare the 4,4’-di(acrylamido)azobenzene (AZO1) crosslinker, 4,4’-azoaniline was substituted with acryloyl chloride. The di-vinyl structure of AZO1 allows it to partially or fully substitute with the commonly used crosslinker, N,N’-methylenebisacrylamide (BIS), in commercial PA hydrogels.

The AZO1 crosslinker was dissolved in THF and its photoisomerisation properties recorded using a UV-Vis spectroscopy (Figure 5.1).

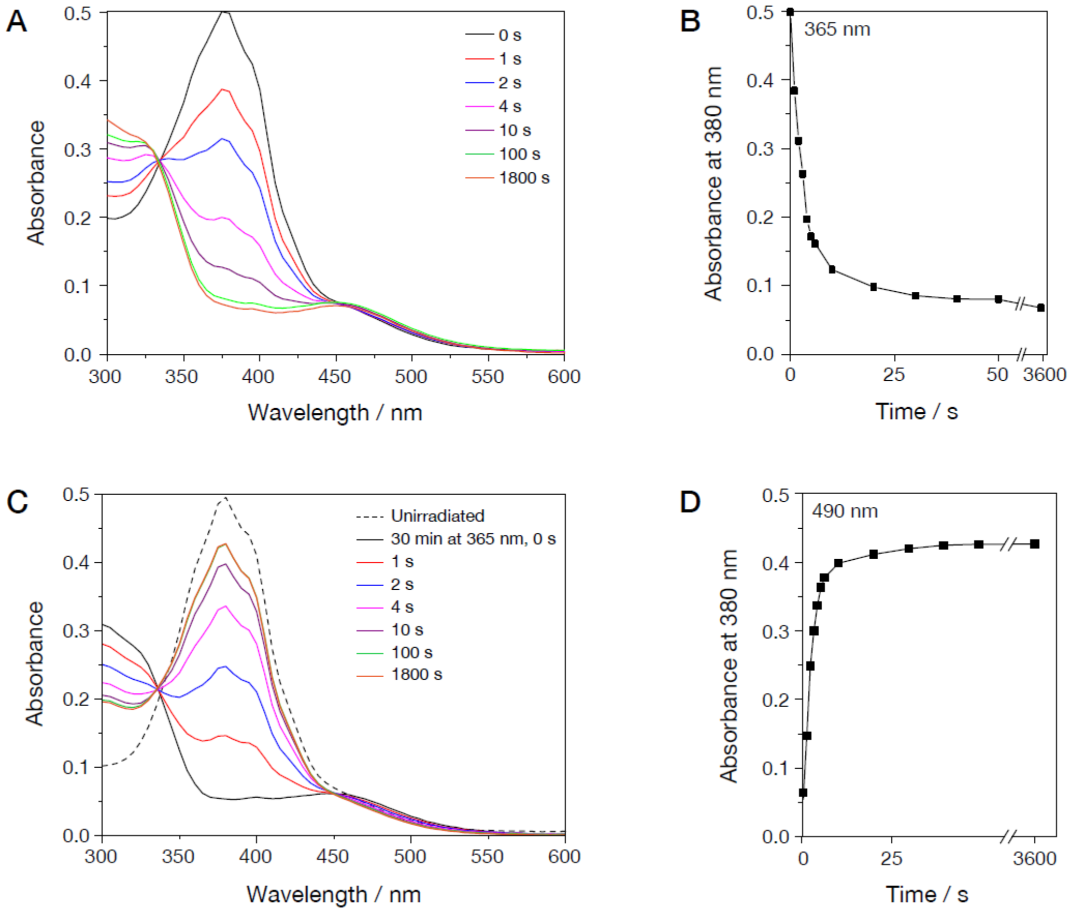

Figure 5.1 UV–vis absorbance spectra of AZO1 in THF solution. (A) Representative sequential absorbance spectra after exposure to 365 nm irradiation for various durations. (B) Plot of absorbance at the AZO1 λ_{max} (380 nm) against duration of 365 nm irradiation. (C) Representative sequential absorbance spectra after exposure to 365 nm irradiation for 30 min, followed by 490 nm for varying durations. (D) A plot of absorbance at the AZO1 λ_{max} (380 nm) against duration of 490 nm irradiation, demonstrating degree of reversibility of photoisomerisation.[213]

AZO1 was found to photoisomerise (*trans* to *cis*) in solution upon irradiation at 365 nm, reaching a PSS consisting of 90% *cis* isomer within 30 s (Panel A and B, Figure 5.1). Further irradiation resulted in no significant change. The isomerisation was then reversed (*cis* to *trans*) upon 60 s of photoirradiation at 490 nm to reach a PSS of 86.2% *trans* isomer, with no significant change after 100 s of irradiation (Panel C and D, Figure 5.1).

5.4.1.2 Formulation of AZO1-PA hydrogel

After the photoreversibility of AZO1 was ascertained, the crosslinker was used to substitute or replace BIS in the fabrication of AZO1-PA hydrogel. Initially a range of pre-polymer formulations was tested that comprised varying quantities of acrylamide, BIS and AZO then screened for the presence of a stable, clear and homogeneous hydrogel upon polymerisation (Appendix 10). Initial strategy was aimed to use variable water miscible solvents, *i.e.,* DMSO, DMF and EtOH, to fully dissolve AZO1 and enable formation of a homogenous hydrogel while maximising the quantity of AZO1 incorporation. An attempt to minimise the quantity of solvent required was then conducted. The inclusion of BIS was initially investigated as a means to generate stable hydrogels. Finally, the selected formulations were tested with the aim of maximising the amount of AZO1 incorporated. Of those formulations that met the criteria for being stable and homogeneous with the least solvent incorporated, selected formulations were taken for further mechanical testing (Appendix 11). Amongst the four candidates, AZO1 was selected for further testing of its mechanical and photophysical properties.

5.4.2 Characterisation of AZO1-PA hydrogels

5.4.2.1 Mechanical properties of AZO1-PA hydrogel

AZO1-PA hydrogel was photoirradiated at 365 nm for 3 h followed by storage in the dark at 37 °C for 2 weeks to allow for gradual thermal reversion (Figure 5.2).

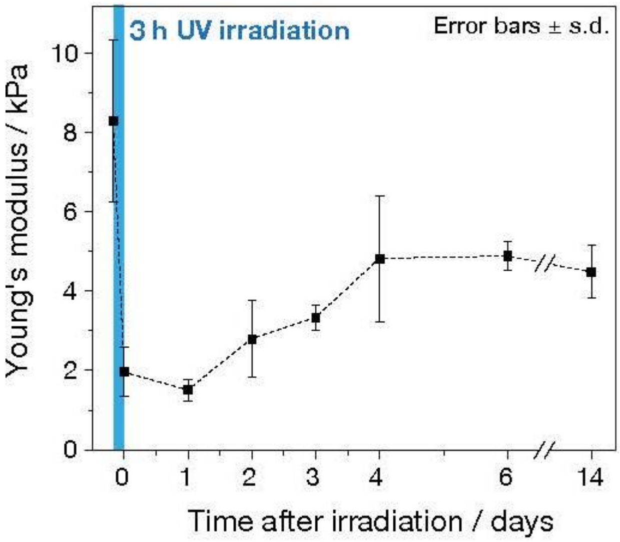

Figure 5.2 Graph of Young's modulus against time for the AZO1-PA hydrogel. The hydrogel was photoirradiated at 365 nm for 3 h then stored in the dark for up to 14 days.

The stiffness of the sample was measured at various intervals throughout, finding that the stiffness of the hydrogel only recovered to 4.5 ± 0.7 kPa after 2 weeks, with little apparent change in stiffness after 6 days. To test whether a relatively long exposure to UV may have resulted in degradation of the AZO linkers and the loss of full reversibility, a thermal reversibility experiment was then performed (Figure 5.3).

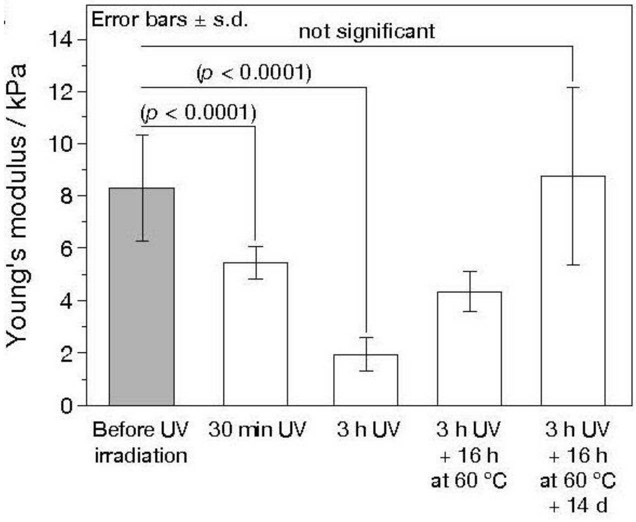

Figure 5.3 Graph of Young's modulus against time after up to 3 h of photoirradiation at 365 nm for the AZO1-PA hydrogel and following prolonged storage after heat isomerisation. *p* values calculated from Kruskal-Wallis tests by Dr. Joe Swift.

AZO1-PA was irradiated for 3 h, thermally reversed by heating to 60 °C for 16 h, then stored in the dark under ambient condition for 2 weeks. Thermal reversibility was ascertained by measuring Young's modulus approximately 15 min after 16 h of heating to allow the hydrogel to cool to room temperature prior to mechanical testing using AFM. An immediate increase in stiffness at 4.3 ± 0.8 kPa was observed after heat treatment. The hydrogel was then stored in DPBS for up to 2 weeks and full reversal of stiffness was observed, at 9.0 ± 3.0 kPa at the end of the storage period. These observations indicate that the stiffness of the hydrogel was fully reversible, but extremely slowly. This low rate of background reversibility therefore enabled a longer term set of experiments, for days to weeks, such that it would be suitable material for general cell culture applications.

5.4.2.2 Photoisomerisation of AZO1-PA hydrogel

The photophysical properties of the AZO1-PA hydrogel were then examined by photoirradiation (Figure 5.4).

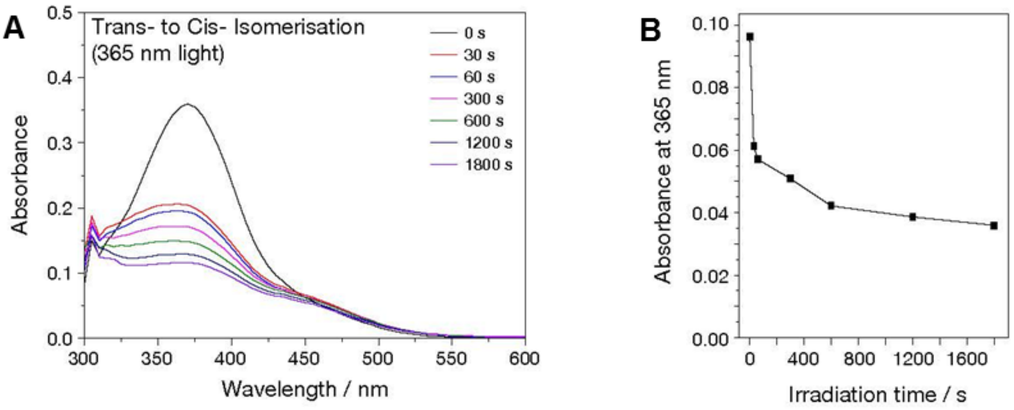

Figure 5.4 UV–vis absorbance spectra of AZO1-PA hydrogel. (A) UV-vis spectra of the hydrogel after exposure to light at 365 nm for varying durations and (B) graph of UV-vis absorbance at 365 nm against time.

Notably, the photophysical analysis of the AZO1-PA hydrogels by UV-visible spectroscopy demonstrated that the *trans*-azobenzene group had reached the PSS within approximately 30 min of irradiation with 365 nm light (Panel A and B, Figure 5.4). This difference in rapid isomerisation of the crosslinker relative to the change in macroscopic stiffness is thought to be due to a requirement for the remodelling of the polymer matrix, which is hypothesised to be much slower than the rate of photoisomerisation in molecular scope. This delayed change in physical properties was found consistent with reports of other hydrogel materials incorporating azobenzene switches.[216]

Since only 30 min of irradiation was sufficient to reach the PSS yet approximately 3 h was needed to reach minimum stiffness, a range of shorter irradiation times were investigated followed by a rest period prior to stiffness measurements (Figure 5.5).

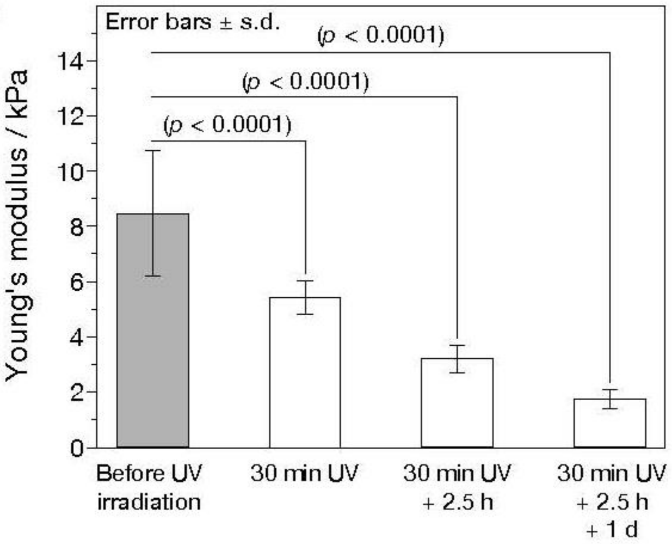

Figure 5.5 Graph of Young's modulus of the AZO1-PA hydrogel after 30 min irradiation at 365 nm, followed by various rest periods. Error bars represent standard deviation. *p* values calculated from Kruskal−Wallis tests and provided by Dr. Joe Swift.

It was found that irradiation for 30 min followed by incubation of the material in the dark for 2.5 h under ambient conditions resulted in a repeatable stiffness change to 2.5 ± 0.2 kPa. This optimised regimen was therefore used for subsequent experiments.

5.4.3 Light induced softening and stiffening of AZO1-PA hydrogels

As the proposed AZO1-PA hydrogel was intended to be used in cell culture applications, FN was pre-coated onto the hydrogel surfaces to provide binding sites to enable cell adhesion. In order to conduct a study of the interaction between cells and the AZO1-PA hydrogels, a two-day experimental programme was designed and mechanical properties in the absence of cells assessed as designed (Figure 5.6).

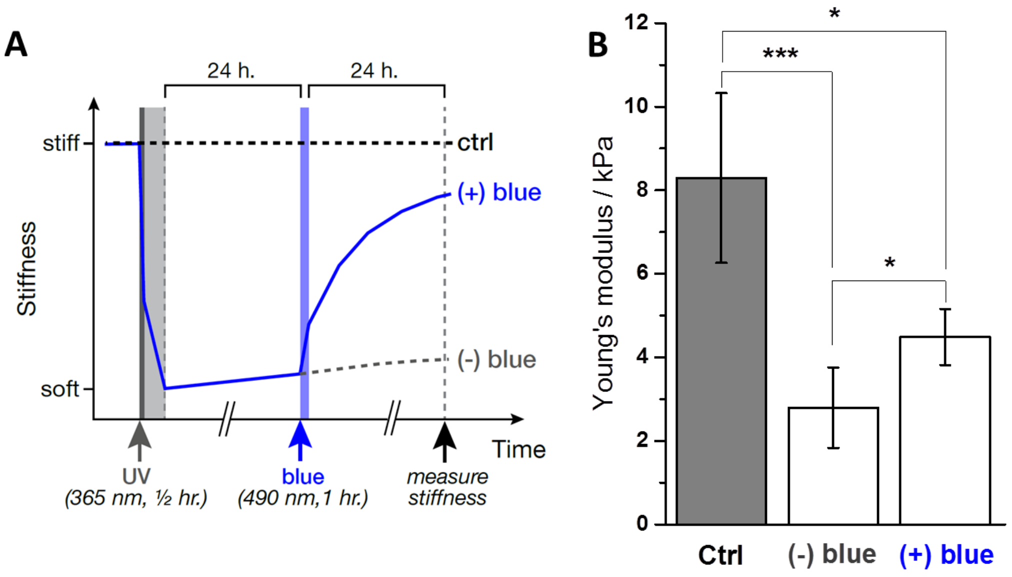

Figure 5.6 (A) Schematic overview of experimental design showing treatments to the photo-responsive hydrogels prior to mechanical characterisation. Following preparation, fibronectin-coated gels were softened by UV irradiation at 365 nm for 30 min; 24 h later "(+) blue" gels were exposed to blue light at 490 nm for 1 h, while "(-) blue" gels were unirradiated and stored in the dark. Stiffness measurements were made after a further 24 h then compared to control gels ("ctrl") that had not been exposed to UV or blue light. This schematic diagram was drawn by collaborator in the published paper, Dr. Joe Swift. (B) Graph of hydrogel stiffnesses over various irradiation treatments obtained using AFM. "*" represents $p < 0.05$, a significant difference; "*" represents $p < 0.0005$, a significant difference. Error bars represent standard deviation of the mean.**

The AZO1-PA hydrogel was designed to be photoirradiated under UV at 365 nm for 30 min, followed by a 2.5 h rest period to allow structural reorganisation (Panel A, Figure 5.6). The hydrogel was then stored in the dark for 24 h and photoirradiated with blue light at 490 nm for 1 h. It was then stored in the dark for 24 h.

Mechanical analysis using AFM demonstrated that FN pre-coated hydrogels were significantly softened by exposure to UV light as described previously, measured approximately 48 h after irradiation (sample "(-) blue" in Panel B, Figure 5.6) at 2.7 ± 0.9 kPa, compared to a control sample that was stored in the dark (sample "ctrl" in Panel B, Figure 5.6) at 8.3 ± 2.0 kPa. In contrast, exposure of the AZO1-PA hydrogels to blue light at 490 nm for 60 min after 24 h caused significant recovery of stiffness recovery after 48 h (sample "(+) blue" in Panel B, Figure 5.6), at 4.5 ± 0.7 kPa.

To test the reversibility of isomerisation, the AZO1-PA hydrogel was subjected to a five-cycle photoirradiation at each wavelength, *i.e.,* each cycle involved a 30 min photoirradiation at 365 nm followed immediately by 1 h of photoirradiation at 490 nm (Figure 5.7).

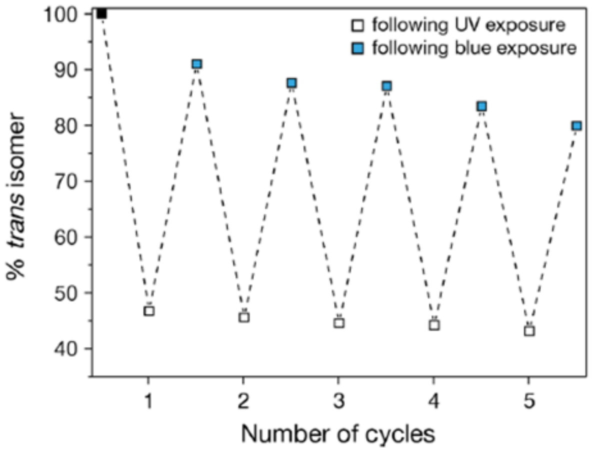

Figure 5.7 Graph of % *trans* isomer after each photoswitching cycle for AZO1-PA gel following cycles of 30 min at 365 nm after 60 min at 490 nm, demonstrating AZO1 stability upon serial photoisomerisation.

Consistent with previously presented results, a PSS of 89% *trans* isomer was achieved after the first cycle, with an approximate 2% loss for every subsequent cycle. Considering the length of exposure times, these results indicated a photostability that was sufficient for several cycles and for general cell culture experiments.

5.4.4 Effects of photoisomerisation on hydrogel surfaces

It has been previously reported that PA-based hydrogels formed with conventional crosslinkers exhibited an inverse relationship between pore size and concentrations of monomer/crosslinkers.[217] To eliminate the posibility of porosity effects on future cell applications, the photoresponsive AZO1-PA hydrogel surfaces were imaged using ESEM in a hydrated state to examine the effects of photoirradiation on surface morphologies. AZO1-PA hydrogels were treated with identical experiment timelines as the mechanical properties were measured (Figure 5.8).

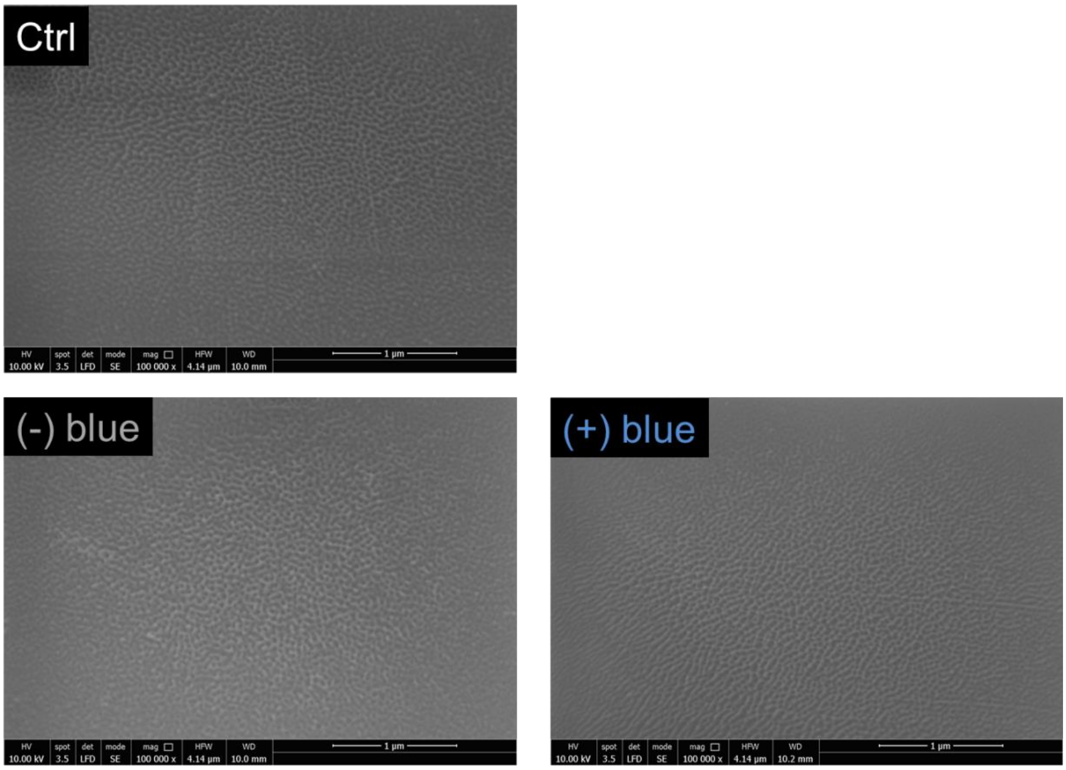

Figure 5.8 Environmental scanning electron microscopy images of photoresponsive AZO1-PA hydrogels before and after photoirradiation. The images were recorded following the treatments indicated in Panel A, Figure 5.6, at the point of stiffness measurement. Control (ctrl) sample: AZO hydrogels not subjected to irradiation. (−) blue sample: hydrogel treated with UV at 365 nm irradiation. (+) blue sample: hydrogel treated with UV at 365 nm and subsequent blue light irradiation at 490 nm.

In all cases, these images demonstrated a uniform surface with apparent pore features in the nanometre size scale. No differences in morphology were readily apparent confirming that photoirradiation did not affect AZO1-PA hydrogel surface porosity. However, the quality of the images at high magnification were not sufficiently well resolved to perform fully quantitative measurements. Several manual measurements suggest pore widths of approximately 30−50 nm in all cases, which were far below the size of biological cells.

5.4.5 Effect of photoirradiation conditions on cell viability

The effects of established dosage of light on cell viability were then considered. This study was performed using mesenchymal stem cells (MSCs) in collaboration with Dr. Oana Dorbe, Dr. Joe Swift (Wellcome Trust Centre for Cell-Matrix Research, University of Manchester), David Richards, and Dr. Stephen Richardson (Division of Cell Matrix Biology and Regenerative Medicine, School of Biological Sciences, University of Manchester). All results were conducted by Dr. Oana Dorbe or David Richards, presented by Dr. Joe Swift and have been published in a peer-reviewed journal.[213]

MSCs cultured under standard conditions were subjected to the proposed photoirradiation, and viability assessed by DNA damage staining (Figure 5.9).

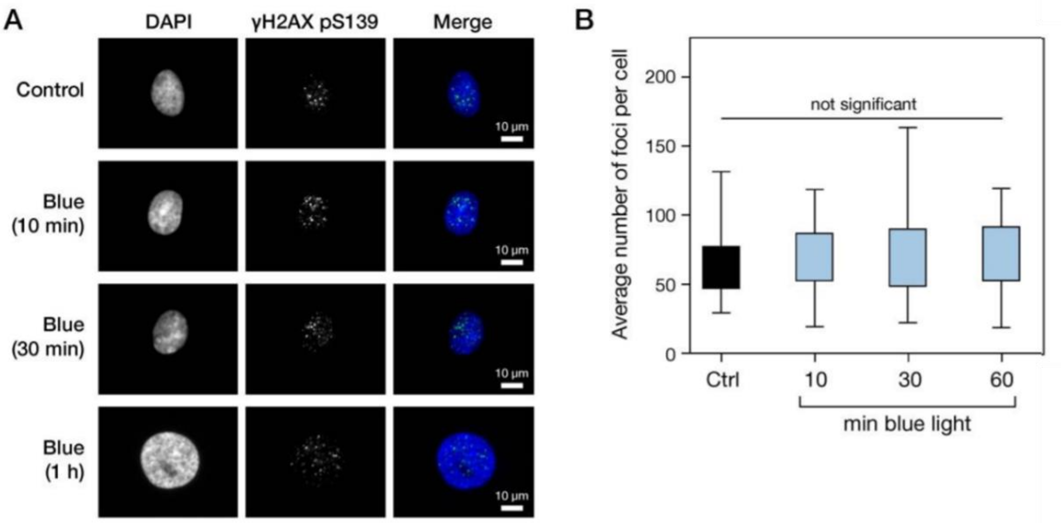

Figure 5.9 DNA damage following blue light irradiation. (A) Primary human MSCs subjected to blue light irradiation were imaged with nuclei stained with DAPI and immuno-stained against γH_{2A}X pS139 (scale bar = 10 µm). (B) Quantification of the number of γH_{2A}X pS139 foci per nucleus. Blue light exposure for up to 1 h did not significantly increase the number of foci. n > 57 measurements, cells from three donors; significance tested using a 1-way ANOVA. These results were obtained by Dr. Oana Dorbe and David Richards and presented by Dr. Joe Swift.

Exposure to light emitted from a blue LED for up to 1 h did not significantly alter DNA damage, compared to cells on control samples. UV irradiation was excluded from the call viability tests as the 2-day experiments were designed for cell seeding after UV irradiation. It was established that the designed experimental scheme was suitable for initial cell culture applications.

5.4.6 Preparation and photophysical properties of AZO2 crosslinker

Although AZO1-PA hydrogels demonstrated a superior dynamic range than the previously reported azobenzene-containing hydrogel[212], the capacity of AZO1 incorporation was limited due to its water insolubility. To improve the solubility of azobenzene-based crosslinkers within the hydrogel pre-polymer, a more water soluble version of the azobenzene-based crosslinker was prepared. Tert-butyl ester was first substituted with the hydrogen on nitrogen to form AZO1.5. The tert-butyl protecting groups were then removed to yield AZO2, as a highly water soluble salt. The photophysical properties of the AZO2 crosslinker was conducted by David Richards (Division of Cell Matrix Biology and Regenerative Medicine, School of Biological Sciences, University of Manchester, under supervision of Dr. Steven Richardson and Dr. Joe Swift) as part of a collaboration project (Figure 5.10).

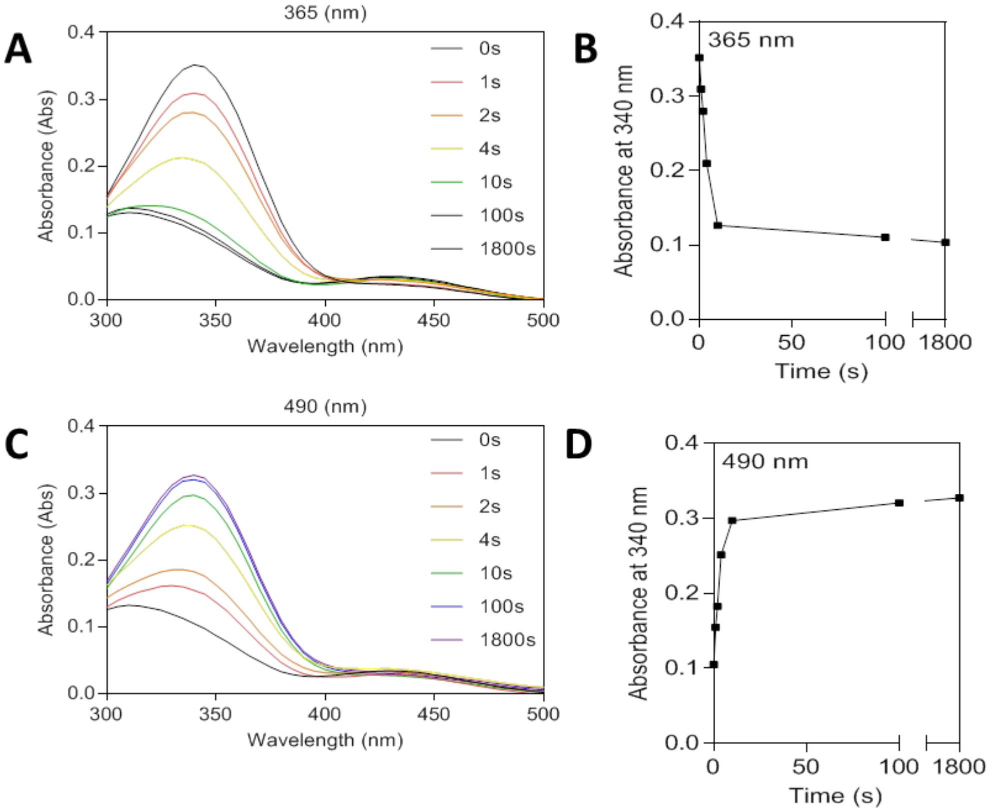

Figure 5.10 UV–vis absorbance spectra of AZO2 in aqueous solution. (A) Representative sequential absorbance spectra after exposure to 365 nm irradiation for varying durations. (B) Plot of absorbance at the AZO2 λ_{max} (340 nm) against length of time under 365 nm irradiation. (C) Representative sequential absorbance spectra after exposure to 365 nm irradiation for 30 min, followed by 490 nm for varying durations. (D) A plot of absorbance at the AZO1 λ_{max} (340 nm) against length of time under 490 nm irradiation, showing the degree of reversibility in photoisomerisation. The experiments were conducted and result graphs kindly provided by David Richards.

AZO2 was found to photoisomerise (*trans* to *cis*) in solution upon irradiation at 365 nm, reaching a PSS consisting of 70% *cis* isomer within 10 s (Panel A and B, Figure 5.10). Further irradiation resulted in no significant change. The isomerisation was then reversed (*cis* to *trans*) upon 10 s photoirradiation at 490 nm to reach a PSS of 91% *trans* isomer, with no significant change after 100 s of irradiation (Panel C and D, Figure 5.10).

5.4.7 Formulation and mechanical properties of AZO2-PA hydrogel

Formulation of the AZO2-PA hydrogel and its mechanical properties were conducted by David Richards. Briefly, gel formulation was attempted by increasing the quantities of AZO2 crosslinker incorporated within the hydrogel pre-polymer. The mechanical properties of the selected AZO2-PA hydrogels were then tested, also by David Richards, on a Bruker Catalyst AFM coupled with a Nikon Eclipse Ti microscope, operated in peak force tapping mode using a cantilever tipped with a 5 µm diameter borosilicate glass sphere (CP-CONT-BSG-A; sQUBE, Windsor Scientific, U.K.) (Figure 5.11).

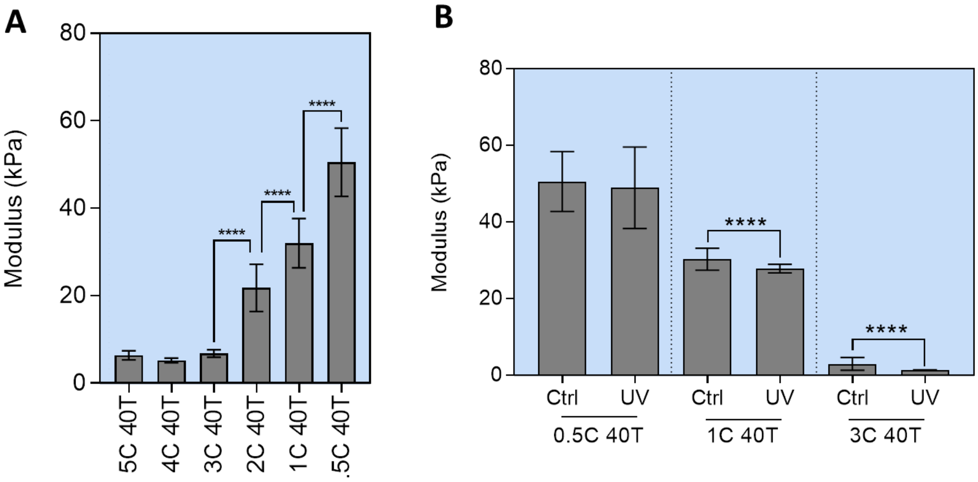

Figure 5.11 Mechanical properties of AZO2-PA hydrogel. (A) An inverse relationship between Young's modulus and AZO2 crosslinker concentration incorporated within the hydrogel network and (B) Stiffness measurements of selected candidates before and after UV irradiation at 365 nm for 30 min showing no apparent change in 0.5C40T gel. "**" represents *p* < 0.0001, significant difference. The experiments were conducted and result graphs kindly provided by David Richards.**

The AZO2-PA hydrogels were formulated at a final polymer concentration (T) of 40% (w/v) with cross-linker concentrations (C) from 0.5% to 5% (w/w) compared with the previously proposed AZO1-PA hydrogel which utilised constituents of approximately 0.3C 30T based upon a novel calculation system developed and provided by David Richards (Appendix 12).

The results indicate an inverse relationship between stiffness and AZO2 crosslinker concentration incorporated within the hydrogel network (Panel A, Figure 5.11). Amongst the 6 selected candidates, 0.5, 1 and 3C AZO2-PA hydrogels were examined for change in stiffness before and after 30 min UV irradiation at 365 nm, with results indicating no significant stiffness changes for 0.5C 40T gel (Panel B, Figure 5.11). Concersely, an approximate 8% reduction in stiffness was experienced for 1C 40T gel, from 30.24 ± 2.85 to 27.75 ± 1.13 kPa, after UV irradiation and an approximate 56% reduction with 3C 40T gel, observed from 2.92 ± 1.65 kPa to 1.28 ± 0.08 kPa after UV irradiation, showing no improvement from the previously proposed AZO1-PA hydrogel.

AZO2 was synthesised in salt formation originally aimed at increasing water solubility, therefore the potential higher concentration incorporated within the hydrogel network. However, similar to polyacrylic acid-based hydrogels, AZO2 in aqueous solution provided carboxylic acid groups on the polymer chain facilitating an extensive swelling ratio within the hydrogel network (Appendix 13).[218] It was thus hypothesised that by increasing the concentration of AZO2 within the hydrogel network, a higher quantity of carboxylic acid was introduced in its ionic state, thus allowing higher water absorption and resulting in a decrease in stiffness.

5.5 Conclusions

In summary, this chapter aimed to isolate material variables to observe the purely mechanical signalling events in a submicron-scale environment. Photoresponsive AZO1-PA hydrogel was synthesised and characterisation demonstrated that, in comparison to an earlier azobenzene-incorporating hydrogel,[212] it demonstrated a superior isolated dynamic range (76% reduction in stiffness vs ~2%) and a longer maintenance of the softer “on” state (2 weeks vs ~10 h). It could therefore be used as a platform to study mechanosignaling in cells responding to dynamic and potentially spatially defined changes, over biologically relevant stiffnesses and timescales. Cell viability on materials from the initial experimental design indicated that they were viable for applications with MSCs.

The AZO1-PA hydrogel formulation could be utilised in nanofabrication methods such as inkjet bioprinting or polymer pen lithography to fabricate mechanical stimuli in sub-micron scale offering a new platform to study mechanotransduction signalling pathways.

With improved solubility, the AZO2 crosslinker had potential for incorporation within the hydrogel network at multiple times greater concentration than possible with AZO1. However, due to the ionic structure, it was difficult to control the swelling ratio and potentially leading to uncontrollable changes in stiffness and an inverse relationship between AZO2 concentration and AZO2-PA hydrogel stiffness. Future improvement could be made by replacing the carboxylic acids with more water soluble organic molecules, such as polyethylene glycol.

Nonetheless, the non-cytotoxic properties of AZO1-PA hydrogel and its controllable stiffness would allow it to be used in PPL applications as an “ink” to fabricate nanoarrays for model surfaces for stem cell applications in the future.

Summary

A range of large-area homogeneous chemical nano-arrays were fabricated with 2 different presenting chemistries, carboxyl (-CO_2H) and amino (-NH_2) groups, with controlled feature sizes (dβ) of 300 nm. Various arrays of features were introduced that reduced centre-to-centre distance (dα) from 3.14 to 1.01 µm and increased the number of quantitative integrin binding sites from 36 to 324 μm^2 per region of 10^4 μm^2 (100 x 100 µm).

Human mesenchymal stem cells (MSCs) were cultured in contact with these surfaces. Initial cell adhesion and prolonged cell differentiation pathways were evaluated. Initial cell adhesion suggested that MHA nanoarrays provided a greater number of MSC adhesion sites than AUT nanoarrays, because cells were observed adhered on MHA20 but not on AUT20 (Panel A and D, Figure 2.6). After 7 days of culture, MSCs on MHA40, MHA60 and AUT40 were extensively clustered while flattened on MHA20 and AUT60 (Figure 2.6). Cell differentiation assays indicated that by 28 days cells on MHA20 had differentiated towards a hypertrophic cartilage phenotype, being positive for collagen type X. MSCs on MHA40 and MHA60 differentiated along a chondrogenesis pathway, whereas AUT40 and AUT60 potentially induced adipogenesis, as cells were positive for CBFA1 but negative for osteocalcin and type II collagen.

The materials were then cultured in contact with terminally differentiated human articular chondrocytes to examine the maintenance of a differentiated chondrogenic phenotype *in vitro*. Immunocytochemistry results indicated that MHA40 and AUT60 successfully supported a chondrogenic phenotype for short term experimental designs as shown by fluorescently labelled collagen type II expression.

The results above, where MHA40 stimulated MSCs towards a chondrogenic phenotype and successfully supported terminal differentiation to chondroctyes, suggested that MHA40 in combination with MHA20, which supported hypertrophic cartilage phenotype, could potentially be suitable candidates for repair of cartilage and the zone of hypertrophy.

To investigate future potential applications in regenerative medicine, the defined model material parameters were investigated on biodegradable surface materials in Chapter 4. A number of surface modifications were tested to optimise the most viable path for recreating the defined parameters on biodegradable thin films. The maleimide-thiol click mechanism was chosen to introduce these nanoarrays on E1001(1k) degradable polymer thin films, a clinically-relevant polymer. The surface reaction was characterised using water contact angle, ATR-FTIR and X-ray photoelectron spectroscopy. Surface topography was optimised using AFM. The results demonstrated that the chosen methods of modification successfully introduced overall homogeneous surface topography at the nano-scale, *i.e.,* the cellular response was not exposed to varying complicated heterogeneous signals.

In addition to controlling cellular response *via* chemical modifications, cell response to dynamic change was studied at the molecular scale for prospective applications as “ink” in PPL applications. A range of photoresponsive hydrogels was synthesised and characterised as potential “ink”. Preliminary MSC response to *in situ* change in stiffness on AZO1-PA hydrogel surfaces was investigated to validate the potential of these non-toxic model hydrogel structures to better understand the mechanotransduction signalling pathways and to validate their potential use as PPL “ink”. An improved solubility crosslinker, AZO2, was synthesised by addition of hydrophilic functional groups. AZO2 aimed to increase water solubility in order to incorporate higher quantities of photoresponsive crosslinker within the hydrogel network thus increasing the potential dynamic range of the hydrogel. It was found, however, that due to the ionic structure of AZO2, when characterised AZO2-PA hydrogels had extensive swelling properties and limited dynamic change. Future improvements could be made by replacing ionic carboxylic acid with more water soluble organic molecules, such as polyethylene glycol. This would enable water solubility to be achieved while retaining the overall organic structure and would avoid uncontrolled swelling.

The fabricated materials with a variety of surface parameters have demonstrated the ability to control cellular response. The data collected demonstrated our fundamental understanding of cellular response *via* mechanotransduction. These findings suggest that defined nanostructures and stiffness could potentially be the key to understanding mechanosignalling events for future applications in regenerative medicine.

Chapter 7

Concluding Remarks

This thesis has encompassed four separate sub-projects, with the overall goal of controlling biological responses using chemically-defined homogeneous surface materials. This has been primarily achieved by utilising polymer pen lithography (PPL) as a novel approach to fabricate versatile large-area chemically-defined nanoarrays.

Firstly, the thiol-gold chemisorption mechanism was used to fabricate model surfaces using polymer pen lithography. A range of chemical nano-arrays were fabricated in sub-micron resolution to identify mesenchymal stem cell response to physical cues, instead of complex biological reagents such as extracellular matrix and peptides. Nanoarray features were characterised by AFM and optical microscopy. An initial cell-surface interaction was also observed by fluorescent labelling of the arrays. The stimulus from these nanoarrays on mesenchymal stem cell differentiation pathways, in addition to control of cell phenotype against macro-environment were also achieved. To explore the mechanism of designed chemical nanoarrays on stem cell fate, a wide range of protein initial adsoption on the materials could be studied. Proteomics could potentially be applied for a large-scale screening of initial protein adsorption on the material surface prior to cell adhesion.

Advanced surface fabrication chemistry was developed on biodegradable surface materials. The aim was to achieve successful control of biological responses for practical applications in regenerative medicine. The developed reaction methodology could be applied in large-area homogeneous fabrication of biodegradable surface polymer using developed PPL technique to replicate stem cell response to defined chemical nanoarrays.

An *in situ* photoresponsive hydrogel was developed, aimed at large-area screening of cell response in dynamic changes at a defined nanometre resolution utilising polymer pen lithography.

The current limitations of PPL are principally addressed by the ability to fabricate large-areas of materials to meet the requirements for cell applications. The technique developed allows homogeneous fabrication of model surfaces over a 2 x 2 cm region due to purchased silicon moulds for probe array manufacture a customised AFM sample stage currently available. These limitations could be overcome by redesigning the AFM sample stage and silicon moulds in the future allowing fabrications over a considerably larger areas. This would enable rapid fabrication for potential future applications in regenerative medicine combining controllable stiffness and chemistry.

Overall, this approach developed in this thesis has demonstrated a capacity for manipulation of cell phenotype by control of initial cell interaction with surfaces having varying featured. This would enable a better understanding of cell interaction with physical and chemical cues at the point of contact.

References

1. R. Langer and J. P. Vacanti, *Science*, 1993, **260**, 920-926.
2. R. J. McMurray, M. J. Dalby and P. M. Tsimbouri, *J. Tissue Eng. Regen. Med.*, 2015, **9**, 528-539.
3. F. Berthiaume, T. J. Maguire and M. L. Yarmush, *Annu. Rev. Chem. Biomol. Eng.*, 2011, **2**, 403-430.
4. O. V. Horst, M. G. Chavez, A. H. Jheon, T. Desai and O. D. Klein, *Dent. Clin. North. Am.*, 2012, **56**, 495-520.
5. L. de Girolamo, E. Lucarelli, G. Alessandri, M. A. Avanzini, M. E. Bernardo, E. Biagi, A. T. Brini, G. D'Amico, F. Fagioli, I. Ferrero, F. Locatelli, R. Maccario, M. Marazzi, O. Parolini, A. Pessina and M. L. Torr, *Curr. Pharm. Des.*, 2013, **19**, 2459-2473.
6. D. Howard, L. D. Buttery, K. M. Shakesheff and S. J. Roberts, *J. Anat.*, 2008, **213**, 66-72.
7. D. C. Ding, W. C. Shyu and S. Z. Lin, *Cell transplantation*, 2011, **20**, 5-14.
8. C. C. Ude, A. Miskon, R. B. H. Idrus and M. B. Abu Bakar, *Mil. Med.*, 2018, **5**, 7-24.
9. P. Bianco , M. Riminucci , S. Gronthos and P. G. Robey, *Stem Cells*, 2001, **19**, 180-192.
10. G. H. Wu and S. H. Hsu, *J. Med. Biol. Eng.*, 2015, **35**, 285-292.
11. Y. Y. Li, T. H. Choy, F. C. Ho and P. B. Chan, *Biomaterials*, 2015, **52**, 208-220.
12. M. Kornek and D. Schuppan, *J. Hepatol.*, 2012, **57**, 1144-1146.
13. X. Gao, Y. Cao, X. Song, Z. Zhang, X. Zhuang, C. He and X. Chen, *Macromol. Biosci.*, 2014, **14**, 565-575.
14. J. A. Hunt, R. Chen, T. van Veen and N. Bryan, *J. Mater. Chem. B*, 2014, **2**, 5319.
15. A. F. von Recum and M. LaBerge, *J. Appl. Biomater.*, 1995, **6**, 137-144.
16. I. Gotman, *J. Urol.*, 1997, **11**, 383-389.
17. S. Daghighi, J. Sjollema, H. C. van der Mei, H. J. Busscher and E. T. Rochford, *Biomaterials*, 2013, **34**, 8013-8017.
18. H. J. Busscher, H. C. van der Mei, G. Subbiahdoss, P. C. Jutte, J. J. A. M. van den Dungen, S. A. J. Zaat, M. J. Schultz and D. W. Grainger, *Sci. Transl. Med.*, 2012, **4**, 1-10.
19. M. Franklin and K. Russek, *Surg. Endosc.*, 2011, **25**, 1693-1694.
20. K. S. Jehle, A. Rohatgi and M. K. Baig, *J. Wound Care*, 2007, **16**, 36-37.
21. B. Alpert and D. Seligson, *J. Oral. Maxillofac. Surg.* , 1996, **54**, 618-621.
22. J. A. Rowley and D. J. Mooney, *J. Biomed. Mater. Res.*, 2002, **60**, 217-223.
23. T. W. Chung, J. Yang, T. Akaike, K. Y. Cho, J. W. Nah, S. I. Kim and C. S. Cho, *Biomaterials*, 2002, **23**, 2827-2834.
24. C. E. Schmidt and J. M. Baier, *Biomaterials*, 2000, **21**, 2215-2231.
25. I. Vesely, D. Boughner and T. Song, *Ann. Thorac. Surg.*, 1988, **46**, 302-308.
26. L. S. Nair and C. T. Laurencin, *Prog. Polym. Sci.*, 2007, **32**, 762-798.

27. D. S. Katti, S. Lakshmi, R. Langer and C. T. Laurencin, *Adv. Drug Deliv. Rev.*, 2002, **54**, 933-961.
28. M. H. R. Magno, J. Kim, A. Srinivasan, S. McBride, D. Bolikal, A. Darr, J. O. Hollinger and J. Kohn, *J. Mater. Chem.*, 2010, **20**, 8885-8893.
29. A. Banerjee, K. Chatterjee and G. Madras, *Mater. Sci. Technol.*, 2014, **30**, 567-573.
30. J. P. Santerre, R. S. Labow, D. G. Duguay, D. Erfle and G. A. Adams, *J. Biomed. Mater. Res.*, 1994, **28**, 1187-1199.
31. H. S. Azevedo and R. L. Reis, *Understanding the Enzymatic Degradation of Biodegradable Polymers and Strategies to Control Their Degradation Rate*, Boca Raton, CRC Press, 2005.
32. P. Roach, D. Eglin, K. Rohde and C. C. Perry, *J. Mater. Sci. Mater. Med.*, 2007, **18**, 1263-1277.
33. S. A. Fawcett, J. M. Curran, R. Chen, N. P. Rhodes, M. F. Murphy, P. Wilson, L. Ranganath, J. P. Dillon, J. A. Gallagher and J. A. Hunt, *Calcif. Tissue Int.*, 2017, **100**, 95-106.
34. O. Mashinchian, L.-A. Turner, M. J. Dalby, S. Laurent, M. A. Shokrgozar, S. Bonakdar, M. Imani and M. Mahmoudi, *Nanomedicine*, 2015, **10**, 829-847.
35. E. K. Yim, E. M. Darling, K. Kulangara, F. Guilak and K. W. Leong, *Biomaterials*, 2010, **31**, 1299-1306.
36. M. J. Dalby, N. Gadegaard and R. O. C. Oreffo, *Nat. Mater.*, 2014, **13**, 558-569.
37. A. Saez, M. Ghibaudo, A. Buguin, P. Silberzan and B. Ladoux, *Proc. Natl. Acad. Sci. U.S.A.*, 2007, **104**, 8281-8286.
38. A. J. Engler, S. Sen, H. L. Sweeney and D. E. Discher, *Cell*, 2006, **126**, 677-689.
39. P. M. Kharkar, K. L. Kiick and A. M. Kloxin, *Chem. Soc. Rev.*, 2013, **42**, 7335-7372.
40. D. S. Benoit, M. P. Schwartz, A. R. Durney and K. S. Anseth, *Nat. Mater.*, 2008, **7**, 816-823.
41. J. M. Curran, R. Stokes, E. Irvine, D. Graham, N. A. Amro, R. G. Sanedrin, H. Jamil and J. A. Hunt, *Lab Chip*, 2010, **10**, 1662-1670.
42. R. K. Jaiswal, N. Jaiswal, S. P. Bruder, G. Mbalaviele, D. R. Marshak and M. F. Pittenger, *J. Biol. Chem.*, 2000, **275**, 9645-9652.
43. G. Mbalaviele, Y. Abu-Amer, A. Meng, R. Jaiswal, S. Beck, M. F. Pittenger, M. A. Thiede and D. R. Marshak, *J. Biol. Chem.*, 2000, **275**, 14388-14393.
44. M. J. Dalby, N. Gadegaard, R. Tare, A. Andar, M. O. Riehle, P. Herzyk, C. D. Wilkinson and R. O. Oreffo, *Nat. Mater.*, 2007, **6**, 997-1003.
45. J. M. Curran, F. Pu, R. Chen and J. A. Hunt, *Biomaterials*, 2011, **32**, 4753-4760.
46. N. Wang, *J. Phys. D Appl. Phys.*, 2017, **50**.
47. F. Li, S. D. Redick, H. P. Erickson and V. T. Moy, *Biophys. J.*, 2003, **84**, 1252-1262.
48. P. Atherton, B. Stutchbury, D. Y. Wang, D. Jethwa, R. Tsang, E. Meiler-Rodriguez, P. Wang, N. Bate, R. Zent, I. L. Barsukov, B. T. Goult, D. R. Critchley and C. Ballestrem, *Nat. Commun.*, 2015, **6**, 1-12.
49. M. K. L. Han and J. de Rooij, *Trends. Cell Biol.*, 2016, **26**, 612-623.

50. N. K. Chaki and K. Vijayamohanan, *Biosens. Bioelectron.*, 2002, **17**, 1-12.
51. Y. Wang, J. Cai, H. Rauscher, R. J. Behm and W. A. Goedel, *Chem. Eur. J.*, 2005, **11**, 3968-3978.
52. M. Mrksich, L. E. Dike, J. Tien, D. E. Ingber and G. M. Whitesides, *Exp. Cell Res.*, 1997, **235**, 305-313.
53. S. Fereol, R. Fodil, M. Barnat, V. Georget, U. Milbreta and F. Nothias, *Cytoskeleton*, 2011, **68**, 373-388.
54. R. McBeath, D. M. Pirone, C. M. Nelson, K. Bhadriraju and C. S. Chen, *Dev. Cell*, 2004, **6**, 483-495.
55. K. A. Kilian, B. Bugarija, B. T. Lahn and M. Mrksich, *Proc. Natl. Acad. Sci. U.S.A.*, 2010, **107**, 4872-4877.
56. J. M. Curran, R. Chen and J. A. Hunt, *Biomaterials*, 2006, **27**, 4783-4793.
57. J. M. Curran, R. Chen and J. A. Hunt, *Biomaterials*, 2010, **31**, 1463-1464.
58. J. M. Curran, R. Chen and J. A. Hunt, *Biomaterials*, 2005, **26**, 7057-7067.
59. B. K. K. Teo, S. T. Wong, C. K. Lim, T. Y. S. Kung, C. H. Yap, Y. Ramagopa, L. H. Romer and E. K. F. Yim, *ACS Nano*, 2013, **7**, 4785-4798.
60. P. M. Tsimbouri, R. J. McMurray, K. V. Burgess, E. V. Alakpa, P. M. Reynolds, K. Murawski, E. Kingham, R. O. C. Oreffo, N. Gadegaard and M. J. Dalby, *ACS Nano*, 2012, **6** 10239–10249.
61. D. Fuard, T. Tzvetkova-Chevolleau, S. Decossas, P. Tracqui and P. Schiavone, *Microelectron. Eng.*, 2008, **85**, 1289-1293.
62. J. N. Lee, C. Park and G. M. Whitesides, *Anal. Chem.*, 2003, **75**, 6544-6554.
63. J. Zhou, D. A. Khodakov, A. V. Ellis and N. H. Voelcker, *Electrophoresis*, 2012, **33**, 89-104.
64. J. Chen, J. S. and K. Park, *Handbook of biodegradable polymers.*, 1997.
65. J. L. Drury and D. J. Mooney, *Biomaterials*, 2003, **24**, 4337-4351.
66. W. E. Hennink and C. F. v. Nostrum, *Adv. Drug Delivery Rev.*, 2002, **54**, 13–36.
67. B. Baroli, *J. Pharm. Sci.*, 2007, **96**, 2197-2223.
68. G. Chamberlain, J. Fox, B. Ashton and J. Middleton, *Stem Cells*, 2007, **25**, 2739-2749.
69. Z. Hamidouche, E. Hay, P. Vaudin, P. Charbord, R. Schule, P. J. Marie and O. Fromigue, *FASEB J.*, 2008, **22**, 3813-3822.
70. I. H. Song, A. I. Caplan and J. E. Dennis, *J. Orthop. Res.*, 2009, **27**, 916-921.
71. F. Langenbach and J. Handschel, *Stem Cell Res. Ther.*, 2013, **4**, 117-123.
72. G. Xiao, R. Gopalakrishnan, D. Jiang, E. Reith, M. D. Benson and R. T. Franceschi, *J. Bone Miner. Res.*, 2002, **17**, 101-110.
73. M. Westhrin, M. Xie, M. O. Olderoy, P. Sikorski, B. L. Strand and T. Standal, *PloS one*, 2015, **10**, 1-16.
74. D.-A. Yu, J. Han and B.-S. Kim, *Int. J. Stem Cells*, 2012, **5**, 16-22.
75. M. S. Park, Y. H. Kim and J. W. Lee, *Matrix Biol.*, 2010, **29**, 135-142.
76. T. Doerks, R. R. Copley, J. Schultz, C. P. Ponting and P. Bork, *Genes Dev.*, 2002, **12**, 47-56.
77. K. Tanaka, Y. Yokosaki, F. Higashikawa, Y. Saito, A. Eboshida and M. Ochi, *Matrix Biol.*, 2007, **26**, 409-418.
78. E. A. Zemskov, A. Janiak, J. Hang, A. Waghray and A. M. Belkin, *Front. Biosci.*, 2006, **11**, 1057-1076.

79. H. Takahashi, T. Isobe, S. Horibe, J. Takagi, Y. Yokosaki, D. Sheppard and Y. Saito, *J. Biol. Chem.*, 2000, **275**, 23589-23595.
80. I.S. Kima, F. Ottob, B. Zabela and S. Mundlos, *Mech. Dev.*, 1999, **80**, 159-170.
81. J. Bonaventure, N. Kadhom, L. Cohen-Solal, K. H. Ng, J. Bourguignon, C. Lasselin and P. Freisinger, *Exp. Cell Res.*, 1994, **212**, 97-104.
82. Y. M. Yoon, S. J. Kim, C. D. Oh, J. W. Ju, W. K. Song, Y. J. Yoo, T. L. Huh and J. S. Chun, *J. Biol. Chem.*, 2002, **277**, 8412-8420.
83. S. Li, X. Wang, B. Cao, K. Ye, Z. Li and J. Ding, *Nano Lett.*, 2015, **15**, 7755-7765.
84. T. C. Otto and M. D. Lane, *Crit. Rev. Biochem. Mol. Biol.*, 2005, **40**, 229-242.
85. J. Liu, S. M. DeYoung, M. Zhang, M. Zhang, A. Cheng and A. R. Saltiel, *Cell Metab.*, 2005, **2**, 165-177.
86. D. L. Angst and G. W. Simmons, *Langmuir.*, 1991, **7**, 2236-2242.
87. A. Ulman, *Chem. Rev.*, 1996, **96**, 1533-1554.
88. C. D. Bain, E. B. Troughton, Y. T. Tao, J. Evall, G. M. Whitesides and R. G. Nuzzo, *J. Am. Chem. Soc.*, 1989, **111**, 321-335.
89. C. Haensch, S. Hoeppener and U. S. Schubert, *Chem. Soc. Rev.*, 2010, **39**, 2323-2334.
90. A. Ivanisevic and C. A. Mirkin, *Cell. Mol. Bioeng.*, 2001, **123**, 7887-7889.
91. S. Kuddannaya, Y. J. Chuah, M. H. Lee, N. V. Menon, Y. Kang and Y. Zhang, *ACS Appl. Mater. Interfaces*, 2013, **5**, 9777-9784.
92. S. Onclin, B. J. Ravoo and D. N. Reinhoudt, *Angew. Chem. Int. Ed. Engl.*, 2005, **44**, 6282-6304.
93. B. Arkles, *Chem. Tech.*, 1977, **7**, 766-778.
94. P. Silberzan, L. Leger, D. Ausserre and J. J. Benattar, *Langmuir.*, 1991, **1991**, 8.
95. S. R. Culler, H. Ishida and J. LKoenig, *J. Colloid Interface Sci.*, 1986, **109**, 1-10.
96. E. T. Vandenberg, L. Bertilsson, B. Liedberg, K. Uvdal, R. Erlandsson, H. Elwing and I. Lundström, *J. Colloid Interface Sci.*, 1991, **147**, 103-118.
97. N. Balachander and C. N. Sukenik, *Langmuir.*, 1990, **6**, 1621-1627.
98. Y. Ofir, N. Zenou, I. Goykhman and S. Yitzchaik, *J. Phys. Chem. B*, 2006, **110**, 8002-8009.
99. H. Y. Song, M. H. Ngai, Z. Y. Song, P. A. MacAry, J. Hobley and M. J. Lear, *Org. Biomol. Chem.*, 2009, **7**, 3400-3406.
100. A. D. Baldwin and K. L. Kiick, *Polym. Chem.*, 2013, **4**, 133-143.
101. C. F. Brewer and J. P. Riehm, *Anal. Biochem.*, 1967, **18**, 248-255.
102. A. Hozumi, Y. Yokogawa, T. Kameyama, H. Sugimura, K. Hayashi, H. Shirayama and O. Takai, *J. Vac. Sci. Technol. A*, 2001, **19**, 1812-1816.
103. S. Shiota, S. Yamamoto, A. Shimomura, A. Ojida, T. Nishino and T. Maruyama, *Langmuir.*, 2015, **31**, 8824-8829.
104. C. A. G. N. Montalbetti and V. Falque, *Tetrahedron*, 2005, **61**, 10827-10852.
105. E. Valeur and M. Bradley, *Chem. Soc. Rev.*, 2009, **38**, 606-631.

106. A. Ebner, P. Hinterdorfer and H. J. Gruber, *Ultramicroscopy*, 2007, **107**, 922-927.
107. G. Leriche, L. Chisholm and A. Wagner, *Bioorg. Med. Chem.*, 2012, **20**, 571-582.
108. T. I. Al-Warhi, H. M. A. Al-Hazimi and A. El-Faham, *J. Saudi Chem. Soc.*, 2012, **16**, 97-116.
109. H. C. Kolb, M. G. Finn and K. B. Sharpless, *Angew. Chem. Int. Ed.*, 2001, **40**, 2004-2021.
110. C. E. Hoyle, A. B. Lowe and C. N. Bowman, *Chem. Soc. Rev.*, 2010, **39**, 1355-1387.
111. D. P. Nair, M. Podgórski, S. Chatani, T. Gong, W. Xi, C. R. Fenoli and C. N. Bowman, *Chem. Mater.*, 2013, **26**, 724-744.
112. B. N. Naidu, M. E. Sorenson, J. J. Bronson, M. J. Pucci, J. M. Clark and Y. Ueda, *Bioorg. Med. Chem. Lett.*, 2005, **15**, 2069-2072.
113. K. Y. Tan, H. Lin, M. Ramstedt, F. M. Watt, W. T. Huck and J. E. Gautrot, *Integrative biology : quantitative biosciences from nano to macro*, 2013, **5**, 899-910.
114. L. R. Giam, M. D. Massich, L. Hao, L. S. Wong, C. C. Mader and C. A. Mirkin, *Proc. Natl. Acad. Sci. USA*, 2012, **109**, 4377-4382.
115. R. Garcia, R. V. Martinez and J. Martinez, *Chem. Soc. Rev.*, 2006, **35**, 29-38.
116. G. Binnig, C. F. Quate and C. Gerber, *Phys. Rev. Lett.*, 1986, **56**, 930-933.
117. H. J. Mamin and D. Rugar, *Appl. Phys. Lett.*, 1992, **61**, 1003-1005.
118. E. K. Dimitriadis, F. Horkay, J. Maresca, B. Kachar and R. S. Chadwick, *Biophys. J.*, 2002, **82**, 2798–2810.
119. R. E. Mahaffy, C. K. Shih, F. C. MacKintosh and J. Käs, *Phys. Rev. Lett.*, 2000, **85**, 880-883.
120. D. S. Ginger, H. Zhang and C. A. Mirkin, *Angew. Chem. Int. Ed. Engl.*, 2004, **43**, 30-45.
121. D. A. Weinberger, S. Hong, C. A. Mirkin, B. W. Wessels and T. B. Higgins, *Adv. Mater.*, 2000, **12**, 1600-1603.
122. H. Jung, R. Kulkarni and C. P. Collier, *J. Am. Chem. Soc.*, 2003, **125**, 12096–12097.
123. S. E. Kooi, L. A. Baker, P. E. Sheehan and L. J. Whitman, *Adv. Mater.*, 2004, **16**, 1013-1016.
124. A. Noy, A. E. Miller, J. E. Klare, B. L. Weeks, B. W. Woods and J. J. DeYoreo, *Nano Lett.*, 2002, **2**, 109-112.
125. A. B. Braunschweig, F. Huo and C. A. Mirkin, *Nat. Chem.*, 2009, **1**, 353-358.
126. F. Huo, Z. Zheng, G. Zheng, L. R. Giam, H. Zhang and C. A. Mirkin, *Science*, 2008, **321**, 1658-1660.
127. K. Salaita, Y. Wang, J. Fragala, R. A. Vega, C. Liu and C. A. Mirkin, *Angew. Chem. Int. Ed. Engl.*, 2006, **45**, 7220-7223.
128. R. Kumar, A. Bonicelli, S. Sekula-Neuner, A. C. Cato, M. Hirtz and H. Fuchs, *Small*, 2016, **12**, 5330-5338.
129. F. Brinkmann, M. Hirtz, A. M. Greiner, M. Weschenfelder, B. Waterkotte, M. Bastmeyer and H. Fuchs, *Small*, 2013, **9**, 3266-3275.

130. J. M. Curran, R. Chen, R. Stokes, E. Irvine, D. Graham, E. Gubbins, D. Delaney, N. Amro, R. Sanedrin, H. Jamil and J. A. Hunt, *J. Mater. Sci. Mater. Med.*, 2010, **21**, 1021-1029.
131. M. Mrksich, C. S. Chen, Y. Xia, L. E. Dike, D. E. Ingber and G. M. Whitesides, *Proc. Natl. Acad. Sci. U.S.A.*, 1996, **20**, 10775-10778.
132. N. D. Gallant, K. A. Lavery, E. J. Amis and M. L. Becker, *Adv. Mater.*, 2007, **19**, 965-969.
133. H. D. Yu, M. D. Regulacio, E. Ye and M. Y. Han, *Chem. Soc. Rev.*, 2013, **42**, 6006-6018.
134. M. Onoue, M. Fujita and H. Ushijima, *Mol. Cryst. Liq. Cryst.*, 2009, **505**, 118/[356]-123/[361].
135. I.-N. Lee, J. Hosford, S. Wang, J. A. Hunt, J. M. Curran, W. P. Heath and L. S. Wong, *J. Vis. Exp.*, 2018.
136. X. Liao, A. B. Braunschweig, Z. Zheng and C. A. Mirkin, *Small*, 2010, **6**, 1082-1086.
137. S. Wang, J. Hosford, W. P. Heath and L. S. Wong, *RSC Adv.*, 2015.
138. D. J. Eichelsdoerfer, X. Liao, M. D. Cabezas, W. Morris, B. Radha, K. A. Brown, L. R. Giam, A. B. Braunschweig and C. A. Mirkin, *Nat. Protoc.*, 2013, **8**, 2548-2560.
139. L. R. Giam, M. D. Massich, L. Hao, L. Shin Wong, C. C. Mader and C. A. Mirkin, *Proc. Natl. Acad. Sci. U.S.A.*, 2012, **109**, 4377-4382.
140. E. Repo, T. A. Kurniawan, J. K. Warchol and M. E. Sillanpaa, *Journal of hazardous materials*, 2009, **171**, 1071-1080.
141. B. Gmeiner, H. Leibl, G. Zerlauth and C. Seelos, *Arch. Biochem. Biophys.*, 1995, **321**, 40-42.
142. I. Migneault, C. Dartiguenave, M. J. Bertrand and K. C. Waldron, *BioTechniques*, 2004, **37**, 790-802.
143. J. Ge, L. Guo, S. Wang, Y. Zhang, T. Cai, R. C. Zhao and Y. Wu, *Stem Cell Rev.*, 2014, **10**, 295-303.
144. K. Burridge and J. R. Feramisco, *Cell*, 1980, **19**, 587-595.
145. J. D. Humphries, P. Wang, C. Streuli, B. Geiger, M. J. Humphries and C. Ballestrem, *J. Cell Biol.*, 2007, **179**, 1043-1057.
146. I. I. Singer and P. R. Paradiso, *Cell*, 1981, **24**, 481-492.
147. N. O. Chahine, N. M. Collette, C. B. Thomas, D. C. Genetos and G. G. Loots, *Tissue Eng. Part A*, 2014, **20**, 2305-2315.
148. A. J. Ridley, *Bioessays*, 1994, **16**, 321-327.
149. D. A. Cheresh, J. Leng and R. L. Klemke, *J. Cell Biol.*, 1999, **146**, 1107-1116.
150. H. E. Johnson, S. J. King, S. B. Asokan, J. D. Rotty, J. E. Bear and J. M. Haugh, *J. Cell Biol.*, 2015, **208**, 443-455.
151. J. Veevers-Lowe, S. G. Ball, A. Shuttleworth and C. M. Kielty, *J. Cell Sci.*, 2011, **124**, 1288-1300.
152. Z. Hamidouche, O. Fromigué, J. Ringe, T. Häupl, P. Vaudin, J.-C. Pagès, S. Srouji, E. Livne and P. J. Marie, *Proc. Natl. Acad. Sci. U.S.A.*, 2009, **106**, 18587-18591.
153. M. Kisiel, M. M. Martino, M. Ventura, J. A. Hubbell, J. Hilborn and D. A. Ossipov, *Biomaterials*, 2013, **34**, 704-712.

154. H. Enomoto, T. Furuichi, A. Zanma, K. Yamana, C. Yoshida, S. Sumitani, H. Yamamoto, M. Enomoto-Iwamoto, M. Iwamoto and T. Komori, *J. Cell Sci.*, 2004, **117**, 417-425.
155. S. I. Deliloglu-Gurhan, H. S. Vatansever, F. Ozdal-Kurt and I. Tuglub, *Acta Histochem.*, 2006, **108**, 49-57.
156. C. G. James, C. T. Appleton, V. Ulici, T. M. Underhill and F. Beier, *Mol. Biol. Cell*, 2005, **16**, 5316-5333.
157. L. Duan, Y. Liang, B. Ma, W. Zhu and D. Wang, *Am. J. Transl. Res.*, 2015, **7**, 2127-2140.
158. K. Mithoefer, T. McAdams, R. J. Williams, P. C. Kreuz and B. R. Mandelbaum, *Am. J. Sports Med.*, 2009, **37**, 2053-2063.
159. B. Ma, J. C. Leijten, L. Wu, M. Kip, C. A. van Blitterswijk, J. N. Post and M. Karperien, *Osteoarthr. Cartil.*, 2013, **21**, 599-603.
160. W. Bartlett, J. A. Skinner, C. R. Gooding, R. W. Carrington, A. M. Flanagan, T. W. Briggs and G. Bentley, *J. Bone Joint Surg. Br.*, 2005, **87**, 640-645.
161. M. E. Cooke, M. J. Pearson, R. J. A. Moakes, C. J. Weston, E. T. Davis, S. W. Jones and L. M. Grover, *APL Bioeng.*, 2017, **1**, 016104.
162. W. L. Murphy, T. C. McDevitt and A. J. Engler, *Nat. Mater.*, 2014, **13**, 547-557.
163. X. Wang, S. Li, C. Yan, P. Liu and J. Ding, *Nano Lett.*, 2015, **15**, 1457-1467.
164. E. Langelier, R. Suetterlin, C. D. Hoemann, U. Aebi and M. D. Buschmann, *J. Histochem. Cytochem.*, 2000, **48**, 1307–1320.
165. K. R. Brodkin, A. J. Garcia and M. E. Levenston, *Biomaterials*, 2004, **25**, 5929-5938.
166. N. Taquet, S. Dumont, J. L. Vonesch, D. Hentsch, J. M. Reimund and C. D. Muller, *Mediators Inflamm.*, 2009, **2009**, 285812.
167. C. Vogel, S. Abreu Rde, D. Ko, S. Y. Le, B. A. Shapiro, S. C. Burns, D. Sandhu, D. R. Boutz, E. M. Marcotte and L. O. Penalva, *Mol. Syst. Biol.*, 2010, **6**, 1-9.
168. B. C. Dickson, A. M. Mulligan, H. Zhang, G. Lockwood, F. P. O'Malley, S. E. Egan and M. Reedijk, *Mod. Pathol.*, 2007, **20**, 685-693.
169. V. L. MacKay, X. Li, M. R. Flory, E. Turcott, G. L. Law, K. A. Serikawa, X. L. Xu, H. Lee, D. R. Goodlett, R. Aebersold, L. P. Zhao and D. R. Morris, *Mol. Cell. Protemics*, 2004, **3**, 478-489.
170. L. S. Wong, C. V. Karthikeyan, D. J. Eichelsdoerfer, J. Micklefield and C. A. Mirkin, *Nanoscale*, 2012, **4**, 659-666.
171. D. J. Pena, M. P. Raphael and J. M. Byers, *Langmuir.*, 2003, **19**, 9028-9032.
172. M. Su, X. Liu, S.-Y. Li, V. P. Dravid and C. A. Mirkin, *J. Am. Chem. Soc.*, 2002, **124**, 1560-1561.
173. R. D. Piner, J. Zhu, F. Xu, S. Hong and C. A. Mirkin, *Science*, 1999, **283**, 661-663.
174. S. Rozhok, R. Piner and C. A. Mirkin, *J. Phys. Chem. B*, 2003, **107**, 751-757.
175. D. Saya, T. Leïchlé, J. B. Pourciel, C. Bergaud and L. Nicu, *J. Micromech. Microeng.*, 2007, **17**, N1-N5.
176. J. Xu, M. Lynch, S. Nettikadan, C. Mosher, S. Vegasandra and E. Henderson, *Sens. Actuators B Chem.*, 2006, **113**, 1034-1041.
177. J. Gu, X. Xiao, B. R. Takulapalli, M. E. Morrison, P. Zhang and F. Zenhausern, *Journal of vacuum science & technology. B, Microelectronics*

and nanometer structures : processing, measurement, and phenomena : an official journal of the American Vacuum S, 2008, **26**, 1860-1865.

178. B. M. Rosen, G. Lligadas, C. Hahn and V. Percec, *J. Polym. Sci. A*, 2009, **47**, 3940-3948.
179. Scifinder, *Version 2018, Chemical Abstract Service: OH, 2018, RN 121-44-8, Calculated using Advanced Chemistry Development (ACD/Labs) Software V11.02 ACD/Labs 1994-2018*, Accessed 09 Aug, 2018.
180. H. Kim, H.-G. Kim, S. Kim and S. S. Kim, *J. Memb. Sci.*, 2009, **344**, 211-218.
181. R. Singh and G. M. Whitesides, in *The Chemistry of Sulphur-Containing Functional Groups*, eds. Saul Patai and Z. Rappoport, John Wiley & Sons Ltd., Chichester, UK, Editon edn., 1993, pp. 633-658.
182. K. A. Totaro, X. Liao, K. Bhattacharya, J. I. Finneman, J. B. Sperry, M. A. Massa, J. Thorn, S. V. Ho and B. L. Pentelute, *Bioconjug. Chem.*, 2016, **27**, 994-1004.
183. Z. Grabarek and J. Gergely, *Anal. Biochem.*, 1990, **185**, 131-135.
184. S. Flink, F. C. J. M. van Veggel and D. N. Reinhoudt, *Journal of Physical Organic Chemistry*, 2001, **14**, 407-415.
185. F. Zhang, K. Sautter, A. M. Larsen, D. A. Findley, R. C. Davis, H. Samha and M. R. Linford, *Langmuir.*, 2010, **26**, 14648-14654.
186. B. D. Mather, K. Viswanathan, K. M. Miller and T. E. Long, *Prog. Polym. Sci.*, 2006, **31**, 487-531.
187. D. P. Nair, M. Podgórski, S. Chatani, T. Gong, W. Xi, C. R. Fenoli and C. N. Bowman, *Chem. Mater.*, 2014, **26**, 724-744.
188. Y. Wang, J. Cai, H. Rauscher, R. J. Behm and W. A. Goedel, *Chem.–Eur. J.*, 2005, **11**, 3968-3978.
189. J. F. Moulder, W. F. Stickle, P. E. Sobol and K. D. Bomben, *Handbook of X-ray Photoelectron Spectroscopy*, Perkin-Elmer Corporation, 1993.
190. H. Min, P. L. Girard-Lauriault, T. Gross, A. Lippitz, P. Dietrich and W. E. Unger, *Anal. Bioanal. Chem.*, 2012, **403**, 613-623.
191. R. J. Pelham and Y. Wang, *Proc. Natl. Acad. Sci. U.S.A.*, 1997, **94**, 13661-13665.
192. J. Swift, I. L. Ivanovska, A. Buxboim, T. Harada, P. C. D. P. Dingal, J. Pinter, J. D. Pajerowski, K. R. Spinler, J.-W. Shin, M. Tewari, F. Rehfeldt, D. W. Speicher and D. E. Discher, *Science*, 2013, **341**, 1240104.
193. Z. Z. Khaing, R. C. Thomas, S. A. Geissler and C. E. Schmidt, *Materials Today*, 2014, **17**, 332-340.
194. K. Peng, J. Sun, Y. Wang, Y. Li, B. Zhang and B. Wang, *J. Appl. Polym. Sci.*, 2014, **131**, in press. DOI:10.1002/app.40930.
195. M. E. Smithmyer, L. A. Sawicki and A. M. Kloxin, *Biomater. Sci.*, 2014, **2**, 634-650.
196. W. L. Chen, M. Likhitpanichkul, A. Ho. and C. A. Simmons, *Biomaterials*, 2010, **31**, 2489-2497.
197. J. H. Wen, L. G. Vincent, A. Fuhrmann, Y. S. Choi, K. C. Hribar, H. Taylor-Weiner, S. Chen and A. J. Engler, *Nat. Mater.*, 2014, **13**, 979-987.
198. W. E. Hennink and C. F. van Nostrum, *Adv. Drug Deliv. Rev.*, 2002, **54**, 13–36.
199. B. Baroli, *Journal of pharmaceutical sciences*, 2007, **96**, 2197-2223.

200. B. N. Mason, J. P. Califano and C. A. Reinhart-King, in *Engineering Biomaterials for Regenerative Medicine*, ed. S. K. Bhatia, Springer, New York, Editon edn., 2012, pp. 19-37.
201. C. Yang, M. W. Tibbitt, L. Basta and K. S. Anseth, *Nat. Mater.*, 2014, **13**, 645-652.
202. M. T. Frey and Y.-L. Wang, *Soft Matter*, 2009, **5**, 1918-1924.
203. A. A. Beharry and G. A. Woolley, *Chem. Soc. Rev.*, 2011, **40**, 4422–4437.
204. D. J. W. Bullock, C. W. N. Cumper and A. I. Vogel, *J. Chem. Soc.*, 1965, 5316-5323.
205. T. K. Mudiyanselage and D. C. Neckers, *Soft Matter*, 2008, **4**, 768-774.
206. D. A. James, D. C.Burns and G. A. Woolley, *Protein Eng.*, 2001, **41**, 983–991.
207. A. A. Beharry and G. A. Woolley, *Chem. Soc. Rev.*, 2011, **40**, 4422-4437.
208. C. Brieke, F. Rohrbach, A. Gottschalk, G. Mayer and A. Heckel, *Angew. Chem. Int. Ed.*, 2012, **51**, 8446-8476.
209. L. Jianwei, N. Jun, Z. Yufei and H. Yong, *J. Photoch. Photobio. A*, 2010, **211**, 20-25.
210. A. Goulet-Hanssens, K. L. W. Sun, T. E. Kennedy and C. J. Barrett, *Biomacromolecules*, 2012, **13**, 2958-2963.
211. M. Sailer, L. W. Sun, O. Mermut, T. E. Kennedy and C. J. Barrett, *Biomaterials*, 2012, **33**, 5841-5847.
212. A. M. Rosales, K. M. Mabry, E. M. Nehls and K. S. Anseth, *Biomacromolecules*, 2015, **16**, 798-806.
213. I.-N. Lee, O. Dobre, D. Richards, C. Ballestrem, J. M. Curran, J. A. Hunt, S. M. Richardson, J. Swift and L. S. Wong, *ACS Appl. Mater. Interfaces*, 2018, **10**, 7765-7776.
214. J. Calbo, C. E. Weston, A. J. White, H. S. Rzepa, J. Contreras-Garcia and M. J. Fuchter, *J. Am. Chem. Soc.*, 2017, **139**, 1261-1274.
215. M. J. Rosenbluth, W. A. Lam and D. A. Fletcher, *Biophys. J.*, 2006, **90**, 2994-3003.
216. Y. Li, Y. He, X. Tong and X. Wang, *J. Am. Chem. Soc.*, 2005, **127**, 2402-2403.
217. B. Trappmann, J. E. Gautrot, J. T. Connelly, D. G. T. Strange, M. L. O. Yuan Li, M. A. C. Stuart, H. Boehm, B. Li, V. Vogel, J. P. Spatz, F. M. Watt and W. T. S. Huck, *Nat. Mater.*, 2012, **11**, 642-649.
218. J. E. Elliott, M. Macdonald, J. Nie and C. N. Bowman, *Polymer*, 2004, **45**, 1503-1510.

Appendix

Appendix 1 A link to time-lapsed video of MSC cultured in contact with nanoarrays is attached below showing that MSc has mobility to detach from a pattern and relocate on neighbouring patterns on the fabricated nanoarrays.

https://youtu.be/UIaiGt_9A9w

Appendix 2 A representative image of hMSC cultured in contact with MHA20-FN bridging between neighbouring patterns. Fibronectin pre-coated patterns were stained with fluorescently conjugated antibody (red) subsequent to the fixation of 24 h hMSC culture. Sample was stained with F-actin (green) and nuclei (blue). Scale bar represents 20 μm.

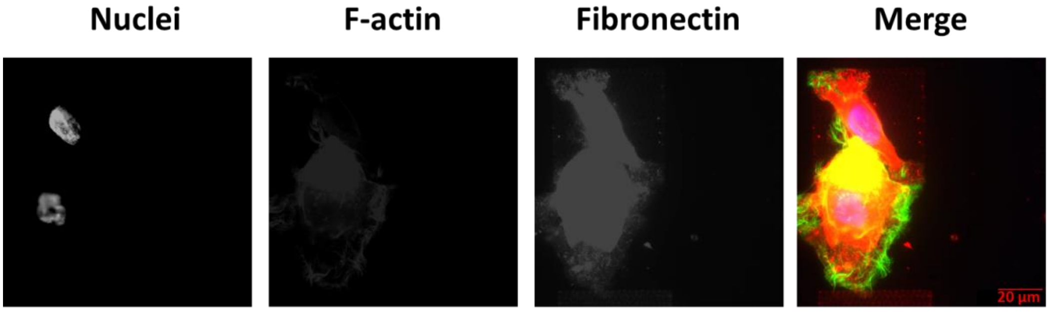

Appendix 3 An illustrative scheme showing indirect immunofluorescence mechanism. Unconjugated primary antibody was first bound to antigen within fixed cells or, in this case bound protein on surface. Multiple fluorophore-conjugated secondary antibodies were then bound to primary antibody.

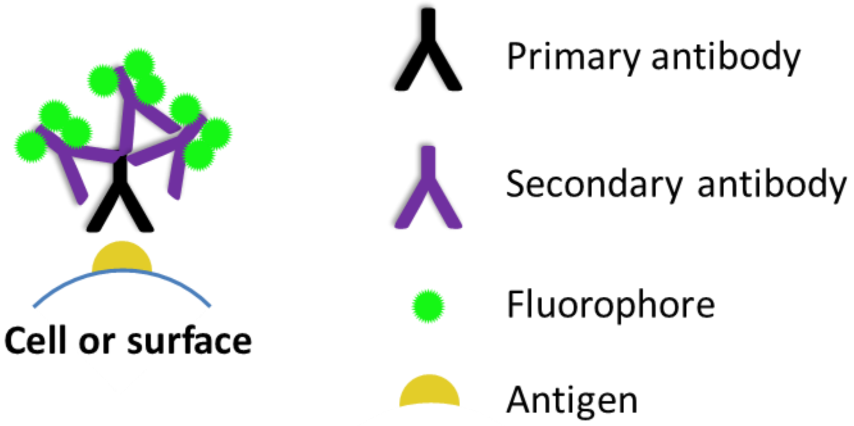

Appendix 4 Chondrocytes cultured in contact with MHA nanoarrays for 3 passages. Cells were fixed at 7 day at each passage and counterstained with collagen type II (green), pFAK$_{y397}$ (red) and nuclei (blue). Scale bars represent 50 µm.

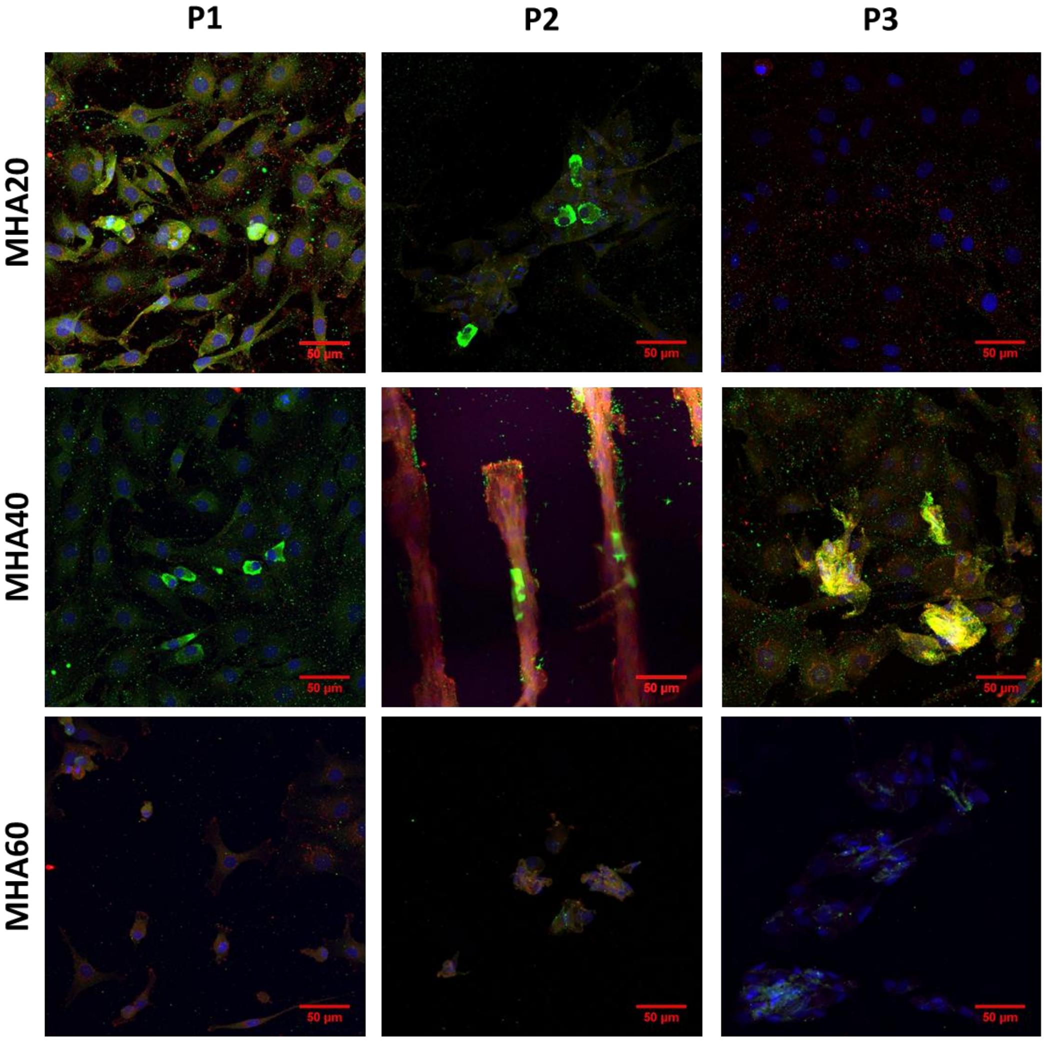

Appendix 5 Chondrocytes cultured in contact with AUT nanoarrays for 3 passages. Cells were fixed at 7 day at each passage and counterstained with collagen type II (green), $pFAK_{y397}$ (red) and nuclei (blue). Scale bars represent 50 µm.

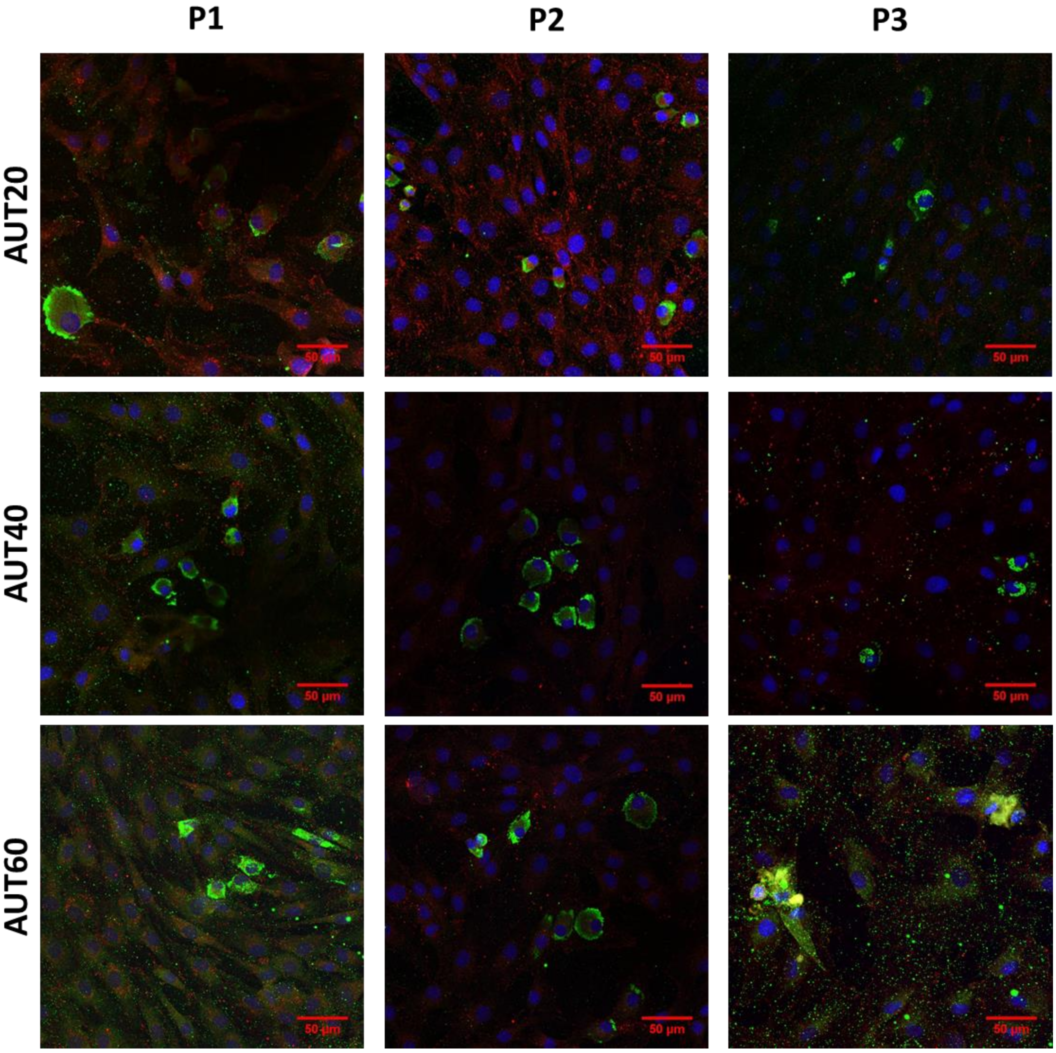

Appendix 6 Table shows the *p* values of one way-ANOVA of the normalised gene expression level of collagen type I expressed in chondrocyte at 1st passage in Figure 3.9, panel A.

Collagen I	MHA20	MHA40	MHA60	AUT20	AUT40	AUT60
MHA20		-- 0.21504	-- 0.249	-- 0.12258	-- 0.93363	-- 0.52803
MHA40	-- 0.21504		-- 0.70877	-- 0.53251	-- 0.10558	-- 0.36
MHA60	-- 0.249	-- 0.70877		-- 0.24842	-- 0.05209	-- 0.44371
AUT20	-- 0.12258	-- 0.53251	-- 0.24842		* 0.03198	-- 0.15943
AUT40	-- 0.93363	-- 0.10558	-- 0.05209	* 0.03198		-- 0.45454
AUT60	-- 0.52803	-- 0.36	-- 0.44371	-- 0.15943	-- 0.45454	

"--": $p > 0.05$, no significant difference. ; "*": $p < 0.05$, significant difference.

Appendix 7 Table shows the *p* values of one way-ANOVA of the normalised gene expression level of collagen type II expressed in chondrocyte at 1st passage in Figure 3.9, panel B.

Collagen II	**MHA20**	**MHA40**	**MHA60**	**AUT20**	**AUT40**	**AUT60**
MHA20		-- 0.70156	-- 0.89734	* 0.01358	-- 0.0651	* 0.01933
MHA40	-- 0.70156		-- 0.79358	* 0.02557	-- 0.10328	* 0.03617
MHA60	-- 0.89734	-- 0.79358		* 0.01762	-- 0.07979	* 0.02532
AUT20	* 0.01358	* 0.02557	* 0.01762		-- 0.20627	-- 0.24455
AUT40	-- 0.0651	-- 0.10328	-- 0.07979	-- 0.20627		-- 0.54293
AUT60	* 0.01933	* 0.03617	* 0.02532	-- 0.24455	-- 0.54293	

"--": $p > 0.05$, no significant difference; "*": $p < 0.05$, significant difference.

Appendix 8 Table shows the *p* values of one way-ANOVA of the normalised gene expression level of aggrecan expressed in chondrocyte at 1st passage in Figure 3.9, panel C.

Aggrecan	MHA20	MHA40	MHA60	AUT20	AUT40	AUT60
MHA20		-- 0.1874	-- 0.19506	-- 0.92102	-- 0.60612	* 0.02248
MHA40	-- 0.1874		-- 0.81736	-- 0.35041	-- 0.33748	* 0.03686
MHA60	-- 0.19506	-- 0.81736		-- 0.3766	-- 0.31386	** 0.00718
AUT20	-- 0.92102	-- 0.35041	-- 0.3766		-- 0.7053	* 0.01446
AUT40	-- 0.60612	-- 0.33748	-- 0.31386	-- 0.7053		* 0.01289
AUT60	* 0.02248	* 0.03686	** 0.00718	* 00.01446	* 0.01289	

"--": *p* > 0.05, no significant difference; "*": *p* < 0.05, significant difference; "**": *p* < 0.01, significant difference.

Appendix 9 Table shows the *p* values of one way-ANOVA of the normalised gene expression level of SOX9 expressed in chondrocyte at 1st passage in Figure 3.9, panel D.

SOX-9	MHA20	MHA40	MHA60	AUT20	AUT40	AUT60
MHA20		-- 0.73709	-- 0.99942	-- 0.34871	-- 0.43555	-- 0.13257
MHA40	-- 0.73709		-- 0.76933	-- 0.32532	-- 0.40183	-- 0.16638
MHA60	-- 0.99942	-- 0.76933		-- 0.48417	-- 0.50471	-- 0.23791
AUT20	-- 0.34871	-- 0.32532	-- 0.48417		-- 0.71658	-- 0.27168
AUT40	-- 0.43555	-- 0.40183	-- 0.50471	-- 0.71658		-- 0.90164
AUT60	-- 0.13257	-- 0.16638	-- 0.23791	-- 0.27168	-- 0.90164	

“--”: *p* > 0.05, no significant difference.

Appendix 10

Table S1. Formulations with ratios of AM/BIS/AZO monomers in DMF and EtOH.

Formula	Monomer/Crosslinker			Solvent System						
	AM (M)	BIS (mM)	AZO (mM)	EtOH (µL)	DMF (µL)	DMSO (µL)	H_2O (µL)	PBS(a) (µL)	Heating(b)	Observation(c)
1	1.65	26.26	10.12	--	500	--	500	225	--	x
2	1.72	27.37	--	--	225	--	725	225	--	x
3	1.65	26.26	--	--	500	--	500	225	--	x
4	1.84	29.22	--	--	150	--	725	225	--	hydrogel
5	1.84	29.22	--	225	150	--	500	225	--	hydrogel
6	1.84	29.22	11.26	--	150	--	725	225	--	precipitation
7	1.84	29.22	5.63	225	150	--	500	225	--	precipitation
8	1.92	30.60	2.95	225	100	--	500	225	--	precipitation
9	1.92	30.60	2.95	225	100	--	500	225	70°C	hydrogel
10	0.41	6.59	--	100	--	--	625	250	--	hydrogel
11	0.46	7.33	--	45	--	--	580	250	--	hydrogel
12	0.41	6.59	--	45	100	--	580	250	--	hydrogel
13	0.46	7.33	--	45	200	--	380	250	--	x
14	0.46	7.33	--	--	625	--	--	250	--	x
15	0.41	6.59	--	413	100	--	212	250	--	x

(a) PBS: phosphate buffered saline

(b) "--" in this column indicates reaction was performed at room temperature.

(c) "x" in this column indicates no gel formation observed, mixture remained liquid

Table S2. Formulations with minimal AM/BIS monomers in different solvent systems.

Formula	Monomer/Crosslinker			Solvent System						
	AM (M)	BIS (mM)	AZO (mM)	EtOH (µL)	DMF (µL)	DMSO (µL)	H_2O (µL)	PBS[a] (µL)	Heating[b]	Observation[c]
16	0.46	7.33	--	625	--	--		250	--	x
17	0.46	7.33	--	--	--	--	625	250	--	x
18	2.81	0.14	--	--	--	--	765	225	--	hydrogel
19	2.81	0.11	--	--	--	--	765	225	--	hydrogel
20	2.81	0.07	--	--	--	--	765	225	--	hydrogel
21	2.79	0.14	--	225	--	--	550	225	--	hydrogel
22	2.79	0.03	--	225	--	--	550	225	--	x

(a) PBS: phosphate buffered saline

(b) "--" in this column indicates reaction was performed at room temperature.

(c) "x" in this column indicates no gel formation observed, mixture remained liquid

Table S3. Formulation of AM/BIS/AZO polymer heated during polymerisation.

Formula	Monomer/Crosslinker			Solvent System						
	AM (M)	BIS (mM)	AZO (mM)	EtOH (μL)	DMF (μL)	DMSO (μL)	H_2O (μL)	PBS[(a)] (μL)	Heating[(b)]	Observation[(c)]
23	2.87	45.68	4.40	100	--	--	600	--	70℃	hydrogel
24	0.80	12.72	6.13	200	--	--	300	--	70℃	hydrogel
25	1.32	20.92	10.08	100	--	--	200	--	70℃	hydrogel
26	0.45	7.13	3.43	400	--	--	500	--	70℃	x
27	0.45	7.13	3.43	--	--	--	900	--	70℃	precipitate
28	0.45	7.13	3.43	--	--	200	700	--	70℃	precipitate
29	0.45	7.13	3.43	--	--	200	700	--	70℃	precipitate
30	0.45	7.13	3.43	--	--	200	700	--	70℃	precipitate
31	0.45	7.13	3.43	--	--	600	300	--	70℃	precipitate
32	0.45	7.13	3.43	--	--	600	300	--	70℃	precipitate
33	0.40	6.36	3.06	100	--	--	100	800	70℃	precipitate

(a) PBS: phosphate buffered saline

(b) "--" in this column indicates reaction was performed at room temperature.

(c) "x" in this column indicates no gel formation observed, mixture remained liquid

Table S4. Formulations with high concentrations of monomers.

Formula	Monomer/Crosslinker			Solvent System						
	AM (M)	BIS (mM)	AZO (mM)	EtOH (μL)	DMF (μL)	DMSO (μL)	H_2O (μL)	PBS[(a)] (μL)	Heating[(b)]	Observation[(c)]
34	0.50	--	0.35	--	--	--	880	--	--	precipitate
35	0.80	0.28	4.46	--	--	--	650	--	--	precipitate
36	0.66	0.23	3.68	--	--	350	450	--	--	x
37	0.66	0.23	3.68	--	--	250	550	--	--	x
38	0.66	0.23	3.68	250	--	--	550	--	--	x
39	2.56	0.08	3.55	225	--	--	420	225	--	precipitate
40	2.30	0.07	3.19	325	--	--	420	225	--	precipitate
41	1.72	0.07	3.19	425	--	--	320	225	--	precipitate
42	1.15	0.07	3.19	525	--	--	220	225	--	precipitate
43	1.76	--	3.26	425	--	--	300	225	--	precipitate
44	1.76	--	3.26	--	--	225	500	225	--	precipitate
45	1.72	0.07	3.19	--	--	225	520	225	--	x
46	0.59	0.07	--	--	--	225	500	225	--	x
47	1.15	0.07	3.19	--	--	225	520	225	--	x
48	0.57	0.07	3.19	--	--	325	420	225	--	x

(a) PBS: phosphate buffered saline

(b) "--" in this column indicates reaction was performed at room temperature.

(c) "x" in this column indicates no gel formation observed, mixture remained liquid

Table S5. Formulations of AM/BIS/AZO monomers with various solvents.

Formula	Monomer/Crosslinker			Solvent System						
	AM (M)	BIS (mM)	AZO (mM)	EtOH (μL)	DMF (μL)	DMSO (μL)	H_2O (μL)	PBS[a] (μL)	Heating[b]	Observation[c]
49	2.30	0.07	1.59	325	--	--	420	225	--	hydrogel
50	1.72	0.07	1.59	425	--	--	320	225	--	hydrogel
51	1.15	0.07	1.59	525	--	--	220	225	--	hydrogel
52	1.76	--	3.26	--	--	225	500	225	--	hydrogel
53	1.76	0.04	1.63	--	--	225	500	225	--	hydrogel
54	1.17	0.04	1.63	--	--	125	600	225	--	precipitate
55	1.17	0.04	1.63	--	--	100	625	225	--	hydrogel
56	1.76	--	1.63	--	--	225	300	425	--	hydrogel
57	1.06	--	1.47	--	--	100	200	750	--	precipitate
58	1.06	--	1.47	--	--	100	725	225	--	precipitate
59	1.17	--	1.63	--	--	225	200	525	--	precipitate
60	1.06	--	1.47	--	--	100	725	225	--	hydrogel
61	0.59	--	1.63	--	--	100	625	225	--	x
62	1.17	0.04	1.63	--	--	225	500	225	--	hydrogel

[a] PBS: phosphate buffered saline

[b] "--" in this column indicates reaction was performed at room temperature.

[c] "x" in this column indicates no gel formation observed, mixture remained liquid

Table S5. Continued.

Formula	Monomer/Crosslinker			Solvent System						
	AM (M)	BIS (mM)	AZO (mM)	EtOH (μL)	DMF (μL)	DMSO (μL)	H_2O (μL)	PBS[a] (μL)	Heating[b]	Observation[c]
63	0.59	--	1.63	--	--	225	100	625	--	x
64	1.76	--	0.81	--	--	225	300	425	--	hydrogel
65	1.17	--	0.41	--	--	113	200	637	--	hydrogel
66	1.13	--	0.16	--	--	45	200	737	--	hydrogel
67	1.17	--	0.81	--	--	225	200	525	--	hydrogel
68	1.17	0.04	0.41	--	--	113	200	637	--	hydrogel
69	1.17	0.04	0.16	--	--	45	200	705	--	hydrogel
70	1.76	--	8.14	200	--	225	300	225	--	hydrogel
71	1.59	--	7.37	225	--	100	300	425	--	precipitate
72	1.56	--	7.23	120	--	220	300	430	--	precipitate
73	1.56	--	7.23	220	--	220	300	330	--	precipitate
74	2.45	--	7.27	225	--	100	375	150	--	precipitate
75	2.20	--	3.40	225	--	100	360	225	--	hydrogel

[a] PBS: phosphate buffered saline

[b] "--" in this column indicates reaction was performed at room temperature.

[c] "x" in this column indicates no gel formation observed, mixture remained liquid

Table S6. Formulations of AM/AZO polymer using improved conditions based on previous formulations.

Formula	Monomer/Crosslinker			Solvent System						
	AM (M)	BIS (mM)	AZO (mM)	EtOH (µL)	DMF (µL)	DMSO (µL)	H_2O (µL)	PBS[a] (µL)	Heating[b]	Observation[c]
76	2.20	--	6.79	225	--	100	360	225	--	hydrogel with precipitated particulates
77	2.20	--	5.10	225	--	100	360	225	--	hydrogel with precipitated particulates
78	2.20	--	3.40	180	--	60	360	310	--	hydrogel
79	2.20	--	6.79	180	--	60	360	310	--	hydrogel with precipitated particulates
80	2.20	--	3.40	100	--	60	360	390	--	hydrogel with precipitated particulates
81	2.20	--	3.40	100	--	80	360	370	--	hydrogel

[a] PBS: phosphate buffered saline

[b] "--" in this column indicates reaction was performed at room temperature.

[c] "x" in this column indicates no gel formation observed, mixture remained liquid

Table S6. Continued.

Formula	Monomer/Crosslinker			Solvent System						
	AM (M)	BIS (mM)	AZO (mM)	EtOH (µL)	DMF (µL)	DMSO (µL)	H_2O (µL)	PBS[(a)] (µL)	Heating[(b)]	Observation[(c)]
82	2.03	--	3.13	100	--	80	360	450	--	hydrogel with precipitated particulates
83	4.05	--	3.13	100	--	80	720	90	--	hydrogel
84	1.01	--	3.13	100	--	80	180	630	--	precipitation
85	4.05	--	3.13	100	--	160	720	10	--	x
86	4.40	--	6.79	100	--	80	720	10	--	precipitation

(a) PBS: phosphate buffered saline

(b) "--" in this column indicates reaction was performed at room temperature.

(c) "x" in this column indicates no gel formation observed, mixture remained liquid

Appendix 11 A chart of Young's modulus measurements of the hydrogels made from the four selected candidate formulations comparing the differences between before and after 3 h photoirradiation at 365 nm. p-Values indicated from Kruskal-Wallis tests.

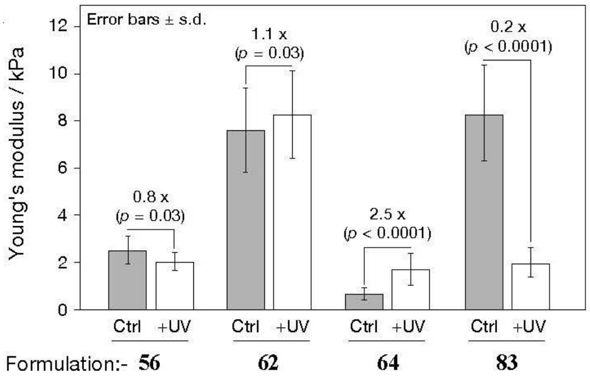

The selected candidates were photoirradiated for 3 h (+UV) and young's modulus was measured. Of all the selected candidates, formulation 83 showed most significant stiffness change upon irradiation. This formulation was then selected for further experiments and abbreviated as AZO1.

Appendix 12 A novel calculation system developed and provided by David Richards for the concentration of monomer and crosslinker involved in hydrogel systems. T represents total concentration of monomer and AZO-based crosslinker within hydrogels, presented as % (w/v). C represents percentage of AZO-based crosslinker involved in total monomer/crosslinker, presented as % (w/w).

$$T\ (w/v) = \frac{acrylamide\ (g) + AZO\ (g)}{total\ volume\ (mL)} 100\%$$

$$C\ (w/w) = \frac{AZO\ (g)}{acrylamid\ (g) + AZO(g)} 100\%$$

Appendix 13 A graph of swelling ratio against time. AZO2-PA hydrogel with increased concentration of AZO2 crosslinker resulted in increased degree of swell within hydrogel network. The experiments were conducted and results were kindly provided by David Richards.